CONTENTS

Measurement of heart chambers and mediastinal vascular structures on raw axial chest MDCT in the pediatric age group

Sercin Ozkok, Servet Erdemli, Ahmet Aslan, Adnan Kabaalioglu

Istanbul Medeniyet University, Goztepe Training and Research Hospital, Department of Radiology, Istanbul, Turkey

SUMMARY

Determining the normal range of mediastinal vascular structures and heart chambers is important for accurate evaluation and diagnosis of cardiopulmonary diseases. The aim of this work was to determine the average sizes of heart chambers, mediastinal vascular structures, and the ratio of the main pulmonary artery-to-ascending aorta (MPA-to-AA) in children without congenital or acquired cardiopulmonary diseases on contrast-enhanced (CE) chest multidetector computed tomography (MDCT). In total, 356 participants (range 0-216 months) were enrolled. The interobserver correlation (ICC) analysis performed and P-value is considered significant if <0.05. The mean diameters for the left and right ventricle and atrium, ascending aorta, descending aorta at the level of the mediastinum, descending aorta at the level of the diaphragm, main pulmonary artery, right pulmonary artery, and MPA-to-AA ratio were revealed for 6 age groups. Mediastinal vascular structures have excellent and heart chambers have a substantial-to-excellent ICC agreement. The diameters of heart chambers and mediastinal vascular structures on CE-chest MDCT are easy to measure and might be used as a reference to refer patients for further investigations.

Corresponding author:
Sercin Ozkok, MD. Istanbul Medeniyet University, Goztepe Training and Research Hospital, Department of Radiology, Istanbul, Turkey. Phone: +905055022882. E-mail: sercinbas2005@gmail.com

INTRODUCTION

Congenital or acquired cardiopulmonary diseases may alter the size of the heart chambers and mediastinal great vessels in the pediatric age. Reliable and reproducible methods for measuring these cardiovascular structures are critical not only for diagnosis and follow-up but also for determining the appropriate treatment strategies (Rossi and Vassanelli, 2003; Pritchett et al., 2003; Leung et al., 2008). These values might help clinician for assessing the cardiovascular pathologies in daily pediatric cardiology and radiology practice.

Heart chambers and mediastinal great vessels can be assessed by two-dimensional echocardiography, invasive conventional catheter angiography, electrocardiogram (ECG) gated, or non ECG-gated multidetector computed tomography (MDCT), cardiovascular magnetic resonance imaging (MRI). However, MDCT of the chest is one of the most commonly performed radiologic examinations in pediatric age, which is usually carried out to assess the lung, heart and extracardiac structures. Despite the fact

that the heart and mediastinal vascular system are included in the axial chest MDCT, basal measurements are generally made by visual desicion in daily practice and cardiovascular findings are commonly underestimated (Choy et al., 2013; Sverzellati et al., 2016).

In the literature, normal values of mediastinal great vessles in children and young adults have been assessed by echocardiography (Poutanen et al., 2013), conventional catheter angiography (Rammos et al., 2005) and cardiac MRI (Voges et al., 2012). Besides, the normal ranges of heart chambers on raw-axial chest MDCT have been evaluated in adults (Dogan et al., 2006; Long et al., 2010; Al-Mousily et al., 2010). However, to our knowledge there is no study that has evaluated the normal sizes of heart chambers on raw axial CE-chest MDCT in pediatric patients. This is the first study in which the diameters of heart chambers have been evaluated in healthy children on raw axial chest MDCT.

In this study, we aimed to determine the normal values of the heart chambers [right atrium (RA), left atrium (LA), right ventricle (RV), and left ventricle (LV)] and mediastinal vascular structures [ascending aorta (AA), descending aorta at the level of the mediastinum (DA-m) and diaphragm (DA-d), main pulmonary artery (MPA), left pulmonary artery (LPA), right pulmonary artery (RPA)] in children according to their age groups who underwent CE-chest MDCT.

MATERIALS AND METHODS

Ethical approval of this retrospective study was obtained from the Ethical Committee of the Istanbul Medeniyet University, Goztepe Training and Research Hospital. The informed consent was waived.

Study Group

Between January 2015 and June 2018, all chest MDCTs with or without contrast agent administration of 1396 pediatric patients [aged under 216 months (18 years)] performed at the well-established pediatric institution of our hospital were retrospectively evaluated. The radiologic findings of pneumonia, minor trauma with mild pneumothorax and/or mild pleural effusion, and pulmonary nodule revealed on CE-chest MDCT included in the study. CE-chest MDCT of patients with the exact diagnosis of respiratory and systemic disease, congenital heart disease (intracardiac shunts, failure or heart valves stenosis), and pulmonary hypertension confirmed by echocardiography revealed from the hospital information system were excluded from the study. Examinations without contrast agent administration and with severe image artifacts were also excluded. The patients out of normal body height and weights according to their age reported in the hospital information system also excluded from the study. The remaining 356 CE-chest MDCT of the 1396 patients were included in the study (Fig. 1).

Demographic data such as sex, age with initial and exact diagnosis, echocardiography reports of patients are obtained from the hospital information system. The patients were divided into six groups according to their age: Group 1, 0-12 months (0-1 year); Group 2, 13-36 months (1-3 years); Group 3, 37-72 months (3-6 years); Group 4, 73-120 months (6-10 years); Group 5, 121-180 months (10-15 years) and Group 6, 181-216 months (15-18 years) (Table 1). According to the medical records, the body weight and height of all patients in the study group were within normal limits according to their age groups.

Chest Multidetector Computed Tomography Protocol

All examinations were performed with a 64 detectors MDCT machine (Discovery, GE Healthcare, Milwaukee, WI, USA). A 300 mg/ml of non-ionic contrast material (1-2 ml/kg and maximum volume of 20-50 cc) with an injection rate of 2-3 cc/second was administered via a peripheral vein. Bolus tracking technique was used and the region of interest was located in the descending aorta. The areas between the apex and the base of the lungs were scanned. Variable dose parameters were applied according to patient weight stated in our institutional pediatric protocol (range 30-60 mA and 80-120 kV) with dose reducing technique. The scan parameters were as follows: reconstruction interval 0.75, the pitch factor 0.67-1.72, rotation time 0.5-0.75 seconds, and the collimation 64 x 0.625 mm.

1396 patients referred for axial chest CT between January 2015 and June 2018

784 non-contrast enhanced chest CT

28 congenital heart disease or pulmonary hypertension

23 chronical-interstitial lung disease, connective tissue disease orarteritis

16 respiratory distress syndrome or cystic fibrosis

13 congenital chest wall or skeletal abnormalities

32 major trauma, massive pleural effusion, empyema

26 extensive pulmonary infection,

18 proven malignancy

356 patients with axial CE chest CT reviewed by 2 blinded observers

222 normal chest CT findings

94 focal parenchymal consolidation

15 subsegmental atelectasis

8 mild pleural effusion

6 mild pneumothorax

6 pulmonary nodule

5 focal pulmonary contusion

Fig. 1.- Study flow chart with the inclusion and exclusion of the patients.

Table 1. Demographic data of the study groups.

Group	Age Groups (months)	Number (%)	Mean age ± SD (months)	Female n (%)	Male n (%)
Group 1	0 - 12	53 (15)	6.1 ± 2.8	15 (28.3)	38 (71.7)
Group 2	13 - 36	62 (17)	21.4 ± 6.5	23 (37.1)	39 (62.9)
Group 3	37 - 72	45 (13)	55.3 ± 10.6	22 (48.9)	23 (51.1)
Group 4	73 - 120	56 (16)	93.8 ± 12.4	32 (57.1)	24 (42.9)
Group 5	121 - 180	70 (20)	148.5 ± 19	33 (47.1)	37 (52.9)
Group 6	181 - 216	70 (20)	199.8 ± 11.1	22 (31.4)	48 (68.6)
Total	0 - 216	**356 (100)**	94.9 ± 72.1	147 (41.3)	209 (58.7)

Results are presented as number (%) and mean ± SD where applicable.

Measurements

Two radiologists, blinded to the patient's clinical findings and diagnosis, measured the diameters of mediastinal vascular structures and heart chambers independently. All the measurements were performed on raw axial CE-chest MDCT after image reconstruction of 1.25 mm slice thickness on a workstation (Centricity, GE Healthcare, Milwaukee, WI, USA) at standardized mediastinal window settings (window level, 30-40 HU; and window width of 300-400 HU). The diameter of LV and RV were measured as the greatest distance between the interventricular septum and lateral wall from inner to inner contour perpendicular to the long axis of the ventricle, LV below the level of the mitral valve and RV on midventricular level (Fig. 2). LA and RA were measured in its largest anterior-posterior dimension from inner-to-inner contour to emulate linear LA measurement taken on M-mode echocardiography and two-dimensional parasternal views (Fig. 3) (Lu et al., 2012). The largest diameter of pulmonary arteries was measured on the axial plane, perpendicular to their long axis. MPA was measured at 2-3 millimeters above the pulmonary valve, RPA and LPA were measured 1.5-2 cm after the pulmonary artery bifurcation (Fig. 4). AA and DA-m measured at the level of pulmonary artery bifurcation (Fig. 5a), and DA-d measured at the level of diaphragm (Fig. 5b). The mean MPA-to-AA ratio was also calculated according to all age groups.

Statistical analysis

SPSS version 20.0 software (IBM Corporation, Armonk, NY, USA) was used for statistical analysis. The results were expressed as the mean of both observers' measurements and presented as the mean ± standard deviation. Pearson's correlation analysis was used to evaluate the relationship between the age and the measurements. Analysis of variance (ANOVA) test was used to compare the measurements of six age groups. A two-way mixed model was used to evaluate intraclass correlation (ICC) analysis to evaluate the agreement between two readers. ICC coefficient value higher than 0.8 indicates excellent, between 0.8-0.6 indicates substantial, between 0.6-0.4 indicates moderate, and lower than 0.4 indicates poor agreements. Results were accepted as statistically significant if the p-value is lower than 0.05.
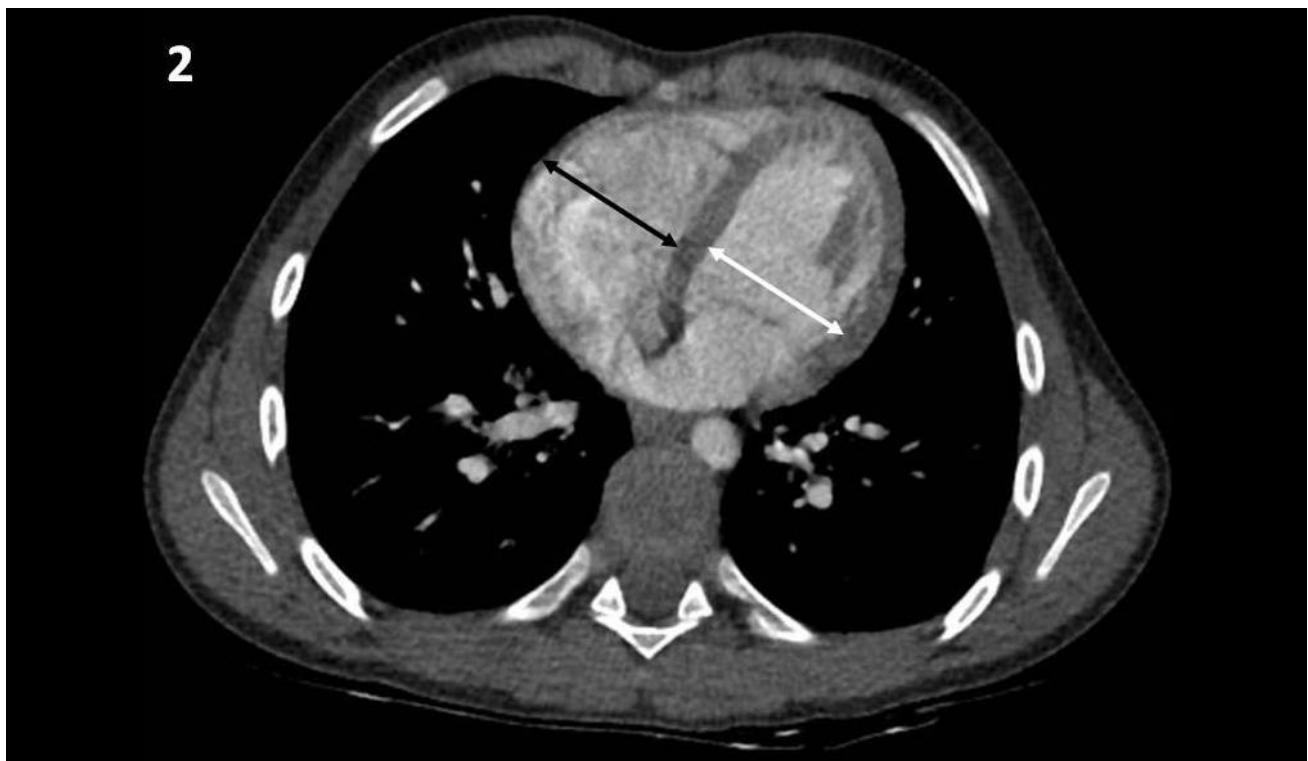
Fig. 2.- Contrast enhanced chest MDCT image demonstrates the measurement of the right (black arrow) and left (white arrow) ventricle between interventricular septum and lateral wall from inner to inner contour perpendicular to the long axis of the ventricle, left ventricle below the level of the mitral valve and the right ventricle on midventricular level.
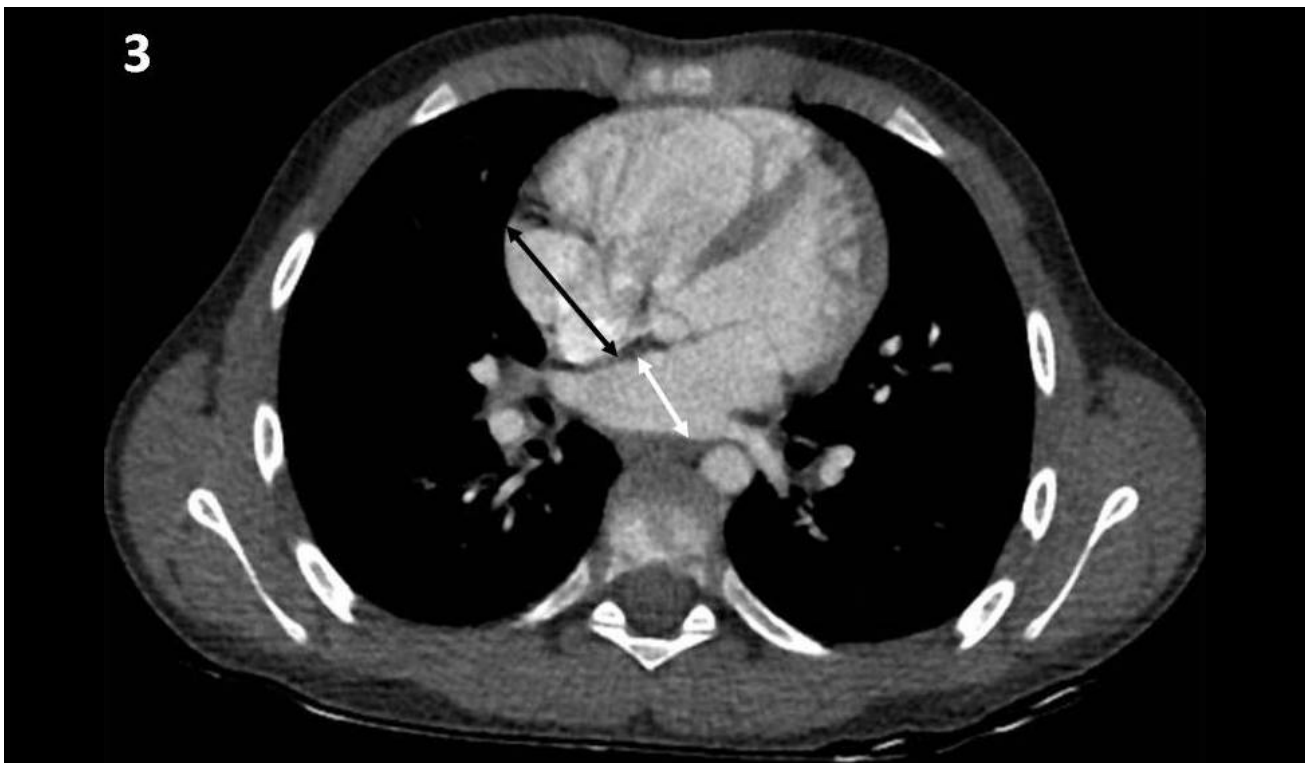
Fig. 3.- Contrast enhanced chest MDCT image demonstrates the measurement of the right (black arrow) and left (white arrow) atrium in its largest anterior-posterior dimension from inner to inner contour.
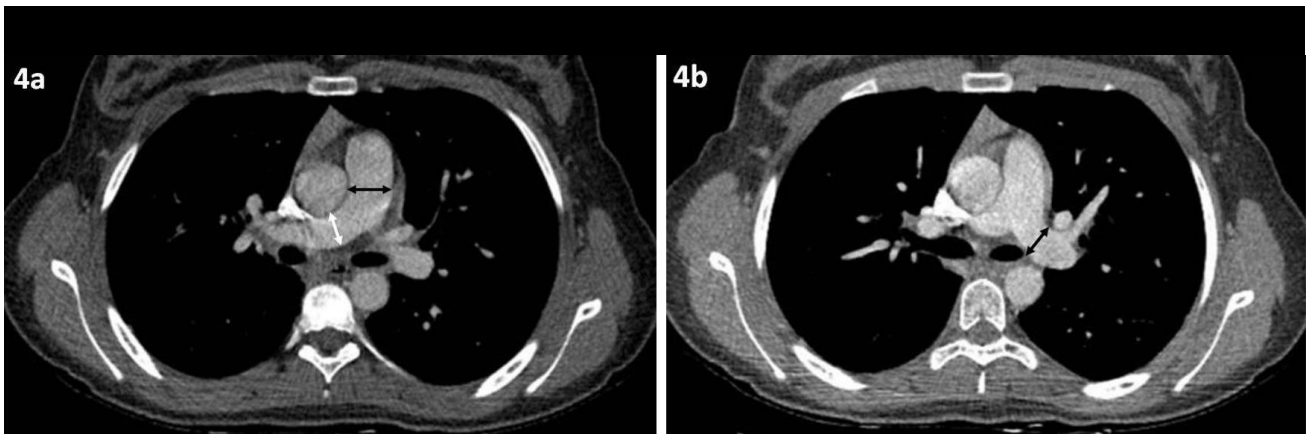
Fig. 4.- Contrast-enhanced chest MDCT image demonstrates the measurement of the main (**a**, black arrow), right (**a**, white arrow) and left pulmonary artery (**b**, black arrow) perpendicular to their long axis.
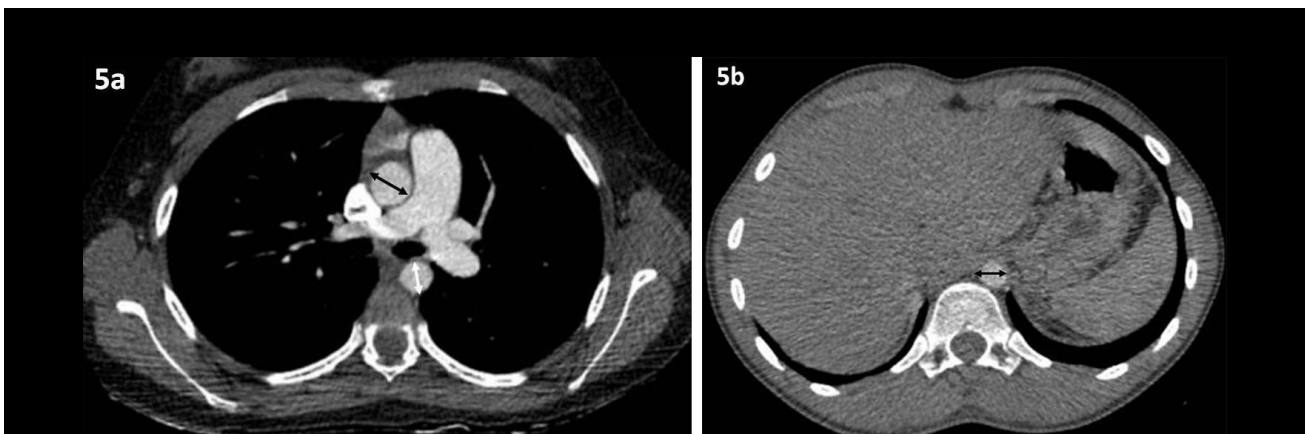

Fig. 5.- Contrast-enhanced chest MDCT image demonstrates the measurement of the ascending (**a**, black arrow**)**, proximal descending aorta (**a**, white arrow) at the level of pulmonary artery bifurcation and distal descending aorta at the level of diaphragm (**b**, black arrow).

RESULTS

In this retrospective study CE-chest MDCT examinations of 356 patients with a male: female ratio of 1.8: 1 (209 male and 147 female). The mean patient age was 94.9 ± 72.1 (range 2 to 216 months). The distribution of patients in age groups is demonstrated in Table 1. Preliminary clinical diagnosis were as follows; pneumonia (n = 164, 34%), minor trauma (mild pneumothorax, mild pleural effusion) (n = 90, 18%), chronic cough (n=74, 15%),interstitial lung disease (n = 58, 12%), congenital heart disease or pulmonary hypertension (n = 42, 9%), respiratory distress (n = 31, 6%), lung metastasis (n = 27, 6%). Chest CT findings of the patients in the study group were as follows: normal CT findings (n = 222, 62%), focal parenchymal consolidation (n=94, 26%), subsegmental atelectasis (n = 15, 4%), mildpleural effusion (n = 8, 3%), mild pneumothorax (n = 6, 2%), pulmonary nodule (n=6, 2%), and focal pulmonary contusion (n = 5, 1%) (Fig.1).

The mean diameters of mediastinal vascular structures and cardiac chambers for all groups were measured by two observers and the ICC values among observers demonstrated in Tables 2 and 3. The ICC analysis revealed that the measurements of mediastinal vascular structures have excellent (ICC between 0.887 - 0.956) and heart chambers have substantial-to-excellent (ICC between 0.681 - 0.958) agreement.

The mean diameters of each cardiovascular structure, revealed by the sum of the measurements of two observers, showed high, positive, and statistically significant correlations with the patients' age (p < 0.001) (Table 4). But there was no statistically significant correlation between the MPA-to-AAratio and the patients' age (p = 0.782) (Table 4). When we evaluated the differences between the diameter of the left and right pulmonary artery, there was no statistically significant difference (p = 0.853). The mean diameters of mediastinal vascular structures and

Table 2. The mean diameter of the vascular structures and the ratio of the pulmonary artery to ascending aorta with intraclass correlation coefficients analysis among the two observers.

		AA (mm)	DA-m (mm)	DA-d (mm)	MPA (mm)	RPA (mm)	LPA (mm)	MPA/AA
Group 1	Observer 1	10.7 ± 1.75	7.94 ± 1.34	6.85 ± 0.91	11.32 ± 1.77	7.08 ± 1.17	7.51 ± 1.41	1.07 ± 0.18
	Observer 2	11.23 ± 1.59	7.08 ± 1.11	7.11 ± 0.97	11.23 ± 1.86	7.62 ± 1.47	7.66 ± 1.39	1 ± 0.12
Group 2	Observer 1	13.27 ± 1.98	9.78 ± 1.46	8.29 ± 1.23	13.29 ± 2.41	9.3 ± 2.33	9 ± 1.51	1.01 ± 0.19
	Observer 2	13.73 ± 1.87	9.5 ± 1.38	8.45 ± 1.13	13.34 ± 2.22	9.58 ± 2.32	9.27 ± 1.48	0.98 ± 0.15
Group 3	Observer 1	14.73 ± 3.12	11.71 ± 1.96	9.49 ± 1.56	15.73 ± 2.65	11.2 ± 3.28	10.64 ± 1.71	1.09 ± 0.24
	Observer 2	16.33 ± 2.71	11.22 ± 1.63	10.02 ± 1.49	15.89 ± 2.62	11.87 ± 3.27	11.18 ± 1.54	0.98 ± 0.16
Group 4	Observer 1	16.96 ± 2.65	13.55 ± 1.81	10.93 ± 1.45	17.29 ± 3.28	12.61 ± 3.5	11.5 ± 2.19	1.04 ± 0.24
	Observer 2	19.04 ± 2.44	12.8 ± 1.67	11.52 ± 1.5	17.48 ± 3.12	13.38 ± 3.25	12.63 ± 2.03	0.92 ± 0.14
Group 5	Observer 1	20.01 ± 3.12	15.77 ± 2.21	12.86 ± 1.96	20.53 ± 3.56	13.4 ± 2.94	12.79 ± 2.06	1.04 ± 0.22
	Observer 2	22.04 ± 2.73	15.17 ± 2.01	13.89 ± 2.04	20.91 ± 3.35	14.61 ± 2.87	14.3 ± 2.04	0.95 ± 0.12
Group 6	Observer 1	22.33 ± 2.82	17.91 ± 2.3	14.86 ± 1.87	21.3 ± 2.68	15.14 ± 3.49	13.71 ± 2.32	0.96 ± 0.13
	Observer 2	23.97 ± 2.19	17 ± 1.99	16.07 ± 2.48	22.31 ± 2.92	16.01 ± 3.21	15.46 ± 2.08	0.93 ± 0.11
Total		17.4 ± 4.8	12.9 ± 3.7	11.2 ± 3.3	17.1 ± 4.6	12 ± 3.9	11.5 ± 2	1.02 ± 0.47
ICC (95% CI)		0.935 (0.810-0.938)	0.946 (0.924-0.961)	0.942 (0.901-0.963)	0.956 (0.945-0.65)	0.887 (0.781-0.933)	0.887 (0.781-0.933)	0.691 (0.533-0.785)
P		<0.0001	<0.0001	<0.0001	<0.0001	<0.0001	<0.0001	<0.0001

Results are presented as mean ± SD. **P:** p value of ICC. Abbreviations: **AA:** ascending aorta, **DA-m:** descending aorta at the level of the mediastinum, **DA-d:** descending aorta at the level of the diaphragm, **MPA:** main pulmonary artery, **RPA:** right pulmonary artery, **LPA:** left pulmonary artery, **MPA/AA:** the MPA-to-AA ratio.

heart chambers with the MPA-to-AA ratio for all six age groups are shown in Tables 5 and 6. There was no significant difference between age groups and the MPA-to-AA ratio.

DISCUSSION

In daily clinical practice, two-dimentional echocardiography is commonly used as a first-line imaging tool for diagnosis and follow-up of the disorders of the heart and the mediastinal great vessels. However, its operator-dependent quality and impaired acoustic window limit the performance. Besides, conventional catheter angiography due to invasiveness and containing ionizing radiation has limited use (Bacher et al., 2011). Also, MRI is a non-invasive, ionized radiation-free imaging tool widely used in assessment of the heart structures and great vessels in children with congenital heart disease. However, cardiac MRI requires longer scanning time and deeper anesthesia compared with MDCT (Sanborn et al., 2005).

On the other hand, CE-chest MDCT has become one of the most preferred diagnostic choice in the assessment of congenital or acquired cardiopulmonary disease in the pediatric age population (Fitzgerald et al., 1987; Frush and Herlong, 2005; Paterson and Frush, 2007; Karazincir et al., 2008). CE-chest MDCT has led to an expanded application to evaluate lung in congenital heart disease in the pre-operative or postoperative period compared to two-dimentional echocardiography, conventional catheter angiography, and cardiac MRI (edwards et al., 1998; Ng et al., 1999; Gilkeson et al., 2003; Poutanen et al., 2013). Nevertheless, MDCT has some advantages and disadvantages in clinical practice. The main disadvantege is the exposure to ionizing radiation, especially in younger children because of the higher sensitivity to radiation. However, by the advances in detector technology and dose reduction techniques, MDCT provides an increase in temporal and spatial resolution, motion artifact, and a decrease in ionizing radiation.

Table 3. The mean diameter of the heart chambers with intraclass correlation coefficients analysis among the two observers.

		LV (mm)	RV (mm)	LA (mm)	RA (mm)
Group 1	Observer 1	13.68 ± 2.53	21.23 ± 3.3	17.94 ± 2.62	14.21 ± 3.16
	Observer 2	17.68 ± 2.83	20.6 ± 3.79	22.83 ± 3.66	16.81 ± 3.17
Group 2	Observer 1	17.19 ± 3.72	24.26 ± 3.18	21.55 ± 4.02	16.84 ± 3.24
	Observer 2	21.11 ± 3.57	24.92 ± 3.89	26.22 ± 3.96	18.55 ± 2.66
Group 3	Observer 1	20.02 ± 3.51	28.67 ± 4.95	26.64 ± 5.5	18.87 ± 3.45
	Observer 2	24.69 ± 3.67	30.31 ± 5.48	31.84 ± 4.31	22.4 ± 3.97
Group 4	Observer 1	22.93 ± 4.69	32.96 ± 4.62	27.66 ± 5.33	20.98 ± 4.47
	Observer 2	28.18 ± 4.04	34.69 ± 4.9	35.21 ± 5.18	24.62 ± 4.49
Group 5	Observer 1	25.62 ± 5.31	37.03 ± 5.15	30.43 ± 5.67	22.39 ± 4.12
	Observer 2	32.3 ± 5.18	38.83 ± 5.51	39.81 ± 6.35	27 ± 5.26
Group 6	Observer 1	27.9 ± 5.78	39.84 ± 4.91	31.63 ± 5.87	23.04 ± 4.41
	Observer 2	33.57 ± 5.41	42.27 ± 6.02	41.94 ± 5.7	27.96 ± 4.93
Total		24.2 ± 6.6	32 ± 8.5	30 ± 7.3	21.5 ± 5.2
ICC (95% CI)		0.958 (0.933-0.972)	0.777 (0.018-0.917)	0.768 (0.216-0.898)	0.681 (0.147-0.876)
P		<0.0001	<0.0001	<0.0001	<0.0001

Results are presented as mean ± SD. **P:** p value of ICC. Abbreviations: **LA:** left atrium, **LV:** left ventricle, **RA:** right atrium, **RV:** right ventricle.

Table 4. Mean diameters of the diameters of vascular structures and heart chambers and correlation with age.

	Measurements (mm)	r	P value
AA	17.4 ± 4.8	0.888	<0.0001
DA-m	12.9 ± 3.7	0.903	<0.0001
DA-d	11.2 ± 3.3	0.896	<0.0001
MPA	17.1 ± 4.6	0.834	<0.0001
RPA	12 ± 3.9	0.798	<0.0001
LPA	11.5 ± 2	0.811	<0.0001
MPA/AA	1.02 ± 0.47	-0.015	0.782
LV	24.2 ± 6.6	0.790	<0.0001
RV	32 ± 8.5	0.835	<0.0001
LA	30 ± 7.3	0.789	<0.0001
RA	21.5 ± 5.2	0.688	<0.0001

Results are presented as mean ± SD. **r**: correlation coefficient, **p:** p value of Pearson's test. Abbreviations: **LA:** left atrium, **LV:** left ventricle, **RA:** right atrium, **RV:** right ventricle.

Table 5. The mean diameter (mm) of the vascular structures and the ratio of the pulmonary artery to ascending aorta in each group.

	AA	DA-m	DA-d	MPA	RPA	LPA	MPA/AA
Group 1	10.9 ± 1.5	7.9 ± 1	7 ± 1	11.3 ± 1.7	7.3 ± 1.3	7.6 ± 1.3	1.03 ± 0.12
Group 2	13.6 ± 1.7	9.7 ± 1.1	8.4 ± 1	13.5 ± 2	9.4 ± 2.2	9.2 ± 1.2	0.99 ± 0.15
Group 3	15.3 ± 2	11.4 ± 1.7	10 ± 1.5	15.8 ± 2.5	11.5 ± 3.2	10.9 ± 1.5	1.04 ± 0.16
Group 4	17.9 ± 2.3	13.2 ± 1.5	11.2 ± 1.4	17.4 ± 3.1	13 ± 3.3	12.1 ± 1.9	0.97 ± 0.18
Group 5	20.1 ± 2.7	15.5 ± 1.9	13.4 ± 1.9	20.8 ± 3.3	14 ± 2.7	13.5 ± 1.8	1.11 ± 1.01
Group 6	23.2 ± 2.2	17.5 ± 1.9	15.5 ± 1.9	21.9 ± 2.4	15.6 ± 3.2	14.6 ± 2	0.95 ± 0.09
p	<0.0001	<0.0001	<0.0001	<0.0001	<0.0001	<0.0001	0.408

Results are presented as mean ± SD. **P:** p value of ANOVA test. Abbreviations: **AA:** ascending aorta, **DA-m:** descending aorta at the level of mediastinum, **DA-d:** descending aorta at the level of diaphragm, **MPA:** main pulmonary artery, **RPA:** right pulmonary artery, **LPA:** left pulmonary artery, **MPA/AA**: The MPA-to-AA ratio.

Table 6. The mean diameter of the heart chambers in each group.

Heart chambers (mm)	LV	RV	LA	RA
Group 1	15.7 ± 2.2	20.9 ± 3.2	20.4 ± 2.5	15.5 ± 2.8
Group 2	19.3 ± 3.2	24.6 ± 3.3	24 ± 3.4	17.8 ± 2.4
Group 3	22.4 ± 3.1	29.5 ± 4.9	31.4 ± 4.5	20.6 ± 3.5
Group 4	25.6 ± 3.6	33.8 ± 4.5	31.4 ± 4.5	22.8 ± 4
Group 5	28.8 ± 4.5	37.9 ± 5.1	35 ± 5.3	24.8 ± 4.2
Group 6	30.7 ± 5.1	41.1 ± 5.1	36.8 ± 4.8	25.5 ± 4.3
p	<0.0001	<0.0001	<0.0001	<0.0001

Results are presented as mean ± SD. **P:** p value of ANOVA test. Abbreviations: **LV:** left ventricle, **RV:** right ventricle, **LA:** left atrium, **RA:** right atrium.

Measurements of Heart Chambers

Two-dimensional echocardiography is usually employed to assess the size and function of the heart chamber in a daily pediatric cardiology practice. However, it can underestimate or overestimate the values of the measurement when compared with the MRI, which is accepted as the reference diagnostic modality (Lang et al., 2005; Kawel-Boehm et al., 2015). In the literature, measurement of LV in adult patients on non ECG-gated chest MDCT has been assessed in limited studies (Huckleberry et al., 2012; Kathiria et al., 2015; Murphy et al., 2016). To our knowledge, there is no study that has evaluated the normal ranges of cardiac chambers on raw axial CE-chest MDCT in pediatric patients. In our study, we measured the diameters of heart chambers on raw axial images without multiplanar reconstruction. Although recently developed advanced post-processing software programs, including volume-rendered and multiplanar reconstruction images, provide better image quality (Burrill et al., 2007; Karazincir et al., 2008), the diameters derived from the raw-axial images proved to be more practical, because extra time is needed for the multiplanar reconstruction and post-processing. Huckleberry et al. (2012) reported that raw axial measurements of the LA and LV were found superior to measurements on multiplanar reconstruction (areas under ROC was 0.82 for LV and 0.87 for LA). In our study, we found statistically significant correlations between the diameter of cardiac chambers and patients' age (p < 0.001). Although the measurements of the right ventricle and both atriums had relatively lower ICC values compared with the left ventricle, measurements of heart chambers showed substantial-to-excellent (ICC between 0.681-0.958) ICC value. We believe that a relatively lower interobserver agreement is associated with a more complex geometry of the right ventricle and both atria. The other reason may be cardiac pulsation and respiratory artifacts. ECG-gated CE-chest MDCT can be preferred for better imaging quality and synchronization of the cardiac cycle (Torres et al., 2017). However, Lu et al. (2009) demonstrated a high correlation between non-gated and gated end-diastolic diameter ratios, area, and volume measurements of ventricles. Kathiria et al. (2015) also reported that non-gated CE-chest MDCT scan can be used to recognize LV enlargement with the reported value of LV diameter, a sensitivity of 78%, specificity of 100% compared with two-dimentional echocardiography. In another study by Murphy at al. (2016) with the assessment of LV diameter measured on a raw axial CE-chest MDCT comparison with cardiac MRI reported that there was a good correlation between the measurement of raw axial CE-chest MDCT and cardiac MRI with a sensitivity of 93% and a specificity of 88%.

On the other hand, ECG-gated MDCT technique has some limitation as a longer acquisition time than comparable protocols without ECG-gating and a greater patient radiation dose (Lu et al., 2009). Longer scanning time in pediatric age patients may require sedation and cause increased respiratory artifacts. Despite the better temporal and spatial resolution of newer scanners, respiratory and the cardiac motion artifacts can still be seen. When all there benefits and limitations are taken into consideration, ECG-gated CE-chest MDCT is not still performing in routine radiology practice for the assessment of cardiopulmonary and congenital heart disease in our department. The measurement of the heart chambers should be a component of the radiology reporting for non ECG-gated MDCT studies.

Measurements of Mediatinal Great Vessels

Systemic or inflammatory diseases such as Takayasu arteritis, Marfan syndrome, Turner syndrome, Loey-Dietz syndrome may be presented with changes of the diameter of the heart chambers and mediastinal great vessels (Dean, 2007; Johnson et al., 2007; Matura et al., 2007; Civilibal et al., 2008). These structures can be measured on routine raw-axial CE-chest MDCT, and further assessment should be recommended. A limited number of MDCT study evaluated the size of the normal thoracic aorta in healthy children and determined that the ranges of thoracic aorta measurements increased significantly with age, and the result of our study shows concordance with these studies (Matura et al., 2007; Akay et al., 2009; Compton et al., 2015; Kawel-Boehm et al., 2015; Bayindir et al.,

2016). Our study shows statistically significant and positive correlations between the diameter of the aorta in all levels and age groups with an excellent interobserver agreement for all levels of aorta similar to previous studies (Fitzgerald et al., 1987; Compton et al., 2015; Bayindir et al., 2016). Measurement of the aorta at all levels on an axial plane will help the clinicans to rapid assessment of the incidental aortic pathologies such as a stenosis and/or aneurysmal dilatation in busy daily practice.

The pulmonary artery is one of the other important great vascular structure of the mediastinum. The increased diameter of pulmonary artery has been reliably accepted criteria for the diagnosis of pulmonary hypertension, since the dilatation is one of the important radiologic sign in adulthood (Ng et al., 1999; Chaudry et al., 2007).

Although right heart catheterization is accepted as a gold standard technique in the evaluation of the pulmonary hypertension, a good correlation with a good interobserver agreement of the measurement of pulmonary artery on MDCT has been shown in many studies (Edwards et al., 1998; Ng et al., 1999; Karazincir et al., 2008; Truong et al., 2012). Therefore, MDCT can be accepted as a reliable, non-invasive imaging technique in the evaluation of pulmonary hypertension compared to right heart catheterization especially in children (Compton et al., 2015; Caro-Dominguez et al., 2016).

In the assessment of pulmonary artery diameter in pediatric age, different results have been published about the relationship between the MPA diameter and the patient age (Edwards et al., 1998; Ng et al., 1999; Karazincir et al., 2008). In the literaure, the diameter of pulmonary arteries were measured in raw axial CE-chest MDCT in limited studies (Akay et al., 2009; Bayindir et al., 2016). Bayindir et al. (2016) evaluated 520 pediatric patients and demonstrated a remarkable correlation between the diameter of MPA and the patient's age (p < 0.001) and revealed the mean value of LPA is higher than RPA for each age groups (p < 0.001). Akay et al. (2009) also showed significant correlations between the diameters of MPA, RPA, LPA, and the patient's age in their study. In the same study, it is also found that

there was no significant difference between the diameter of LPA and RPA. In our study, we found statistically significant difference between the diameters of MPA, RPA, and LPA for all age groups (p < 0.001). However, no statistically significant difference was found between the diameter of LPA and RPA (p = 0.853). We reached high ICC values for measuring pulmonary arteries similar to the study by Bayindir et al. (2016), but our ICC values for LPA and RPA measurements were relatively lower.

In recent years, not only measurements of the AA and MPA , but also the ratio of the MPA-to-AA are suggested to be mentioned in clinical practice. It is calculated by dividing the diameter of the MPA at the level of pulmonary bifurcation by the diameter of the ascending aorta. Because, in pulmonary hypertension, pulmonary arteries show enlargement without aortic dilatation with an exception in neonatal period, as MPA may be larger than AA because of the increased pulmonary arterial vascular pressure during fetal life (Compton et al., 2015).

The MPA-to-AA ratio has been suggested to be a reliable sign of pulmonary hypertension in adults with the 92% specificity and 96% positive predictive value if it is higher than 1 (Ng et al., 1999). It is also mentioned that the MPA-to-AA ratio should be accepted as 1.1 for the highest diagnostic accuracy in adults (Boerritger et al., 2010). In the study by Pırınc et al. MPA-to-AA ratio was mentioned to be minimum 0.44 cm, maximum 1.41 cm among all individuals aged between 18 and 89 years (Pirinc et al., 2020). And significant difference has been found between age 18-39 years (0.9±0.18) and 40-60 years (0.81±0.15) in the same study (Pirinc et al., 2020).

However, normal range of this ratio has been evaluated by a few studies in children and different results have been revealed from adults (Compton et al., 2015; Bayindir et al., 2016; Caro-Dominguez et al., 2016). Bayindir et al. (2016) reported that the normal value of the MPA-to-AA ratio for healthy pediatric patients was 0.93 ± 0.09 without a statistically significant difference among age groups and genders. In the study by Compton et al. (2015), MPA-to-AA ratio of 200 healthy children without proven pulmonary

hypertension has been defined as 1.085, which is higher than 1 in all age groups. More recently, Caro-Dominguez et al. (2016) evaluated the MPA-to-AA ratio with the age and gender-matched groups (44 children proved pulmonary hypertension by right heart catheterization and 44 children without pulmonary hypertension) and revealed that the study group has a significantly higher MPA-to-AA ratio (1.46) than the control group (1.11). The ratio of MPA-to-AA showed difference between adult and pediatric age groups in the study by Caro-Dominguez et al. (2016). It is also mentioned that, the ratio of 1.3 has a positive predictive value of 97% and specificity of 98% for the diagnosis of pulmonary hypertension which is higher than 1 (Caro-Dominguez et al., 2016). In our study, we revealed that the MPA-to-AA ratio was 1.02 ± 0.47. Although Compton et al. (2015) and Caro-Dominguez et al. (2016) were suggessted to have significant difference between age groups, we found no significant difference between ages like Bayindir et al. (2016).

There are a few limitations of our study. One of the main limitations is measurements of the heart chambers are obtained on an raw axial image without doing multiplanar reconstruction. But we thought that the measurement on a raw axial plane rather than on a multiplanar reconstructed image is more practical and easy in the daily practice of high volume radiology and pediatric cardiology clinics. Also, we believe that measurement errors may be seen if readers had poor practice in creating multiplanar reconstruction images and standardized measurements in routine clinical practice. The second limitation is images acquired randomly in any phase of the cardiac cycle instead of the diastolic phase on ECG-gated chest MDCT or cardiac MRI. Although many studies have revealed that ECG-gated MDCT is accurate in the assessment of heart chambers, non ECG-gated CE-chest MDCT is more frequently used to assess cardiovascular and/or pulmonary diseases in routine daily clinic. We know that ECG-gated MDCT is rarely preferred with the indication of congenital heart disease in pediatric patients, and we do not suggset using ECG-gated MDCT to assess the normal diameters of mediastinal vascular and cardiac structures. In our institute,

most of the pediatric patients with various clinical indication are referred to non ECG-gated CE-chest MDCT, and the diameters of mediastinal great vessels and heart chambers assessed on raw axial CE-chest MDCT. In conclusion, mean diameters of cardiac chambers and mediastinal vascular structures can be used as a reference in routine radiology practice to refer patients for further investigations, such as echocardiography or right heart catheterization to early diagnosis of cardiovascular and/or pulmonary disease.

Ethical Standards. The authors assert that all procedures contributing to this work comply with the ethical standards of the relevant national guidelines on human experimentation in Turkey and with the Helsinki Declaration of 1975, as revised in 2008.

REFERENCES

AKAY OH, OZMEN AC, BAYRAK HA, SENTURK S, KATAR S, NAZAROGLU H, TASKESEN M (2009) Diameters of normal thoracic vascular structures in pediatric patients. *Surg Radiol Anat*, 31: 801-807.

AL-MOUSILY F, SHIFRIN RY, FRICKER FJ, FERANEC N, QUINN NS, CHANDRAN A (2010) Use of 320-detector computed tomographic angiography for infants and young children with congenital heart disease. *Pediatr Cardiol*, 32: 426-432.

BACHER K, BOGAERT E, LAPERE R, DE WOLF D, THIERENS H (2011) Patient-specific dose and radiation risk estimation in pediatric cardiac catheterization. *Circulation*, 111: 83-89.

BAYINDIR P, BAYRAKTAROGLU S, CEYLAN N, SAVAS R, ALPER HH. (2016) Multidetector computed tomographic assessment of the normal diameters for the thoracic aorta and pulmonary arteries in infants and children. *Acta Radiol*, 57: 1261-1267.

BOERRIGTER B, MAURITZ GJ, MARCUS JT, HELDERMAN F, POSTMUS PE, WESTERHOF N, VONK-NOORDEGRAAF A (2010) Progressive dilatation of the main pulmonary artery is a characteristic of pulmonary arterial hypertension and is not related to changes in pressure. *Chest*, 138: 1395-1401.

BURRILL J, DABBAGH Z, GOLLUB F, HAMADY M (2007) Multidetector computed tomographic angiography of the cardiovascular system. *Postgrad Med J*, 83: 698-704.

CARO-DOMÍNGUEZ P, COMPTON GL, HUMPL T, MANSON D (2016) Pulmonary arterial hypertension in children: diagnosis using ratio of main pulmonary artery to ascending aorta diameter as determined by multidetector computed tomography. *Pediatr Radiol*, 46: 1378-1383.

CHAUDRY G, MACDONALD C, ADATIA I, GUNDOGAN M, MANSON D (2007) CT of the chest in the evaluation of idiopathic pulmonary arterial hypertension in children. *Pediatr Radiol*, 37: 345-350.

CHOY G, KRÖPIL P, SCHERER A, EL-SHERIEF AH, CHUNG J, ROJAS CA, ABBARA S (2013) Pertinent reportable incidental cardiac findings on chest CT without electrocardiography gating: review of 268 consecutive cases. *Acta Radiol*, 54: 396-400.

CIVILIBAL M, SEVER L, NUMAN F, ALTUN G, OCAK S, CANDAN C, KASAPCOPUR O, CALISKAN S, CANTASDEMIR M, ARISOY N (2008) Dissection of the abdominal aorta in a child with Takayasu'sarteritis. *Acta Radiol*, 49: 101-114.

COMPTON GL, FLORENCE J, MACDONALD C, YOO SJ, HUMPL T, MANSON D (2015) Main pulmonary artery–to–ascending aorta diameter ratio in healthy children on MDCT. *Am J Roentgenol*, 205: 1322-1325.

DEAN JC (2007) Marfan syndrome: clinical diagnosis and management. *Eur J Hum Genet*, 15: 724-733.

DOĞAN H, KROFT LJ, BAX JJ, SCHUIJF JD, VAN DER GEEST RJ, DOORNBOS J, DE ROOS A (2006) MDCT assessment of right ventricular systolic function. *Am J Roentgenol*, 186: S366-370.

EDWARDS PD, BULL RK, COULDEN R (1998) CT measurement of main pulmonary artery diameter. *Br J Radiol*, 71: 1018-1020.

FITZGERALD SW, DONALDSON JS, POZNANSKI AK (1987) Paediatric thoracic aorta: normal measurements determined with CT. *Radiology*, 165: 667-669.

FRUSH DP, HERLONG JR (2005) Paediatric thoracic CT angiography. *Pediatr Radiol*, 35: 11-25.

GILKESON RC, CIANCIDELLO L, ZAHKA K (2003) Multidetector CT evaluation of congenital heart disease in pediatric and adult patients. *Am J Roentgenol*, 180: 973-980.

HUCKLEBERRY J, HALTOM S, ISSAC T, GABALDON J, KETAI L (2012) Accuracy of non-ECG gated computed tomography angiography of the chest in assessment of left-sided cardiac chamber enlargement. *J Thorac Imaging*, 27: 354-358.

JOHNSON PT, CHEN JK, LOEYS BL, DIETZ HC, FISHMAN EK (2007) Loeys-Dietz syndrome: MDCT angiography findings. *Am J Roentgenol*, 189: 29-35.

KARAZINCIR S, BALCI A, SEYFELI E, AKOĞLU S, BABAYIĞIT C, AKGÜL F, YALÇIN F, EĞILMEZ E (2008) CT assessment of main pulmonary artery diameter. *Diagn Interv Radiol*, 14: 72-74.

KATHIRIA NN, DEVCIC Z, CHEN JS, NAEGER DM, HOPE MD, HIGGINS CB, ORDOVAS KG (2015) Assessment of left ventricular enlargement at multidetector computed tomography. *J Comput Assist Tomogr*, 39: 794-796.

KAWEL-BOEHM N, MACEIRA A, VALSANGIACOMO-BUECHEL ER, VOGEL-CLAUSSEN J, TURKBEY EB, WILLIAMS R, PLEIN S, TEE M, ENG J, BLUEMKE DA (2015) Normal values for cardiovascular magnetic resonance in adults and children. *J Cardiovasc Magn Reson*, 17: 29.

LANG RM, BIERIG M, DEVEREUX RB, FLACHSKAMPF FA, FOSTER E, PELLIKKA PA, PICARD MH, ROMAN MJ, SEWARD J, SHANEWISE JS, SOLOMON SD, SPENCER KT, SUTTON MS, STEWART WJ (2005) Recommendations for chamber quantification: a report from the American Society of Echocardiography's Guidelines and Standards Committee and the Chamber Quantification Writing Group, developed in conjunction with the European Association of Echocardiography, a branch of the European Society of Cardiology. *J Am Soc Echocardiogr*, 18: 1440-1463.

LEUNG DY, BOYD A, NG AA, CHI C, THOMAS L (2008) Echocardiographic evaluation of left atrial size and function: current understanding, pathophysiologic correlates, and prognostic implications. *Heart J*, 156: 1056-1064.

LONG YG, YANG YY, HUANG IL, PAN JY, WU MT, WENG KP, HSIEH KS (2010) Role of multi-slice and three-dimensional computed tomography in delineating extracardiac vascular abnormalities in neonates. *Pediatr Neonatol*, 51: 227-234.

LU MT, CAI T, ERSOY H, WHITMORE AG, LEVIT NA, GOLDHABER SZ, RYBICKI FJ (2009) Comparison of ECG-gated versus non-gated CT ventricular measurements in thirty patients with acute pulmonary embolism. *Int J Cardiovasc Imaging*, 25: 101-107.

MATURA LA, HO VB, ROSING DR, BONDY CA (2007) Aortic dilatation and dissection in Turner syndrome. *Circulation*, 116: 1663-1670.

MURPHY DJ, LAVELLE LP, GIBNEY B, O'DONOHOE RL, RÉMY-JARDIN M, DODD JD (2016) Diagnostic accuracy of standard axial 64-slice chest CT compared to cardiac MRI for the detection of cardiomyopathies. *Br J Radiol*, 89: 20150810.

NG CS, WELLS AU, PADLEY SP (1999) A CT sign of chronic pulmonary arterial hypertension: the ratio of main pulmonary artery to aortic diameter. *J Thorac Imaging*, 14: 270-278.

PATERSON A, FRUSH DP (2007) Dose reduction in paediatric MDCT: general principles. *Clin Radiol*, 62: 507-517.

PIRINC B, FAZLIOGULLARI, KOPLAY M, KARABULUT AK, UNVER DOGAN N (2020) Pulmonary trunk to ascending aorta ratio and reference values for diameters of pulmonary arteries and main bronchi in healthy adults. *Anatomy*, 14(1): 22-28.

POUTANEN T, TIKANOJA T, SAIRANEN H, JOKINEN E (2013) Normal aortic dimensions and flow in 168 children and young adults. *Clin Physiol Funct Imaging*, 23: 224-229.

PRITCHETT AM, JACOBSEN SJ, MAHONEY DW, RODEHEFFER RJ, BAILEY KR, REDFIELD MM (2003) Left atrial volume as an index of left atrial size: a population-based study. *J Am Coll Cardiol*, 41: 1036-1043.

RAMMOS S, APOSTOLOPOULOU SC, KRAMER HH, KOZLIK-FELDMANN R, HEUSCH A, LASKARI CV, ANAGNOSTOPOULOS C (2005) Normative angiographic data relating to dimensions of the aorta and pulmonary trunk in children and adolescents. *Cardiol Young*, 15: 119-124.

ROSSI A, VASSANELLI C (2003) Leftatrium: no longer neglected. *Ital Heart J*, 2005; 6: 881-885.

SANBORN PA, MICHNA E, ZURAKOWSKI D, BURROWS PE, FONTAINE PJ, CONNOR L, MASON KP (2005) Adverse cardiovascular and respiratory events during sedation of pediatric patients for imaging examinations. *Radiology*, 237: 288-294.

SVERZELLATI N, ARCADI T, SALVOLINI L, DORE R, ZOMPATORI M, MEREU M, BATTISTA G, MARTELLA I, TONI F, CARDINALE L, MAFFEI E, MAGGI F, CADEMARTIRI F, PIRRONTI T (2016) Under-reporting of cardiovascular findings on chest CT. *Radiol Med*, 121: 190-199.

TORRES FS, FOLADOR L, EIFER DA, FOPPA M, HANNEMAN K (2017) Measuring left ventricular size in non–electrocardiographic-gated chest computed tomography-what radiologists should know. *J Thorac Imaging*, 33: 81-87.

TRUONG QA, MASSARO JM, ROGERS IS, MAHABADI AA, KRIEGEL MF, FOX CS, O'DONNELL CJ, HOFFMANN U (2012) Reference values for normal pulmonary artery dimensions by non contrast cardiac computed tomography: the Framingham heart study. *Circ Cardiovasc Imaging*, 5: 147-154.

VOGES I, JEROSCH-HEROLD M, HEDDERICH J, PARDUN E, HART C, GABBERT DD, HANSEN JH, PETKO C, KRAMER HH, RICKERS C (2012) Normal values of aortic dimensions, distensibility, and pulse wave velocity in children and young adults: a cross-sectional study. *JCMR*, 14: 77-90.

Assessment of lateral lingual foramen using cone-beam computed tomography

Emre Aytuğar[1], Ceren Özeren Keşkek[2]

[1] *Department of Oral and Maxillofacial Radiology, Faculty of Dentistry, Izmir Katip Celebi University, Izmir, Turkey*

[2] *Izmir Training Dental Hospital, Izmir, Turkey*

SUMMARY

The lateral lingual foramen is an anatomical structure that can be found unilateral or bilateral in the lingual surface of the mandible. The aim of this study is to determine the localization and prevalence of the lateral lingual foramen (LLF) and to evaluate the lateral lingual canal (LLC) using cone-beam computed tomography (CBCT). CBCT images of 741 patients were examined retrospectively. The prevalence and localization of LLF were assessed by gender and age groups. The distance of the LLF to the mandibular alveolar crest (MAC) and to the inferior border of the mandible (MIB) was measured. The angle of entry of the LLC (LLCA) was also measured. These data were analyzed statistically.

582 LLFs were observed in 396 (53,4%) of 741 patients. LLFs were most frequently observed in the premolar region (87.6%). The mean of the LLF-MAC was 23.28 mm and the mean of the LLF-MIB was 4.71 mm. A statistically significant difference was found in LLF-MAC distance for gender and age groups (p=0.000). This study presented a high prevalence of LLF in the Turkish population. Since the LLF includes inferior alveolar canal or mandibular incisive canal structures, it is necessary to be informed about the existing variations before surgical procedures to prevent complications. Compared to previous studies, higher LLF-MAC distance and lower LLF-MIB distance were observed in the Turkish population. This result can provide confidence in implant applications.

Key words: Cone-beam computed tomography – Lateral lingual canal – Lateral lingual foramen – Mandible

INTRODUCTION

The anterior region of the mandible is considered to be a safe area for implant surgery after tooth loss or rehabilitation after trauma due to bone density and the absence of primary vascular structures (Kawai et al., 2007; He et al., 2016). However, an incomplete understanding of the anatomical structures of the region such as the lingual foramen, inferior alveolar canal and lingual surface may cause complications such as bleeding, hematoma, loss of sensation and edema (Kalpidis and Konstantinidis, 2005; Sekerci et

Corresponding author:
Ceren Özeren Keşkek. İzmir Training Dental Hospital, Fevzipasa Boulevard, Akinci district, No.172/2 Konak, Izmir, Turkey. E-mail: cerenozeren35@gmail.com

al., 2014; He et al., 2016). The hematoma can cause swelling in the floor of the mouth and even obstruction of the respiratory tract (Kilic et al., 2014; Direk et al., 2018). This is usually caused by perforation of the cortical bone in the lingual surface during the drilling process or damage to the vessels by the implant material placed (Uchida et al., 2015). Therefore, it is important to determine the mandibular lingual foramen and associated neurovascular structures before surgical procedures such as implant applications (Yildirim et al., 2014).

Foramens in the lingual surface of the mandible are divided into two main groups. Those located at or near the midline are called medial lingual foramen (MLF), and those located laterally are called lateral lingual foramen (LLF) (Sahman et al., 2014; Krishnan et al., 2018). Since the canal structures of these foraminas contain different arterial branches or anastomoses of the arteries, they are called the vascular canal. The canal of the LLF is called the lateral lingual canal (LLC) (He et al., 2017). Nakajima et al. (2014) reported that the type of LLCs that anastomoses with the inferior alveolar artery are of submental artery origin and they defined it as the branch of communication. They reported that the non-anastomotic LLC divides into the incisal and labial branches, and surprisingly, the nourishment of the incisor area takes place only in this way.

It is very difficult to detect the presence of MLF or LLF with two-dimensional radiography techniques (Wang et al., 2015; Wei et al., 2020). Cone-beam computed tomography (CBCT) has become a very useful tool in the assessment of anatomical formations such as inferior alveolar canal, mental foramen, LLF as well as determining the size of the existing bone in dental implant applications (Gahleitner et al., 2001). It is widely used in the maxillofacial area due to fast scanning, high resolution and low radiation exposure (von Arx et al., 2011; He et al., 2016).

Clinicians may consider the likelihood of LLF injury to be low due to its distance from the alveolar crest. However, since life-threatening bleeding was reported to occur, it was necessary to study this issue with a large sample group (Kalpidis and Setayesh, 2004). For this reason, we aimed to obtain useful information by investigating the frequency and localization of LLF and the anatomical features of the LLC with CBCT.

MATERIALS AND METHODS

CBCT images of 1000 patients taken for various reasons in the Department of Oral and Maxillofacial Radiology were evaluated. Images of 259 patients were excluded from the study according to the exclusion criteria. The exclusion criteria were unerupted tooth or fracture, pathological condition and surgical treatment in the mandible, bone loss at the mental foramen level, and artifacts that prevented interpretation of the images. The study followed the Helsinki declaration and was conducted with the permission of the Izmir Katip Celebi University Non- Interventional Clinical Studies Ethics Committee (IRB:2018/220). Informed consent was obtained from all patients or their legal guardians before the CBCT procedure was performed.

All of the CBCT images used were acquired at 110 kVp using a CBCT device (NewTom 5G, Quantitative Radiology, Verona, Italy). CBCT images with 15 × 12 cm FOV range and 0.200 mm
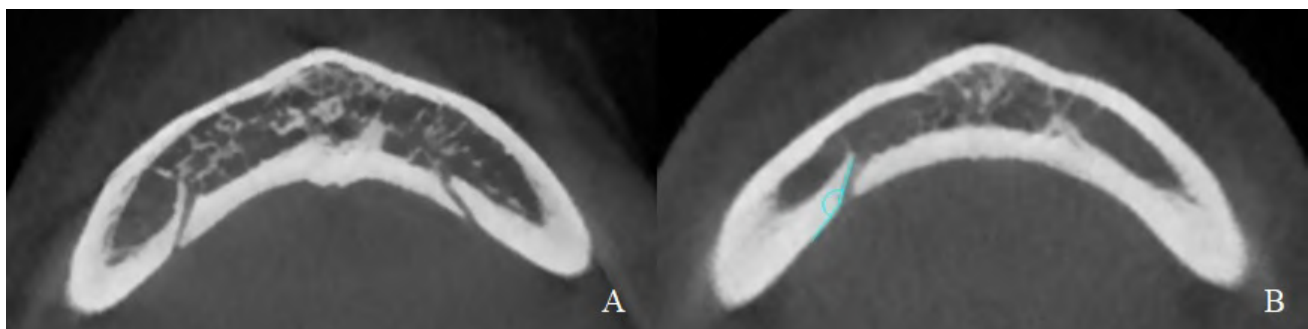

Fig. 1.- Images of the lateral lingual canal in axial sections. (**A**) Bilateral lateral lingual canal. (**B**) Measurement of lateral lingual canal angle.

voxel size were used. Digital images were analyzed using NNT (NNT Software Version 8.0; NewTom; Italy) computer software.

Firstly, the presence of LLC from the canine teeth to the second molars on both sides in the reconstructed axial sections was investigated (Fig. 1A). LLCs were defined as canals connected to the inferior alveolar canal or mandibular incisive canal. Canals not connected to the inferior alveolar canal or the mandibular incisive canal were considered as nutritional canals and were not included in LLF and LLC measurements.

The entry angle of the detected LLC to the mandible (LLCA) was measured in the axial section (Fig. 1B). Then, the distance of LLF to the mandibular alveolar crest (MAC) and the inferior border of the mandible (MIB) was measured in cross-sections (Fig. 2). After the occlusal plane is placed parallel to the ground in three-dimensional images, the localization of the LLF according to the tooth number was determined (Fig. 3). Individuals with tooth deficiency preventing detection of the localization of the LLF were excluded from the study. There was no tooth loss in the area where LLFs were detected.

The data obtained were evaluated using descriptive statistical methods (mean, frequency, percentage). Kolmogorov-Smirnov test was used to evaluate data distribution. Mann-Whitney U test and Kruskal-Wallis tests were used to test the differences between the means of groups that did not show normal distribution. The chi-square test was used to compare categorical variables. IBM SPSS Version 26 was used for statistical analysis. The level of significance (p-value) was accepted as 0.05.

RESULTS

The study population was 397 males (Mean age:41.3) and 344 females (Mean age:37.9). 582 LLFs were detected in 396 patients (53.4%). LLF was observed in 174 (50.6%) of the females and 222 of the males (56%). There was no significant difference between the presence of LLF and gender (p=0.169).

LLF was most frequently detected at the level of the 35th tooth (24.9%) (FDI tooth notation system). LLFs were most frequently observed in the premolar region (87.6%) (Fig. 4). There was no statistically significant difference in the


Fig. 2.- Measurement of the distance of the lateral lingual foramen to the mandibular alveolar crest (LLF-MAC) and mandibular inferior border (LLF-MIB).
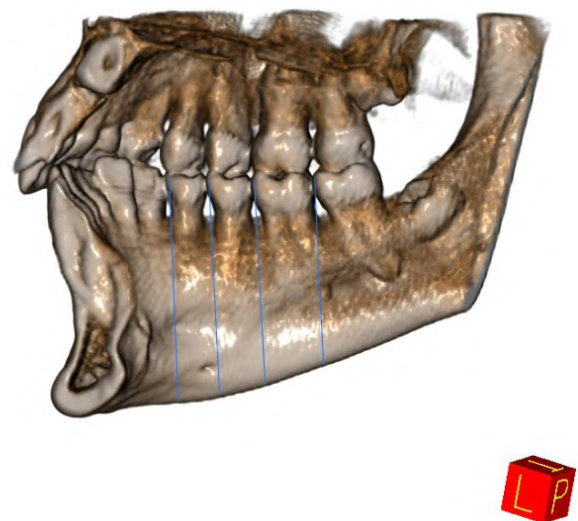
Fig. 3.- Determination of the localization of the lateral lingual foramen with 3D reconstruction.

localization of LLF according to gender and age groups (p=0.210, p=0.316). LLF was bilateral in 38.9% of patients with LLF.

Table 1 presents LLCA, LLF-MAC and LLF-MIB values by gender and age groups. While there was no statistically significant difference in LLCA, LLF-MIB values according to gender (p=0.979, p=0.148), LLF-MAC distance was higher in males with a statistically significant difference (p=0.000). The LLF-MAC and LLF-MIB distances were statistically significant according to age groups (p=0.000, p=0.015). LLF-MAC distance was significantly longer in the 20-49 age group than in other age groups, but this distance was similar in the 11-19 and 50≤ age groups. LLF-MIB distance was significantly shorter in the 11-19 age group compared to the other age groups, but this distance was similar in the 20-49 and 50≤ age groups.

DISCUSSION

LLF, accessory mental foramen (AMF), retromolar foramen and accessory mandibular foramen are anatomical variations observed in the mandible (Iwanaga et al., 2019). AMF is defined as the foramina in the mental foramen area that is connected with the mandibular canal and smaller than the mental foramen (Lam et al., 2019). The retromolar canal contains branches of the inferior alveolar nerve and terminates as the retromolar foramen distal to the third molar and in the retromolar region (Kikuta et al., 2018; Ngeow and Chai, 2021). On the lingual surface of the mandible, the foramen on the midline is called MLF, and the foramen on the lateral surfaces of the lingual surface of the mandible is called LLF (Krishnan et al., 2018). Accessory foramina are not rare. Therefore, radiological examination is recommended to prevent complications before a surgical procedure in the mandible (Haghanifar and Poorsattar Bejeh Mir, 2015).
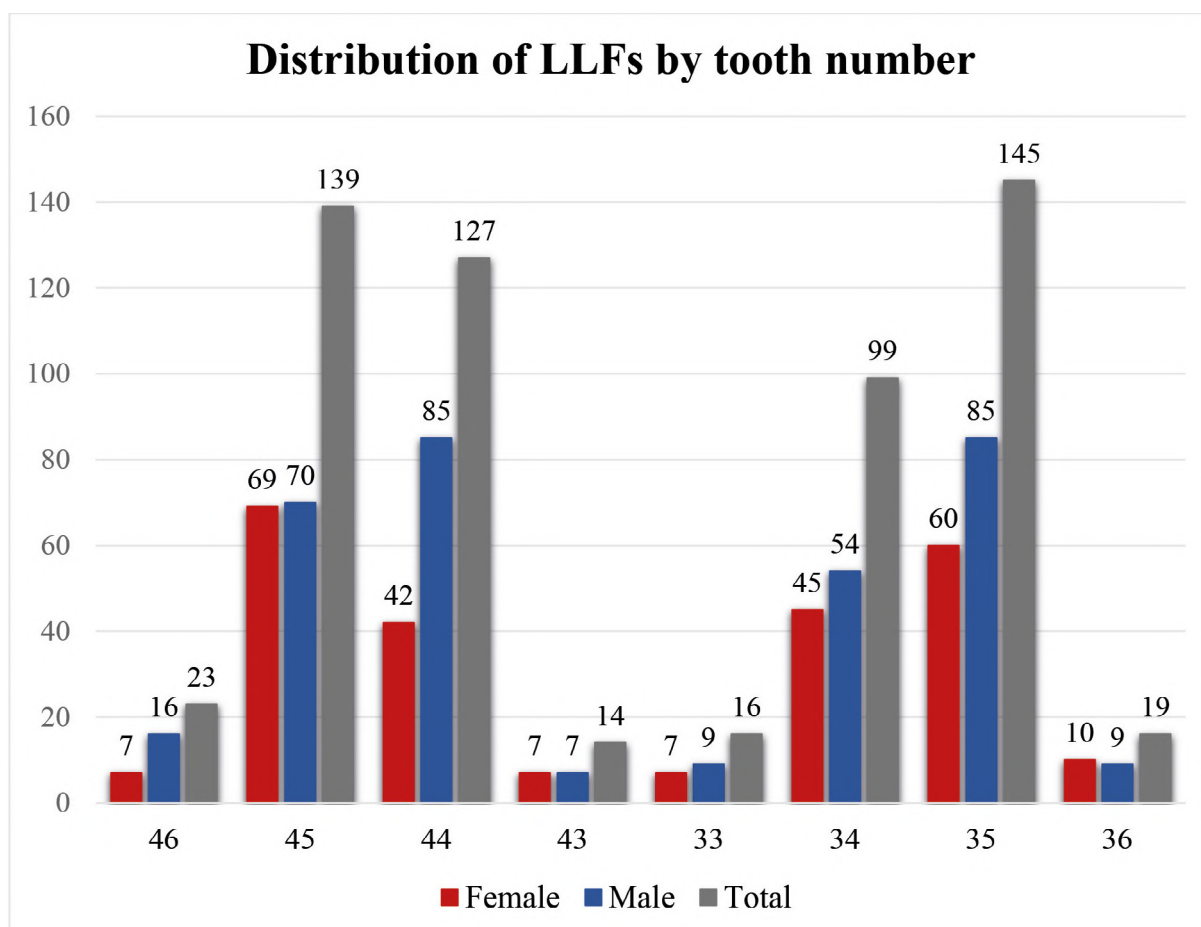

Fig. 4.- Distribution of the localization of lateral lingual foramen according to tooth numbers.

Table 1. Comparison of measured values by gender and age groups.

Gender	LLCA	LLF-MAC	LLF-MIB
Female	152.1°	21.79	4.89
Male	152.6°	24.38	4.58
Total	152.4°	23.28	4.71
p-value	0.979	0.000*	0.148
Age groups			
11-19 (N:132)	151.9°	22.50	4.47
20-49 (N:285)	152.9°	24.14	4.79
50≤ (N:165)	151.8°	22.43	4.78
p-value	0.411	0.000*	0.015*

LLCA, the angle of lateral lingual canal; MAC, mandibular alveolar crest; MIB, mandibular inferior border; *Significance (p ≤ 0.05)

CBCT examinations are performed before surgical procedures in dentistry (Sanomiya Ikuta et al., 2016). CBCT devices provided a detailed assessment of the foramina in the mandible, with adequate image quality and lower radiation dose compared to computed tomography (CT). Large section thickness can mask smaller diameter structures (Wang et al., 2015). Therefore, small anatomical structures can be hidden and not detected in CT devices that generally use voxels larger than 0.3 mm, but CBCT provides detailed evaluation with high resolution with a voxel size of 0.3 mm or less in all three axes (He et al., 2017). Besides, Iwanaga et al. (2017) evaluated 20 AMF in surface-rendered images using CBCT, and reported that AMFs smaller than 1.3 mm² are not clearly defined in images created on the surface. In this study, images with a voxel size of 0.2 mm were obtained and the LLF was examined in detail in axial, cross-sections and three- dimensional images.

There is no consensus in the literature regarding the classification of mandibular lingual foramina. Some authors have classified the mandibular lingual foramina as midline, paramedian, and posterior lingual foramen (von Arx et al., 2011; Sekerci et al., 2014). Although some researchers classify foramen detected in the midline and near the symphysis as MLF and LLF determined in the lateral (He et al., 2016; Zhang et al., 2018; Trost et al., 2020), these studies have shown boundary differences. Krishnan et al. (2018) and Sanomiya Ikuta et al. (2016) defined LLF as foramina located in the lingual of the premolar and molar teeth. Gahleitner et al. (2001) and Sahman et al. (2014) have also included the foramina in the canine tooth region. In this study, the foramina located on the lingual surface of the mandible from the canine teeth to the second molars were evaluated as LLF, and the foramina located on the anterior of the canines as MLF.

It has been reported in the literature that the prevalence of LLF is between 14.9% and 80% (Tagaya et al., 2009; Sahman et al., 2014; He et al., 2016; Sanomiya Ikuta et al., 2016; Krishnan et al., 2018; Moro et al., 2018; Zhang et al., 2018; Xie et al., 2019; Trost et al., 2020; Wei et al., 2020). Previous studies are presented in table 2, together with the imaging techniques used and the prevalence of LLF. The wide variation in the prevalence of LLFs can be attributed to differences in study method, examination techniques, sample size, and differences in ethnic characteristics of individuals in the study. LLF prevalence was found between 21.1% and 32% in studies conducted in the Turkish population (Yildirim et al., 2014; Direk et al., 2018). In our study, it was observed in a higher percentage than in previous studies (53.4%). Yildirim et al. (2014) used images obtained with both spiral CT and CBCT in their studies and did

not give information about the slice thickness. Direk et al. (2018) used multislice CT images in their study and examined the presence of LLF at 0.5 mm axial slice thickness. Some LLFs may be overlooked depending on the slice thickness. In our study, we think that we detected a higher rate of LLF due to the examination of the images with a slice thickness of 0.2 mm.

Krishnan et al. (2018) reported that LLF was most frequently detected at the level of the first premolar, while Zhang et al. (2018) and Sahman et al. (2014) reported that it was most frequently observed at the level of the second premolar. Although the prevalence of LLF varied widely across studies, LLF was most commonly observed in the premolar region (Tagaya et al., 2009; Sahman et al., 2014; Krishnan et al., 2018; Xie et al., 2019; Wei et al., 2020). In our study, LLF was found mostly at the level of the premolar teeth (87.6%), and among them, the most frequently at the level of the second premolar teeth.

Knowledge of the LLF-MAC distance is particularly important, as it represents the safe area for invasive procedures such as implant placement (He et al., 2017). Uchida et al. (2015) and Yildirim et al. (2014) reported that they found the mean of LLF-MAC distance of 19.3 and 18.4 mm, respectively, and it was statistically significantly higher in males. In our study, this

distance was determined as 23.2 mm and a statistically significant difference was observed. In previous studies, the mean of LLF-MIB distance has been determined between 5.2 mm and 7.7 mm (Tagaya et al., 2009; Krishnan et al., 2018). Zhang et al. (2018), He et al. (2016) and Wei et al. (2020) reported that they found the LLF-MIB distance of 7.02, 7.08 and 7.1 mm, respectively, and it was statistically significantly higher in males. In our study, this distance was determined as 4.7 mm and no statistically significant difference was observed according to gender. Compared to previous studies, higher LLF-MAC distance and lower LLF-MIB distance may provide confidence in surgical procedures such as implant applications in the Turkish population. According to this result, regional anatomical differences should be taken into consideration before implant applications due to anatomical variations in different racial groups.

He et al. (2016) reported the LLF-MAC distance as 16.82 mm in the 10-19 age group, 16.42 mm in the 20-49 age group and 16.62 mm in the 50 and over age group. They reported the LLF-MIB distance as 12.69 mm in the 10-19 age group, 14.11 mm in the 20-49 age group and 13.91 mm in the 50 and over age group. There was no statistically significant difference between LLF-MAC and LLF-MIB distances and age groups. In our study, LLF-MAC and LLF-MIB distances were found as 24.14 and 4.79 mm in the 20-49 age group, respectively.

Table 2. Literature comparison in studies reporting the presence of LLF.

	Imagine Technique	Number of Patients	Presence of LLF (%)
Tagaya et al., 2009	CT	200	80
Sahman et al., 2014	CBCT	500	24.8
Yildirim et al., 2014	CT	639	21.1
Ikuta et al., 2016	CBCT	100	39
He et al., 2016	CBCT	200	14.9
Direk et al., 2018	CT	100	32
Moro et al., 2018	CT	58	75.9
Krishnan et al., 2018	CBCT	109	20.4
Zhang et al., 2018	CBCT	299	63.2
Xie et al., 2019	CBCT	1008	54.3
Wei et. al., 2020	CBCT	306	69.9
Trost et al., 2020	CT	460	38.9
Present Study	CBCT	741	53.4

There was a statistically significant difference in these distances for age groups. The shorter LLF-MAC and LLF- MIB distances in the 11-19 age group compared to the 20-49 age group may be due to incomplete bone development. The short LLF-MAC distance in individuals aged 50 and over may be due to the decrease in alveolar bone sizes with age.

LLCs are admitted to have a connection with the inferior alveolar canal or mandibular incisive canal (Sahman et al., 2014). It has been shown that the canals in the molar region are connected with the inferior alveolar canal, and those in the premolar region with the mandibular incisive canal (von Arx et al., 2011). In this study, canals connected to the inferior alveolar canal or mandibular incisive canal were evaluated as LLC.

The measurement of LLCA was reported in one study to the best of our knowledge (Krishnan et al., 2018). The mean of LLCA was reported as 148.2°. In our study, the mean of LLCA was 152.4° and there was no statistically significant difference according to gender and age groups. This angle may be especially important during dental implant applications because the reduction of LLCA may increase the risk of damage. As the LLCA increases, the canal may become parallel to the mandibular lingual surface and may move slightly away from the implant site.

Procedures such as reconstruction, implant surgery, removal of roots, a biopsy of cysts and tumors, and osteotomy are performed in the mandible where the lingual foramina are located. Therefore, data on the localization and prevalence of lingual foramina are necessary to reduce the risk of complications, to perform the procedure safely and to avoid damage to important structures.

In conclusion, the radiological characteristics of LLFs are presented using the data obtained with the largest sample size among studies conducted in the Turkish population, and it is noteworthy that the LLF prevalence has the highest value among these studies. Compared to previous studies, higher LLF-MAC distance and lower LLF-MIB distance were observed in the Turkish population. This can provide confidence in surgical procedures such as implant applications.

However, it is recommended to perform a radiological examination of the relevant region, especially the premolar region, before the surgical procedure and to have knowledge about anatomical variations.

REFERENCES

DIREK F, UYSAL, II, KIVRAK AS, FAZLIOGULLARI Z, UNVER DOGAN N, KARABULUT AK (2018) Mental foramen and lingual vascular canals of mandible on MDCT images: anatomical study and review of the literature. *Anat Sci Int,* 93(2): 244-253.

GAHLEITNER A, HOFSCHNEIDER U, TEPPER G, PRETTERKLIEBER M, SCHICK S, ZAUZA K, WATZEK G (2001) Lingual vascular canals of the mandible: evaluation with dental CT. *Radiology,* 220(1): 186-189.

HAGHANIFAR S, POORSATTAR BEJEH MIR A (2015) Accessory mental foramina, incisive nerve plexus and lingual canals with unusual emergence paths: Report of two rare cases. *Indian J Dent,* 6(1): 44-48.

HE P, TRUONG MK, ADEEB N, TUBBS RS, IWANAGA J (2017) Clinical anatomy and surgical significance of the lingual foramina and their canals. *Clin Anat,* 30(2): 194-204.

HE X, JIANG J, CAI W, PAN Y, YANG Y, ZHU K, ZHENG Y (2016) Assessment of the appearance, location and morphology of mandibular lingual foramina using cone beam computed tomography. *Int Dent J,* 66(5): 272-279.

IWANAGA J, WATANABE K, SAGA T, KIKUTA S, TABIRA Y, KITASHIMA S, FISAHN C, ALONSO F, TUBBS RS, KUSUKAWA J, YAMAKI KI (2017) Undetected small accessory mental foramina using cone-beam computed tomography. *Cureus,* 9(5): e1210.

IWANAGA J, KIKUTA S, TANAKA T, KAMURA Y, TUBBS RS (2019) Review of risk assessment of major anatomical variations in clinical dentistry: accessory foramina of the mandible. *Clin Anat,* 32(5): 672-677.

KALPIDIS CD, KONSTANTINIDIS AB (2005) Critical hemorrhage in the floor of the mouth during implant placement in the first mandibular premolar position: a case report. *Implant Dent,* 14(2): 117-124.

KALPIDIS CD, SETAYESH RM (2004) Hemorrhaging associated with endosseous implant placement in the anterior mandible: a review of the literature. *J Periodontol,* 75(5): 631-645.

KAWAI T, ASAUMI R, SATO I, YOSHIDA S, YOSUE T (2007) Classification of the lingual foramina and their bony canals in the median region of the mandible: cone beam computed tomography observations of dry Japanese mandibles. *Oral Radiology,* 23(2): 42-48.

KIKUTA S, IWANAGA J, NAKAMURA K, HINO K, NAKAMURA M, KUSUKAWA J (2018) The retromolar canals and foramina: radiographic observation and application to oral surgery. *Surg Radiol Anat,* 40(6): 647-652.

KILIC E, DOGANAY S, ULU M, ÇELEBI N, YIKILMAZ A, ALKAN A (2014) Determination of lingual vascular canals in the interforaminal region before implant surgery to prevent life- threatening bleeding complications. *Clin Oral Implants Res,* 25(2): e90-93.

KRISHNAN U, MONSOUR P, THAHA K, LALLOO R, MOULE A (2018) A limited field cone-beam computed tomography-based evaluation of the mental foramen, accessory mental foramina, anterior loop, lateral lingual foramen, and lateral lingual canal. *J Endod,* 44(6): 946-951.

LAM M, KOONG C, KRUGER E, TENNANT M (2019) Prevalence of accessory mental foramina: a study of 4,000 CBCT scans. *Clin Anat,* 32(8): 1048-1052.

MORO A, ABE S, YOKOMIZO N, KOBAYASHI Y, ONO T, TAKEDA T (2018) Topographical distribution of neurovascular canals and foramens in the mandible: avoiding complications resulting from their injury during oral surgical procedures. *Heliyon,* 4(9): e00812.

NAKAJIMA K, TAGAYA A, OTONARI-YAMAMOTO M, SEKI K, ARAKI K, SANO T, OKANO T, NAKAMURA M (2014) Composition of the blood supply in the sublingual and submandibular spaces and its relationship to the lateral lingual foramen of the mandible. *Oral Surg Oral Med Oral Pathol Oral Radiol,* 117(1): e32-38.

NGEOW WC, CHAI WL (2021) The clinical significance of the retromolar canal and foramen in dentistry. *Clin Anat,* 34(4): 512-521.

SAHMAN H, SEKERCI AE, ERTAS ET (2014) Lateral lingual vascular canals of the mandible: a CBCT study of 500 cases. *Surg Radiol Anat,* 36(9): 865-870.

SANOMIYA IKUTA CR, PAES DA SILVA RAMOS FERNANDES LM, POLETI ML, ALVARES CAPELOZZA AL, FISCHER RUBIRA-BULLEN IR (2016) Anatomical study of the posterior mandible: lateral lingual foramina in cone beam computed tomography. *Implant Dent,* 25(2): 247-251.

SEKERCI AE, SISMAN Y, PAYVEREN MA (2014) Evaluation of location and dimensions of mandibular lingual foramina using cone-beam computed tomography. *Surg Radiol Anat,* 36(9): 857-864.

TAGAYA A, MATSUDA Y, NAKAJIMA K, SEKI K, OKANO T (2009) Assessment of the blood supply to the lingual surface of the mandible for reduction of bleeding during implant surgery. *Clin Oral Implants Res,* 20(4): 351-355.

TROST M, MUNDT T, BIFFAR R, HEINEMANN F (2020) The lingual foramina, a potential risk in oral surgery. A retrospective analysis of location and anatomic variability. *Ann Anat,* 231: 151515.

UCHIDA Y, GOTO M, DANJO A, YAMASHITA Y, SHIBATA K, KURAOKA A (2015) Anatomical relationship between the sublingual fossa and the lateral lingual foramen. *Int J Oral Maxillofac Surg,* 44(9): 1146-1151.

VON ARX T, MATTER D, BUSER D, BORNSTEIN MM (2011) Evaluation of location and dimensions of lingual foramina using limited cone-beam computed tomography. *J Oral Maxillofac Surg,* 69(11): 2777-2785.

WANG YM, JU YR, PAN WL, CHAN CP (2015) Evaluation of location and dimensions of mandibular lingual canals: a cone beam computed tomography study. *Int J Oral Maxillofac Surg,* 44(9): 1197-1203.

WEI X, GU P, HAO Y, WANG J (2020) Detection and characterization of anterior loop, accessory mental foramen, and lateral lingual foramen by using cone beam computed tomography. *J Prosthet Dent,* 124(3): 365-371.

XIE L, LI T, CHEN J, YIN D, WANG W, XIE Z (2019) Cone-beam CT assessment of implant- related anatomy landmarks of the anterior mandible in a Chinese population. *Surg Radiol Anat,* 41(8): 927-934.

YILDIRIM YD, GÜNCÜ GN, GALINDO-MORENO P, VELASCO-TORRES M, JUODZBALYS G, KUBILIUS M, GERVICKAS A, AL-HEZAIMI K, AL-SADHAN R, YILMAZ HG, ASAR NV, KARABULUT E, WANG HL, TÖZÜM TF (2014) Evaluation of mandibular lingual foramina related to dental implant treatment with computerized tomography: a multicenter clinical study. *Implant Dent,* 23(1): 57-63.

ZHANG C, ZHUANG L, FAN L, MO J, HUANG Z, GU Y (2018) Evaluation of mandibular lingual foramina with cone-beam computed tomography. *J Craniofac Surg,* 29(4): e389-e394.

Comparative study of the length of human laryngeal nerves and their variations: functional and clinical considerations

Eva Maranillo[1], Clara Simón de Blas[2], María del Carmen Górriz[3], Sara Quinones[1], Enrique Verdú[4], Miquel Quer[5], Xavier León[5], Teresa Vázquez[1], José R. Sañudo[1], Marko Konschake[6]

[1] Department of Anatomy and Embryology, Medical School, Complutense University of Madrid, Spain

[2] Department of Computer Sciences and Statistics, Rey Juan Carlos University, Madrid, Spain

[3] Otorhinolaryngology Service, Puerta de Hierro University Hospital, Majadahonda, Madrid, Spain

[4] Medical Sciences Department, University of Girona, Spain

[5] Department of Otolaryngology-Head and Neck Surgery, University Hospital de la Santa Creu i Sant Pau, Universitat Autonoma de Barcelona, Barcelona, Spain

[6] Institute of Clinical and Functional Anatomy, Medical University of Innsbruck (MUI), Innsbruck, Austria

SUMMARY

The difference in length between the laryngeal nerves on both sides is one of the factors that may affect the synchronicity of nerve impulses arrival to laryngeal muscles and therefore the synchronicity of vocal fold function. As there are very few studies on the length of these nerves, the goal of this work is to study the length and morphology of whole laryngeal nerves in a much larger human sample, taking into account side, gender and path variations. 111 necks from human embalmed cadavers were dissected (58 females, 53 males). All laryngeal nerves on both sides and their variations were measured and a statistical analysis of the results was carried out.

In reference to the side of corpses, significant differences were found between both recurrent inferior laryngeal nerves and both internal and external laryngeal nerves with the superior laryngeal nerves, being greater on the left side in all cases. In reference to the gender of the corpses, significant differences were found between the lengths of both external laryngeal nerves, being greater in males in all cases. A non-recurrent laryngeal nerve and an absence of superior laryngeal nerve were found. The intramuscular path of the external laryngeal nerve was analysed (Friedman's classification). All laryngeal nerves are significantly longer on the left side. These differences may affect the synchronicity of glottic opening and closure. Therefore, these results would have to be taken into account in functional studies (neurostimulation, electromyography) and in clinical procedures (reinnervation, denervation).

Key words: Laryngeal nerve – Length – Neurostimulation – Electromyography – Vocal fold – Larynx – Reinnervation

Corresponding author:
Dr. Eva Maranillo Alcaide. Department of Anatomy and Embryology, Medical School, Complutense University of Madrid, Plaza Ramón y Cajal s/n, Ciudad Universitaria, 28040 Madrid, Spain. E-mail: emaranil@ucm.es

INTRODUCTION

The length of motor laryngeal nerves is one of the morphological parameters involved in nerve conduction, which is essential for performing the different laryngeal functions (protection of the respiratory tract, swallowing, breathing, phonation, etc.) (Krmpotic, 1958; Shin and Rabuzzi, 1971; Steiss and Marshall, 1988; Prades et al., 2012). The difference in length between the right and left recurrent inferior laryngeal nerves (RLN) poses a controversial question about the synchronous (Shin and Rabuzzi, 1971; Harrison, 1981) or asynchronous (Atkins, 1973; Prades et al., 2012) arrival of nerve impulses to the muscles on both sides of the larynx, affecting glottic closure and opening. However, it is important to note that electromyographic studies in humans have shown that laryngeal muscles can receive a double innervation. Therefore, nerve impulses can arrive to them, not only through the external laryngeal nerve (ELN) or RLN, as classically described (Testut and Latarjet, 1972; Williams, 1995) but also from the internal laryngeal nerve (ILN) to the posterior cricoarytenoid muscle (Martín-Oviedo et al., 2019), from the ELN to thyroarytenoid, posterior cricoarytenoid, arytenoid and contralateral cricothyroid muscles (Martín-Oviedo et al., 2011; 2019) and from the RLN to ipsilateral and contralateral cricothyroid muscles (Martín-Oviedo et al., 2011; 2019). So, it could be thought that this double innervation of laryngeal muscles may intervene in the synchronicity of glottic closure too.

In the same way that nerve length has an important role in motor fiber nerve conduction, it also has a role in the sensory fibers that participate in the laryngeal closure and cough reflexes.

Despite all that has been said above, there are very few works that have studied the length of human laryngeal nerves, and these are based on small and non-homogeneous samples. No study about the entire laryngeal nerve length has been found in the literature consulted.

Therefore, the aim of our work is to study the length and morphology of all laryngeal nerves in a much larger human sample, taking into account side, gender and variations.

MATERIALS AND METHODS

The necks of 111 Caucasian human embalmed cadavers were dissected and examined (58 females, 53 males; 64-100 years of age). No pathology of the neck was observed. All cadavers were inside the size and weight range established by Cambridge University for the acceptance of body donation (weight 44.5-85 kg, height <180 cm), and all the donors were received under the auspices of the Anatomy Act 1984, whereby medical schools may accept a body for the purposes of anatomical education, teaching and research. The donors would have provided written consent for the use of their bodies for such purposes before decease. The 222 heminecks were partially dissected by Cambridge preclinical medical students and then further dissected by the authors using magnification. In order to measure the nerves in a correct way, the carotid arteries and the internal jugular vein were removed, as well as the anterior part of the rib cage and the clavicle. All measurements of nerves were made, on both sides, with the head in a centred supine position as follows:

- *Vagus nerve (X cn):* from the nodose ganglion to origin of RLN (Fig. 1. From 1 to 2 and 2').

- *Recurrent inferior laryngeal nerve (RLN)*: from its exit from the vagus nerve to its entrance to the larynx at the inferior horn of thyroid cartilage. (Fig. 1. From 2 to 3 on the right side and from 2' to 3' on the left)

- *Superior laryngeal nerve (SLN)*: from its exit from the vagus nerve to its division in its terminal branches (internal and external laryngeal nerves) (Fig. 1. From 1 to 4 on both sides).

- *Internal laryngeal nerve or internal branch of superior laryngeal nerve (ILN)*: from SLN to the thyrohyoid membrane (Fig. 1. From 4 to 5).

- *External laryngeal nerve or external branch of superior laryngeal nerve (ELN)*: from SLN to the cricothyroid muscle (Fig. 1. From 4 to 6).

All these lengths were evaluated using a silk thread placed along the course of nerves, marking the proximal and distal ends of the nerve with tweezers, and later superimposing the silk thread marked by both forceps on a graduated ruler to measure the length.

Statistical analysis

To analyze relationships between the lengths of the laryngeal nerves, gender and side a two-factor experimental design was considered in this research and we used the Scheffés method to determine the number of groups. Significant differences between the average lengths of laryngeal nerves were analyzed using T tests. All tests were studied considering a significance level α = 0.05.

RESULTS

For an easier understanding of the results obtained, the lengths of the RLNs are presented first, followed by those of the SLNs and its branches.

Recurrent inferior laryngeal nerve

The right RLN arose from the vagus nerve at 6.5-17.5 cm (average 13.990±1.682 cm) from the nodose ganglion. It then recurred below the left subclavian artery (SA) and entered the larynx at the level of the cricothyroid joint. The length of the right RLN from its origin to the larynx was 4-9.5 cm (average 6.740±1.111 cm) (Table 1A., Fig. 2A). A right non-recurrent inferior laryngeal nerve (non-RLN) was found on the right side in one female (0.9%, 1/111). It arose from the vagus nerve at the level of the cricothyroid joint and coursed 4 cm transversely to the larynx, above the level of the inferior thyroid artery (type 2A). In this case, the non-RLN was associated with a retroesophageal SA (lusoria artery).
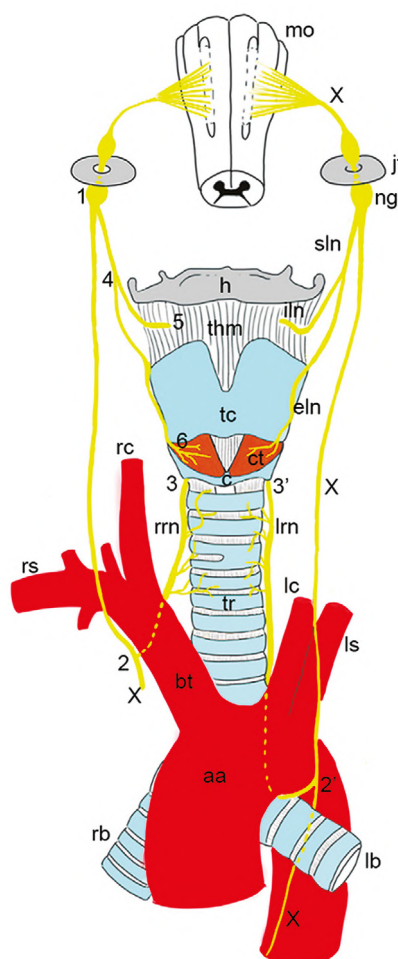
Fig. 1.- Drawing of laryngeal nerves and their measurement points. **aa**, aortic arch; **bt**, brachiocephalic arterial trunk; **c**, cricoid cartilage; **ct**, cricothyroid muscle; **eln**, external laryngeal nerve; **h**, hyoid bone; **iln**, internal laryngeal nerve; **jf**, jugular foramen; **lb**, left bronchi; **lc**, left common carotid artery; **lrn**, left recurrent inferior laryngeal nerve; **ls**, left subclavian artery; **mo**, medulla oblongata; **ng**, nodose ganglion; **rb**, right bronchi; **rc**, right common carotid artery; **rrn**, right recurrent inferior laryngeal nerve; **rs**, right subclavian artery; **sln**, superior laryngeal nerve; **tc**, thyroid cartilage; **thm**, thyrohyoid membrane; **tr**, trachea; **X**, vagus nerve. **1**, jugular foramen; **2**, origin right recurrent laryngeal nerve; **2'**, origin left laryngeal nerve; **3**, entry of RLN into the larynx; **4**, terminal division of SLN; **5**, entry of ILN into the larynx through the thyrohyoid membrane; **6**, entry of ELN to cricothyroid muscle.
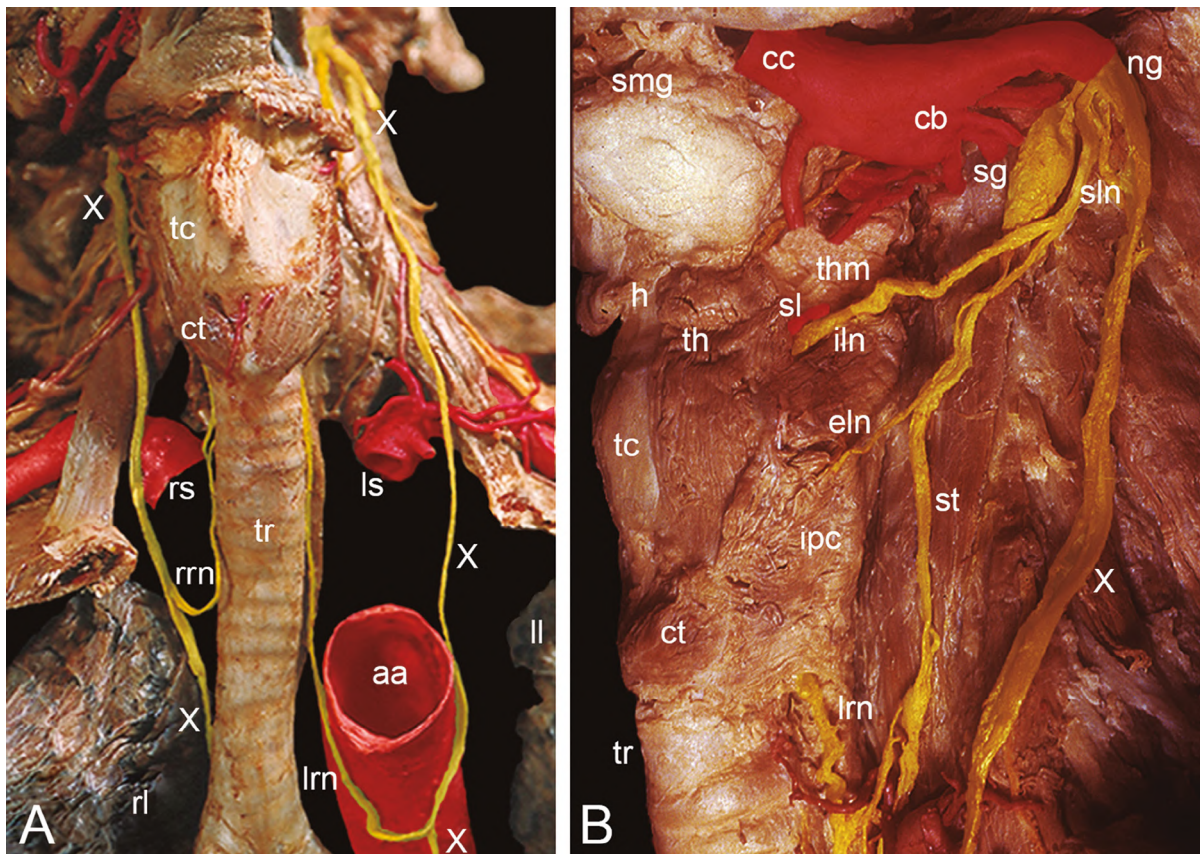
Fig. 2.- A. Origin and way of right and left recurrent inferior laryngeal nerves. Anterior view of neck and mediastinum. The heart, the ascending aorta, the proximal part of aortic arch and the carotid arteries have been removed. **B.** Origin and way of superior laryngeal nerve and its terminal branches. Left lateral view of neck. The common carotid artery has been sectioned proximally and reclined upward. **aa**, aortic arch; **cb**, carotid bifurcation; **cc**, common carotid artery; **ct**, cricothyroid muscle; **eln**, external laryngeal nerve; **h**, hyoid bone; **iln**, internal laryngeal nerve; **ipc**, inferior pharyngeal constrictor muscle; **ll**, left lung; **lrn**, left recurrent inferior laryngeal nerve; **ls**, left subclavian artery; **ng**, nodose ganglion; **rl**, right lung; **rrn**, right recurrent inferior laryngeal nerve; **rs**, right subclavian artery; **sg**, superior cervical sympathetic ganglion; **sl**, superior laryngeal artery; **sln**, superior laryngeal nerve; **smg**, submandibular gland; **st**, sympathetic trunk; **tc**, thyroid cartilage; **th**, thyrohyoid muscle; **thm**, thyrohyoid membrane; **tr**, trachea; **X**, vagus nerve.
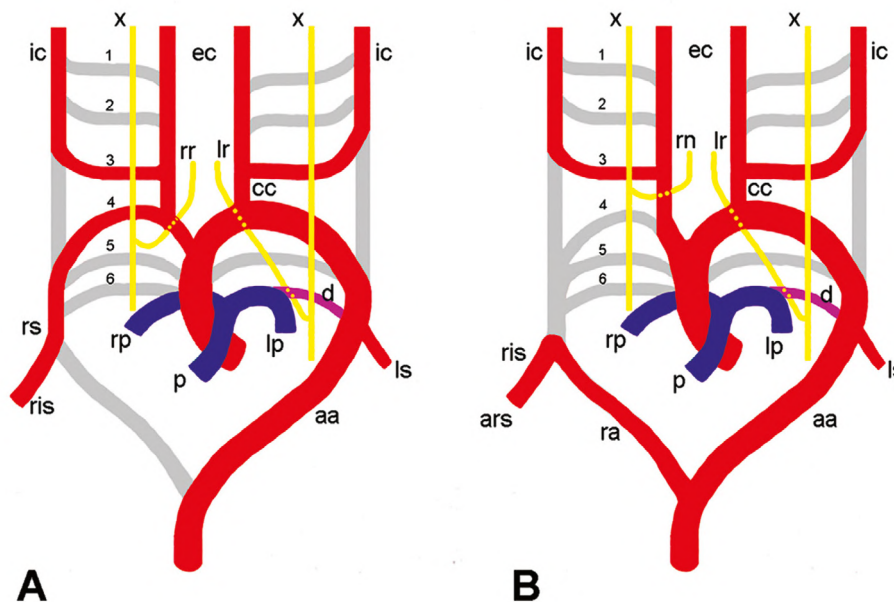
Fig. 3.- A. Drawing of development of right and left normal recurrent inferior laryngeal nerves. **B.** Drawing of development of right non-recurrent inferior laryngeal nerve associated with an aberrant subclavian artery and a normal left recurrent inferior laryngeal nerve. **aa**, aortic arch; **ars**, aberrant right subclavian artery; **cc**, common carotid artery; **d**, ductus arteriosus; **ec**, external carotid artery; **ic**, internal carotid artery; **ris**, part of subclavian artery from the right 7th intersegmentary artery; **lp**, left pulmonary artery; **lr**, left recurrent inferior laryngeal nerve; **ls**, left subclavian artery; **rn**, right non-recurrent inferior laryngeal nerve; **p**, pulmonary arterial trunk; **ra**, persistent portion of the right dorsal aorta artery **rp**, right pulmonary artery; **rr**, right recurrent inferior laryngeal nerve; **rs**, right subclavian artery; **X**, vagus nerve. **1-6**, aortic arches. The arches coloured in gray regress disappearing.

The left RLN arose from the vagus nerve at 15-23 cm (average 19.060±1.653 cm) of the nodose ganglion. It then recurred below the aortic arch and entered the larynx at the level of the cricothyroid joint. The length of the left RLN from its origin to the larynx was 9-17.5 cm (average 13.320±1.653 cm) (Table 1A., Fig. 2A).

The length of the extracranial course of their fibers (RLN+Vagus nerve) was between 11.3-26.2 cm (average 20.8±2.31 cm) on the right side and from 27 to 40.5 cm (average 32.4±2.56 cm) on the left side (Table 1A).

Significant differences in relation to the side of the neck were found in the lengths of RLNs (p-value≈0) and vagus nerves (p-value≈0), being longer on the left side on both cases. With respect to the gender of the corpses, no significant differences in the lengths of RLNs were found (p-value=0.509). Additionally, the vagus nerve was found to be significantly longer in males than in females (p-value=0.007). No significant differences were found in the total length of extracranial course RLNs fibers (RLN+vagus) with respect to the gender of the corpses (p-value=0.096) (Table 1A).

Table 1. Average and range (between brackets) of laryngeal nerves lengths (centimetres). Distribution by side and gender. **1-A**, Results of recurrent laryngeal nerve (RLN); **1-B**, Results of superior (SLN) and internal laryngeal nerve (ILN); **1-C**, Results of external laryngeal nerve (ELN). **e.m**, extramuscular path of ELN; **i.m**, intramuscular path of ELN; **1-D**, Results of Friedman's classification types for side and gender. Percentage of cases (%) and number of cases/number of sample (between brackets).

1-A	RIGHT			LEFT		
	MALE	FEMALE	TOTAL	MALE	FEMALE	TOTAL
RLN	6.99±1.06 [4.5;9.5]	6.53±1.12 [4;9]	6.740±1.111 [4;9.5]	13.36±1.97 [9;17.5]	13.28±1.33 [10.4;16.5]	13.320±1.653 [9;17.5]
VAGUS	14.64±1.37 [11;17.5]	13.43±1.73 [6.5;16.6]	13.990±1.682 [6.5;17.5]	19.56±1.52 [15;23]	18.61±1.65 [16,22]	19.060±1.653 [15;23]
RLN + VAGUS	21.63±2.1 [15.5;26.2]	19.97±2.23 [11.3;25.5]	20.8±2.31 [11.3;26.2]	32.92±2.77 [27;40.5]	31.89±2.29 [27;37]	32.4±2.56 [27;40.5]
1-B	RIGHT			LEFT		
	MALE	FEMALE	TOTAL	MALE	FEMALE	TOTAL
SLN	1.97±0.9 [0.3;4]	1.82±0.88 [0;4]	1.890±0.891 [0;4]	1.85±0.67 [0.5;3.5]	2.08±0.84 [0.5;4]	1.970±0.770 [0.5;4]
ILN	4.15±1.05 [1.8;6.5]	4.08±0.98 [2;7]	4.110±1.013 [1.8;7]	4.41±1.03 [2;6.5]	4.07±0.87 [2;6]	4.230±0.960 [2;6.5]
ILN+SLN	6.08±0.97 [3.5;8]	5.84±0.95 [3.5;9]	5.961±0.965 [3.5;9]	6.18±0.92 [4;8.5]	6.12±1.02 [4.4;8.5]	6.147±0.971 [4;8.5]
1-C	RIGHT			LEFT		
	MALE	FEMALE	TOTAL	MALE	FEMALE	TOTAL
ELN e.m path	6.65±1.01 [4;8.5]	6.36±0.92 [5;9.5]	6.5±0.97 [4;9.5]	7.18±0.84 [4.5;9]	6.43±0.92 [4.5;9.3]	6.8±0.95 [4.5;9.3]
ELN i.m path	1.35±0.51 [0.3;2.2]	1±0.41 [0.3;1.7]	1.17±0.9 [0.3;2.2]	1.18±0.42 [0.5;2]	1.17±0.47 [0.3;2]	1.17±0.44 [0.3;2]
ELN total path	7.83±0.99 [5.5;10]	6.93±0.96 [5.8;10]	7.42±1.06 [5.5;10]	8.34±0.73 [6.7;10]	7.28±0.79 [6;9.5]	7.81±0.92 [6;10]
ELN total path + SLN	9.87±1.04 [8;12]	8.98±1.08 [7.8;12]	9.47±1.13 [7.8;12]	10.16±0.99 [8.3;16]	9.41±1.17 [8.20;13]	9.78±1.13 [8.2;13]
1-D	RIGHT			LEFT		
	MALE	FEMALE	TOTAL	MALE	FEMALE	TOTAL
TYPE 1 (No i.m path)	0 [0/26]	4.2% [1/24]	2% [1/50]	0 [0/23]	0 [0/25]	0 [0/48]
TYPE 2 (≥ 1cm)	38.5% [10/26]	58.3% [14/24]	48% [24/50]	54.2% [13/24]	45.8% [11/24]	50% [24/48]
TYPE 3 (>1cm)	61.5% [16/26]	37.5% [9/24]	50% [25/50]	45.8% [11/24]	92.8% [13/24]	50% [24/48]

Superior laryngeal nerve

The SLN arose from the lower pole of the inferior ganglion of the vagus nerve (nodose ganglion) (Fig. 2B). After coursing 0.3-4 cm (average 1.933±0.831 cm), it divided into its terminal branches (Table 1B., Fig. 2B). In one case, on the right side of a female, the SLN was absent and the ILN and ELN arose directly from the nodose ganglion (0.45%, 1/222).

No significant differences in SLN lengths were found regarding the side (p-value =0.497) or gender (p-value=0.692) (Table 1B).

Internal laryngeal nerve

The ILN descends from its origin from SLN to enter into the larynx through the thyrohyoid membrane, in an anteromedial oblique course (Fig. 2B). The length of this pathway ranged from 1.8 to 7 cm (average 4.172±0.986 cm) and, considering it in conjunction with the SLN, the length ranged from 3.5 to 9 cm (average 6.054±0.970 cm) (Table 1B). In the case where the ILN arose directly from the vagus nerve its length was 4 cm.

No significant differences in ILN lengths were found regarding the side (p-value=0.367) or gender (p-value=0.128). However, when the lengths of the ILN and SLN were added, significant differences per side were found, being longer on the left side (p-value p≈0). No differences were detected in gender (p= 0.601) (Table 1B).

External laryngeal nerve

The ELN arose from the SLN as one of its terminal branches and descended describing an anterosuperior concavity, over the lateral surface of the inferior pharyngeal constrictor muscle (IPCM) (Fig. 2B). It then bended to go medially towards the cricothyroid muscle. The length of this pathway was between 5.5-10 cm (average 7.6±1.01 cm) (Table 1C). It should be noted that a variable part of its path coursed between the fibres of IPCM (intramuscular path), in some cases (Table 1C., Fig. 2B). Based on the length of this intramuscular path, the ELN was grouped in three different types, according to Friedman's classification; Type 1, the nerve runs superficial to the IPCM in all its pathway; Type 2, it has a distal intramuscular course of 1 cm or less and Type 3, with an intramuscular course of more than 1 cm (Friedman et al., 2002) (Table 1D).

Significant differences in the total path of ELN were found regarding the corpse's gender (p-value ≈0), being larger for males (8.07±0.905 cm) than females (7.11±0.881 cm), but no significant differences were found with respect to the corpse's side (p-value=0.067) (Table 1C). However, when the lengths of the ELN and SLN were added, significant differences per side were found, being longer on the left side (p-value p=0.01) and gender being greater on males (p= 0.001) (Table 1C).

The ELN extramuscular path presented significant differences with respect to the corpse's gender (p-value≈0), being larger for males (6.91±0.96 cm) than females (6.39±0.917 cm) ,and the corpse's side (p-value=0.034), being larger for the left side (6.78±0.954 cm) than the right side (6.5±0.973 cm). No significant differences were found by gender (p-value=0.058) or side (p-value=0.94) for the ELN intramuscular way. In relation to Friedman's classification, no significant differences were found regarding the gender (p-value=0.687) and side (p-value=0.789) of the corpse.

DISCUSSION

Electromyographic studies in humans have shown that all laryngeal nerves, including the ILN, can supply a secondary innervation to other laryngeal muscles, so that all of them can receive nerve impulses from two different laryngeal nerves and some of them from three (posterior cricoarytenoid and cricothyroid muscles) or four (cricothyroid muscle). It should be noted that in the case of the cricothyroid muscle, part of this innervation comes from the contralateral ELN and RLN (Martín-Oviedo et al., 2011; 2019).

The length of these motor laryngeal nerves is one of the morphological parameters involved in nerve conduction, which is essential for performance of laryngeal functions (Krmpotic, 1958; Shin and Rabuzzi, 1971; Steiss and Marshall, 1988; Prades et al., 2012). The existence of muscular double innervation and the difference in length between

the laryngeal nerves on both sides may affect the synchronicity of nerve impulse arrival to laryngeal muscles, and therefore the synchronicity of vocal fold function. In the same way, the length of sensory nerve fibers may have an important role in laryngeal closure and cough reflexes.

Nonetheless, there are very few studies about the length of laryngeal nerves.

The discussion of results obtained in this study will be carried out following the same order as presented.

Recurrent inferior laryngeal nerve

The length of the RLN has been studied with more detail in only three works, one of them being one of our previous studies (Asgharpour et al., 2012). All authors measured both RLNs from its origin at the vagus nerve to their entry into the larynx, obtaining similar results (Table 2). The length of the extracranial pathway of both RLNs fibres (RLN+vagus) has not been reported by the authors of the bibliography consulted.

Comparison of the results based on gender is not feasible because one of the authors did not specify the gender of the samples (Liebermann-Meffert et al., 1999) and the other has only used females in his work (Prades et al., 2012). In our study, no statistically significant differences have been found between males and females (p=0.509) as in our previous study (Asgharpour et al., 2012).

The difference between the lengths of both RLNs (p≈0) is due to the fact that, in the human embryo, the ductus arteriosus drags the left RLN down when the heart descends and the neck elongates, lengthening it (Fig. 3A). However, on the right side the distal part of right sixth aortic arch involutes completely, to the extent that the fifth aortic arches

also disappear; when the heart descends and the neck elongates, no vascular structure pulls down the right RLN. It migrates freely into the neck, and curves around the proximal portion of right SA derived from fourth aortic arch, the proximal right dorsal aorta and the seventh intersegmental artery (Gray et al., 1976; Sadler and Langman, 2012) (Fig. 3A). Therefore, as the course of RLN is determined by the arterial development, its alterations give rise to anatomical variations that can affect the length of RLNs such as non-RLN (Gray et al., 1976; Sadler and Langman, 2012). The non-RLN is more common on the right side (0%-4.76%) (Sturniolo et al., 1999; Monfared et al., 2002) than on the left (0-0.04%) (Henry et al., 1988) The right non-RLN has been reported in association with absence of the brachiocephalic trunk and existence of an aberrant SA (lusoria artery), which arises from aortic arch, after the origin of the left subclavian artery (89.3% of cases) (Henry et al., 2017). To reach the right upper limb, the course of the aberrant SA may be retroesophageal (80%), tracheo-esophageal (15%) or pretracheal (5%) (Vuillard et al., 1978), being in our case retroesophageal. Due to these pathways in front of or behind the esophagus, the aberrant SA may compress the oesophagus causing dysphagia, known as dysphagia lusoria (Lam et al., 2020).

The aberrant development of right SA and therefore of a non-RLN, is caused on one hand by the involution of right fourth aortic arch and the proximal right dorsal aorta and on the other by the persistence of a distal right dorsal aorta and the right seventh intersegmental artery (Gray et al., 1976; Sadler and Langman, 2012) (Fig. 3B).

The left non-RLN is associated with a situs inversus, a retroesophageal left subclavian artery

Table 2. Length of RLNs: results of previous authors (centimetres).

AUTHORS	SAMPLE		RANGE		AVERAGE	
	RIGHT	LEFT	RIGHT	LEFT	RIGHT	LEFT
Liebermann-Meffert et al. (1999)	23	23	6 - 8	12 - 14	7	13
Asgharpour et al. (2012)	108	106	4 - 9.5	9 - 17.5	6.7	13.3
Prades et al. (2012)	6	6	6.5 - 9	11.5 - 14.5	7.5	13.7
Our study. (2021)	111	111	4 - 9.5	9 - 17.5	6.76	13.32

and right ligamentum arteriosus. The complexity of these vascular variations would explain its lower incidence (0.04%, 2/4673) (Henry et al., 1988).

The coexistence of right or left non-RLN and variations of great arteries allows a preoperative diagnosis of them using radiological techniques such a computed tomography (Watanabe et al., 2016) or ultrasonography (Citton et al., 2016).

The right non-RLN is more frequent in females (88%, 15/17; 90%, 28/31) than in males (12%, 2/17; 10%, 3/31) (Avisse et al., 1998; Toniato et al., 2004) in accordance with our results.

The course of non-RLNs from the vagus nerve to the larynx is highly variable, and different classifications have been described in relationship to the level where it originates and the shape of its course (Stewart et al., 1972; Soustelle et al., 1976; Abboud and Aouad, 2004; Hong et al., 2014). The most popular classification distinguishes two different types; in type 1 or high, the non-RLNs arise from the vagus nerve at or above the level of the laryngotracheal junction and run a short and transversal path to the cricothyroid joint (0%-73.3% of non-RLN) (Stewart et al., 1972; Soustelle et al., 1976; Vuillard et al., 1978; Proye et al., 1982; Henry et al., 1988; Avisse et al., 1998; Toniato et al., 2004; Dolezel et al., 2015; Watanabe et al., 2016) while in the type 2 or low, the non-RLNs arise from the vagus below the laryngotracheal junction and run an oblique course to the cricothyroid joint (0%-100% of non-RLN) (Stewart et al., 1972; Soustelle et al., 1976; Vuillard et al., 1978; Proye et al., 1982; Henry et al., 1988; Avisse et al., 1998; Monfared et al., 2002; Toniato et al., 2004; Dolezel et al., 2015; Watanabe et al., 2016). This last type has been subdivided in type 2A, when the nerve courses above the inferior thyroid artery (64.5%-100% of non-RLN), and type 2B, when the nerve courses below this artery (0-19.35% of non-RLN) (Abboud and Aouad, 2004; Toniato et al., 2004; Prades et al., 2012; Watanabe et al., 2016) Therefore, type 2 is longer than type 1, and subtype 2B longer than 2A. The case in our study corresponded to type 2A.

A good knowledge of non-RLN is essential to avoid injuring this nerve during neck surgical procedures and to avoid the complications of vocal

fold dysfunction derived from this (dysphonia, aspirations, pneumonia) (Avisse et al., 1998; Hong et al., 2014; Watanabe et al., 2016).

Superior laryngeal nerve

The length of the SLN has been measured from its origin in the nodose ganglion to its bifurcation in its terminal branches by all of authors, ranging from 0 to 4.18 cm (Durham and Harrison, 1964; Kambic et al., 1984; Lang et al., 1987; Melamed et al., 2002; Furlan et al., 2003; Kiray et al., 2006; Oliveira and Silva, 2007). Only three authors have provided more detailed information about this topic (Table 3). None of them found significant differences in the lengths of the SLN in relation to the side of corpse in agreement with our results (Furlan et al., 2003; Kiray et al., 2006; Oliveira and Silva, 2007). Two authors have analyzed the length of the SLN with respect to corpses' gender (Furlan et al., 2003; Oliveira and Silva, 2007). One of them found significant differences, being longer in males than females (p = 0.01) (Furlan et al., 2003), while the other did not find them (Oliveira and Silva, 2007), in agreement with our results. Greater length was found in corpses over 25 years of age (p<0.05) (Oliveira and Silva, 2007), while in relation to height (p=0.33) and ethnic group (p=0.24), no significant differences were found (Furlan et al., 2003).

Absence of the SLN has been reported between 5% (4/80) (Kambic et al., 1984) and 6% (6/100) of cases (Furlan et al., 2003), being our incidence lower (0.45%, 1/222).

Internal laryngeal nerve

The length of the ILN has been measured from its origin to the thyrohyoid membrane by most authors, being between 2.1 cm and 8.49 cm (Lang et al., 1987; Espinoza et al., 1989; Furlan et al., 2003; Kiray et al., 2006; Oliveira and Silva, 2007). Studies of length of ILN in relation to age (Oliveira and Silva, 2007), gender (Furlan et al., 2003; Oliveira and Silva, 2007), side (Furlan et al., 2003; Kiray et al., 2006; Oliveira and Silva, 2007) or ethnic group (Furlan et al., 2003) did not find any significant difference (p<0.05). In agreement with these authors, our study shows no significant differences for side and gender

(Table 3). In relation to corpse's height, there are discrepancies since one study reported that the increase in height is accompanied by an increase in ILN length (Oliveira and Silva, 2007), while this was not observed in the other study (p=0.71) (Furlan et al., 2003).

The total length of the SLN+ILN reported was 7.1 cm (Kiray et al., 2006), being slightly shorter in our results (6.054±0.970) (Table 3).

External laryngeal nerve

The length of the ELN from its origin to its entry into the cricothyroid muscle has been measured by various authors, ranging from 4 cm to 12 cm (Kambic et al., 1984; Lang et al., 1987; Espinoza et al., 1989; Furlan et al., 2003; Oliveira and Silva, 2007) (Table 3).

No significant difference has been found in the length of the ELN for sides (p=0.26) and gender (p= 0.69) in agreement with our results, nor for ethnicity (p=0.42) (Furlan et al., 2003). In relation to the height, there are discrepancies since one study reported that the increase in height is accompanied by an increase in ELN length (Oliveira and Silva, 2007), but this was not observed in the other study (p=0.96) (Furlan et al., 2003).

The intramuscular course of the ELN has been reported by several authors following Friedman's classification (Table 4). Most of them have found type 1 as the most frequen. However, in our study it was the type 2, being type 1 the least frequent (Table 4). The different types were not affected by genders on both sides (p =0.519 on the right and p = 1.000 on the left) (Taytawat et al., 2010), as in our study (p-value= 0.695 on the right, p-value= 0.864 on the left). In addition, no significant differences for side have been found in the present work (p-value= 0.687).

Table 3. Length of SLN, ILN and ELN: results of previous authors in centimetres (average and range between brackets). (A= Pheoderma, B= Melanoderma).

SLN	MALE	FEMALE	RIGHT	LEFT	WHITE	NOWHITE
Furlan et al. (2003)	1.85±0.11	1.38±0.11	1.68±0.14	1.67±0.12	1.72±0.11	1.61±0.16
Kiray et al. (2006)	?	?	1.48±0.44	1.35±0.4	?	?
Oliveira & Silva (2007)	2.5±0.6 [1.0;3.0]	0	2.5±0.6 [1.0;3.0]	2.5±0.6 [1.0;3.0]	2.5±0.5 [1.5;3.0]	A: 2.4±0.8 [1.0;4.0] B: 2.6±0.5 [2.0;3.0]
Our study (2021)	1.91± 0.792 [0.3;4]	1.95± 0.868 [0;4]	1.9±0.891 [0;4]	1.96±0.770 [0.5;4]	1.93±0.831 [0.3;4]	0
ILN	**MALE**	**FEMALE**	**RIGHT**	**LEFT**	**WHITE**	**NOWHITE**
Furlan et al. (2003)	4.5±0.16	4.48±0.14	4.57±0.14	4.4±0.16	4.39±0.14	4.64±0.16
Kiray et al. (2006)	?	?	5.8±0.82	5.63±0.74	?	?
Oliveira & Silva (2007)	5.4±.1.0 [4;7.5]	0	5.3±0.9 [4;7]	5.3±0.9 [4;7]	5.4±1.1 [4;7.5]	A: 5.3±0.8 [4.5;7.2] B: 6.2±0.9 [4.5;7.0]
Our study (2021)	4.28±1.045 [1.8;6.5]	4.075±0.922 [2;7]	4.11±1.013 [1.8;7]	4.27±0.960 [2;6.5]	4.17±0.986 [1.8;7]	0
ELN	**MALE**	**FEMALE**	**RIGHT**	**LEFT**	**WHITE**	**NOWHITE**
Furlan et al. (2003)	6.3±0.12	6.2±0.23	6.13±0.17	6.39±0.16	6.19±0.12	6.38±0.24
Oliveira & Silva (2007)	7.2±1.1 [4.0;9.5]	0	7.0±1.0 [5.0;9.0]	7.0±1.0 [5.0;9.0]	7.1±1.2 [4.0;9.5]	A: 7.0±0.8 [5.0;8.0] B: 8.4±0.6 [7.5;9.0]
Our study (2021)	8.08±0.60 [5.5;10]	7.1±0.917 [5.8;10]	7.38±0.974 [5.5;10]	7.81±0.954 [6;10]	7.6±0.971 [5.5;10]	0

Table 4. Distribution of Friedman's classification types for sides. Results of previous authors (Percentage of cases and number of cases/number of sample).

AUTHORS	TYPE 1			TYPE 2			TYPE 3		
	RIGHT	**LEFT**	**TOTAL**	**RIGHT**	**LEFT**	**TOTAL**	**RIGHT**	**LEFT**	**TOTAL**
Ozlugedik et al. (2007)	?	?	22.5% [9/40]	?	?	67.5% [27/40]	?	?	10% [4/40]
Taytawat et al. (2010)	95.5% [63/66]	94.1% [64/68]	94.78% [127/134]	4.5% [3/66]	5.9% [4/68]	5.22% [7/134]	0% [0/66]	0% [0/66]	0% [0/134]
Patnaik et al. (2012)	53% [9/17]	47% [8/17]	50% [17/34]	35.3% [6/17]	35.3% [6/17]	35.3% [12/34]	11.7% [2/17]	17.6% [3/17]	14.7% [5/34]
Gavid et al. (2017)	?	?	50% [4/8]	?	?	25% [2/8]	?	?	25% [2/8]
Uludag et al. (2017)	?	?	59.7% [126/211]	?	?	11.3% [24/211]	?	?	29% [61/211]
Cheruiyot et al. (2018)	?	?	50% [250/500]	?	?	35% [175/500]	?	?	15% [75/500]
Our study (2021)	2% [1/50]	0 [0/48]	1% [1/98]	48% [24/50]	50% [24/48]	49% [48/98]	50% [25/50]	50% [24/48]	50% [49/98]

It should be noted that during thyroid surgery, type 1 has the greatest risk of injury and type 3 the least, since the IPCM protects the ELN in most of its pathway. On the other hand, this fact makes the ELN must be identified by intraoperative neurostimulation (Friedman et al., 2002; Ozlugedik et al., 2007).

CONCLUSIONS

All laryngeal nerves are significantly longer on the left side (RLN, ILN+SLN, ELN+SLN, and extramuscular path of ELN) and the ELN (extramuscular path, total path and ELN+SLN) is significantly longer in males than females. These differences may affect the synchronicity of nerve impulse arrival to laryngeal muscles, and therefore the synchronicity of vocal fold function. In the same way, the length of sensory nerve fibers may have an important role in laryngeal closure and cough reflexes. In addition, these results would have to be taken into account in functional studies (neurostimulation, electromyography) and in some clinical procedures (reinnervation, denervation).

ACKNOWLEDGEMENTS

REFERENCES

ABBOUD B, AOUAD R (2004) Non-recurrent laryngeal nerve in thyroid surgery: report of three cases and review of the literature. *J Laryngol Otol*, 118: 139-142.

ASGHARPOUR E, MARANILLO E, SAÑUDO JR, PASCUAL-FONT A, RODRIGUEZ-NIEDENFÜHR M, VALDERRAMA FJ, VIEJO F, PARKIN IG, VÁZQUEZ T (2012) Recurrent laryngeal nerve landmarks revisited. *Head Neck*, 34(9): 1240-1246.

ATKINS JP (1973) An electromyographic study of recurrent laryngeal nerve conduction and its clinical applications. *Laryngoscope*, 83 (5): 796-807.

AVISSE C, MARCUS C, DELATTRE JF, MARCUS C, CAILLIEZ-TOMASI JP, PALOT JP, LADAM-MARCUS V, MENANTEAN B, FLAMENT JB (1998) Right nonrecurrent inferior laryngeal nerve and arteria lusoria: the diagnostic and therapeutic implications of an anatomic anomaly. Review of 17 cases. *Surg Radiol Anat*, 20: 227-232.

CHERUIYOT I, KIPKORIR V, HENRY BM, MUNGUTI J, CIROCCHI R, ODULA P, WONG LM, OLABU B, WALOCHA J (2018) Surgical anatomy of the external branch of the superior laryngeal nerve: A systematic review and meta-analysis. *Langenbeck's Arch Surg*, 403: 811-823.

CITTON M, VIEL G, IACOBONE M (2016) Neck ultrasonography for detection of non-recurrent laryngeal nerve. *Gland Surg*, 5 (6): 583-590.

DOLEZEL R, JAROSEK J, HANA L, RYSKA M (2015) Clinical relevance and surgical anatomy of non-recurrent laryngeal nerve: 7 year experience. *Surg Radiol Anat*, 37: 321-325.

DURHAM CF, HARRISON TS (1964) The surgical anatomy of the superior laryngeal nerve. *Surg Gynecol Obstet*, 118: 38-44.

ESPINOZA J, HAMOIR M, DHEM A (1989) La préservation du rameau externe du nerf laringé supérieur en chirurgie thyroïdienne. *Ann Otol Laryngol* (Paris), 106: 127-134.

FRIEDMAN M, LOSAVIO P, IBRAHIM H (2002) Superior laryngeal nerve identification and preservation in thyroidectomy. *Arch Otolaryngol Head Neck Surg*, 128 (3): 296-303.

FURLAN JC, BRANDAO LG, FERRAZ AR, RODRIGUES AJ Jr (2003) Surgical anatomy of the extralaryngeal aspect of the superior laryngeal nerve. *Arch Otolaryngol Head Neck Surg*, 129 (1): 79-82.

GAVID M, DUBOIS MD, LARIVÉ E, PRADES JM (2017) Superior laryngeal nerve in thyroid surgery: anatomical identification and monitoring. *Eur Arch Otorhinolaryngol*, 274 (9): 3519-3526.

GRAY SW, SKANDALAKIS JE, AKIN JT (1976) Embryological considerations of thyroid surgery: developmental anatomy of the thyroid, parathyroids and the recurrent laryngeal nerve. *Am Surg*, 42: 621-628.

HARRISON DF (1981) Fibre size frequency in the recurrent laryngeal nerves of man and giraffe. *Acta Otolaryngol*, 91: 383-389.

HENRY JF, AUDIFFRET J, DENIZOT A, PLAN M (1988) The nonrecurrent inferior laryngeal nerve: review of 33 cases, including two on the left side. *Surgery*, 104: 977-984.

HENRY BM, SANNA S, GRAVES MJ, VIKSE J, SANNA B, TOMASZEWSKA IM, TUBBS RS, WALOCHA JA, TOMASZEWSKI KA (2017) The non-recurrent laryngeal nerve: a meta-analysis and clinical considerations. *PeerJ*, 5 e3012.

HONG KH, PARK HT, YANG YS (2014) Characteristic travelling patterns of non-recurrent laryngeal nerves. *J Laryngol Otol*, 128: 534-539.

KAMBIC V, ZARGI M, RADSEL Z (1984) Topographic anatomy of the external branch of the superior laryngeal nerve. *J Laryngol Otol*, 98: 1121-1124.

KIRAY A, NADERI S, ERGUR I, KORMAN E (2006) Surgical anatomy of the internal branch of the superior laryngeal nerve. *Eur Spine J*, 15 (9): 1320-5.

KRMPOTIC J. (1958). Anatomisch-histologische und funktionelle Verhältnisse des rechten und des linken Nervus recurrens mit Rücksicht auf die Geschwindigkeit der Impuls leitung bei einer Ursprungsanomalie der rechten Schlüsselbeinarterie. *Arch fur Onr Kehi Heilkunde*, 173: 490-496.

LAM K, TAN EW, LEE JC (2020) Case of dysphagia lusoria in a patient with a non-recurrent laryngeal nerve. *ANZ J Surg*, 90 (7-8): 1487-1489.

LANG J, NACHBAUR S, FISCHER K, VOGEL E (1987) The superior laryngeal nerve and the superior laryngeal artery. *Acta Anat (Basel)*, 130 (4): 309-318.

LIEBERMANN-MEFFERT D, WALBRUN B, HIEBERT C, SIEWERT J (1999) Recurrent and superior laryngeal nerves: a new look with implications for esophageal surgeons. *Ann Thorac Surg*, 67: 217-223.

MARTIN-OVIEDO C, MARANILLO E, LOWY-BENOLIEL A, PASCUAL-FONT A, MARTINEZ-GUIRADO T, RODRIGUEZ-NIEDENFÜHR M, SAÑUDO J, SCOLA B, VAZQUEZ T (2011) Functional role of human laryngeal nerve connections. *Laryngoscope*, 121 (11): 2338-2343.

MARTÍN-OVIEDO C, MARANILLO E, SAÑUDO JR, PÉREZ-LLORET P, VERDÚ E, MARTÍNEZ-GUIRADO T, ÁLVAREZ-MONTERO O, GÓMEZ MARTÍN-ZARCO JM, VÁZQUEZ T (2019) The human laryngeal innervation revisited-the role of the neural connections. *Anat Rec (Hoboken)*, 302 (4): 646-651.

MELAMED H, HARRIS MB, AWASTHI D (2002) Anatomic considerations of superior laryngeal nerve during anterior cervical spine procedures. *Spine*, 27 (4): E83-E86.

MONFARED A, GORTI G, KIM D (2002) Microsurgical anatomy of the laryngeal nerves as related to thyroid surgery. *Laryngoscope*, 112: 386-392.

OLIVEIRA LR, SILVA AL (2007) Superior laryngeal nerve anatomy in corpses not preserved in formaldehyde: contribution to the operative technique. *Acta Cir Bras*, 22 (3): 220-228.

OZLUGEDIK S, ACAR HI, APAYDIN N, TEKDEMIR I, ELHAN A, COMERT A (2007) Surgical anatomy of the external branch of the superior laryngeal nerve. *Clin Anat*, 20 (4): 387-391.

PATNAIK U, NILAKANTAN A, SHRIVASTAVA T (2012). Anatomical variations of the external branch of the superior laryngeal nerve in relation to the inferior constrictor muscle: cadaveric dissection study. *J Laryngol Otology*, 126: 907-912.

PRADES JM, DUBOIS MD, DUMOLLARD JM, TORDELLA L, RIGAIL J, TIMOSHENKO AP, PEOC'H M (2012) Morphological and functional asymmetry of the human recurrent laryngeal nerve. *Surg Radiol Anat*, 34: 903-908.

PROYE C, DUMONT HG, DEPADT G, LAGACHE G (1982) Le nerf "recurrent non récurrent" danger en chirurgie thyroidienne – quinze observations. *Ann Chir*, 36 (7): 454-458.

SADLER TW, LANGMAN J (2012) *Langman's Medical Embryology*, Twelfth Edition. Philadelphia: *Wolters Kluwer Health/Lippincott Williams & Wilkins*. Chap 13, pp 185-191.

SHIN T, RABUZZI DD (1971) Conduction studies of the canine recurrent laryngeal nerve. *Laryngoscope*, 8: 586-596.

SOUSTELLE J, VUILLARD P, TAPISSIER J, JUVANON L (1976) La non-recurrence du nerf larynge inferieur: a propos de 9 cas. *Lyon Chir*, 72: 57-71.

STEISS JE, MARSHALL AE (1988) Electromyographic evaluation of conduction time and velocity of the recurrent laryngeal nerves of clinically normal dogs. *Am J Vet Res*, 49: 1533-1536.

STEWART GR, MOUNTAIN JC, COLCOCK BP (1972) Non-recurrent laryngeal nerve. *Brit J Surg*, 59: 379-381.

STURNIOLO G, D'ALIA C, TONANTE A, GAGLIANO E, TARANTO F, GRAZIA LO SCHIAVO M, D'ALIA C, TONANTE A, GAGLIANO E, TARANTO F, LO SCHIAVO MG (1999) The recurrent laryngeal nerve related to thyroid surgery. *Am J Surg*, 177: 485-488.

TAYTAWAT P, VIRAVUD Y, PLAKORNKUL V, ROONGRUANGCHAI J, MANOONPOL C (2010) Identification of the external laryngeal nerve: its anatomical relations to inferior constrictor muscle, superior thyroid artery, and superior pole of the thyroid gland in Thais. *J Med Assoc Thai*, 93 (8): 961-968.

TESTUT L, LATARJET A (1972) *Tratado de Anatomía Humana*. Barcelona: Salvat. Vol. 1, pp 882-942.

TONIATO A, MAZZAROTTO R, PIOTTO A, BERNANTE P, PAGETTA C, PELIZZO MR (2004) Identification of the nonrecurrent laryngeal nerve during thyroid surgery:20-year experience. *World J Surg*, 28: 659-661.

ULUDAG M, AYGUN N, KARTAL K, CITGEZ B, BESLER E, YETKIN G, KAYA C, OZSAHIN H, MIHMANLI M, ISGOR A (2017) Contribution of intraoperative neural monitoring to preservation of the external branch of the superior laryngeal nerve: a randomized prospective clinical trial. *Langenbeck's Arch Surg*, 402 (6): 965-976.

VUILLARD P, BOUCHET A, GOUILLAT C, ARMAND D (1978) Non-recurrent inferior laryngeal nerve (15 operative cases). *Bull Assoc Anat*, 62 (179): 497-505.

WATANABE A, TANIGUCHI M, KIMURA Y, ITO S, HOSOKAWA M, SASAKI S (2016) Efficient, effective, safe procedure to identify nonrecurrent inferior laryngeal nerve during thyroid surgery. *Head Neck*, 38: 573-577.

WILLIAMS PL. (1995) *Gray´s Anatomy, Thirty-eighth Edition*. New York: Churchill-Livingstone, pp 1253.

Age-related changes of the tongue and Weber's salivary glands in male albino mice: A histopathological and morphometric study

Islam O. Abdel Fattah[1], Wael A. Nasr El-Din[1,2]

[1]*Department of Human Anatomy and Embryology, Faculty of Medicine, Suez Canal University, Ismailia, Egypt*

[2]*Department of Anatomy, College of Medicine and Medical Sciences, Arabian Gulf University, Manama, Bahrain*

SUMMARY

The tongue and salivary glands are affected by aging process. This study aimed to assess the age-related structural changes of the tongue and Weber's salivary glands in mice. Mice were grouped as adult (5.9 ± 0.5 months old) and aged (21.2 ± 0.6 months old) groups. After sacrifice, the tongues in both groups were dissected and underwent a histopathological examination using haematoxylin and eosin (Hx&E) stain, as well as morphometric analysis. The aged group exhibited thin epithelium, atrophied papillae, engorged blood vessels, disorganized myofibers and increased adipose tissue deposition. In addition, the lingual salivary gland revealed acinar cell atrophy and increased interacinar stroma. The lingual lymphoid tissue showed diffusely arranged lymphoid cells and increased stroma. Morphometrically, the aged group exhibited a significant decrease in the height and number of filiform papillae, in addition to a significant decrease in epithelial layer thickness, diameter and length of myofibers, length of myonuclei, and the number of sarcomeres. Furthermore, the aged group showed a significant increase in lamina propria/submucosal thickness, length of sarcomeres and stromal tissue percentage of the Weber's salivary glands. Aging induces significant structural changes in the tongue and Weber's salivary glands in mice.

Key words: Aging – Tongue – Salivary gland – Histopathology – Morphometry

INTRODUCTION

Feeding is considered as a critical factor that ensures the success for adaptation to the environment and the persistence through procreation (Iwasaki, 2002). The tongue is considered a mirror reflecting general personal health, particularly the filiform papillae (Altayeb and Salem, 2017). Structurally, it is a muscular organ enclosed by epithelium, and contributes to taste, speech, swallowing, suckling and respiratory functions (Byahatti et al., 2010; Nagai et al., 2008; Patil et al., 2013). The papillae on the dorsal surface of the tongue are divided into 2 types; mechanical papillae and gustatory papillae (Goździewska-Harłajczuk et al., 2018). Moreover,

Corresponding author:
Islam Omar Abdel Fattah, Lecturer. Department of Human Anatomy and Embryology, Faculty of Medicine, Suez Canal University, 4.5 Km the Ring Road, 41511 Ismailia, Egypt. Phone: +201286203737. E-mail: islam_omar2007@yahoo.com

the taste buds are widely distributed over its dorsal and lateral surfaces indicating the critical importance of the tongue in feeding and taste (Iwasaki, 2002).

The aging process is implicated in several anatomical and functional changes (Junior et al., 2014). One of the largely affected organs by these aging changes is the tongue because it continues to grow even at advanced age affecting both taste acuity and structure (Rother, et al., 2002; Conger and Wells, 1969). For example, by the age of 75-90 years old, it was reported that the number of taste buds is 50% less than that in younger individuals (Mistretta, 1984). Furthermore, there is a progressive decline in skeletal muscle mass and strength with age (Cheng et al., 2017). Even histologically, as noted in human cadaveric tongues, with progressive aging there is a corresponding reduction in tongue muscle fiber diameter of the superior longitudinal muscle fibers (Nakayama, 1991).

Age-related lingual dysfunction may largely affect swallowing due to muscle fibers affection and an increased noncontractile tissue, causing a stiffer tongue; in addition, aging could also increase the risk of aspiration, as it increases the probability of bolus retention in the pharynx (Connor et al., 2009; Cichero, 2018; Yoshida et al., 2006). Furthermore, age-related taste disorder consequences may take place such as anorexia, loss of appetite, changes in food preferences, weight loss and malnutrition (Imoscopi et al., 2012). These impaired functions may finally cause considerable morbidity and mortality through increased risk of starvation, dehydration, aspiration pneumonia and airway obstruction (Palmer et al., 2000).

So, the aim of this study was to investigate the age-related histopathological and morphometric changes of the tongue and Weber's salivary glands by comparing aged and adult mice.

MATERIAL AND METHODS

Animals

Twenty pathogen-free Swiss-albino male mice were purchased from the Animal House of the Faculty of Veterinary Medicine, Suez Canal University, Ismailia, Egypt. All experimental procedures were performed regarding the National Institutes of Health guide for the care and use of laboratory animals (NIH Publications No. 8023, revised 1978).

Experimental design

The obtained mice were selected according to their ages to be divided into 2 age groups (n=10): adult group (5.9 ± 0.5 months old) and aged group (21.2 ± 0.6 months old). These age groups were chosen to be equivalent to human ages of about 20 years old for the adult group and about 70 years old for the aged group. This estimation of age in mice in comparison to the human was calculated according to the following equation:

9.125 mice days = 1 human year (Dutta and Sengupta, 2016).

Histopathological study

All animals were euthanized by an overdose of intraperitoneal sodium pentobarbital. The tongue was carefully dissected out and submersed in 10% formal saline for not more than 6 hours. Specimens were then dehydrated, cleared in xylene and embedded in paraffin. Sections of 5 µm thickness were cut at the mid-sagittal plane of the tongue with vertical cuts, stained with haematoxylin and eosin (Hx&E) stain and then examined by light microscope (Olympus, Tokyo, Japan). The dorsal aspect of the anterior part of the tongue was examined for mucosal and muscle layers, while its posterior part was examined for its lymphoid tissue and Weber's salivary glands.

Morphometric study

Morphometric measurements were performed on the original images using the ImageJ® (version 1.53) software. To avoid the inter-observer bias, only one investigator performed the morphometric measurements. From each animal, 5 sections were observed and from each section 5 different regions were investigated. In a pre-elementary pilot study, we found that formalin fixation for not more than 6 hours of tongue specimens resulted in 6.4 ± 0.3% tissue shrinkage, so we considered

this observation during our measurements and the statistical analysis. The following parameters were measured in Hx&E-stained sections regarding mucosal layer at a magnification of ×400:

1. Total epithelial thickness: the distance between the basal lamina of the epithelial layer to the surface of horny layer.

2. Horny layer thickness: the distance between the end of granular layer to the tips of filiform papillae.

3. Total height of filiform papillae: the distance between the base to the tip of filiform papillae.

4. Lamina propria/submucosa thickness: the distance between the basal lamina of the epithelial layer and the muscle layer.

5. The number of papillae/mm.

6. Percentage of stromal tissue of Weber's salivary glands: the percentage of the stromal tissue surface area in relation to the total surface area of the examined image.

7. Proportions of total epithelial, horny layer and lamina propria/submucosal thicknesses according to the total thickness of the tongue were calculated. The total thickness of the tongue was measured at median sagittal Hx&E-stained sections at a magnification of ×40 by measuring the distance between a horizontal line passing through the midway between dorsal and ventral surfaces, and the dorsal surface exactly at the middle of it to avoid duplication between the layers of the dorsal and ventral sides during the calculation of these proportions. The middle point of the dorsal surface was determined by measuring the total length of it from the tip of the tongue to its root, so the midpoint was detected (Fig. 1).

Furthermore, the following measurements were applied regarding the muscle layer at a magnification of ×1000:

1. Diameter of myofibers.
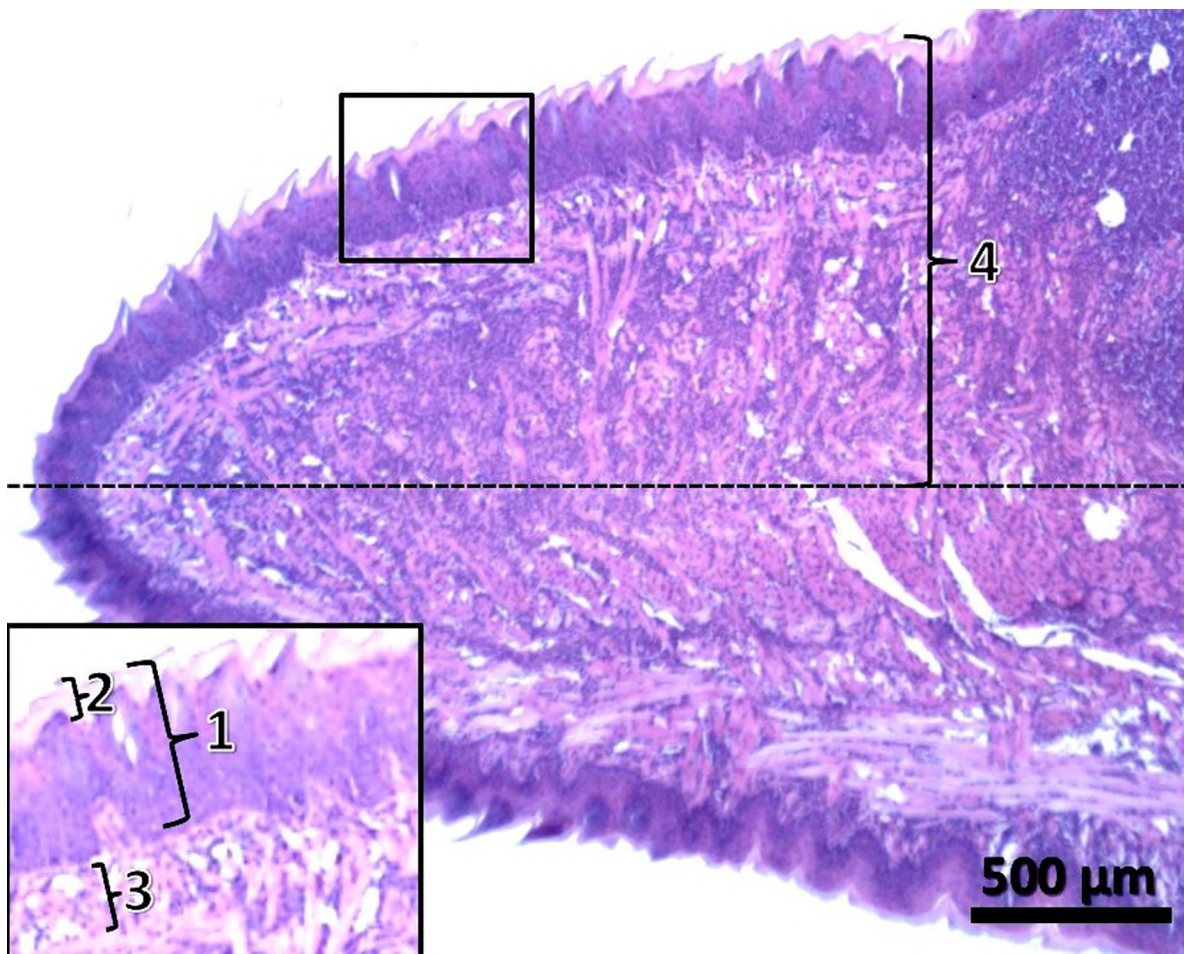
Fig. 1.- Procedures for measurement of proportions of the total epithelial (1), horny layer (2) and lamina propria/submucosal (3) thicknesses according to total tongue thickness (4). (Hx&E; ×40 – scale bar = 500 μm).

2. Length of myonuclei.

3. Length of sarcomeres (Vidal et al., 2020): the distance between two successive Z-lines. At high magnification, this Z-line appeared in Hx&E-stained sections as a dark line extending in the middle of the lightly stained I-band (Fig. 2).

4. Number of sarcomeres/mm (Vidal et al., 2020): each sarcomere is the area extending between two successive Z-line (Fig. 2). The number of sarcomeres was counted within the total width of the image then this counted number was divided on the total width of the image that was 0.958 mm.

Statistical analysis

The data analysis was performed using Statistical Package for Social Sciences® (SPSS) software version 25.0 for Windows. Results were expressed as the mean±standard deviation (SD). Data underwent testing for normality by Shapiro-Wilk test and revealed that the data has non-normal (non-parametric) distribution. Thus, for comparisons between the two groups, significance was evaluated using the Mann-Whitney non-parametric U-test.

RESULTS

Histopathological study

The Hx&E-stained sections of the adult group exhibited that the dorsal aspect of the anterior part of the tongue was covered by keratinized stratified squamous epithelium showing lingual papillae mostly of filiform type. The subepithelial layer of loose connective tissue was seen separating the overlying epithelial layer from the underlying muscle layer. The muscle layer showed well-arranged myofibers of different directions with distinct striations and peripheral myonuclei (Figs. 3A, B). On the other hand, the posterior part of the tongue showed embedded Weber's salivary
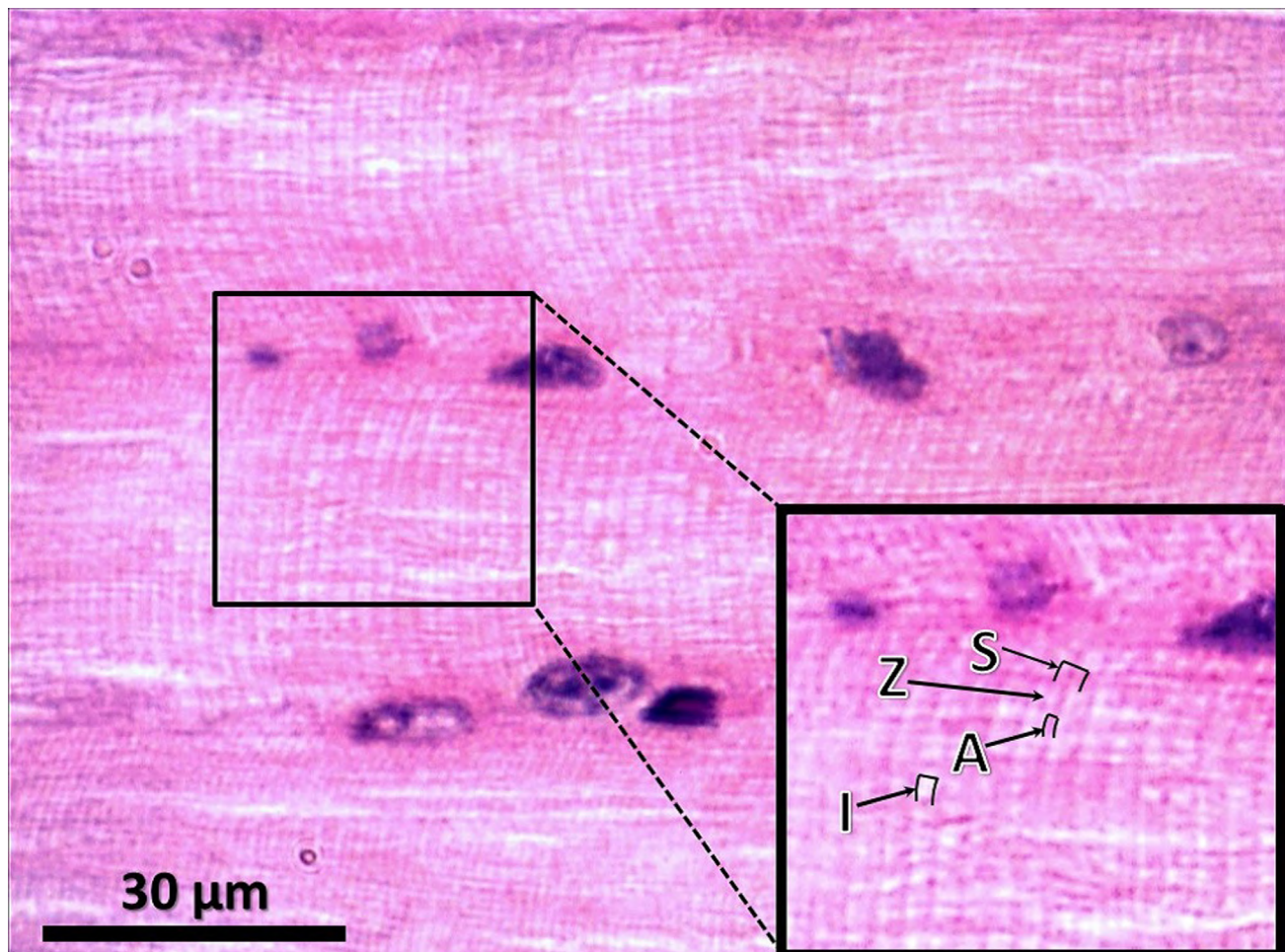
Fig. 2.- Structure of a tongue muscle fiber at high magnification showing structures used in morphometry including Z-line (Z), sarcomere (S), A-band (A) and I-band (I). (Hx&E; ×1000 – scale bar = 30 μm).

glands within the submucosa and muscle layer with purely mucous acini having a clear basophilic cytoplasm with scanty stroma in between (Fig. 3C). Furthermore, the posterior part of the tongue exhibited closely packed lymphoid cell aggregates with little stroma in between and surrounded by a distinct fibrous capsule (Fig. 3D).

The epithelial layer in the aged group revealed massive thinning of the covering keratin and areas of absent papillae. Furthermore, the underlying connective tissue was massively condensed with highly congested blood vessels (Fig. 4A). On the other hand, the muscle layer showed massive disarrangement of its myofibers, loss of most of their striations, and massive deposition of adipocytes in between muscle fibers (Figs. 4B, C). Moreover, many acini of Weber's salivary glands

demonstrated loss of their epithelium and an increase in the amount of interacinar stroma (Fig. 4D). In addition, the lymphoid aggregates in the posterior part of the tongue had loosely arranged lymphoid cells with an increase in the amount of the stroma in between and thickening of the surrounding capsule (Fig. 4E).

Morphometric assessment

The total epithelial and horny layer thicknesses and proportions were significantly decreased in the aged group compared to the adult one, while the lamina propria/submucosa thickness and proportion, and percentage of the stroma of Weber's salivary glands were significantly increased in the aged group compared to the adult one (Table 1). On the other hand, both total
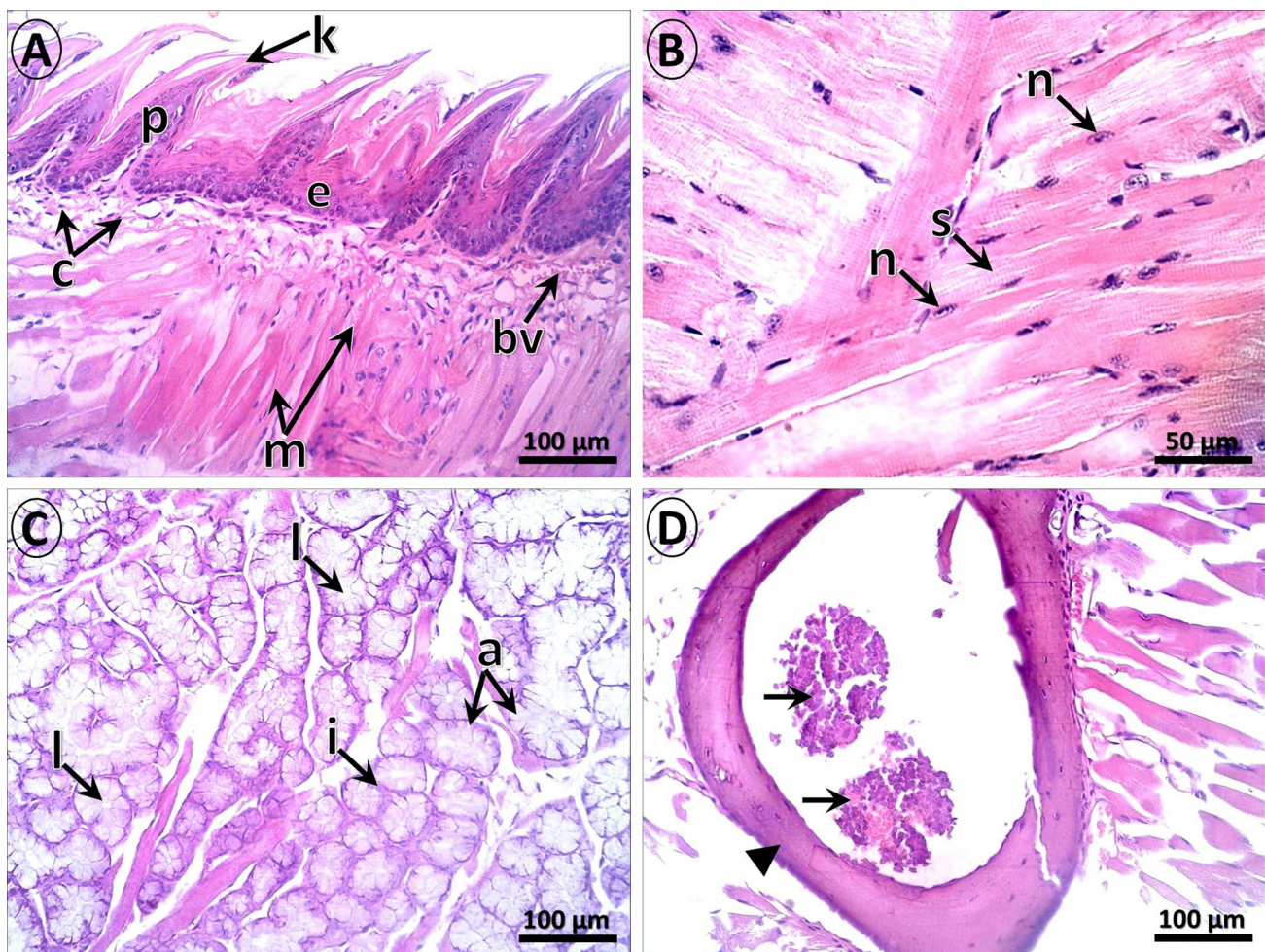

Fig. 3.- Sections of the tongue and Weber's salivary glands of the adult group. **A.** The dorsum of anterior part of the tongue showing a covering layer of keratinized stratified squamous epithelium (e) with filiform lingual papillae (p) that are covered by a keratin layer (k). There is a subepithelial layer of loose connective tissue (c) showing normally appearing blood vessel (bv), in addition to the muscle layer (m). **B.** The muscle layer of the tongue shows well-arranged muscle bundles of different directions with distinct striations (s) and peripheral myonuclei (n). **C.** The posterior part of the tongue shows Weber's salivary glands within the muscle layer with relatively large mucous acinar cells having a clear basophilic cytoplasm, central lumens (l) and scanty interacinar stroma (i). **D.** The posterior part of the tongue shows packed lymphoid cell aggregates with little amount of stroma in between (arrows), surrounded by a fibrous capsule (arrowhead). (Hx&E; A, C, D and E ×200 – scale bar = 100μm; B ×400 – scale bar = 50μm).

height of filiform papillae and their number were significantly decreased in the aged group compared to the adult one (Fig. 5). According to muscle layer morphometry, the diameter and length of myofibers, the number of sarcomeres, and length of myonuclei were significantly decreased in the aged group compared to the adult one. However, the length of sarcomeres was significantly increased in the aged group compared to the adult one (Table 2).

DISCUSSION

The tongue has a critical role in swallowing, speech and breathing (Kletzien et al., 2018). Since aging disrupts the body functions leading to increased morbidity, the tongue is one of the seriously affected organs with these aging changes manifested mainly by depapillization, in addition to reduced saliva production that makes the oral mucosa massively inelastic and dry (Kletzien et al., 2018; Warraich et al., 2020). In addition to surface fissuring and taste disturbances, as a common effect of aging on the tongue, the lingual muscles show loss of their usual tone (Malik et al., 2015; Zagaria,

2019). The current study assessed age-related changes in tongue mucosa, muscles, and lymphoid tissue, and also those involving the Weber's salivary glands in mice based on histopathological and morphometric examinations.

Experimental non-human models are essential in studying the aging process (Folgueras et al., 2018). For that, mice are considered extremely similar to humans in many physiologies and cellular functions. For example, the digestive, immune, musculoskeletal and endocrine systems of mice are quite equivalent to that of humans in both function and structure (Vanhooren and Libert, 2013). Mice are therefore a unique tool for the assessment of aging changes. In addition, the fact that mice have a short life span is an advantage, so mouse histological alterations can be examined at all stages of the aging (Nadon, 2004; Folgueras et al., 2018).

However limited, previous studies have experimentally investigated tongue age-related structural and histomorphometic alterations (Stablein and Meyer, 1986; Meisel et al., 1987). For example, and in agreement with our results,
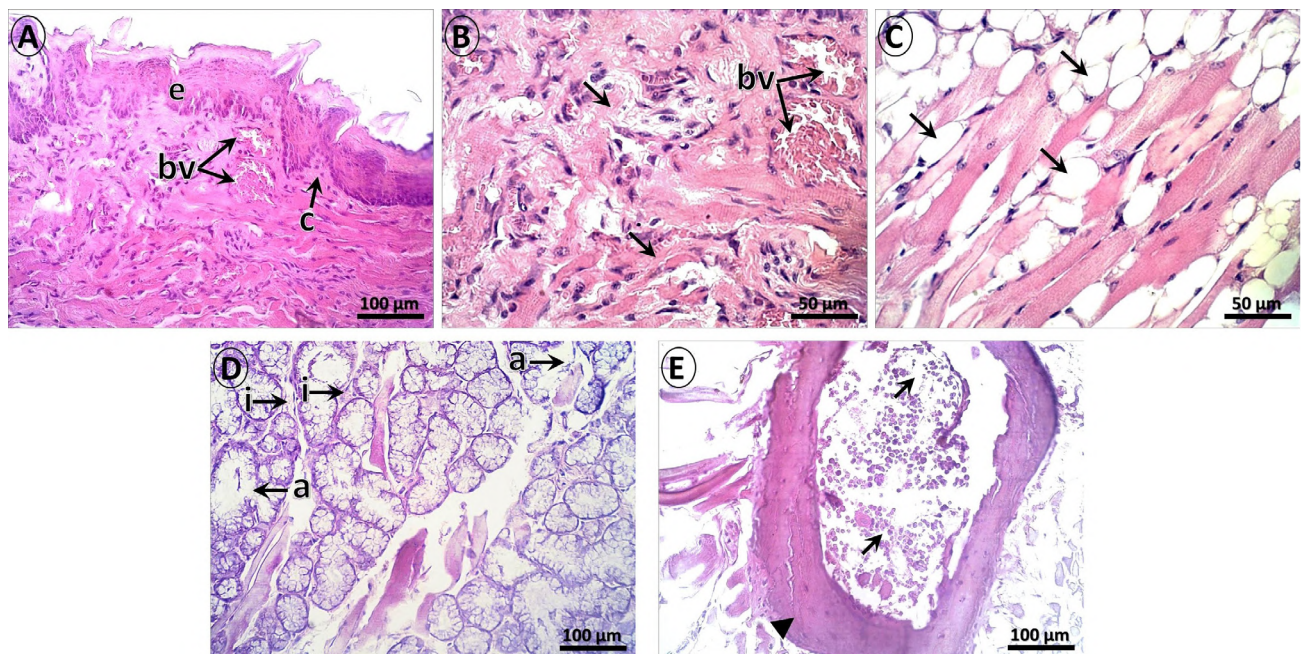
Fig. 4.- Photomicrographs of sections of the tongue and Weber's salivary glands of the aged group. **A.** The dorsum of anterior part of the tongue shows thinning of the epithelial layer (e), in addition to the absence of most the papillae. The underlying connective tissue is highly condensed (c) with massive congestion of the blood vessels (bv). **B.** The muscle layer of the tongue shows massively disorganized myofibers with loss of the boundaries between them (arrows). Note the highly congested blood vessels (bv). **C.** The muscle layer of the tongue shows infiltration with adipocytes in between its muscle fibers (arrows). **D.** The posterior part of the tongue shows Weber's salivary glands revealing degeneration of many acinar cells with loss of cell boundaries in between (a), in addition to an increase in amount of interacinar stroma (i). **E.** The posterior part of the tongue showing massively diffuse arranged lymphoid cells with increased stroma (arrows) and thickened surrounding capsule (arrowhead). (Hx&E; A, D and E ×200 – scale bar = 100μm; B and C ×400 – scale bar = 50μm).

Meisel et al. (1987) reported that aging causes various lingual mucosal changes in 18 month-old mice in form of atrophic hyperkeratotic changes of lingual epithelium with blunt disorganized filiform papillae. Nonetheless, most of the studies were concerned with the assessment of human age-related tongue changes (Scott et al., 1983; Bässler, 1987; Nakayama, 1991; Sasaki, 2004). Scott et al. (1983) found that lingual epithelial thickness in humans undergoes reduction by about 30% comparing the ages of 18 with 98 years old. Also, the current study results revealed that there is a reduction in total epithelial thickness by 38.69% in the aged mice compared to the adult ones. Furthermore, Nakayama (1991) found that the aged human tongue undergoes progressive epithelial layer degeneration, atrophy of the acini of the Weber's salivary glands and decreased
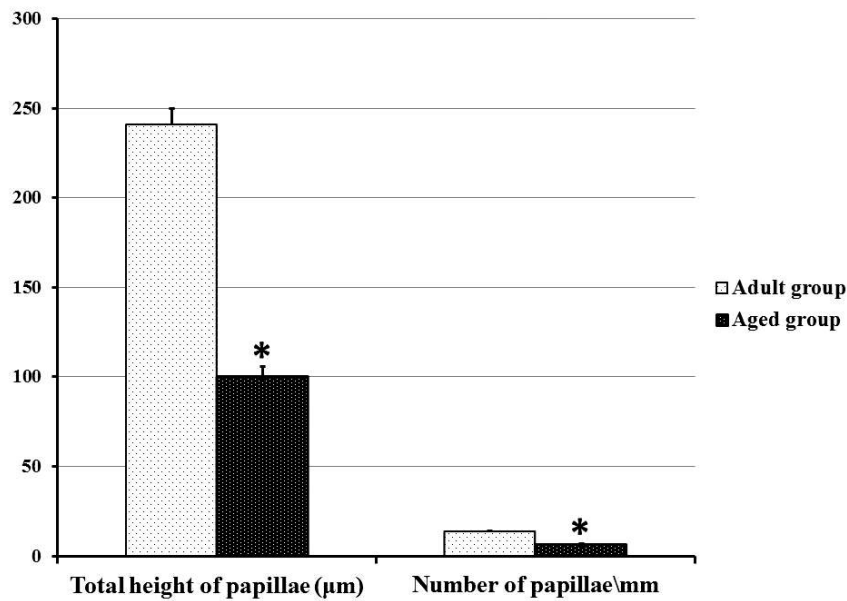
Fig. 5.- Morphometric parameters of filiform papillae of the study groups according to total hight and number of papillae. Values are mean±SD. *p<0.05 *vs* adult group, as determined by Mann-Whitney *U*-test.

Table 1. Morphometric parameters of lingual mucosa and Weber's salivary glands of the study groups, and proportions of tongue layers according to total tongue thickness.

Parameter	Total tongue thickness (µm)	Epithelial layer		Horny layer		Lamina propria/ submucosal layer		Stromal tissue percentage of Weber's salivary glands (%)
Group		Thickness (µm)	Proportion (%)	Thickness (µm)	Proportion (%)	Thickness (µm)	Proportion (%)	
Adult group	916.27± 0.64	135.42 ± 6.49	14.78 ± 0.71	70.62 ± 6.56	7.71 ± 0.72	40.81 ± 5.76	4.45 ± 0.63	7.82 ± 0.49
Aged group	740.76± 1.65*	83.02 ± 7.26*	11.21 ± 0.98*	26.72 ± 5.01*	3.61 ± 0.67*	116.89 ± 10.60*	15.78 ± 1.44*	19.15 ± 0.65*

Values are mean±SD. *p<0.05 vs adult group, as determined by Mann-Whitney U-test.

Table 2. Morphometric parameters of the tongue muscle layer of the study groups.

Parameter Group	Diameter of myofibers (µm)	Length of myonuclei (µm)	Length of sarcomeres (µm)	Number of sarcomeres/ mm
Adult group	35.47 ± 0.86	10.90 ± 0.61	2.03 ± 0.05	492.94 ± 12.62
Aged group	20.12 ± 1.53*	9.92 ± 0.54*	2.43 ± 0.02*	411.85 ± 3.90*

Values are mean±SD. *p<0.05 vs adult group, as determined by Mann-Whitney U-test.

diameter of lingual muscle fibers based on his histopathological evaluation.

Although the actual causes of aging are still unknown, theories were have been produced to explain these changes comprising the damage concept, including the accumulating damage due to DNA breaks, oxidized bases and/or mitochondrial malfunctions; or the programmed aging concept, including internal processes such as DNA telomere shortening (Youssef, 2017).

Reactive oxygen species (ROS) are the key mediators causing aging. According to this theory, oxidative damage occurs due to the over-production of ROS or due to lack of counteraction by the antioxidants (Simioni et al., 2018). With aging, ROS induce DNA damage and downstream damage (Robert and Wagner, 2020). So, it is believed that ROS could produce as many as 50,000 DNA lesions per cell per day contributing to aging (Maynard et al., 2015; Blagosklonny, 2008). In addition, mitochondrial dysfunction may be an important part of such aging process that is due to increasing ROS accumulation producing DNA damage of these organelles (Robert and Wagner, 2020). With the progression of these mitochondrial damaging events, these destructed mitochondria lead to increased ROS amount and produce less ATP during aging (Stefanatos and Sanz, 2018). Importantly, up-regulation of the antioxidative enzyme signaling pathways also has a critical role in decreasing the oxidative stress activity; however, at animal aging, it was proven that there is progressively diminished antioxidant system capacity encouraging the sequelae of ROS accumulation (Vina et al., 2006; Wei and Lee, 2002).

The progressive telomere shortening was the first developed molecular explanation for cell senescence that occurs progressively every cell division (Yousefzadeh et al., 2021). So, telomere length was considered to be the most suitable aging biomarkers during past decades because of its known role in cellular aging (Vaiserman and Krasnienkov, 2021). Despite DNA polymerase is the main responsible for DNA synthesis in the cell, it cannot efficiently replicate the last point of linear DNA leading to progressive telomere shortening every cell cycle (Jiang et al., 2007; Chim et al., 2018). At normal circumstances, telomere capping is essential for differentiation of the chromosomal ends from DNA breaks within the genome (Jiang et al., 2007). Also, oxidative stress is well-known to be implicated in aggravation of telomere shortening, and since telomeres prevent fusion of chromosome ends and also hinder the recognition of chromosomal ends as sites of DNA damage, ROS accumulation is a triggering factor for cellular senescence (Ledda et al., 2020; Jafri et al., 2016).

Aging of the oral mucosa is characterized by decreased epithelial thickness, decreased cellular density and reduced mitotic activity leading to decreased tissue regeneration and healing capacities (Abu Eid et al., 2012). In our study, we found that the lingual mucosa undergoes massive atrophy of its epithelial layer and its papillae, in addition to vascular congestion of the underlying connective tissue with aging. Furthermore, with histomorphometric analysis, there were decreased total epithelial and horny layer thicknesses, while the thickness of the subepithelial connective tissue was significantly increased with age.

Sarcopenia is defined as reduced skeletal muscle mass and strength. It prominently occurs during aging leading to dysphagia in the elderly (Kletzien

et al., 2013). This age-related tongue musculature degeneration is caused by multiple pathways leading to altered muscle fiber chemistry, reduced muscle fiber contraction ability, increased muscle fatigability, and decreased neuromuscular junction size and number (Kletzien et al., 2018). The intrinsic lingual muscles, in this study, showed various structural changes in form of a decreased diameter of their myofibers with decreased number of the sarcomeres and length of the myonuclei, in addition to intramuscular adipose cell accumulation that may refer to the functional disturbances that may affect the elderly concerning defective swallowing. In accordance with our results, Cullins and Connor (2017) reported that with aging the transverse and verticalis muscles in the old group had significantly smaller muscle fibers in 32 months old Fischer 344/Brown Norway rats.

Xerostomia is a common complaint of elderly people that provides a negative impact on their health (Nagler, 2004). Salivary hypofunction can ultimately lead to halitosis, dental caries, gingivitis, dry mouth, dry lips, dysgeusia, dysphagia, mastication problems, mucositis, oropharyngeal candidiasis, poorly fitting prostheses, sleeping difficulty, speech difficulty and traumatic oral lesions (Turner and Ship, 2007). Elsaied (2019) found that there are changes in the Weber's salivary glands included salivary duct lumen widening, stagnation of salivary secretion and slight vascular engorgement in aged rats. In the current study, we found that there is massive atrophy of the acinar cells and increasing fibrous stroma amount.

Conclusion: The present study emphasizes that aging in mice is associated with a wide range of changes affecting the mucosa and musculature of the tongue, in addition to affecting the Weber's salivary glands and lingual lymphoid tissue.

REFERENCES

ABU EID R, SAWAIR F, LANDINI G, SAKU T (2012) Age and the architecture of oral mucosa. *Age (Dordr)*, 34(3): 651-658.

ALTAYEBZM, SALEM MM (2017) The effect of ethanol on rat tongue and the possible protective role of royal jelly: Light and scanning electron microscopic study. *Egyp J Histol*, 40(3): 265-276.

BÄSSLER R (1987) Histopathology of different types of atrophy of the human tongue. *Pathol Res Pract*, 182(1): 87-97.

BLAGOSKLONNY MV (2008) Aging: ROS or TOR. *Cell Cycle*, 7(21): 3344-3354.

BYAHATTI SM, INGAFOU MSH (2010) The prevalence of tongue lesions in Libyan adult patients. *J Clin Exp Dent*, 2(4): e163-168.

CHENG IKY, YIU EML, CHAN KMK (2017) Changes in resting motor threshold of the tongue with normal aging and stroke. *Somatosens Mot Res*, 34(4): 242-247.

CHIM N, JACKSON LN, TRINH AM, CHAPUT JC (2018) Crystal structures of DNA polymerase I capture novel intermediates in the DNA synthesis pathway. *Elife*, 7: e40444.

CICHERO JAY (2018) Age-related changes to eating and swallowing impact frailty: Aspiration, choking risk, modified food texture and autonomy of choice. *Geriatrics (Basel)*, 3(4): 69.

CONGER AD, WELLS MA (1969) Radiation and aging effect on taste structure and function. *Radiat Res*, 37(1): 31-49.

CONNOR NP, RUSSELL JA, WANG H, JACKSON MA, MANN L, KLUENDER K (2009) Effect of tongue exercise on protrusive force and muscle fiber area in aging rats. *J Speech Lang Hear Res*, 52(3): 732-744.

CULLINS MJ, CONNOR NP (2017) Alterations of intrinsic tongue muscle properties with aging. *Muscle Nerve*, 56(6): E119-E125.

ELSAIED HA (2019) Histological and immunohistochemical study on selenium regenerative effect on submandibular and sublingual glands of rats. *Egyp Dent J*, 65: 3413-3426.

FOLGUERAS AR, FREITAS-RODRIGUEZ S, VELASCO G, LOPEZ-OTIN C (2018) Mouse models to disentangle the hallmarks of human aging. *Circ Res*, 123(7): 905-924.

GOŹDZIEWSKA-HARŁAJCZUK K, KLEĆKOWSKA-NAWROT J, BARSZCZ K, MARYCZ K, NAWARA T, MODLIŃSKA K, STRYJEK R (2018) Biological aspects of the tongue morphology of wild-captive WWCPS rats: a histological, histochemical and ultrastructural study. *Anat Sci Int*, 93(4): 514-532.

IMOSCOPI A, INELMEN EM, SERGI G, MIOTTO F, MANZATO E (2012) Taste loss in the elderly: Epidemiology, causes and consequences. *Aging Clin Exp Res*, 24(6): 570-579.

IWASAKI S (2002) Evolution of the structure and function of the vertebrate tongue. *J Anat*, 201(1): 1-13.

JAFRI MA, ANSARI SA, ALQAHTANI MH, SHAY JW (2016) Roles of telomeres and telomerase in cancer, and advances in telomerase-targeted therapies. *Genome Med*, 8(1): 69.

JIANG H, JU Z, RUDOLPH KL (2007) Telomere shortening and ageing. *Z Gerontol Geriatr*, 40(5): 314-324.

JUNIOR HVM, TAVARES JC, MAGALHÃES AAB, GALVÃO HC, FERREIRA MAF (2014) Characterization of tongue pressure in the elderly. *Audiol Commun Res*, 19(4): 375-379.

KLETZIEN H, RUSSELL JA, LEVERSON GE, CONNOR NP (2018) Age-related effect of cell death on fiber morphology and number in tongue muscle. *Muscle Nerve*, 57(1): E29-E37.

KLETZIEN H, RUSSELL JA, LEVERSON GE, CONNOR NP (2013) Differential effects of targeted tongue exercise and treadmill running on aging tongue muscle structure and contractile properties. *J Appl Physiol* (1985), 114(4): 472-481.

LEDDA C, LORETO C, RAPISARDA V (2020) Telomere length as a biomarker of biological aging in shift workers. *Appl Sci*, 10: 2764.

MALIK P, RATHEE M, BHORIA M (2015) Oral tissues: Considerations in geriatric patients. *Int J Appl Dent Sci*, 1(3): 4-7.

MAYNARD S, FANG EF, SCHEIBYE-KNUDSEN M, CROTEAU DL, BOHR VA (2015) DNA Damage, DNA repair, aging, and neurodegeneration. *Cold Spring Harb Perspect Med*, 5(10): a025130.

MEISEL D, SKOBE Z, SHKLAR G (1987) Lingual changes in ageing mice by light and scanning electron-microscopy. *Arch Oral Biol*, 32 (9): 643-649.

MISTRETTA CM (1984) Aging effects on anatomy and neurophysiology of taste and smell. *Gerodontology*, 3(2): 131-136.

NADON NL (2004) Maintaining aged rodents for biogerontology research. *Lab Anim (NY)*, 33: 36-41.

NAGAI H, RUSSELL JA, JACKSON MA, CONNOR NP (2008) Effect of aging on tongue protrusion forces in rats. *Dysphagia*, 23(2): 116-121.

NAGLER RM (2004) Salivary glands and the aging process: Mechanistic aspects, health-status and medicinal-efficacy monitoring. *Biogerontology*, 5(4): 223-233.

NAKAYAMA M (1991) Histological study on aging changes in the human tongue. *Nihon Jibiinkoka Gakkai Kaiho*, 94(4): 541-555.

PALMAR JB, DRENNAN JC, BABA M (2000) Evaluation and treatment of swallowing impairments. *Am Fam Physician*, 61(8): 2453-2462.

PATIL S, KASWAN S, RAHMAN F, DONI B (2013) Prevalence of tongue lesions in the Indian population. *J Clin Exp Dent*, 5(3): e128-e132.

ROBERT G, WAGNER JR (2020) ROS-induced DNA damage as an underlying cause of aging. *Adv Geriatr Med Res*, 2(4): e200024.

ROTHER P, WOHLGEMUTH B, WOLFF W, REBENTROST I (2002) Morphometrically observable aging changes in the human tongue. *Ann Anat*, 184(2): 159-164.

SASAKI M (1994) Histomorphometric analysis of age-related changes in epithelial thickness and Langerhans cell density of the human tongue. *Tohoku J Exp Med*, 173(3): 321-336.

SCOTT J, VALENTINE JA, HILL CAS, BALASOORIYA BA (1983) A quantitative histological analysis of the effects of age and sex on human lingual epithelium. *J Biol Buccale*, 11(4): 303-315.

SIMIONI C, ZAULI G, MARTELLI AM, VITALE M, SACCHETTI G, GONELLI A, NERI LM (2018) Oxidative stress: Role of physical exercise and antioxidant nutraceuticals in adulthood and aging. *Oncotarget*, 9(24): 17181-17198.

STABLEIN M, MEYER J (1986) Age-related changes in the epithelial dimensions and capillaries of the oral mucosa of the rat. *Arch Oral Biol*, 31(9): 609-616.

STEFANATOS R, SANZ A (2018) The role of mitochondrial ROS in the aging brain. *FEBS Lett*, 592(5): 743-758.

TURNER MD, SHIP JA (2007) Dry mouth and its effects on the oral health of elderly people. *J Am Dent Assoc*, 138(9): 15S-20S.

VAISERMAN A, KRASNIENKOV D (2021) Telomere length as a marker of biological age: state-of-the-art. Open issues, and future perspectives. *Front Genet*, 11: 630186.

VANHOOREN V, LIBERT C (2013) The mouse as a model organism in aging research: Usefulness, pitfalls and possibilities. *Ageing Res Rev*, 12(1): 8-21.

VIDAL R, VOLKWEIS G, YWAZAKI JL, RANDI MAF, LOUREIRO APC, GOMES ARS (2020) The effects of stretching on muscle morphometry of ovariectomized rats. *Fisioter Mov*, 33: e003312.

VINA J, BORRAS C, GOMEZ-CABRERA MC, ORR WC (2006) Part of the series: From dietary antioxidants to regulators in cellular signalling and gene expression: role of reactive oxygen species and (phyto) oestrogens in the modulation of adaptive response to stress. *Free Radic Res*, 40(2): 111-119.

WARRAICH U, HUSSAIN F, KAYANI HUR (2020) Aging - oxidative stress, antioxidants and computational modeling. *Heliyon*, 6(5): e04107.

WEI YH, LEE HC (2002) Oxidative stress, mitochondrial DNA mutation, and impairment of antioxidant enzymes in aging. *Exp Biol Med (Maywood)*, 227(9): 671-682.

YOSHIDA M, KIKUTANI T, TSUGA K, UTANOHARA Y, HAYASHI R, AKAGAWA Y (2006) Decreased tongue pressure reflects symptom of dysphagia. *Dysphagia*, 21(1): 61-65.

YOUSEFZADEH M, HENPITA C, VYAS R, SOTO-PALMA C, ROBBINS P, NIEDERNHOFER L (2021) DNA damage—how and why we age?. *Elife*, 10: e62852.

YOUSSEF MM (2017) Study the influence of antioxidant therapy on age- related changes in the buccal mucosa of rats (Histological and immunohistochemical investigation). *Egyp Dent J*, 63: 565-578.

ZAGARIA MAE (2019) Age- and medication-related contributors to upper GI dysfunction in older adults. *US Pharm*, 44(12): 32-35.

Development of the cerebellum vermis: A morphometric study on second trimester fetuses

Daniel Gómez-Padilla, Rogelio Lozano-Garza, Ana María Covarrubias, Omar Cortes-Enríquez, Iván Dávila-Escamilla, Norberto López-Serna, Ramón Castruita-Meza

Embryology Department, Faculty of Medicine of the Autonomous University of Nuevo Leon, Monterrey, Nuevo León, Mexico

SUMMARY

The human cerebellum has a complex process of development. The cerebellum vermis is one of its main structures and its abnormal development has been related to different pathologies. There is still very little information about the normal measures of the cerebellum vermis during its development. Image techniques have a temporality limitation, plus they are operant dependent. The main objective of this research is to establish a nomogram of in vivo measures of human fetuses to contribute to the diagnosis of cerebellum malformations. We made an encephalic dissection of 33 human fetuses from the 14 to 21 weeks of gestation to expose the cerebellum. A dissection of the cerebellum was made to expose the cerebellum vermis, which was measured in three axes: craniocaudal, anteroposterior, and obliquus axes. Results were reported as the mean of each axis in millimeters and with the standard deviation. A Pearson´s correlation test was made between each of the axes with the gestational age.

The three measured axes showed an increasing growth pattern during the studied period. They also showed a strong correlation between these increasing measures as the gestational age increases. We described a series of measures of different axes of the cerebellum vermis. Our results help define the normal dimensions of this structure, which ultimately could ease the diagnosis of a malformation such as a cerebellum vermis hypoplasia or agenesis. Further research should be carried out to increase the validity of these results.

Key words: Cerebellum – Embryology – Abnormalities – Growth and development – Anatomy

INTRODUCTION

The cerebellum vermis is the structure that divides the cerebellum into a right and left hemispheres, and it is originated from the rombencephalic ventricle. The cerebellum vermis is formed from the fusion of the developing cerebellar hemispheres when they both join in the middle line. Thus, vermis could not be developed without the development of the cerebellar hemispheres. The main patterns of vermis malformation are The Dandy-Walker malformation

Corresponding author:
Omar Cortes-Enriquez. Embryology Department, Faculty of Medicine of the UANL. Francisco I. Madero Av. And Jose E. Gonzalez Av. Mitras Centro, 64000 Monterrey, Nuevo Leon, Mexico. Phone: 52 (81) 8329 4187. E-mail: omardcortes@outlook.com

spectrum, the Arnold Chiari malformation, Joubert´s syndrome, tectocerebelar dysraphism and rhombencephalosynapsis (Takanashi, 1999).

Dandy-Walker malformation, the Chiari malformation, and the cerebellum Hypoplasia are among the most common cerebellum malformations diagnosed in-utero. From this, the vermis is one of the most affected structures. Its study is difficult due to an inconsistent classification, unknown pathogenesis, and the lack of consensus about the normal dimensions of the cerebellum (Aldinger et al., 2019).

Dandy Walker´s disease is one of the most frequent malformations, and it is present approximately in 1 out of 25,000-35,000 newborns (Cignini et al., 2016; Jurca et al., 2017). Clinically, hypoplasia of the cerebellum vermis and its related syndromes may present with developmental delay and speaking problems (Wassmer et al., 2003).

Patients with Chiari Malformation present with a displacement of the cerebellar structures. In Chiari Malformation type I, the most affected structures are cerebellar tonsils and the inferior aspect of the vermis. This type of malformation presents with clinical manifestations in early adulthood and middle age (Barkovich, 1986).

Other malformation patterns of the vermis are represented by the Phelan-McDermid and Joubert Syndrome. The first one is caused by a deletion on 22q13.3, and it is defined by a development delay and a mild-to-severe absence of expressive speech, being the most frequent structural malformation of the cerebellum vermis hypoplasia. Joubert syndrome is defined by congenital ataxia with diffuse hypotonia, development delay, abnormal respiratory patterns, and oculomotor apraxia. Pathognomonic radiological findings of this syndrome are the molar tooth sign, that is the result of vermis hypoplasia, thickened and misoriented cerebellum peduncles, and an interpeduncular fossa abnormally deep (Aldinger, 2013; Zaki, 2008).

The prematurity period constitutes a critical period in cerebellar development. More than 19-37 % of the preterm infants evaluated with MRI are diagnosed with cerebellar bleeding, whilst more than 7-9% are diagnosed with the same

pathology by ultrasound. The increasing use of MRI in preterm neonates has demonstrated that cerebellar hypoplasia is a relatively common finding on preterm infants particularly when the study is made during childhood (Gano and Barkovich, 2019).

Cerebellum vermis could suffer from morphological alterations not only from a congenital manner, being an example the infections that affect the cerebellum. Acute cerebellitis is considered an inflammatory syndrome that presents with fever, nausea, headache, and an altered mental status with cerebellar symptoms. The study of patients with rotavirus-related cerebellitis showed on the MRI that the most affected regions were the vermis and cerebellar cortex (Takanashi, 2010). Intracranial abnormalities in the cerebellum have also been described in the in-utero infection with B19 Parvovirus. However, it has been suggested that these were the result of the intrauterine treatment and not from the infection (Glenn et al., 2007).

Outer from the infectious causes, adverse effects on the development of the cerebellum have been described in patients that received corticosteroids either prenatally or neonatally. Preterm neonates are at risk of cerebellar hypoplasia, which is related to a delay in motor and cognitive functions (Tam, 2011).

A malformation on the cerebellum vermis could be detected prenatally either with an ultrasound technique or with a Magnetic Resonance Image (MRI). Nevertheless, image techniques have a temporality limitation. Ultrasonography does not identify cerebellum structures until the 18th week of gestation, and MRI is not recommended before this week because of fetal mobility and the small size of the structures. The intentional study of the human cerebellum before the eighteenth week of gestation increases the number of false-positive results of vermis dysplasia or abnormal communication of the fourth ventricle and cisterna magna (Chapman et al., 2015).

With the increasing availability and the better visualization of posterior fossa structures with MRI, cerebellar malformations are most frequently recognized. Even when they represent the

most frequent structural malformations of the cerebellum, hemisphere and vermis malformations are poorly understood because of the scarce literature on them. Moreover, it is difficult to assure at the moment of diagnosis of a malformed cerebellum if this represents atrophy, hypoplasia, or another malformation in the cerebellum, since there are not enough and appropriate morphological descriptions. Patel and Barkovich (2002) proposed a morphological classification of the cerebellum malformations, which divides them into two main groups: cerebellar hypoplasia and cerebellar dysplasia, each group is divided posteriorly in focal hypoplasia or generalized hypoplasia and focal or generalized dysplasia, respectively (Patel and Barkovich, 2002).

Friede (1973) described the gestational periods in which cerebellum layers are developed. He also described the expected weight of the cerebellum in different gestational periods (Friede, 1973).

Cerebellum Hypoplasia might have a broad spectrum of manifestations and can be present either isolated or with a genetic syndrome (Sarnat and Alcala, 1980).

Many authors have described the cerebellum measures and growth patterns with similar results. Goldstein et al. (1987) did a prospective analysis in which they use ultrasound to measure the cerebellum growth prenatally. They studied 371 women with a normal evolutive pregnancy between 13 to 40 weeks of gestation. Three measures were taken: cerebellum diameter (CD), Biparietal Diameter (BPD), and Cephalic Circumference (CC). They found a statistically significant linear correlation between diameters and gestational age: Cerebellum Diameter ($R2=$ 0.948; $P=$ 0.0001), Biparietal Diameter ($R2=$ 0.956; $P=0.0001$) and Cephalic Circumference ($R2=0.960$; $P=0.0001$) (Goldstein et al., 1987).

Co et al. (1991) measured 80 healthy newborns to describe the normal dimensions of the cerebellum based on their gestational age. They measured: the area, circumference, and vertical length of the vermis as well as the area, transverse length, and circumference of the main part of the cerebellum. They found a strong linear correlation between transverse dimensions and the measure lengths

of the cerebellum and gestational age ($R=0.88$; $P < 0.0001$).

Chong et al., (1997) did the first evaluation of fetal cerebellum by magnetic resonance image (MRI). They studied 26 human specimens in the fetal period between 9 to 24 weeks of gestation. They reported the morphological development of the cerebellum structures depending on gestational age. They also suggested the use of MRI to reduce the delay on cerebellum malformation diagnosis and the usage of a nomogram to avoid confusion on the cerebellum size.

Cerebellum vermis has been less studied than other posterior fossa structures. However, important findings related to this structure have been found.

Using morphological characteristics and predetermined measures of the posterior fossa, Paladini and Volpe (2006) evaluated 51 normal fetuses and 20 fetuses with Dandy Walker´s malformation to identify in an early period malformation on the cerebellum vermis development. They used 3D ultrasound and MRI to measure cerebellum vermis and to evaluate abnormal characteristics such as a cephalic rotation of the vermis and a delay in the development of the vermis. They compared their ultrasound observations with those of the MRI, showing a very small variation.

One of the main findings of the studies that have measured the cerebellum vermis is that, unlike other cerebellar structures, the cerebellum vermis has a linear growth pattern that is highly related to gestational age. Dudek et al. (2018) described a mathematical analysis with measures obtained directly from cerebellum specimens from 101 human fetuses from 15 to 28 weeks of gestational age. They evaluated the normal development of the cerebellum measuring the transverse and ventrodorsal diameters of the cerebellum vermis in the transverse axis and rostrocaudal dimensions from the cerebellum vermis and cerebellum hemispheres on the frontal axis. The analysis showed a linear growth following the gestational week.

It has been described that, in neonates, vermis height is a sensitive marker to evaluate a normal

cerebellar development. Moreover, during the prenatal stage, the evaluation of the transversal diameter of the vermis is more precise to evaluate normal development (Pogliani, 2008). Scott et al. (2012) did 3D reconstructions based on MRI to evaluate cerebellar development and described that cerebellum volume increases its size 7-fold between 20 to 31 weeks of gestation. They measured trans-cerebellar diameter, vermis height, and anteroposterior diameter of the vermis, and, from their results, they calculated linear, quadratic, and exponential estimations of the growth of the cerebellar hemispheres. Unlike the cerebellar area, which is better predicted with a quadratic model, vermis dimensions showed a linear growth pattern, which increased in the same period at about 3.5-fold (Scott et al., 2012).

These findings represent a highly relevant finding for this research, since the study of the cerebellum vermis through ultrasound, the most available image study, should not be done before the 18th week. However, since many authors agree that the vermis has a linear growth pattern, measures before the 18th week could be very useful to predict either retrospectively or prospectively the normal size of the vermis. This could be particularly helpful when vermis hypoplasia in a neonate or infant patient is suspected and a previous measure of his cerebellum vermis was taken. Moreover, as many authors have described, vermis dimensions are a sensitive predictor of cerebellar development, so its measure at the second trimester could predict which should be the normal dimensions of that patient's cerebellar structures in later stages of development.

MATERIALS AND METHODS

This research followed the directions of the Helsinki declaration and was approved by our institutional ethics committee with approbation number PI20-00128. 33 human fetuses, which were product of abortions from ages of 14 to 21 weeks of gestation, were dissected (17 female and 16 male). The sample size was taken under our laboratory availability of human fetuses. Although an increased number of patients would have been ideal, availability of human fetuses, embryos and cadavers for research is scarce

at our institution, and most representative and morphologically normal fetuses for gestational week were intended to be included. An encephalic dissection was made, dissecting by planes first the skull, then the encephalon, and then the encephalic trunk. Once isolated, the encephalic trunk was impregnated with mangold solution for 24 hours to harden encephalic tissue. Cerebellum was dissected with a cut in the median sagittal plane, using the medium dorsal groove, dividing it into right and left hemispheres. For the cerebellum vermis measure three axes were used: The anteroposterior axis (APA) which goes from cerebellum fastigium to the posterior region of the middle line; the obliquus axis (OA), from the anterior region of the central lobule to the posterior region of the cerebellar folia; and finally the cranio-caudal axis (CCA), from the cranial region of the culmen to the caudal region of the uvulae. Measures were taken using a digital stereomicroscope (ZEISS Stemi 2000-C, ZEISS AxioCam ICc 1) using a 0.65 scale. The taken measures are showed in fig. 1. A database with the results was made using Microsoft Excel 365 and was analyzed using the IBM SPSS 24 Software. A Kolmorov Smirnoff test was made to certify the normal distribution of data in terms of mean (standard deviation). A Pearson correlation test was made to determine if a linear relationship between the measures taken and the gestational age exists.

RESULTS

Results from the measured axes are summarized in Table 1. Each measure is described as the mean (standard deviation) of each week from 14 to 21 weeks of gestation. All the axes showed an ascendant pattern related to gestational age.

Although each of the axes measured followed an increasing pattern that correlates with gestational age, they did it at different rates. The cranio-caudal axis was the structure with the most constant growing rate. This was the case, however, by a minimum difference with the other axes.

All of the measured structures increased in an equivalent rate since they doubled the mean length at the 14th week of development: the first
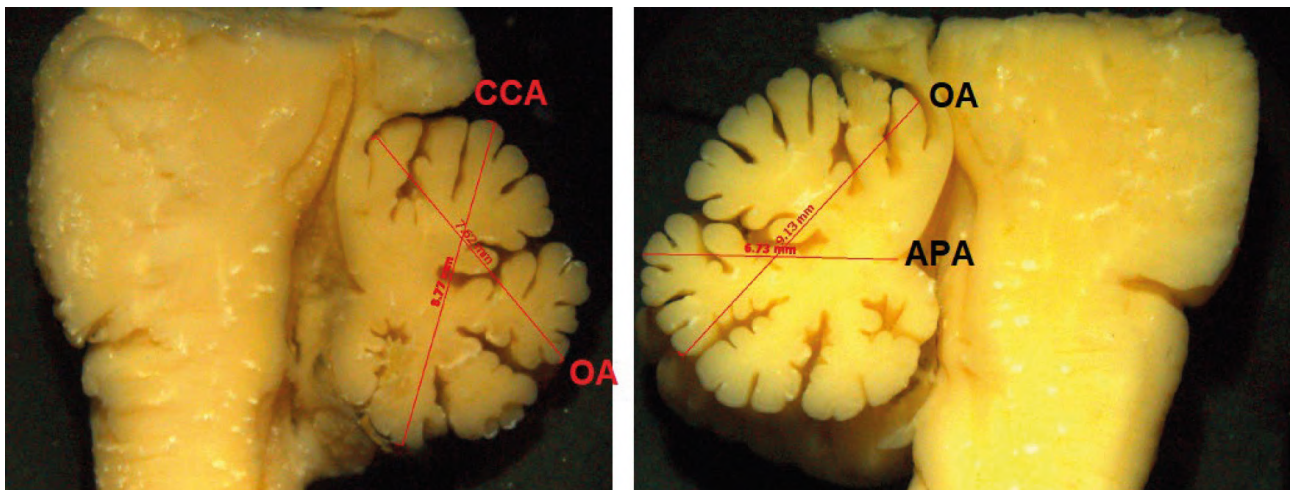
Fig. 1.- Measures of the cerebellum vermis. CCA: cranio-caudal axis. APA: anteroposterior axis. OA: obliquus axis.

one studied, at the 17th week of development and triplicated at the 21st week of development, the last one measured. These results support the knowledge that the cerebellum vermis has a linear growth pattern.

There are certain differences in the growing of the three different axes measured among the studied weeks. While cranio-caudal axis (CCA) and anteroposterior (APA) had their higher increase in length between the 14th to 15th week of development, obliquus axis had its higher increase in length between the 16th to 17th weeks of development, although, as CCA and APA, OA did show a relatively high increase between the 14th to 15th week, suggesting that this might be a period of greater growing and maturation of the vermis.

These measures help set a standard for normal dimensions of the cerebellum vermis and to distinguish an hypoplastic or hypertrophic

structure. Although it is not ideal to establish the diagnosis of an hypoplastic or aplastic vermis so early in the development (before 18 weeks), measures at these stages could help predict the normal dimensions of a certain patient´s vermis in later stages, which could be especially useful in patients with suspicion of a disease involving this structure.

As shown in Table 2, Pearson´s correlation tests were made to identify whether the cerebellum vermis has a constant growth pattern depending on gestational age. All the measured axes showed a strong correlation with gestational age, which shows that the measure of this structure could be a reliable parameter to estimate fetal age. Although the difference on the Pearson´s correlation of each axis with gestational age were minimum, the cranio-caudal axis resulted in the strongest correlation, and thus it could be a

Table 1. Average value of cranio-caudal axis (CCA), anteroposterior axis (APA) and obliquus axis (OA) of the cerebellum vermis.

Weeks of gestation	Cranio-Caudal Axis (CCA) mm Mean (SD)	Anteroposterior Axis (APA) mm Mean (SD)	Obliquus Axis (OA) mm Mean (SD)
14 (n=4)	3.65 (0.45)	2.86 (0.29)	3.73 (0.46)
15 (n=4)	4.96 (0.95)	3.64 (0.55)	4.58 (0.88)
16 (n=4)	5.16 (0.90)	3.59 (0.38)	4.69 (0.60)
17 (n=3)	6.84 (0.46)	4.29 (0.43)	6.11 (0.64)
18 (n=6)	7.46 (0.98)	5.03 (0.53)	6.57 (0.72)
19 (n=4)	8.68 (1.05)	6.12 (0.77)	8.37 (1.20)
20 (n=4)	9.27 (0.76)	6.16 (1.02)	8.88 (0.96)
21 (n=4)	10.23 (1.54)	7.06 (0.63)	9.79 (1.46)

sensitive marker of adequate vermis development in the second trimester of gestation. These strong correlations also support the knowledge about the linear growing pattern of the vermis.

DISCUSSION

The human cerebellum has a complex development mechanism. Thus, it is highly susceptible to congenital malformations. The cerebellum vermis, the dividing structure of the cerebellum, has a constant growth during prenatal development.

As described by Dudek et al. (2018) and Scott et al. (2012), the vermis has a linear growth pattern, unlike other cerebellar structures that show exponential growth and thus the prediction of their normal dimensions could be less precise.

As we report, the three axes that were measured (cranio-caudal axis, anteroposterior axis, and obliquus axis) represent appropriate measures to evaluate the normal growth and development of the cerebellum. Each of them showed to have an increased size with a strong correlation to gestational age. Although the diagnosis of hypoplasia or aplasia of the vermis should not be established before the 18th week of development, its normal dimensions could be predicted with models like the proposed by Scott et al. (2012) using the measures that we report. Moreover, we support that this linear pattern that previous authors report at the third trimester of pregnancy is present also during the second trimester.

These results support the knowledge that the vermis is the structure with the most constant growth rate in the cerebellum, and their dimensions are a representative marker of normal cerebellar development. As Paladini and Volpe (2006) suggested, the variation in the measurements of cerebellar structures with ultrasound compared with MRI is minimum,

we suggest that the evaluation of vermis and other cerebellar structures could be evaluated correctly using ultrasound techniques. Moreover, as more specific types of ultrasonography such as neurosonography become available, the evaluation of the cerebellum should be more precise. This is one of the main reasons to increase morphometrical studies of the cerebellum and other neurological structures, since the descriptions of normal dimensions of many structures are scarce, and the early identification of a malformed structure could improve patient care by the early referral to a specialist.

Our results could be used to set a nomogram for the study of normal dimensions of the cerebellum vermis, and results could be used and compared with measures taken using image techniques such as ultrasound or magnetic resonance image (MRI). Since most of the pathologies that affect the vermis also affect other structures, an intentional search for these should be done in patients with hypoplastic or aplastic vermis.

Our research has certain limitations, as our population is limited in size and further studies should be made to increase the validity of the results. Nevertheless, they bring an important orientation in evaluating if a cerebellum vermis has normal dimensions and could be used with previously established models to predict the future size of the vermis in normal conditions and compare them with the patient´s vermis dimensions in which cerebellar malformations are suspected.

Table 2. Pearson´s correlation test of the measures taken with gestational age.

Parameter	Gestational Age (Pearson´s correlation test) (r)	p value
Cranio-Caudal Axis (CCA)	0.925	0.000
Anteroposterior Axis (APA)	0.916	0.000
Obliquus Axis (OA)	0.918	0.000

then improve patient care. Therefore, these donors and their families deserve our highest gratitude.

REFERENCES

ALDINGER KA, KOGAN J, KIMONIS V, FERNANDEZ B, HORN D, KLOPOCKI E, CHUNG B, TOUTAIN A, WEKSBERG R, MILLEN KJ, BARKOVICH AJ, DOBYNS WB (2013) Cerebellar and posterior fossa malformations in patients with autism-associated chromosome 22q13 terminal deletion. *Am J Med Genet A*, 161A(1):131-136.

ALDINGER KA, TIMMS AE, THOMSON Z, MIRZAA GM, BENNETT JT, ROSENBERG AB, ROCO CM, HIRANO M, ABIDI F, HALDIPUR P, CHENG CV, COLLINS S, PARK K, ZEIGER J, OVERMANN LM, ALKURAYA FS, BIESECKER LG, BRADDOCK SR, CATHEY S, CHO MT, CHUNG BHY, EVERMAN DB, ZARATE YA, JONES JR, SCHWARTZ CE, GOLDSTEIN A, HOPKIN RJ, KRANTZ ID, LADDA RL, LEPPIG KA, MCGILLIVRAY BC, SELL S, WUSIK K, GLEESON JG, NICKERSON DA, BAMSHAD MJ, GERRELLI D, LISGO SN, SEELIG J, ISHAK GE, BARKOVICH AJ, CURRY CJ, GLASS IA, MILLEN KJ, DOHERTY D, DOBYNS WB (2019) Redefining the etiologic landscape of cerebellar malformations. *Am J Hum Genet*, 105(3): 606-615.

BARKOVICH AJ, WIPPOLD FJ, SHERMAN JL, CITRIN CM (1986) Significance of cerebellar tonsillar position on MR. *Am J Neuroradiol*, 7(5): 795-799.

BEAUDIN AE, STOVER PJ (2009) Insights into metabolic mechanisms underlying folate-responsive neural tube defects: a minireview. *Birth Defects Res A Clin Mol Teratol*, 85(4): 274-284.

CHAPMAN T, MAHALINGAM S, ISHAK GE, NIXON JN, SIEBERT J, DIGHE MK (2015) Diagnostic imaging of posterior fossa anomalies in the fetus and neonate: part 1, normal anatomy and classification of anomalies. *Clin Imaging*, 39(1): 1-8.

CHONG BW, BABCOOK CJ, PANG D, ELLIS WG (1997) A magnetic resonance template for normal cerebellar development in the human fetus. *Neurosurgery*, 41(4): 924-928; discussion 928-929.

CIGNINI P, GIORLANDINO M, BRUTTI P, MANGIAFICO L, ALOISI A, GIORLANDINO C (2016) Reference charts for fetal cerebellar vermis height: A prospective cross-sectional study of 10605 fetuses. *PLoS One*, 11(1): e0147528.

CO E, RAJU TN, ALDANA O (1991) Cerebellar dimensions in assessment of gestational age in neonates. *Radiology*, 181(2): 581-585.

DUDEK K, NOWAKOWSKA-KOTAS M, KĘDZIA A (2018) Mathematical models of human cerebellar development in the fetal period. *J Anat*, 232(4): 596-603.

FRIEDE RL (1973) Dating the development of human cerebellum. *Acta Neuropathol*, 23(1): 48-58.

GANO D, BARKOVICH AJ (2019) Cerebellar hypoplasia of prematurity: Causes and consequences. *Handb Clin Neurol*, 162: 201-216.

GLENN OA, BIANCO K, BARKOVICH AJ, CALLEN PW, PARER JT (2007) Fetal cerebellar hemorrhage in parvovirus-associated non-immune hydrops fetalis. *J Matern neonatal Med*, 20(10): 769-772.

GOLDSTEIN I, REECE EA, PILU G, BOVICELLI L, HOBBINS JC (1987) Cerebellar measurements with ultrasonography in the evaluation of fetal growth and development. *Am J Obstet Gynecol*, 156(5): 1065-1069.

JURCĂ MC, KOZMA K, PETCHEȘI CD, BEMBEA M, POP OL, MUȚIU G, COROI MC, JURCĂ AD, DOBJANSCHI L (2017) Anatomic variants in Dandy-Walker complex. *Rom J Morphol Embryol*, 58(3): 1051-1055.

PALADINI D, VOLPE P (2006) Posterior fossa and vermian morphometry in the characterization of fetal cerebellar abnormalities: a prospective three-dimensional ultrasound study. *Ultrasound Obstet Gynecol*, 27(5): 482-489.

POGLIANI L, RADAELLI G, MANFREDINI V, LISTA G, ZUCCOTTI GV (2008) Height of the cerebellar vermis and gestational age at birth. *Ultrasound Obstet Gynecol*, 31(4): 401-405.

SARNAT HB, ALCALÁ H (1980) Human cerebellar hypoplasia: a syndrome of diverse causes. *Arch Neurol*, 37(5): 300-305.

SCOTT JA, HAMZELOU KS, RAJAGOPALAN V, HABAS PA, KIM K, BARKOVICH AJ, GLENN OA, STUDHOLME C (2012) 3D morphometric analysis of human fetal cerebellar development. *Cerebellum*, 11(3): 761-770.

TAKANASHI J, MIYAMOTO T, ANDO N, KUBOTA T, OKA M, KATO Z, HAMANO S, HIRABAYASHI S, KIKUCHI M, BARKOVICH AJ (2010) Clinical and radiological features of rotavirus cerebellitis. *AJNR Am J Neuroradiol*, 31(9): 1591-1595.

TAKANASHI J, SUGITA K, BARKOVICH AJ, TAKANO H, KOHNO Y (1999) Partial midline fusion of the cerebellar hemispheres with vertical folia: a new cerebellar malformation? *AJNR Am J Neuroradiol*, 20(6): 1151-1153.

TAM EWY, CHAU V, FERRIERO DM, BARKOVICH AJ, POSKITT KJ, STUDHOLME C, FOK ED-Y, GRUNAU RE, GLIDDEN DV, MILLER SP (2011) Preterm cerebellar growth impairment after postnatal exposure to glucocorticoids. *Sci Transl Med*, 3(105): 105ra105.

WASSMER E, DAVIES P, WHITEHOUSE WP, GREEN SH (2003) Clinical spectrum associated with cerebellar hypoplasia. *Pediatr Neurol*, 28(5): 347-351.

ZAKI MS, ABDEL-ALEEM A, ABDEL-SALAM G, MARSH SE, SILHAVY JL, BARKOVICH AJ, ROSS ME, SALEEM SN, DOBYNS WB, GLEESON JG (2008) The molar tooth sign: a new Joubert syndrome and related cerebellar disorders classification system tested in Egyptian families. *Neurology*, 70(7): 556-565.

Topographic arrangement of flexor digitorum superficialis tendons in the carpal tunnel and their relationship to the median nerve with regards to its neuropathy

Godwin O. Mbaka

Department of Anatomy, Lagos State University College of Medicine, Ikeja, Lagos State, Nigeria

SUMMARY

Anatomical variations of the flexor digitorum superficialis (FDS) tendon around the carpal tunnel are not too infrequent. Therefore, the awareness of these variations is important during a surgical procedure for carpal tunnel release. The study was carried out with a total of 84 embalmed upper limbs cadavers, 48 males and 36 females, dissected to show different arrangements of FDS tendons. According to the findings, there were four variations in the arrangement pattern of FDS tendons from the dissected upper limb cadavers categorized into three different types with one subtype. These include two-row tendons, three-row tendons, four-row tendons, and a subtype of two rows, one tendon, and fleshy fibres. The two-row of paired FDS tendons, considered the typical arrangement (Fig. 1), exhibited the highest frequency, observed in 41 limbs. It shows a 48.8% prevalence of FDS tendons arrangement in both sexes. In males, the incidence was 28.6% (24), while in females it was 20% (17). The subtype of two rows comprising fleshy and tendinous fibres (fig.2) shows an incidence of 8.3% (7) in both sexes; in males, it constituted 4.8%, and in females,

3.6%. Three tendons in a row type (Fig. 3) show a prevalence of 34.5% (26) in both sexes, 17.9% (15) in males, and 16.7% (14) in females. Four tendons in a row type (fig. 4), which had the least frequency, show an occurrence of 8.3% (7) in both sexes, in males, 6.0% (5), while in females it was 2.4% (2). Therefore it has been made imperative to be familiar with the local anatomy of the wrist region to be able to recognize possible anatomical variations to take due diligence during surgical procedures. By this, complications often encountered during carpal tunnel release can be minimized.

INTRODUCTION

Flexor digitorum superficialis (FDS) is a large extrinsic muscle of the forearm (Garg, 2012). It becomes tendinous distally, splitting into four slips before entering the carpal tunnel (CT), which is also traversed by 4 tendons of flexor digitorum profundus (FDP), the tendon of flexor pollicis longus (FPL), and the median nerve *(*Standring, 2016; Brooks et al., 2019). The arrangement of FDS

Corresponding author:
Godwin O. Mbaka. Department of Anatomy, Lagos State University College of Medicine, PMB, 21266, 1-5 Oba Akinjobi Street, Ikeja, Nigeria.
E-mail: mbaaka2gm@gmail.com

tendons is of interest because of its close contact with the median nerve, the most sensitive structure in the tunnel. According to anatomical texts (Rosse and Gaddum-Rosse, 1985; Sinnatamby, 2011; Standring, 2016), the four tendons are arranged in two pairs in the tunnel: the superficial and the deep pairs. The superficial pair of the tendons go to the middle and ring fingers, while the deep pair goes to the index and little fingers (Caetano et al., 2017). The configurative arrangement of the tendons makes for the convenient passage of the median nerve in the CT.

The carpal tunnel is an area of interest to surgeons due to the clinical event associated with median nerve compression in the tunnel (Adams et al., 1994). It is a site where multiple anatomical variations can occur involving neural, vascular, muscular, and tendinous structures (Mitchell et
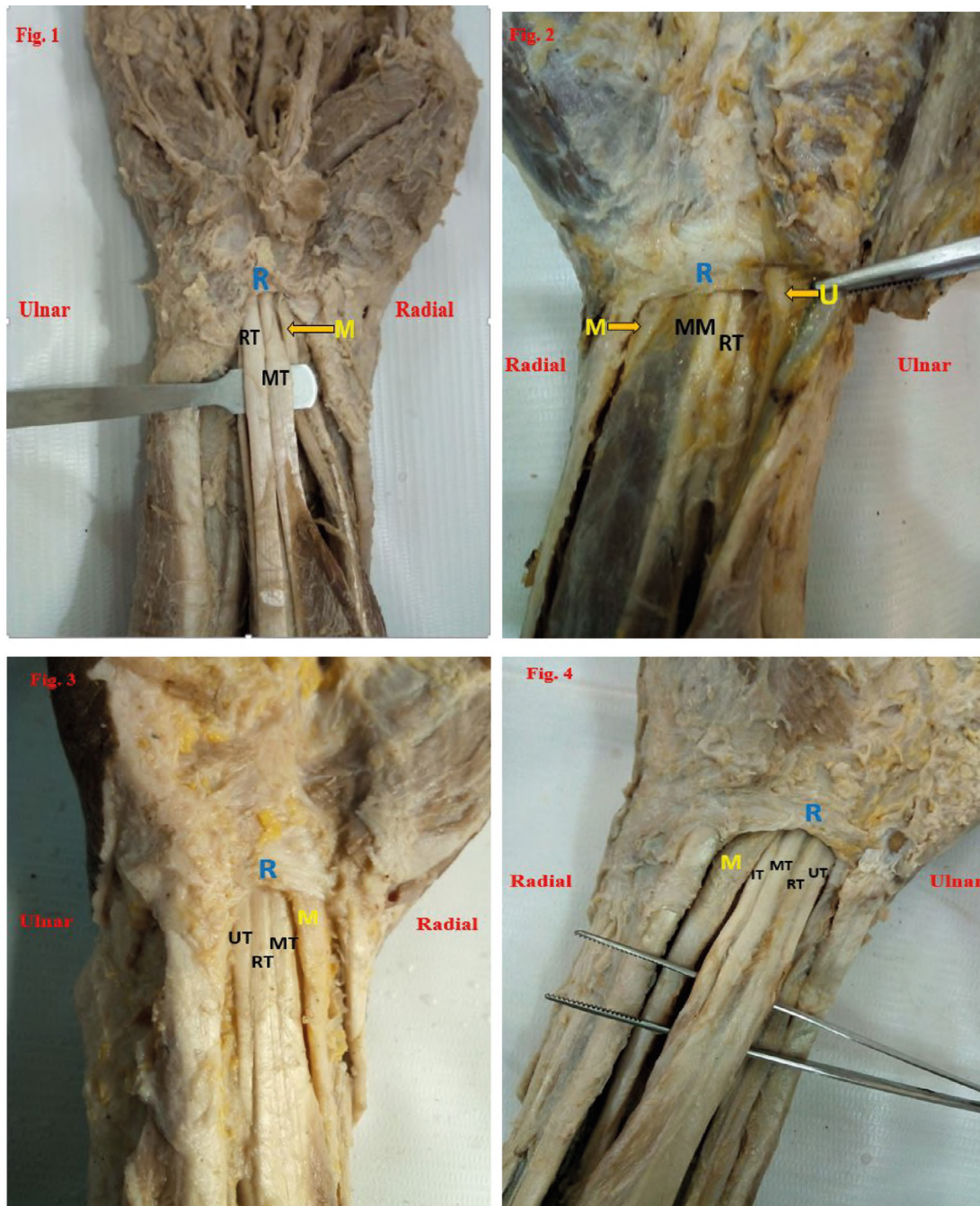
Fig. 1.- Two-row arrangements of flexor digitorum superficialis tendons: RT, ring finger tendon; MT, middle finger tendon; M, median nerve; R, flexor retinaculum. **Fig. 2.-** Two-row arrangement of flexor digitorum superficialis tendon and muscle: MM, middle finger muscle; RT, ring finger tendon; Median nerve; U, ulnar nerve; R, flexor retinaculum. **Fig. 3.-** Three-row arrangement of flexor digitorum superficialis tendons: UT, little finger tendon; RT, ring finger tendon; MT, middle finger tendon; M, median nerve; R, flexor retinacula. **Fig. 4.-** Four-row arrangement of flexor digitorum superficialis tendons: UT, little finger tendon; RT, ring finger tendon; MT, middle finger tendon; index finger tendon, M, median nerve; R, flexor retinaculum.

al., 2009). As regards FDS muscle and its tendons, except for the observed cases of accessory muscle slips (Neumeister et al., 2005; Kerasnoudis, 2012; Okafor and Varacallo, 2019), accessory and duplicate tendons (Yesilada et al., 2013; Caetano et al., 2017), the diverse arrangement of FDS tendons in the CT are largely unknown. Hence, the limited knowledge on how these anomalies can affect the median nerve in the tunnel.

Given the high incidence of median nerve compression in the CT, it was conceivable to investigate the variable topographic arrangement of FDS tendons and their relationship to the median nerve in the CT. The awareness would be of value to clinicians involved in hand surgery for due diligence to minimise the incidence of iatrogenic injury during the carpal tunnel release.

MATERIALS AND METHODS

A longitudinal study was conducted to show the profile and mode of arrangement of FDS tendons in the lower forearm and the CT. Eighty-four upper limb cadavers from our storage system, forty-eight males, and thirty-six females Nigerian cadavers, aged 28-76 years, devoid of any gross pathology, were used for the study. The cadavers used were formalin-fixed in our department with the hands placed in anatomical position (supinated) before fixation. A transverse incision was made 2cm above the anterior aspect of the elbow joint through the thickness of the skin. An incision was made midway the transverse incision extending longitudinally down passing through the midline to the wrist. Another transverse incision was made at the wrist to enable for reflection of skin and fascia to each side, thus exposing the superficial muscle group of the forearm; pronator teres, flexor carpi radialis, palmaris longus, and flexor carpi ulnaris. The first three muscles were cut and retracted, while the last muscle was displaced medially to expose FDS. An incision from the wrist was extended vertically to the middle finger. The skin on the wrist and palm were reflected on either side and later detached exposing the flexor retinaculum, as well as structures in the palm. FDS tendons in synovial sheath enclosures were exposed as far as to the margins of the carpal tunnel. A slit was made longitudinally on the synovial sheath to expose the tendons *in situ* to show their arrangement pattern as they enter the carpal tunnel. The median nerve was also exposed to show its varied course in each type towards the tunnel. The flexor retinaculum was later cut and detached to expose the tendons in the tunnel and their varied relationships with the median nerve. The images of the different anatomical arrangements of FDS tendons and their relationship with the median nerve in the CT were captured with a digital camera. The different anatomical arrangements of FDS tendons and their relationship with the median nerve were also illustrated.
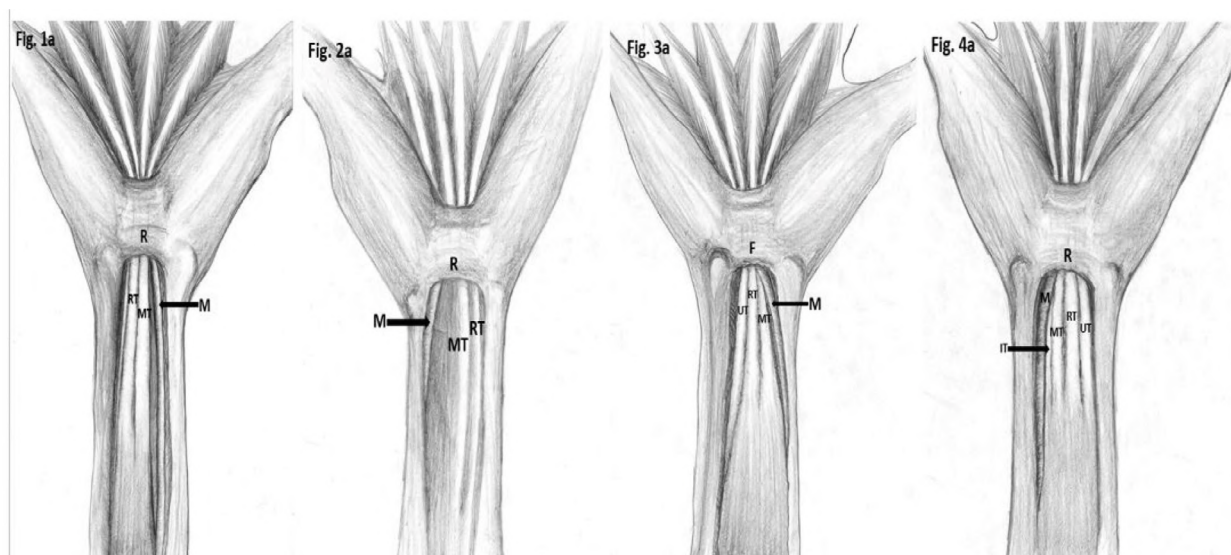
Figs. 1a-4a.- Illustrations of different arrangements of Flexor digitorum superficialis tendons.

STATA software version, 14.0 statistical package, was used to carry out a Fisher's exact test on the small sample size (N =84), and also because there was an expected sample size of 5 or less, as it were in some of the cases. The analysis was to test if the two variables (gender and flexor digitorum superficialis tendons) were associated with each other,

RESULTS

There were four variations in the arrangement pattern of FDS tendons from the dissected upper limb cadavers categorized into three types with one subtype, which include: two-row tendons, three-row tendons, four-row tendons, and a subtype of two rows of one tendon and fleshy fibres. Figs. 1 and 1c depict the two rows of paired FDS tendons entering the carpal tunnel with the
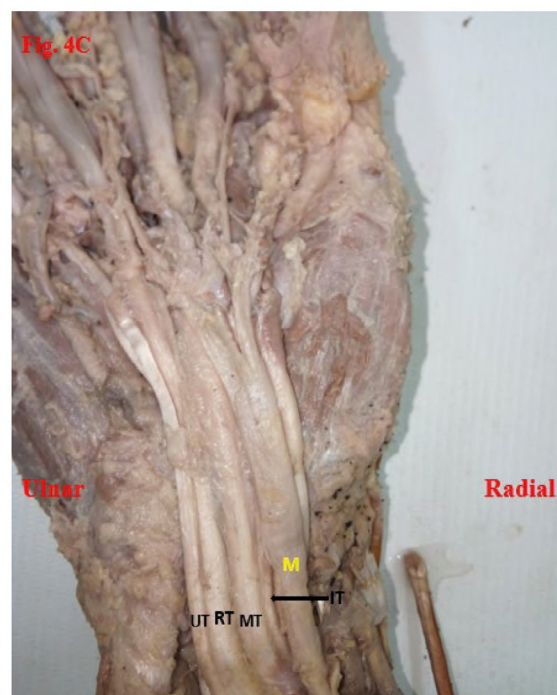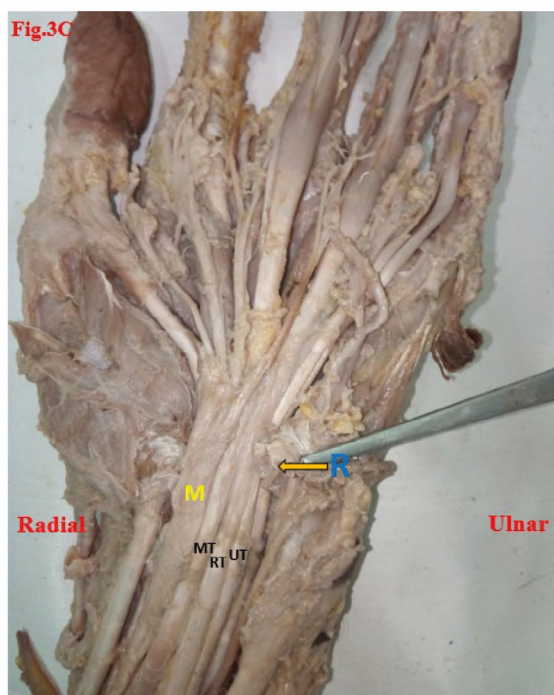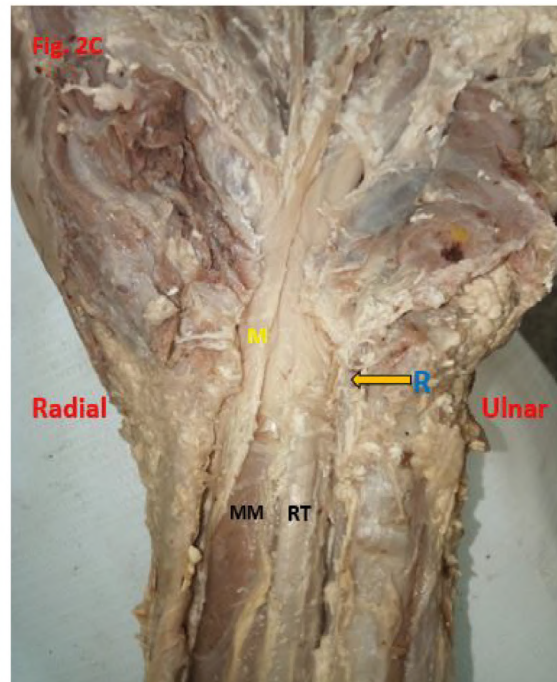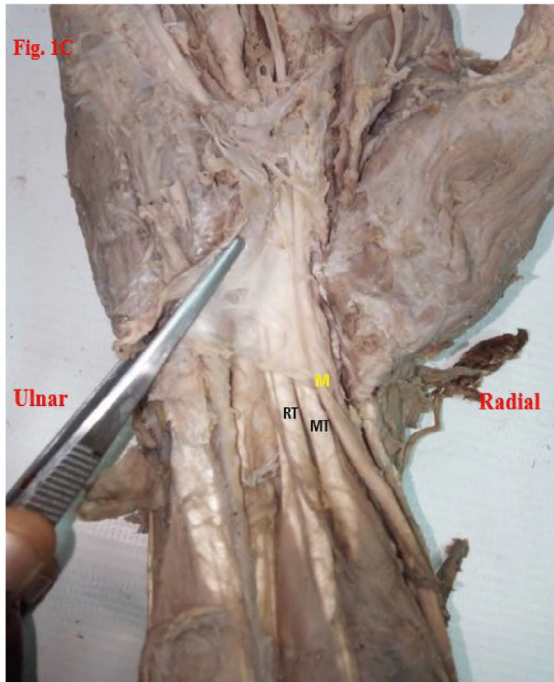
Figs. 1c-4c.- The positions of the median nerve in the carpal tunnel of the four varied tendon arrangement.

median nerve traveling from the lower forearm, inclining more superficially as it enters the CT to lie in a compartment between the tendon of FPL to the lateral and FDS tendons to the index and middle finger to the medial. The two rows of paired FDS tendons, considered the typical arrangement, exhibited the highest frequency, observed in 41 limbs. It shows a 48.8% prevalence of FDS tendons arrangement in both sexes. In males, it exhibits an incidence of 28.6% (24), while in females it is of 20% (17). Figs. 2 and 2c depict an anomalous muscular intrusion into the tunnel. In this case, the median nerve, on reaching the CT, passes above the fleshy fibres of FDS, lying just below the flexor retinaculum inside the tunnel. It continued in front of the tendons to the index and middle finger at the distal third of the tunnel. The subtype of two-row comprising fleshy and tendinous fibres shows an incidence of 8.3% (7) in both sexes; in males, it constituted 4.8%, and in females it was of 3.6%. Figs. 3 and 3c depict three FDS tendons entering the carpal tunnel at the same plane where the tendon to the little finger makes an inclusion in the plane having diverged close to its fleshy origin in the forearm to maintain medial relation with its ring finger counterpart as they traversed the tunnel. In this pattern, the median nerve traveling from the lower forearm gained more superficial positioning and, on reaching the tunnel, it lies in front of the FDS tendon to the middle finger. The three tendons in a row type show a prevalence of 34.5% (26) in both sexes: 17.9% (15) in males and 16.7% (14) in females. Figs. 4 and 4c depict the four FDS tendons entering the carpal tunnel at the same plane where the median nerve completely overlies the FDS tendon to the index finger, just as it emerges from the deep plane of its fleshy fibres at the middle third of the forearm. The relationship of the FDS tendons to the median nerve in the CT was similar to the case of three-row tendons. Four tendons in a row type, which had the least frequency, showed an incidence of 8.3% (7) in both sexes: in males, 6.0% (5) while in females, 2.4% (2). In the general population, the expected range of two-paired tendons in males and females is 58.3% and 55.6% respectively. In the three-row tendons, the range of expectation in males is 31.2%, while in females it is 38.9%. In the

four-row tendons, the range for males is 10.4%, while in females it is 5.6%. Cumulatively, the range of expectation of the variant arrangement is higher in females (43.8%) than in males (41.6%).

Fig. 5 shows the summary of different arrangements of FDS tendons. Fig. 6 indicates the three variant arrangements with the three-row tendon type showing the highest frequency. Table 1 indicates the percentage frequency of different arrangements of FDS tendons. A chi-square test of association was conducted between the different flexor digitorium superficialis tendons across the gender group. The result of the association test revealed that there was no statistically significant difference (p = 0.640) between the flexor digitorium superficialis tendons arrangement in the two genders.

DISCUSSION

It has been established that FDS tendons show the alignment of two rows (Rosse and Gaddum-Rosse, 1985; Sinnatamby, 2011; Standring, 2016). But in this study, a considerable number of the specimens examined exhibited varied orientation of FDS tendons from the seemingly expected topography in the lower forearm and the CT. These were classified based on their mode of arrangement as three-row tendons, four-row tendons, and a subtype of two rows of one tendon and fleshy fibres. The knowledge of this anatomical variant topography of arrangement is of obvious importance to the clinicians, because it might indicate encroachment into the environment of the median nerve leading to its compression. It might also be obvious that many of the complications encountered during surgery at the wrist region could be a consequence of these anatomical variations, considering that in this study their frequency was observed to be statistically significant.

In this study, the two rows of paired FDS tendons entering the carpal tunnel showed the highest frequency. This type represents what is depicted in most anatomical texts, which can be classified as the typical arrangement. In this mode of tendon arrangement (Fig. 1c), the median nerve traveling from the lower forearm inclined

more superficially as it enters the CT to lie in a compartment between the tendon of the flexor pollicis longus to the lateral and FDS tendons to the index and middle finger to the medial. The nerve continued in that conformity into the palm. At the mid-palm, it lies in front of the FDS tendon to the middle finger. It has been made apparent that this arrangement pattern creates a better environment for the median nerve to manoeuvre unfettered in the tunnel during flexion and extension of

Different arrangements of flexor digitorum superficialis tendons
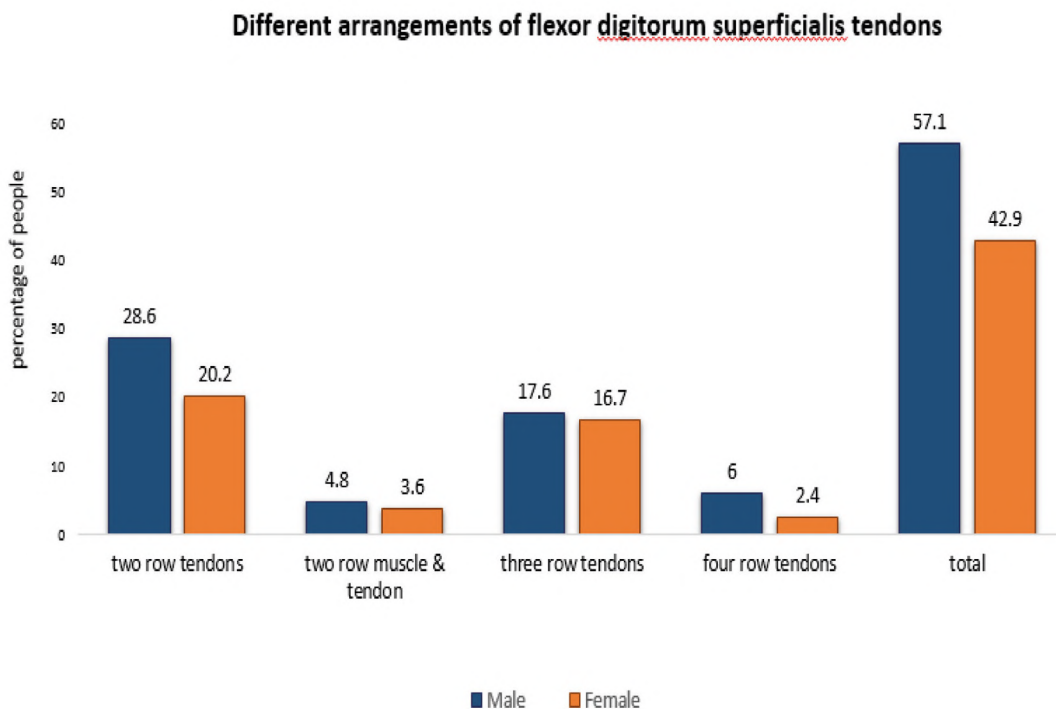
Fig. 5.- Comparative result of different arrangements of flexor digitorum superficialis tendons of both males and females.
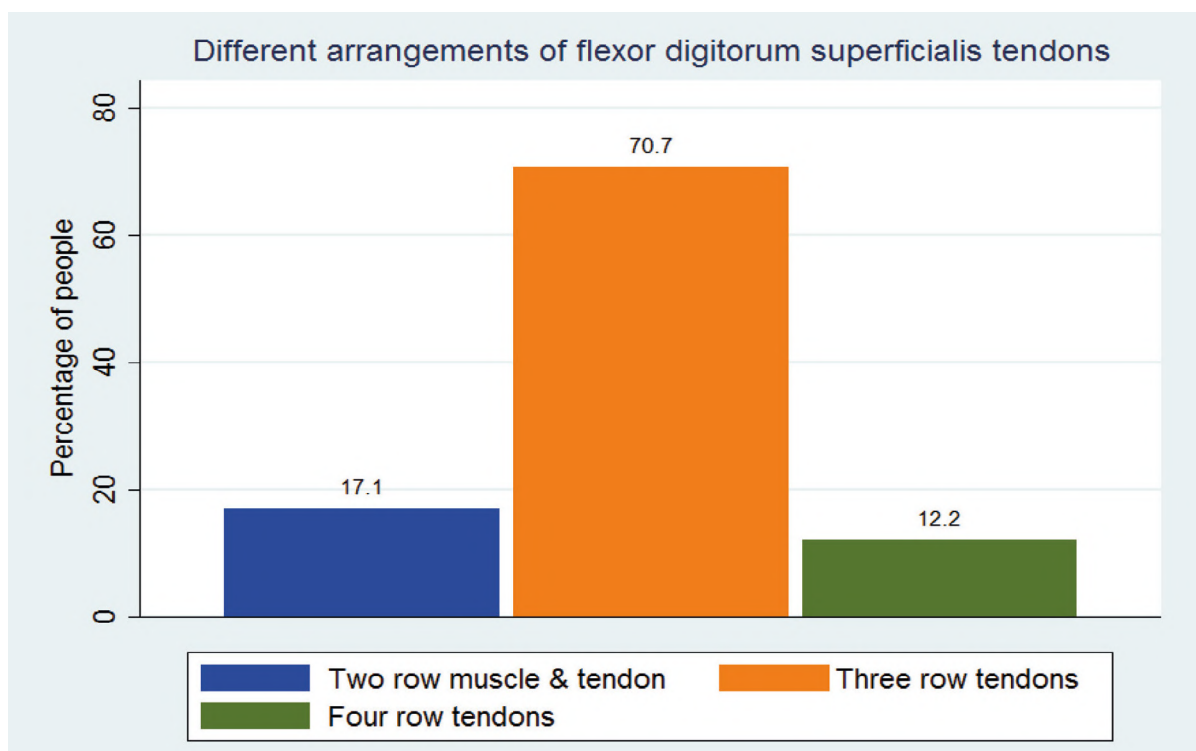
Fig. 6.- Comparative result of the three variable arrangements of flexor digitorum superficialis tendons.

the wrist without mechanical stress, as well as minimising the tendency of its entrapment by the surrounding structures (Dang and Rodner, 2009). Carpal tunnel syndrome (CTS) is the most common compressive syndrome (Chammas et al., 2014) because of the tendency for the median nerve to be compressed at the wrist region. But in this configurative positioning of the adjacent FDS tendons, there is less intricacy for a probable iatrogenic injury to the nerve during a surgical procedure for carpal tunnel release. However, in the subtype of this pattern that appeared not too infrequent in this study, the fleshy fibres of FDS that correspond to the index finger enter the CT. In this anomalous muscular intrusion into the tunnel, the median nerve on reaching the CT passes above the fleshy fibres of FDS, lying just below the flexor retinaculum inside the tunnel. It continued in front of the tendons to the index and middle finger at the distal third of the tunnel (Fig. 2c). This incursion of muscle fibres into the tunnel exposes the median nerve to compression. Those with this anomalous pattern more often exhibit intermittent symptoms with repetitive motion consistent with carpal tunnel syndrome (Caetano et al., 2017).

This study shows two anatomical variations of the FDS tendon arrangement in the CT that have not been previously highlighted. In one of the variant arrangements, three FDS tendons enter the carpal tunnel at the same plane where the tendon going to the little finger makes an inclusion in the plane having diverged close to its fleshy origin in the forearm to maintain medial relation with its ring finger counterpart as they traversed the tunnel. This positioning alteration of FDS tendons equally altered the course of the median nerve in the tunnel (Fig. 3c). The median nerve traveling from the lower

forearm gained more superficial positioning and, on reaching the tunnel, it lies in front of the FDS tendon to the middle finger. It continued in front of the tendon as it traverses the tunnel with flexor retinaculum superficial to it. The danger in this varied positioning is the likelihood of mistaken identity of the nerve for the FDS tendon during surgical procedures. Therefore, identifying the nerve requires dynamic maneuvring of the wrist to first identify the FDS tendons (Presazzi et al., 2011). This variant arrangement also makes the median nerve highly susceptible to entrapment in the tunnel.

In another variation, the four FDS tendons enter the carpal tunnel at the same plane where the median nerve completely overlies the FDS tendon to the index finger just as it emerges from the deep plane of its fleshy fibres at the middle third of the forearm (Fig. 4c). The median nerve relationship with the FDS tendons in the CT was similar, as in the case of three-row tendons. The traversing of the four FDS tendons at the same plain in the tunnel should most likely play a significant role in the positional increase in carpal tunnel pressure, making the median nerve to be more vulnerable to compression. This variant type requires curious assessment because of the likely clinical implications, particularly in situations of tenosynovitis, which is the most common cause of rising canal pressure (Feske et al., 2007). It is certain that at the occurrence of tenosynovitis the pressure impingement on the median nerve would be more severe, which might otherwise come with serious debilitating pain leading to its neuropathy.

In the three variable types, the route of the median nerve in the tunnel was essentially similar but varied markedly from the typical

Table 1. Arrangement variations of flexor digitorum superficialis tendons.

Gender	Flexor digitorum superficialis tendons					P-value
	Two-row tendons Freq (%)	Two-row muscle & tendon Freq (%)	Three-row tendons Freq (%)	Four-row tendons Freq (%)	Total Freq (%)	
Male	24 (58.54)	4 (57.14)	15 (51.72)	5(71.43)	48(57.14)	0.640
Female	17 (41.46)	3 (42.86)	14 (48.28)	2(28.57)	36(42.86)	

Significant at p <0.05

tendons arrangement. The positional change of FDS tendons in these types amount to pressure increase in the CT. Therefore, median nerve compression is a more likely occurrence in a situation of hypertrophy of synovial tissue around the FDS tendons. To appreciate the focal area of the nerve entrapment, two imaging modalities, ultrasound and magnetic resonance imaging (MRI), are most suitable because of their reliability in investigating entrapment syndromes (Maulik and Radswiki, 2010). In the case of CTS where there is a muscle incursion into the tunnel, MR imaging will be very useful, because it can demonstrate abnormalities such as neurogenic muscle edema with T2-weighted or STIR sequencing (Meyer et al., 2018).

Nevertheless, more crucial is the importance of dynamic factors in repetitive movements of the hand such as in extension and flexion, which has been established to have a link with carpal tunnel syndrome (Gelberman et al., 1981). Therefore, the positional change of FDS tendons in the tunnel might constitute a major factor responsible for idiopathic CTS. This change, which often precipitates the entrapment of the median nerve, usually starts with tinkling and mild pain sensations that progress to varying degrees of paresthesias, including hypo/hyperesthesia and anesthesia, allodynia, and hypoalgesia, as well as decreased motor function (Park et al., 2011; Kim and Park, 2014; Andrea et al., 2017).

Cases of CTS are unarguably more prevalent in females, because studies have shown that the incidence in females may be up to three to four times higher than in males (Violante et al., 2007; Farioli et al., 2018). However, the assessment of gender differences in the frequency of variant arrangements of FDS tendons in CT showed little disparity. Although cumulatively the females exhibited slightly higher frequency, their smaller sample size gave lesser strength of comparison with the male samples. In this context, it will be difficult to state categorically that females usually exhibit a higher frequency of variant arrangements of FDS tendons. But if indeed that is established, it can perhaps be considered a factor for the higher incidence of carpal tunnel syndrome in females.

CONCLUSION

This study establishes that flexor digitorum superficialis tendons exhibit varied arrangements in the carpal tunnel. It is therefore important to be familiar with the local anatomy of the wrist region to be able to recognize these possible anatomical variations in order to minimise the incidence of iatrogenic injury to structures during carpal tunnel release.

Study Limitation

It was difficult to obtain a large number of cadavers for the study because they were not easily assessed. Besides, amongst the available cadavers, there was a limited representation from the female specimens.

Future Research

There is the need to conduct this study on different populations using ultrasound for the possibility of having a large sample size that would be truly representative. There is also the need for a racial perspective.

REFERENCES

ADAMS ML, FRANKLIN GM, BARNHART S (1994) Outcome of carpal tunnel surgery in Washington state workers compensation. *Am J Ind Med*, 25: 527-536.

ANDREA A, GONZALES J, IWANAGA J, OSKOUIAN RJ, TUBBS RS (2017) Median nerve palsies due to injections: a review. *Cureus*, 9(5): 5-10. doi:10.7759/cureus.1287.

BROOKS R, KISTLER A, CHOWDHRY S, SWIERGOSZ A, PERLIN K, KASDAN ML, WILHELMI BJ (2019) Anatomic landmarks to locate the median nerve for safe wrist block or carpal tunnel steroid injection. *ePlasty*. 9: 139-146.

CAETANO EB, SABONGI NETO JJ, RIBAS LAA, MILANELLO EV (2017) Accessory muscle of the flexor digitorum superficialis and its clinical implications. *Rev Bras Ortop*, 52(6): 731-734.

CHAMMAS M, BORETTO J, BURMANN LM, RAMOS RM, DOS SANTOS NETO FC, SILVA JB (2014) Síndrome do túnel do carpo – Parte I (anatomia, fisiologia, etiologia e diagnóstico). *Rev Bras Ortop*, 49(5): 429-436.

DANG, AC, RODNER, CM (2009) Unusual compression neuropathies of the forearm, Part II: Median Nerve. *J Hand Surg*, 34A: 1915-1920.

FARIOLI A, CURTI S, BONFIGLIOLI R, BALDASSERONI A, SPATARI G, MATTIOLI S, VIOLANTE S (2018) Observed differences between males and females in surgically treated carpal tunnel syndrome among non-manual workers. A sensitivity analysis of findings from a large population study. *Ann Work Expo Health*, 62(4): 505-515.

FESKE SK, COCHRANE TI (2007) In: *Textbook of Clinical Neurology*, 3rd ed.

GARG K (2012) PD Chaurasia's Human Anatomy. *CBS Publishers*, 5th ed., pp 54-60.

GELBERMAN RH, HERGENROEDER PT, HARGENS AR, LUNDBORG GN, AKESON WH (1981) The carpal tunnel syndrome. A study of carpal canal pressures. *J Bone Joint Surg Am*, 63(3): 380-383.

KERASNOUDIS A (2012) Elongated muscle belly of the flexor digitorum superficial causing carpal tunnel syndrome. *Hand (NY)*, 7(3): 333-334.

KIM HJ, PARK SH (2014) Median nerve injuries caused by carpal tunnel injections. *Korean J Pain*, 27(2): 112.

MEYER P, LINTINGRE P, PESQUER L, POUSSANGE N, SILVERTRE A, DALLAUDIERE B (2018) Median nerve and the carpal tunnel ...and elsewhere. *J Belgian Soc Radiol*, 102(1): 17.

MITCHELL R, CHESNEY A, SEAL S, MCKNIGHT L, THOMA A (2009) Anatomical variations of the carpal tunnel structures. *Can J Plast Surg*, 17(3): e3-7.

NEUMEISTER MW, MOWLAVI A, RUSSELL RC, WILHELMI BJ (2005) Anomalous flexor digitorum superficialis muscle transposition for vascular coverage of the median nerve in recurrent carpal tunnel syndrome. *Can J Plast Surg*, 13(1): 27-30.

OKAFOR L, VARACALLO M (2020) Anatomy, shoulder and upper limb, hand flexor digitorum superficialis muscle. *StatPearls (Internet)*: NBK539723. [PubMed: 29234659].

PARK GY, KIM SK, PARK JH (2011) Median nerve injury after carpal tunnel injection serially followed by ultrasonographic, sonoelastographic, and electrodiagnostic studies. *Am J Phys Med Rehabil*, 90(4): 336-341.

PATEL MS, RADSWIKI (2010) Carpal tunnel syndrome. *Radiopaedia*. https:// radiopaedia.org/article/carpal tunnel-syndrome.1

PRESAZZI A, BORTOLOTTO C, ZACCHINO M, MADONA L, DRAGHI F (2011) Carpal tunnel: Normal anatomy, anatomical variants and ultrasound technique. *J Ultrasound*, 14(1): 40-46.

ROSSE C, GADDUM-ROSSE P (1985) Hollinshead's textbook of anatomy. 5th ed. *Lippincott-Raven*.

SINNATAMBY C (2011) Last's Anatomy Regional and Applied, 12th edition. *Churchill Livingstone*.

STANDRING S (2016) Gray's Anatomy, the Anatomical Basis of Clinical Practice, 41st edition. *Elsevier Limited*, ISBN: 978-0-7020-5230-9.

VIOLANTE FS, ARMSTRONG TJ, FIORENTINI C, GRAZIOSI F, RISI A, VENTURI S, CURTI S, ZANARDI F, COOKE RM, BONFIGLIOLI R, MATTIOLI S (2007) Carpal tunnel syndrome and manual work: a longitudinal study. *J Occup Environ Med*, 49: 1189-1196.

YESILADA AK, TATLIDEDE HS, ÇAKMAK E, KIYAK MV, KILINÇ L (2013) Anomalous large unique muscle belly of flexor digitorum superficialis and the absence of palmaris longus in the forearm. *J Plastic Reconstr Aesthet Surg*, 66(1): 137-139.

Effects of *mondia whitei* on the morphometry and histological structure of the testis of the albino rat

Elizabeth O. Ochieng'[1], Peter B. Gichangi[2], Andrew N. Makanya[3]

[1] *Lecturer, Department of Human Anatomy, Jomo Kenyatta University of Agriculture and Technology, Kenya*

[2] *Associate Professor, Technical University of Mombasa, Kenya*

[3] *Associate Professor, Department of Veterinary Anatomy and Physiology, University of Nairobi*

SUMMARY

The purpose of this study was to describe the effect of Mondia whitei on the histomorphometry of the albino rat testis. The objective of this study was to determine histomorphometric changes in the testicular parenchyma following oral administration of graded doses of Mondia whitei.

This was an experimental study in which 48 male rats of the species Rattus norvegicus were used. These rats were grouped into 4 cohorts. Control group, which was designated as group A, received distilled water via oral gavage daily. Group B received 300 mg/kg. Group C received 600 mg/kg. And Group D received 1200 mg/kg of Mondia whitei extracts daily for 28 days. At the end of the experimental period, body mass changes, histological changes, and volumes of the testis were obtained. Stereological techniques were used in the morphometric analysis of the volume densities and volumes of the parenchymal components of the testis. Statistical comparison of the differences between the groups was done using one way ANOVA followed by a Tukey post hoc test and a p − value of < 0.05 was considered statistically significant.

Administration of Mondia whitei led to hypocellularity of the seminiferous epithelium with loss of cells of the spermatogenic germ series and development of intercellular spaces; moreover, vacuolation of the Sertoli cells was also observed. There was a dose dependent decrease in the body mass of rats in the experimental groups (p < 0.001). This was coupled with a reduction in the volume densities of Leydig cell (LC) (p < 0.005), seminiferous epithelium (SE) (p < 0.001), seminiferous Lumen (SL) (p < 0.013) and interstitium (I) (p < 0.028). A reduction in the volumes of the SE, SL, LC, and I. Changes in the testes volumes were not statistically significant.

The observed histological changes in the seminiferous tubules and body mass draw the need for a cautious approach to the use of Mondia whitei extracts for medicinal purpose.

The hypocellularity of the seminiferous tubules may have been attributed to a reduction of the cells of the spermatogenic germ cell series with injury to the Sertoli cells, which play a pivotal role in maintaining the germ cells.

Key words: *Mondia whitei* − Albino rat testis − Volume density − Stereology − Morphometry

Corresponding author:
Dr Elizabeth Odondi Ochieng'. P.O. BOX 486-40400, MIGORI, KENYA. odondielizabeth@gmail.com

INTRODUCTION

Mondia whitei is a liana plant found in the tropics of the Sub Saharan Africa distributed along the equatorial belt from West to Eastern part of the continent (Lamidi and Bourobou, 2010). *Mondia* root is traditionally used to treat many conditions such as its use as an aphrodisiac, an appetite stimulant, treatment of indigestion, sexually transmitted diseases and as a uterine stimulant among others. The most commonly cited use is as an aphrodisiac (Lampiao et al., 2008; Oketch-Rabah, 2012; Watcho et al., 2013).

Sexual dysfunction is difficulty experienced by an individual or a couple during any stage of a normal sexual activity. This includes premature ejaculation, erectile dysfunction, reduced libido, orgasm disorders and compulsive sexual behaviour (Patel et al., 2011; Prabsattro et al., 2015). Sexual dysfunction has been estimated to affect 15 – 30 million people worldwide, and it occurs in 10-32 % of men and 25-63% of women (Abudayyak et al., 2015). In Kenya, a study done by Likata et al. (2012) concluded that the prevalence of sexual dysfunction is generally high, and male sexual dysfunction can greatly affect the quality of life. It can induce depression, anxiety and debilitating feelings of inadequacy (Baldwin, 2001). Due to the high prevalence and impact of sexual dysfunctions, great efforts have been made in search of effective interventions to improve sexual performance. This has led to the use of aphrodisiacs such as *Mondia whitei.*

An aphrodisiac is defined as a substance that arouses sexual desire (Chauhan et al., 2014). Aphrodisiacs can be classified by their modes of action into three types: those that increase libido, those that increase potency and those that increase sexual pleasure. Several types of modern medicine have been used in the management of sexual dysfunction, but due to their high costs (Yakubu et al., 2005) and some of their reported side effects (Jarrar, 2011; Jarrar and Almansour, 2015; Vidale et al., 2015), individuals now search for natural supplements from medicinal plants. Various herbs have been used in folk medicine in different cultures to treat sexual dysfunctions (Kotta et al., 2013). One such plant is *Mondia whitei* (Lampiao et al., 2008). Studies done on herbal aphrodisiacs such as *Moringa Oleifera* (Zade et al., 2013), *Nigella Sativa* (Al-Sa'aidi et al., 2009) and *Psoralea corylifolia* (Dabhadkar and Zade, 2013) have shown great potential of these herbs. They have been shown to have a potential in increasing testosterone levels, which has an effect on virility and libido (Malviya et al., 2011) and also improve sperm motility and quality. Others confer histomorphological changes on the testis (Zade et al., 2013; Prabsattro et al., 2015). *Mondia whitei* has been shown to cause an increase in the levels of testosterone (Watcho et al., 2004; Lampiao et al., 2008; Oketch-Rabah et al., 2012). There are, however, conflicting reports on its effects on the seminiferous tubules and the rest of the testis parenchyma (Watcho et al., 2001; Kuo et al., 2006).

The current study thus aims to describe possible histomorphometric changes in the seminiferous tubules, Leydig cells and body mass in the rats following use of *Mondia whitei.*

MATERIALS AND METHODS

Fourty eight male rats of the species *Rattus novergicus* of comparable weights and sizes were obtained. These were grouped into 4 cohorts with 12 rats per group.

Preparation of *Mondia whitei*

Fresh roots of *Mondia whitei* were bought from the local market in Kakamega County. Botanical identification of the herb was done at the department of Botany, the School of Biological sciences, University of Nairobi. The fresh roots were diced into small cubes measuring 1cm. These cubes were air-dried for 2 weeks to avoid infestation with fungi. The dried *Mondia whitei* roots were ground into powder form and stored in air tight containers. This was weighed and macerated in Dichloromethane (DCM)/hexane in a ratio of 1:1 for 72 hours. The macerate was filtered and the filtrate was oven dried at 55^0C, and a dark brown extract was obtained. The working solution was obtained by dissolving 100 mg of the residue in 1ml of distilled water to make a concentration of 100 mg/ml.

Determination of body mass changes

The weights of the rats were recorded at different stages of the experimental period using an electronic scale. The first set of measurements were obtained on the first day of the experimental period and this was designated as the body mass on arrival. The second set of measurements were obtained after 2 weeks of acclimatization. The third set of measurements were obtained on the last day of the experiment, and these were designated as the body mass before sacrifice.

Experimental procedure

The male rats of the species *Rattus novergicus* were used in this experiment for 28 days. A total of 48 animals following a sample size calculation were grouped into 4 cohorts: a control group and 3 experimental groups. Group A, being the control group received distilled water daily via oral gavage, group B received 300 mg/kg of *Mondia whitei* daily via oral gavage; group C received 600 mg/kg and group D received 1200 mg/kg.

Perfusion and fixation

At the end of the 28 days, the rats were put under deep anaesthesia by placing them in a lidded glass jar containing cotton wool soaked in halothane. Perfusion fixation of the rats was performed using Bouin's solution. The testicles were harvested and the volumes of the right and left testicle obtained using the Scherle method of volume displacement (Scherle, 1970). This was designated as the reference volume (V (ref)) which was the working volume when calculating the volumes of the various components of the testis thus,

V(c) = Vv (c, ref) x v (ref)

Where

V(c) = Volume of component of interest

Vv (c, ref) = Volume density of the component of interest obtained by point counting methods

The testicles were immersed in Bouin's solution in well labelled specimen bottles.

Tissue sampling and processing

From each rat, one testicle was sliced into 6 slices perpendicular to the long axis of the testicle and the slices were of approximately equal thickness. This was done by laying a transparent plastic ruler along the length of the fixed testis that was now firm, on a flat surface. Using a sharp blade, the testes was cut into 6 slices. Three slices were then sampled, using systematic random sampling with the first slice picked at random then every 2nd slice was picked. The 3 slices were picked at random and processed for paraffin embedding as shown in figure.(1). The tissues were then processed for light microscopy, using standard procedure and staining done using haematoxylin and eosin stain. These were observed under the light microscopy at X100, X400 and X1000 with acquisition of the images done using A12.0736 CX23 Olympus biological microscope.

Determination of morphometric changes

Stereological techniques were used in morphometric analysis of the parenchymal components of the testis. From each slice 6 sections were randomly selected. From each section, sampling field frames were picked in a systematic random way, starting from the top left corner of the section. Consequently, each testis had about 108 fields as shown in Fig. 1. The sampling field frames were generated using the STEPANIZER software (Tschanz et al., 2011).

Volume densities of a components of interest were calculated using the following equation:

Where: Pc = point count on profiles of the components of interest.

Pt = Total number of points on profiles of the reference space

The volume of the component of interest was calculated using the following formula:

Where: V(c) = volume of component of interest

V (ref) = volume of the reference space

Parameters that were estimated are:

Volume density of Leydig cells = Vv (LC, ref)

Volume density of the seminiferous epithelium = Vv (SE, ref)

Volume density of the seminiferous lumen = Vv (SL, ref)

Volume density of the interstitium = Vv (I, ref)

Data analysis and presentation

Data were coded and analysed by computer software, statistical package of social sciences version 23.0. Statistical comparison of the differences between groups was done using ANOVA, followed by a Tukey post hoc test. P-value of <0.05 were considered as statistically significant.

Ethical approval

Ethical approval was sought from the Biosafety, Animal use and Ethics Committee (BAUEC), of the Faculty of Veterinary Medicine, University of Nairobi.

RESULTS

Body mass changes

The mean body mass of the rats at the beginning of the study is as shown in Table 1 for group A–D. The mean body mass after acclimatization was not statistically significant between the different experimental groups. There was a statistically significant difference between the groups in their mean body mass before sacrifice: i.e., after treatment for 28 days (F (3, 20) = 10.953, p< .001, η^2 = 0.622), as shown in Table 1. The Tukey post hoc analysis revealed significant differences between group A and the other experimental groups, as shown in Table 1.

### Histological features of the testis parenchyma in group A.

The testis parenchyma from the rats in the control group consisted of seminiferous tubules with a stratified epithelium, connective tissue stroma between the tubules composed of various cells and blood vessels. At X400 the seminiferous lumen (SL) was fully packed with spermatozoa, and the seminiferous epithelium (SE) was packed with various cells of the spermatogenic series at different stages of spermatogenesis (Fig. 2A).

At a higher magnification (X1000), various cells of the spermatogenic series were clearly
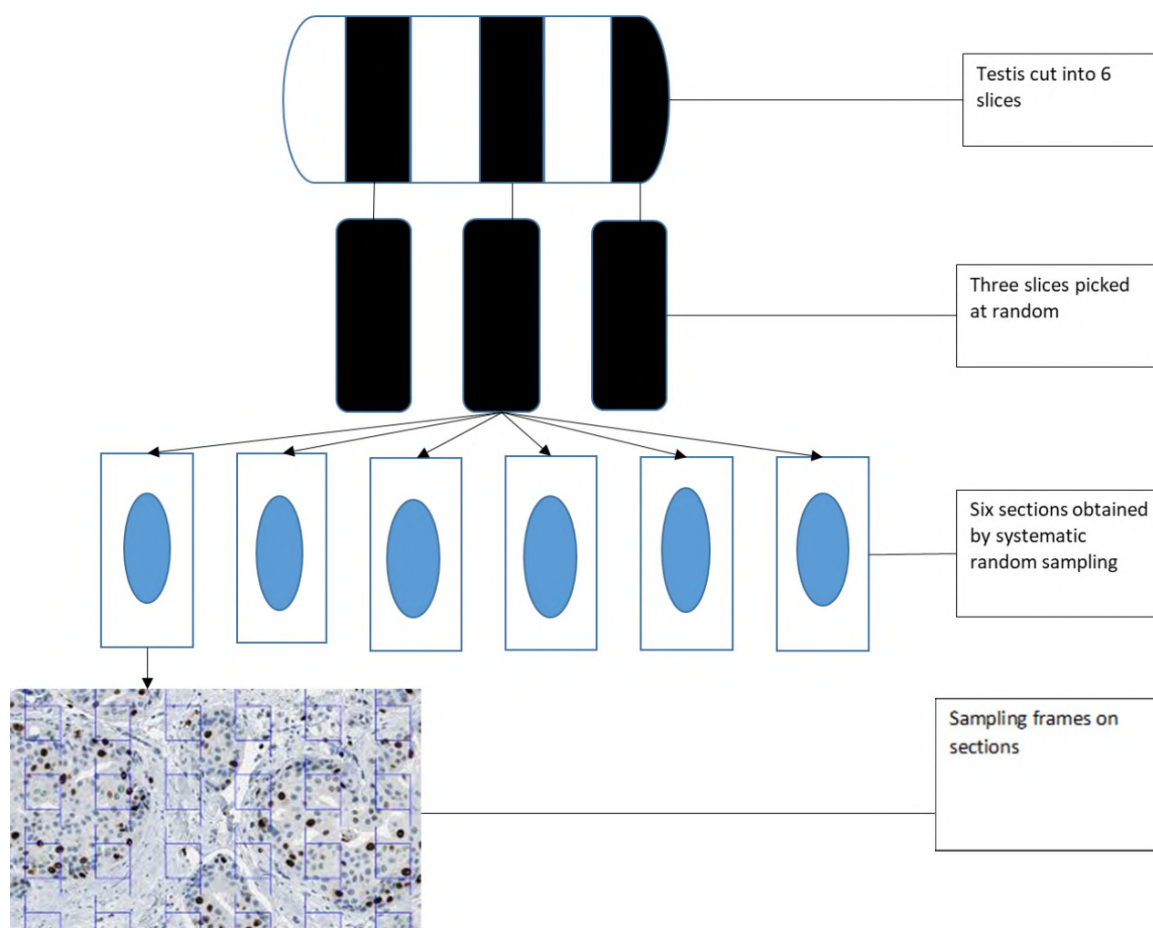
Fig. 1.- Image showing sampling of the testis

recognizable. The spermatogonia (SPG) were evident along the basement membranes, and cells were generally ovoid in shape with prominent nucleoli and dark staining cytoplasm. Sertoli cells (ST) had pale staining cytoplasm and a prominent nuclei and nucleoli. There were several spermatocytes (SPT) with disintegrated nuclei. signifying that the cells were undergoing meiosis. Early spermatids (rSPD) were round in shape with a pale staining cytoplasm, and late spermatids (eSPD) had dark elongated nuclei with inconspicuous cytoplasm buried in the cytoplasm of adjacent Sertoli cells. The connective tissue stroma consisted of Leydig cells (LC) interspersed within it. These cells were ovoid in shape clustered around blood vessels (BV) as seen in Fig. 2B.

Histological changes in the testis parenchyma of rats in the experimental groups B, C and D:

Tissue sections of the rat testes from experimental group B, C and D demonstrated development of prominent IS spaces within the seminiferous epithelium, with progressive increase in dosages. This change was most pronounced in group D, as shown in Fig. 3. Hypocellularity of the epithelium was demonstrated with increase in dosages coupled with a reduction in the cells of the spermatogenic series, as shown in Fig. 4. Microvacuolation of Sertoli cells was also observed with higher dosages of *Mondia whitei,* as shown in Fig. 5. Clamping of spermatids and fragmentation of the seminiferous epithelium was observed for group D (Fig. 6).

Table 1. Mean body mass changes in the various experimental groups.

Parameters	Mean +/- SD				P value
Groups	A (n=12)	B(n=12)	C (n=12)	D(n =12)	
Body mass on arrival	420.8 +/-13.7	393.5 +/- 16.2	414.5 +/- 35.5	406.8 +/- 44.5	0.460
Body mass after acclimatization	421.5 +/-15.2	391.5 +/- 15.5	412.3 +/- 36.8	392.5 +/- 49.3	0.319
Body mass before sacrifice	428.2 +/-11.9	353.7 +/- 17.0	346.7 +/- 42.9	352.8 +/- 31.6	0.001[*]
Tukey post hoc		74.5g	81.5g	75.3g	0.001[**]

Mean +/- SD
[*]P value <0.001 statistically significant difference between the experimental groups following one way ANOVA.
[**]P value = 0.001 following a Tukey post hoc analysis showing statistically significant differences between group A and the other experimental groups.
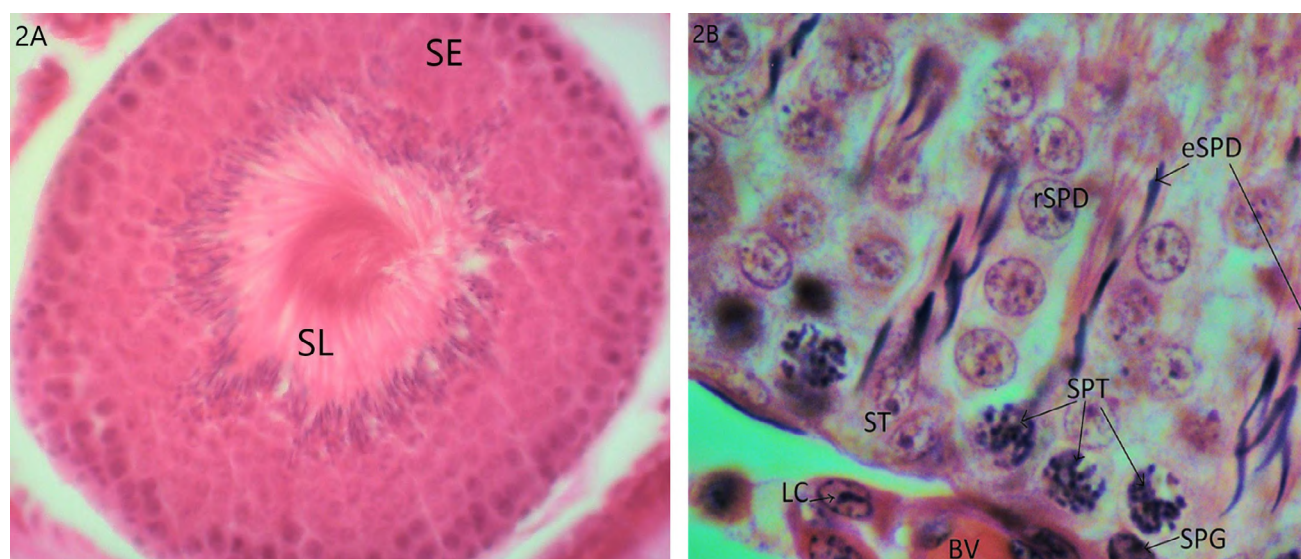
Fig. 2.- The photomicrograph shows the seminiferous epithelium (SE) with cells at different stages of the spermatogenic series and a seminiferous lumen (SL) packed with spermatozoa. Magnification = X400, stain = H&E (A). At a higher magnification a section of the seminiferous tubule shows intact seminiferous epithelium with pale staining Sertoli cells (ST), several primary spermatocytes (SPT), round spermatids (rSPD) and elongated spermatids (eSPD), spermatogonia (SPG), Leydig cells (LC), blood vessels (BV). Magnification = X1000, stain = H&E (B).

Morphometric changes of the testes

Comparative morphometric analysis of components of the testicular parenchyma

The volume densities of the various testicular components were obtained as percentages. The volume densities of the seminiferous epithelium between the experimental groups were significantly different (F (3, 20) = 86.487, p = 0.001, η^2 = 0.928) (Table 2). Tukey post hoc analysis revealed significant differences between group A and the other experimental groups, as shown in Table 2.

The volume densities of the seminiferous lumen between the experimental groups were significantly different (F (3, 20) = 4.615, p = 0.013, η^2 = 0.409) (Table 2). Tukey post hoc analysis revealed significant differences between group A and the other experimental groups as shown in Table 2.
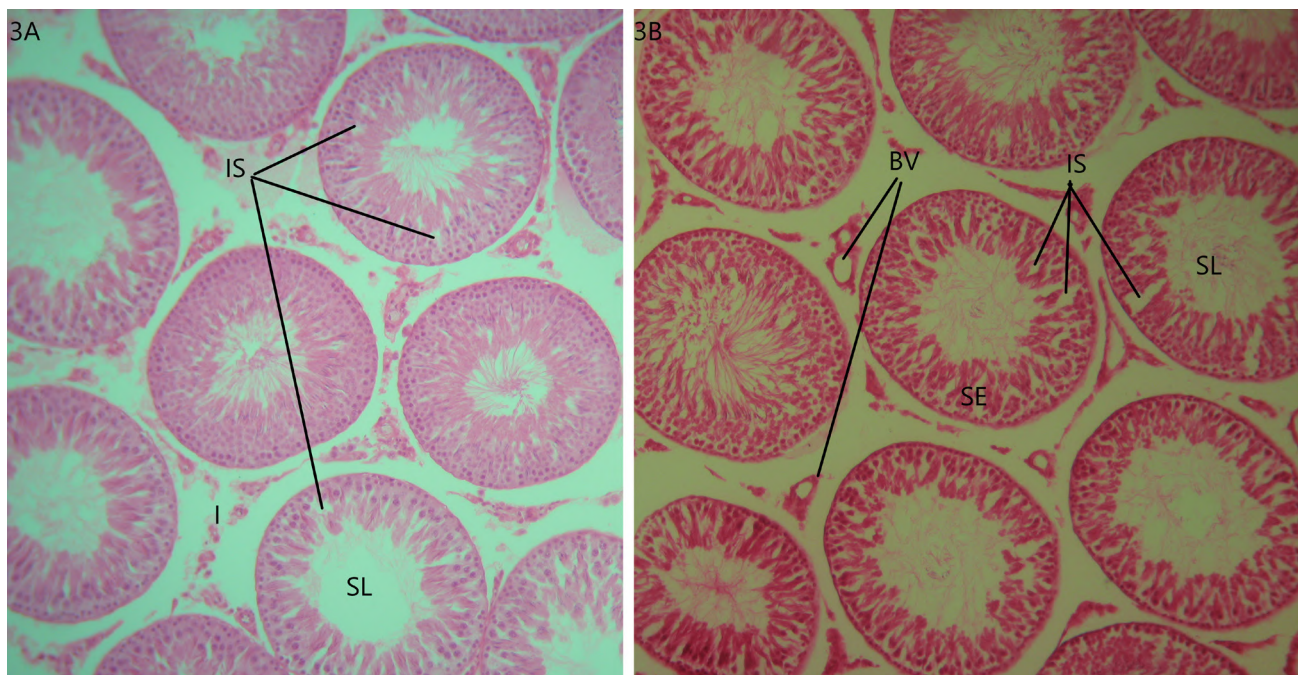
Fig. 3.- The photomicrograph shows subsequent development of interstitial spaces = IS within the seminiferous epithelium of rats in group B. Magnification = X100; Stain = H&E. SL = seminiferous lumen, I = interstitial tissue (A). As a comparison a section of the seminiferous epithelium of a rat from group D shows grossly dilated blood vessels = BV, with prominent interstitial spaces = IS. Magnification = X100, stain = H&E. SL = seminiferous lumen, SE = seminiferous epithelium (B).
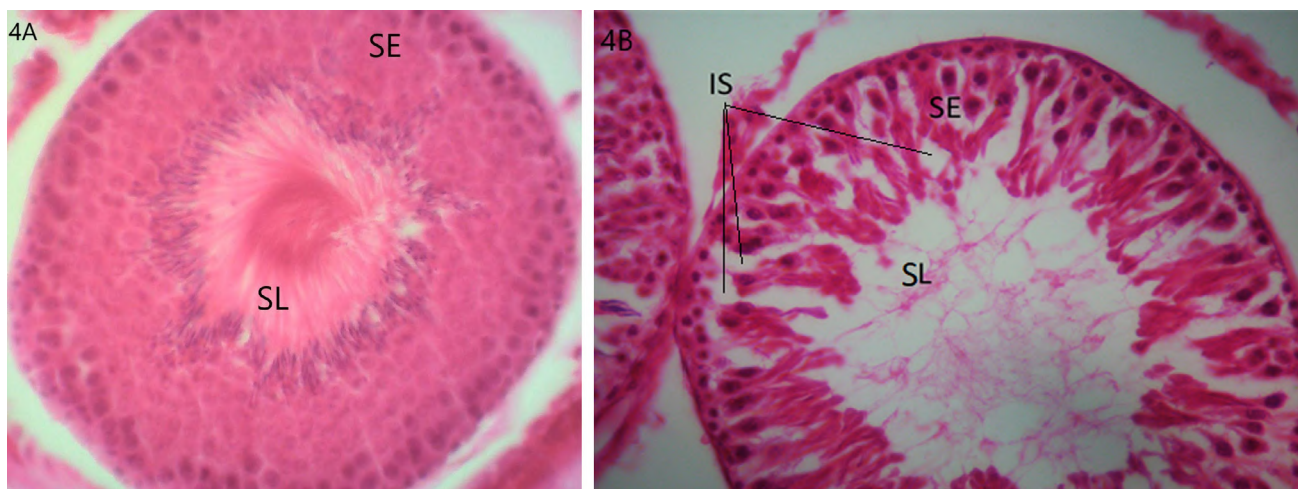
Fig. 4.- The photomicrograph shows a seminiferous tubule of a rat testis from group A with presence of a cellular epithelium (SE) and a packed seminiferous lumen (SL). Magnification = X400, stain = H&E (A). In comparison to a section of the seminiferous tubule of a section of a rat from group D showing presence of a hypocellular seminiferous epithelium (SE) and a less packed seminiferous lumen (SL) with development of intercellular spaces (IS) within the epithelium. Magnification = X400, stain = H&E (B).
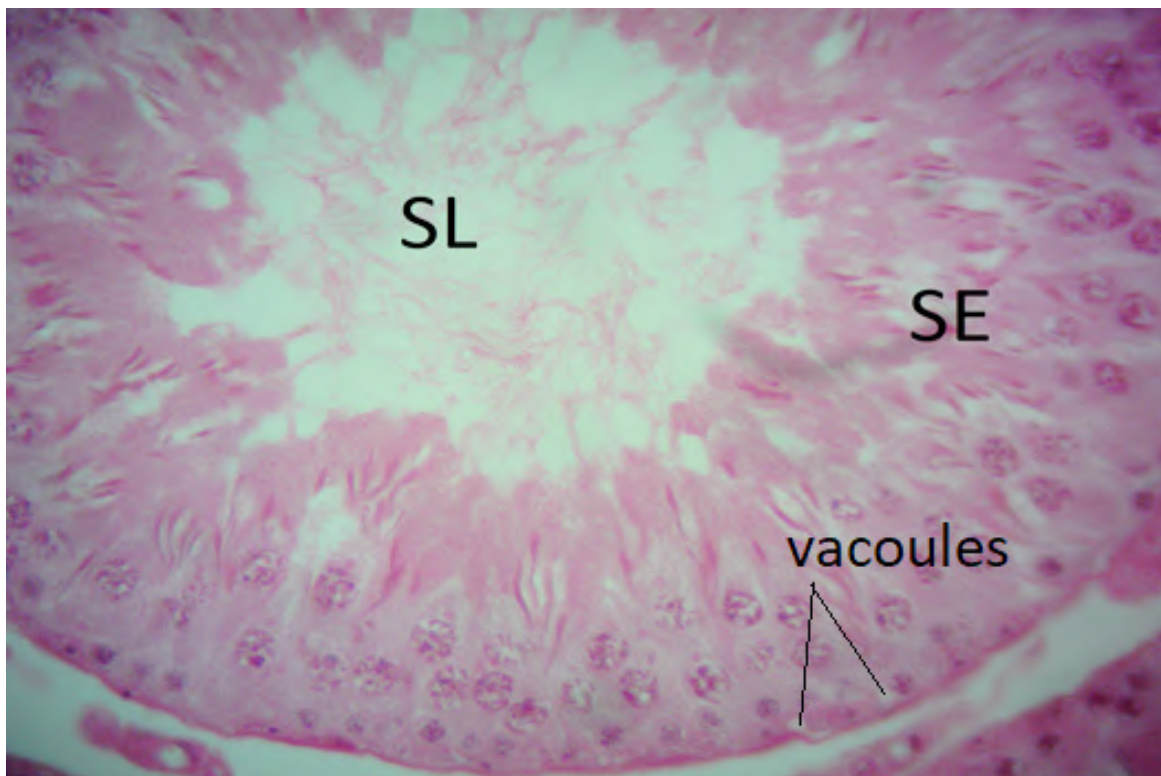
Fig. 5.- The Photomicrograph of a rat testis from group B showing presence of vacuolations in the sertoli cells. Magnification = X400; Stain = H&E. SE = seminiferous epithelium, SL = seminiferous lumen.
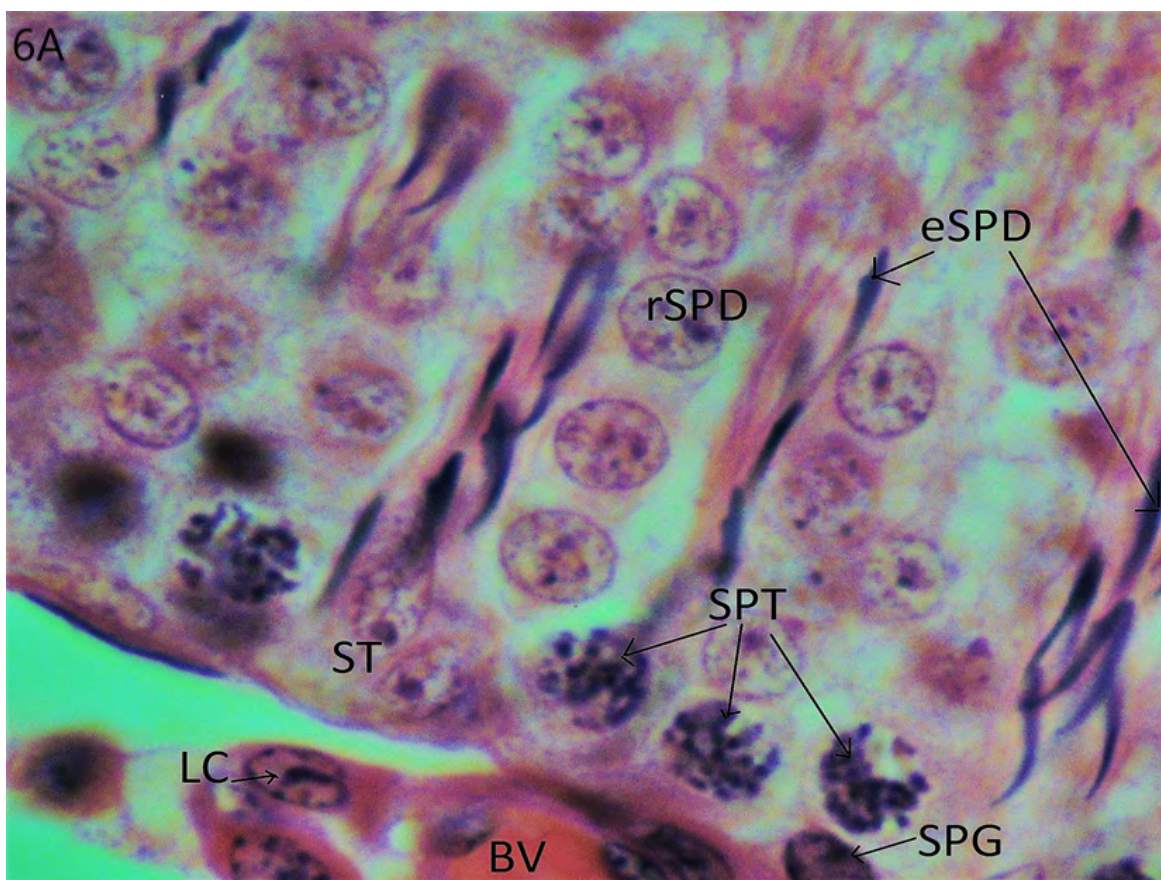
Fig. 6.- The photomicrograph of a section of the seminiferous epithelium of a rat testis from group A shows components of the intact seminiferous epithelium namely pale staining Sertoli cells (ST), several primary spermatocytes (SPT), round spermatids (rSPD) and elongated spermatids (eSPD), spermatogonia (SPG), Leydig cells (LC), blood vessels (BV). Magnification = X1000, stain H&E (A). In comparison to a section of the seminiferous tubule of a rat testis from group D which showed a hypocellular seminiferous epithelium with loss of cells of the spermatogenic series with presence of sparse spermatocytes (SPT), clamping of elongated spermatids (eSPD) and development of intercellular spaces (IS). Magnification = X1000, stain H&E (B).

The differences in volume densities of Leydig cells were statistically significant between the experimental groups (F (3, 20) = 5.807, p = 0.005, η^2 = 0.466) (Table 2). Tukey post hoc analysis revealed significant differences between group A and the other experimental groups, as shown in Table 2.

The volume densities of the interstitium between the experimental groups were significantly different (F (3, 20) = 3.712, p = 0.028, η^2 = 0.358) (Table 2). Tukey post hoc analysis revealed significant differences between group A and C, as shown in Table 2.

Volumes of the components of the testes parenchyma

The volumes of the various testicular components for the different experimental groups were obtained in centimeters cubed (cm^3). The volumes of the seminiferous epithelium was statistically significant between the experimental groups (F (3, 20) = 27.33, p < 0.001) (Table 3). Tukey post hoc analysis revealed significant differences between group A and the other experimental groups, as shown in Table 3.

The volumes of the seminiferous lumen between the experimental groups were significantly different (F (3, 20) = 3.959, p = 0.023) (Table

3). Tukey post hoc analysis revealed that the statistical significance was within groups.

The volumes of interstitium between the experimental groups were significantly different (F (3, 20) = 3.268, p = 0.043) (Table 3). Tukey post hoc analysis revealed the statistical significance was within groups.

The volumes of the Leydig cells between the experimental groups were significantly different (F (3, 20) = 5.833, p = 0.005) (Table 3). Tukey post hoc analysis revealed significant differences between group A and the other experimental groups, as shown in Table 3.

Testicular volumes

The right and left testis volumes were obtained using the Scherle method of volume displacement, and the volumes were as shown in   4. The volumes were not significantly different among the experimental groups, p = 0.478 for the right testis and p = 0.158 for the left testis.

DISCUSSION

This study investigated the effect of *Mondia whitei* on the rat testis following oral administration of the herb. The qualitative evaluation of the

Table 2. Volume densities of the components of the testis parenchyma.

Groups	Mean +/- SD			
Parameters	Vv (SE)	Vv (SL)	Vv (LC)	Vv (I)
A (n = 12)	58.2 +/- 4.1	13.2 +/- 0.8	0.89 +/- 0.1	34.2 +/- 1.5
B (n = 12)	39.0 +/- 2.0	12.5 +/- 1.6	0.66 +/- 0.3	31.5 +/- 2.6
C (n = 12)	35.5 +/- 3.4	10.1 +/- 2.3	0.47 +/- 0.3	29.7 +/- 3.9
D (n = 12)	33.8 +/- 1.5	10.1 +/- 2.1	0.48 +/- 0.1	28.5 +/- 3.9
*P values	0.001	0.013	0.005	0.028
Tukey post hoc				
Group A - B	↓19.2	↓3.02	↓0.43	
Group A - C	↓22.7	↓3.07	↓0.42	↓5.7
Group A - D	↓24.3			
** P values	< 0.001	P = 0.041	P = 0.008	P = 0.025
		P = 0.037	P = 0.010	

Mean +/- SD
*P values, statistically significant differences following a one way ANOVA.
**P value, Tukey post hoc test for the various experimental groups with statistically significant differences.
↓Statistically significant decrease between the various experimental groups following a Tukey post hoc test
Vv = volume density, LC = Leydig cells, SE = seminiferous epithelium, I = interstitium, SL = seminiferous lumen, SD = standard deviation.

rat testis showed noticeable alterations on the tissue sections of the testis at different dosages. The assessment of the quantitative parameters showed a dose-dependent reduction in the volume densities and volumes of the parameters. The changes noted included a reduction in the gross body mass of the rats, a noticeable reduction in the cellularity of the seminiferous tubules, a reduction in the volume densities and volumes of the SE. SL, I and Leydig cells.

Following administration of different dosages of *Mondia whitei,* the body mass of the rats in the experimental groups reduced throughout the duration of the experiment, while for the control group the body mass increased steadily. Body mass may provide some indication of the general health status of animals. Body mass loss in animal studies have been attributed to rejection of food or water by the animals (Thomas et al., 1983; Summers et al., 1990; Uko et al., 2001;

Nottidge et al., 2008), reduced food palatability, treatment induced anorexia and systemic toxicity (Abdulazeez et al., 2009). However it is important to note that the rats in this study received the herb via oral gavage.

Concurrent with these observations, Ihongbe et al. (2012) noted a reduction in the body weight of Wistar rats following administration of *Mondia whitei,* although the authors stated that the mechanism for the weight loss was largely unknown. Contrary to this, Watcho et al. (2001) observed an increase in body weights of rats following administration of *Mondia whitei,* although they equally did not highlight the possible mechanisms for the weight gain observed. In a different study, Watcho et al. (2005) observed no increase in body weights of rats despite administration of higher dosages of *Mondia whitei* up to 1000 mg/kg, and with this the possible mechanisms still remained unknown.

Table 3. Mean volumes of the components of the testis parenchyma.

Groups	Mean +/ - SD			
Parameters	Vc (SE)	Vc (SL)	Vc (I)	Vc (LC)
A (n = 12)	1.101 +/- 0.15	0.25 +/- 0.03	0.65 +/- 0.06	0.02 +/- 0.002
B (n = 12)	0.78 +/ - 0.05	0.25 +/- 0.02	0.63 +/- 0.05	0.013 +/- 0.005
C (n = 12)	0.68 +/ - 0.11	0.19 +/ - 0.05	0.57 +/- 0.09	0.009 +/- 0.005
D (n = 12)	0.64 +/- 0.03	0.19 +/- 0.04	0.53 +/- 0.07	0.009 +/- 0.002
*P values	<0.001	0.023	0.043	0.005
Tukey post hoc				
A – B	↓ 0.32			↓ 0.008
A – C	↓ 0.42			↓ 0.008
A - D	↓ 0.46			
**P values	P < 0.001			P <0.009
				P = 0.011

Mean +/- SD
*P values, statistically significant differences following a one way ANOVA.
**P value, Tukey post hoc test for the various experimental groups with statistically significant differences.
↓ Statistically significant decrease between the various experimental groups following a Tukey post hoc test
LC = Leydig cells, SE = seminiferous epithelium, I = interstitium, SL= seminiferous lumen, SD = standard deviation.

Table 4. Table showing means and standard deviations of the testis volumes of the right and left testis in the various study groups.

Parameters	Mean +/- SD				P value
Groups	A (n =12)	B (n =12)	C (n =12)	D (n =12)	
Right testis volume (cm³)	1.89 +/- 0.20	2.03 +/-0.14	1.83 +/-0.38	1.87 +/- 0.08	0.478
Left testis volume (cm³)	1.89 +/- 0.14	1.98 +/- 0.14	1.99 +/-0.08	1.89 +/- 0.10	0.158

Aphrodisiacs have been shown to cause an increase in the body weights of animals (Watcho et al., 2004; Mohammad et al., 2009; Prabsattro et al., 2015). Authors have proposed that the weight gain observed could be a result of the androgenic effect of the aphrodisiacs (Gauthaman et al., 2003). Androgens increase lean muscle mass (Forbes et al., 1992) and appetite, which has been proposed to contribute to the weight gain observed in rats (Wilson, 1996). The loss in body weight observed may have been due to a reduced appetite, reduction in androgenic hormones as evidenced by the reduction in the volumes, and volume densities of the Leydig cells or systemic toxicity, use of different species of *Mondia whitei* roots which may have been influenced by the different ecological patterns (Van Wyk, 2015), and lastly due to use of a different methodology.

Consequently, the constituents of *Mondia whitei* and the dose administered cannot be ignored, as there was an observed body mass changes in relation to the dose administered and the duration of administration. Whether or not the toxicity observed might be a cause for concern in humans was not examined here.

Administration of *Mondia whitei* led to noticeable alterations on the seminiferous epithelium with a reduction in the cellularity of the epithelium noted, microvacuolations of the Sertoli cells.

Concordant with the current observations, findings by Salisu, who studied a herb known as alomo bitter, whose major constituent was *Mondia whitei,* showed disorganization of testicular tissue germinal cells (Salisu et al., 2012). Another study showed that extracts from *Mondia whitei* had inhibitory effects on spermatogenesis and reduced fertility (Watcho et al., 2001). Other authors also showed cellular changes commensurate (corresponding) with cardiotoxicity (Okon et al., 2012) and neurotoxicity (Dikibo et al., 2012) in rats following administration of *Mondia whitei.* Okon et al. (2012) postulated that the changes observed in the heart may have been due to free-radical-induced myocardial injury, while Dikibo et al. attributed the cellular necrosis observed to changes in the intercellular physiological conditions. In a study done by Choumessi et al. (2012), *Mondia whitei* depicted cytotoxic effects on breast cells, and he proposed that this toxicity involved caspase 3-like signalling, which suggested apoptosis. He stated that *Mondia whitei* resulted in nuclei showing condensed chromatin; thus he concluded by noting that caution should be observed when using high doses of the herb (Choumessi et al., 2012).

Microvacuolation of the basal Sertoli cells was seen, and this is the most common morphological response of Sertoli cells to injury (Creasy, 2001). This is especially so, as Sertoli cells are extremely resistant to cell death. Injury to these cells has consequences, because of its pivotal role in supporting spermatogenesis. Sertoli cells are important in maintaining the internal milieu of the testis. These cells secrete important transport substances such as metal ions, important proteases and protease inhibitors, which play a role in tissue remodelling that takes place during spermiation and secretion of regulatory glycoproteins (Griswold, 1998). Consequently, germ cell degeneration, disorganization or exfoliation are generally seen as subsequent to the injury to Sertoli cells.

The characteristic of germ cell toxicity is rapid apoptosis and phagocytosis of the affected cells by the Sertoli cell, leaving a tubule depleted of a generation of germ cells (Creasy, 2001; Creasy and Chapin, 2015). This could also be the reason for the observed loss of the spermatogenic cells affecting the round spermatids and the elongated spermatids.

The major function of Leydig cells is steroidogenesis, and any substance that interferes with this pathway will produce functional disturbances in hormone balance. Intratesticular concentration of testosterones are usually maintained at higher levels than circulating plasma levels. Sertoli cell function and germ cell development during stage VII and VIII of the spermatogenic cycle are dependent on adequate levels of testosterone. If testosterone levels are reduced, cells in this stage will show increased levels of apoptosis and degeneration. This could be another reason for the observed loss of cells of the spermatogenic series.

Volumes of the testes in the control group increased gradually over the 4-week duration. This can be attributed to normal increase in volume with growth. The volume of the testes in experimental groups that received 300 mg/kg, 600 mg/kg and 1200 mg/kg reduced over the 4-week duration. Contrary to this finding, Ihongbe et al. (2012) observed an increase in testicular weight of the rats, and attributed this increase to increased secretory activity of the testis. Watcho et al. (2001) equally observed an increase in testicular weight, and also attributed this increase to increased levels of testosterone.

Seminiferous tubules make up to 90% of the wet weight of the normal testis; testicular weight loss observed in the different groups may be attributed to the spermatogenic disruption and degeneration of the germinal epithelium (Mishra and Singh, 2008). Sperm production is highly correlated with testicular weight. Alterations in the testis weight may suggest that sperm production and fertility were affected (Monteiro et al., 2012). To the best of our knowledge, there are no published reports that assessed volumetric densities of the testis parenchyma following use of *Mondia whitei.* Nonetheless, stereological measurements of the testis parenchyma have been shown to be reproducible and reliable (Wing and Christensen, 1982; Liu et al., 2009).

Stereology has been shown to be an accurate and reproducible method for morphometric analysis of tissues (Brown, 2017; Rahimi et al., 2021).

There was a reduction in the volume densities and volumes of the components of the testicular parenchyma following administration of *Mondia whitei,* which corresponded with the dosages that were administered.

In interpreting the findings of this study, some limitations need to be considered: we were unable to determine whether the reduction in the number of cells of the seminiferous tubules were due to apoptosis or atrophy or both. Seven um thick sections were used in studying the histology of the testis. Being a highly cellular tissue, this predisposes to tissue overlap and may contribute to underrepresentation of the changes observed.

CONCLUSION

The findings in the current study demonstrated changes in the seminiferous epithelium, which highlight possible effects of *Mondia whitei* on the testes.

There was a decrease in the volume densities and volumes of the components of the testicular parenchyma and the body mass of the rats. These histological changes, in addition to the loss of body mass, may justify the need for a cautious approach when using *Mondia whitei* extracts for medicinal use.

REFERENCES

ABDULAZEEZ MA, AMEH DA, IBRAHIM S, AYO J, AMBALI SF (2009) Effects of fermented and unfermented seed extracts of carica papaya on pre-implantation embryo development in female wistar rats (Rattus Norvegicus). *Sci Res Essays,* 4(10): 1080-1084.

ABUDAYYAK M, ÖZDEMIR NATH E, ÖZHAN G (2015) Toxic potentials of ten herbs commonly used for aphrodisiac effect in Turkey. *Turk J Med Sci*, 45(3): 496-506.

AL-SA'AIDI JAA, AL-KHUZAI ALD, AL-ZOBAYDI NFH (2009) Effects of alcoholic extracts of Nigella sativa on fertility in male rats. *Iraqi J Vet Sci,* 23(suppl 2): 123-128.

BALDWIN DS (2001) Depression and sexual dysfunction. *Br Med Bull,* 52(1): 81-99.

BROWN DL (2017) Practical stereology applications for the pathologist. *Vet Pathol,* 54(3): 358-368.

CHAUHAN NS, SHARMA V, DIXIT VK, THAKUR M (2014) A Review on plants used for improvement of sexual performance and virility. *BioMed Res Int*, Article ID 868062.

CHOUMESSI AT, LOUREIRO R, SILVA AM, MOKEIRA AC, PIERRE AC, TAZOACHA A, OLIVEIRA PJ, PENLAP VB (2012) Toxicity evaluation of some traditional African spices on breast cancer cells and isolated rat hepatic mitochondria. *Food Chem Toxicol*, 50(11): 4199-4208.

CREASY DM, CHAPIN RE (2014) Testicular and epididymal toxicity: Pathogenesis and potential mechanisms of toxicity. *Spermatogenesis*, 4(2): e1005511.

CREASY DM (2001) Pathogenesis of male reproductive toxicity. *Toxicol Pathol*, 29(1): 64-76.

DABHADKAR D, ZADE V (2013) Evaluation of the potential aphrodisiac activity of Psoralea corylifolia in male albino rats. *Asian J Biomed Pharm Sci,* 3(22): 18-27.

DIKIBO E, EHIMIGBAI J, ELOKA CCV, EKOH SN, EZEAH GAC, OKORO CJ (2014). The effect of *Mondia Whitei* on the histology of the brain of Wistar rats. *Int J Drug Discov*, 1(3): 62-67.

FORBES GB, PORTA CR, HERR BE, GRIGGS RC (1992) Sequence of changes in body composition induced by testosterone and reversal of changes after drug is stopped. *JAMA,* 267(3): 397-399.

GAUTHAMAN K, GANESAN AP, PRASAD RN (2003) Sexual effects of puncturevine (*Tribulus terrestris*) extract (protodioscin): an evaluation using a rat model. *J Altern Complement Med,* 9(2): 257-265.

GRISWOLD MD (1998) The central role of Sertoli cells in spermatogenesis. *Semin Cell Dev Biol,* 9(4): 411-416.

IHONGBE JC, SALISU AA, BANKOLE JK, OBIAZI AA, FESTUS O (2012) A study on the effect of *mondia whitei* on organ and body weight of Wistar rats. *Int J Herb Med,* 1(1): 18-23.

JARRAR BM, ALMANSOUR MI (2015) Hepatic histological alterations and biochemical changes induced by sildenafil overdoses. *Pak J Pharm Sci,* 28(6): 2119-2127.

JARRAR BM (2011) Histological alterations in the testicular tissue induced by sildenafil overdoses. *Drug Metab Lett*, 5(2): 99-103.

KOTTA S, ANSARI SH, ALI J (2013) Exploring scientifically proven herbal aphrodisiacs. *Pharmacogn Rev*, 7(13): 1-10.

KUO XK, CHANG LZ, CHEN YW, LIAO JW (2006) Safety evaluation of feeding a newly introduced medicinal plant VUKA (*Mondia whitei* L) to mice, COA: From Taichung DARES. 91: 21-29 (in Chinese). Taichung District Agricultural Improved Market Research Report.

LAMIDI M, BOUROBOU H (2010) *Mondia whitei* (Hook. f.) Skeels. [Online] Record from Protabase. In: Schmelzer GH, Gurib-Fakim A (eds). Wageningen, Netherlands: PROTA (Plant Resources of Tropical Africa/Ressources v´eg´etales de l'Afrique tropicale). Retrieved from http://database.prota.org/search.htm.

LAMPIAO F, KROM D, DU-PLESSIS (2008) The in vitro effects of *Mondia whitei* on human sperm motility parameters. *Phytother Res*, 22(9): 1272-1273.

LIKATA GMU, KURIA MW, OLANDO Y, OWITI FR (2012) Sexual dysfunction among patients with diabetes mealitus. *Greener J Med Sci,* 2(6): 138-145.

LIU Z, CHANG Q, XU Z, ZHANG Z (2009) Stereological measurements of rat seminiferous tubules. *Chin Med J,* 122(21): 2643-2646.

MALVIYA N, JAIN S, GUPTA VB, VYAS S (2011) Recent studies on aphrodisiac herbs for the management of male sexual dysfunction – A review. *Acta Pol Pharm – Drug Research,* 68(1): 3-8.

MISHRA RK, SINGH SK (2008) Safety assessment of Syzygium aromaticum flower bud (clove) extract with respect to testicular function in mice. *Food Chem Toxicol*, 46(10): 3333-3338.

MOHAMMAD MA, MOHAMMAD MMJ, DRADKA H (2009) Effects of black seeds (Nigella Sativa) on spermatogenesis and fertility of male albino rats. *Res J Med Sci,* 4(2): 386-390.

MONTEIRO JC, MATTA SLP, PREDES FS, PAULA TAR (2012). Testicular morphology of adult winstar rats treated with *Rudge Viburnoides* benth leaf infusion. *Braz arch boil technol,* 55(1): 101-105.

NOTTIDGE HO, OMOBOWALE TO, TAIWO VO, OMOTOSO MA (2008) Histopathological studies on the effects of the ethanolic extract of the fruits of Garcinia kola on selected organs of the dog. *Int J Morphol,* 26(4): 1067-1072.

OKETCH-RABAH HA (2012) *Mondia whitei*, a medicinal plant from Africa with aphrodisiac and antidepressant properties: a review. *J Diet Suppl*, 9(4): 272-284.

OKON AU, BANKOLE JK, ENEASATO AP, EZEAH GA, BANKOLE SO (2012) Histological changes in the heart of rats fed diet containing *mondia whitei*. *Int J Basic Appl Innov Res,* 1(4): 105-110.

PATEL DK, KUMAR R, PRASAD SK, HEMALATHA S (2011) Pharmacologically screened aphrodisiac plant – A review of current scientific literature. *Asian Pac J Trop Med,* 1(1): S131-S138.

PRABSATTROO T, WATTANATHORN J, IAMSAARD S, SOMSAPT P, SRITRAGOOL O, THUKHUMMEE W, MUCHIMAPURA S (2015) *Moringa oleifera* extract enhances sexual performance in stressed rats. *J Zhejiang Univ Sci B*, 16(3): 179-190.

RAHIMI A, RAFATI A, NOORAFSHAN A, KARBALAEI N, KARBALAY-DOUST S (2021) Curcumin can prevent the loss of sinoatrial node cells in methionine treated rats: A stereological study. *Saudi J Biol Sci,* 28(6): 3448-3452.

SALISU AA, IHONGBE JC, ANYANWU RA, UWUIGBE M, IZEKOR S (2012) Histological changes in the testis of rats treated with alomo bitter. *J Drug Discov,* 1(2): 33-39.

SCHERLE W (1970) A simple method for volumetry of organs in quantitative stereology *Microscopie,* 26: 57-60.

SUMMERS JD, SPRATT D, BEDFORD M (1990) Factors influencing the response of broiler chickens to calcium supplementation of canola meal. *Poult Sci,* 69(4): 615-622.

THOMAS VM, KATZ RJ, AULD DA, PETERSON CF, SAUTER EA, STEELE EE (1983) Nutritional value of expeller extracted rape and safflower oil seed meals for poultry. *Poult Sci,* 62(5): 882-886.

TSCHANZ SA, BURRIE PH, WEIBEL ER (2011) A simple tool for stereological assessment of digital images: the STEPanizer, *J Microsc,* 243(1): 47-59.

UKO OJ, USMAN A, ATAJA AM (2001) Some biological activities of *Garcinia kola* in growing rats. *Veterinarski ArChiv,* 71(5): 287-297.

VAN WYK BE (2015) A review of commercially important African medicinal plants. *J Ethnopharmacol*, 24(176): 118-134.

VIDALE S, DI PALMA F, REZZONICO M, SAMPIETRO A, ARNABOLDI M (2015) Ischemic stroke as unusual complication of sildenafil use. *Int J Stroke*, 10(4): E38-E38.

WATCHO P, DEFO PBD, WANKEU-NYA M, CARRO-JUAREZ M, NGUELEFACK TB, KAMANYI A (2013) *Mondia whitei* (Periplocaceae) prevents and Guibourtia tessmannii (Caesalpiniaceae) facilitates fictive ejaculation in spinal male rats. *BMC Complement Altern Med*, 13(4): 13-14.

WATCHO P, DONFACK MM, ZELEFACK F, NGUELEFACK TB, WANSI S, NGOULA F, KAMTCHOUING P, TSAMO E, KAMANYI A (2005) Effects of the hexane extract of *Mondia whitei* on the reproductive organs of male rat. *Afri J Complement Altern Med*, 2(3): 302-311.

WATCHO P, FOTSING D, ZELEFACK F, NGUELEFACK TB, KAMTCHOUING P, TSAMO E, KAMANYI A (2004) Effects of *Mondia whitei* extracts on the contractile responses of isolated rat vas deferens to potassium chloride and adrenaline. *Indian J Pharmacol*, 38 (1): 33-37.

WATCHO P, KAMTCHOUING P, SOKENG S, MOUNDIPA PF, TANTCHOU J, ESSAME LJ, KOUETA N (2001) Reversible antispermatogenic and antifertility activities of *mondia whitei* in male albino rat. *Phytother Res,* 15(1): 26-29.

WILSON JD (1996) Androgens. In: Molinoff PB, Ruddon RW (eds). Goodman and Gilman's *The Pharmacological Basis of Therapeutics*. New York: McGraw-Hill, pp 1441-1448.

WING TV, CHRISTENSEN AK (1982) Morphometric studies on rats seminiferous tubules. *Am J Anat*, 165(1): 13-25.

YAKUBU MT, AKANJI MA, OLADIJI AT (2005) Aphrodisiac potential of the aqueous extract of Fadogia agretis stem in male albino rats. *Asian J Androl*, 7(4): 399-404.

ZADE VS, DABHADKAR DK, THAKARE VG, PARE SR (2013) Effect of aqueous extract of Moringa oleifera seed on sexual activity of male albino rats. *BFAIJ,* 5(1): 129-140.

Clinical Significance and Radiological Evaluation of Crista Galli: A CBCT Study

Ceren Özeren Keşkek[1], Emre Aytuğar[2]

[1] *Izmir Training Dental Hospital, Izmir, Turkey*

[2] *Department of Oral and Maxillofacial Radiology, Faculty of Dentistry, Izmir Katip Celebi University, Izmir, Turkey*

SUMMARY

The present study aimed to determine the morphometric dimensions of crista galli (CG) with cone-beam computed tomography (CBCT), to evaluate its position relative to the cribriform plate (CP), and to examine the prevalence of pneumatized CG (PCG). CBCT images of 245 individuals aged 9-77 years were examined, retrospectively. The length, height and width of CG were measured. The position of CG relative to the CP was examined and was classified. The presence of PCG was investigated in coronal, axial and sagittal sections. CG was classified as type I, II and III, and PCG as type IP, IIP and IIIP.

PCG was detected in 5 (2.04%) of 245 patients. Type IP was observed in only 1 patient and type IIP in 4 patients. Type I CG was observed in 161 individuals (65.7%), and type II CG in 79 individuals (32.2%). Type III and type IIIP were not seen. The height, width and length of CG were 13.2 ± 2.4 mm, 4.3 ± 1.2 mm and 12.5 ± 1.7 mm, respectively. These values did not differ significantly by gender (p>0.05). PCG is an anatomical variation of the ethmoid bone. In our study, the prevalence of PCG was quite low compared to previous studies. Besides, this study showed that the length (7.8-17.6 mm), height (6.2-20 mm) and width (1.3-7.5 mm) of the CG are in a very wide range. Further research is needed to determine the morphometry of CG and to compare the prevalence of PCG effectively.

Key words: Anterior skull base surgery – Cone-beam computed tomography – Crista galli – Pneumatization

INTRODUCTION

Crista galli (CG) is a rooster-crest-shaped anatomical formation extending from the middle of the cribriform plate (CP) upwards. It is a useful anatomical point in anterior skull base surgery, as it creates a connection with the falx cerebri posteriorly (Akiyama and Kondo, 2020). CG develops embryologically from the ethmoid bone (Papadopoulou et al., 2021). For this reason, it was thought that CG pneumatization (PCG) originated from ethmoid air cells. However, the other more accepted theory is that it occurs due to increased aeration as a result of the expansion of the frontal sinus adjacent to it (Som et al., 2009; Turna et al., 2014). In addition to these theories, Poje et al. (2014) reported that they considered PCG as a true sinus with the definition of sinus crista galli.

Anatomic variations are frequently observed in the paranasal sinuses and sinonasal regions.

Corresponding author:
Ceren Özeren Keşkek, İzmir Training Dental Hospital, Fevzipasa Boulevard, Akinci district, No.172/2 Konak, Izmir, Turkey.
E-mail: cerenozeren35@gmail.com

Some of these variations are considered as predisposing factors for pathological conditions such as rhinosinusitis. PCG may contain normal upper respiratory tract mucosa. Because of this mucosal layer, it may cause other paranasal sinus pathologies to be seen in PCG (Marjanovic Kavanagh et al., 2020). Drainage between the PCG and neighboring paranasal sinuses occurs through the sinus ostia as in others. When there is an ostial obstruction, infection of the mucosa, formation of mucoceles, and related headache may occur (Mladina et al., 2017). In case reports, it has been reported that PCG may be complicated with processes similar to rhinosinusitis; headache is observed in the frontal region, resistance to drug therapy may be observed; therefore, surgical drainage is the preferred treatment. Transnasal endoscopic surgery is preferred for surgical drainage (Socher et al., 2013; Min and Kim, 2016). Detailed examination with radiological evaluation is essential for the correct planning of the surgical procedure and to prevent complications (Hajiioannou et al., 2010).

Nowadays, interest in PCG has increased due to both its clinical effects and some neurosurgical approaches. The reported prevalence of pneumatization varies widely (Mladina et al., 2017). In this study, it was aimed to determine the anatomical and morphometric dimensions of CG using cone-beam computed tomography (CBCT), to determine the prevalence of PCG, and to evaluate its position relative to the CP.

MATERIAL AND METHODS

CBCT images of 300 patients taken for various reasons in the Department of Oral and Maxillofacial Radiology were examined. High-quality CBCT images with a voxel size of 0.200 mm were included in the study. Exclusion criteria were the presence of pathology or surgical procedure, trauma history, craniofacial deformity or syndrome, and poor-quality images. Images of 55 individuals were excluded from the study, according to these criteria. Ethical approval was obtained from Izmir Katip Celebi University Non-Interventional Clinical Studies Ethical Committee (02.07.2020, IRB:834). All procedures followed were in accordance with the ethical standards

of the responsible committee on human experimentation (institutional and national), and with the Helsinki Declaration of 1975, as revised in 2008. Informed consent is not necessarily due to the retrospective nature of this study.

All of the images used in the study were obtained using the CBCT (NewTom 5G, Quantitative Radiology, Verona, Italy) device operating at 110 kVp. Images with 15 × 12 cm FOV range and 0.200 mm voxel size were used. Images were analyzed by an oral and maxillofacial radiologist using NNT (NNT Software Version 9.1; NewTom; Italy) computer software.

Firstly, PCG was investigated in coronal, axial and sagittal sections; and, if there was pneumatization, where it originated was determined. Maximum CG height and width were measured in coronal sections and maximum CG length was measured in axial sections (Fig. 1).

In coronal sections, the position of CG relative to the CP was examined and confirmed in mid-sagittal sections. It was classified according to Hajiioannou's classification (Hajiioannou et al., 2010) (Fig. 2):

Type I – The base of CG and CP are at the same level.

Type II – Less than 50% of CG height is below CP level.

Type III – More than 50% of CG height is below the CP level.

In the case of pneumatization, this classification was made as IP, IIP, and IIIP.

All statistical analyses were performed in IBM SPSS Version 26. Kolmogorov-Smirnov test was used in order to determine data distribution. The independent samples t-test, Kruskal-Wallis test, and Mann-Whitney U test were used. Spearman's rho and Pearson correlation tests were used for evaluating the correlation between measurements and age. The level of significance (p-value) was accepted as 0.05.

RESULTS

The study group consisted of 245 individuals (Mean age: 37.5), 183 women and 62 men. PCG

was detected in 5 (2.04%) of 245 patients. Type IP (0.4%) was observed in only 1 patient and type IIP (1.6%) in 4 patients (Table 1). All of the individuals with PCG were women. PCG was not observed in men. One of the detected PCGs was associated with the ethmoidal sinus and four PCGs with the frontal sinus (Figs. 3, 4). Type I CG was observed in 161 individuals (65.7%), and type II CG in 79 individuals (32.2%). Type III and type IIIP were not seen.
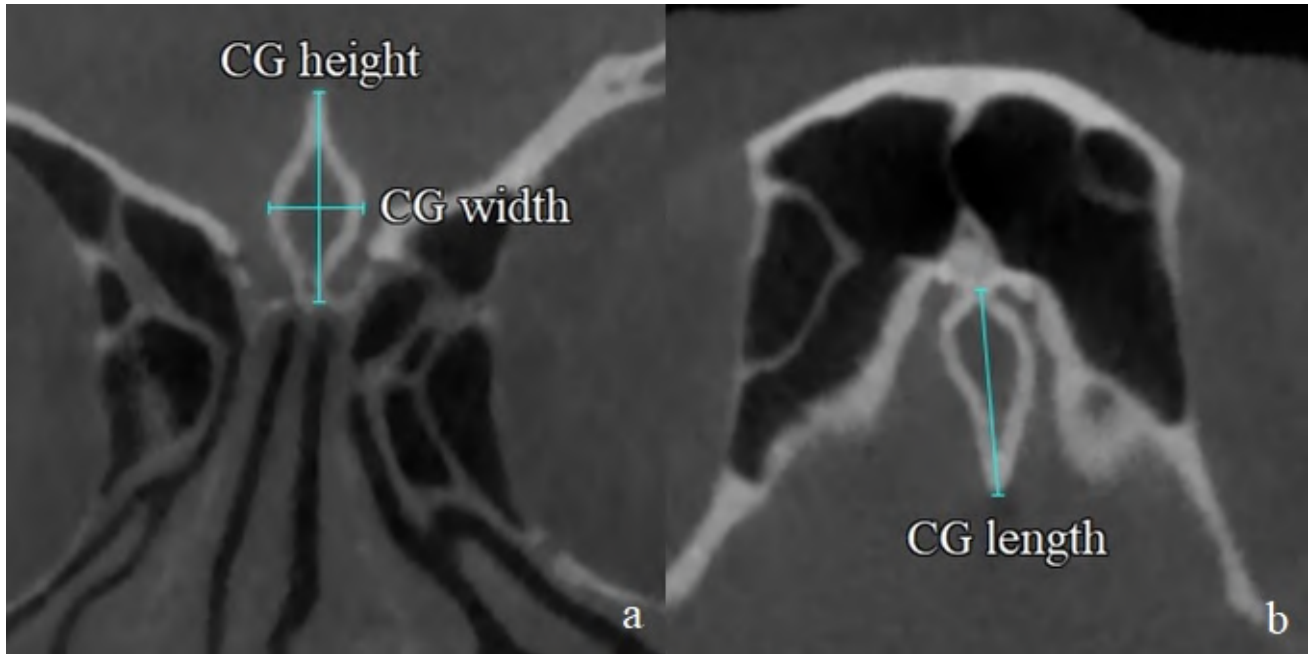
Fig. 1.- Measurements of crista galli (CG). (a) Measurement of height and width in coronal section, (b) Measurement of length in axial section.
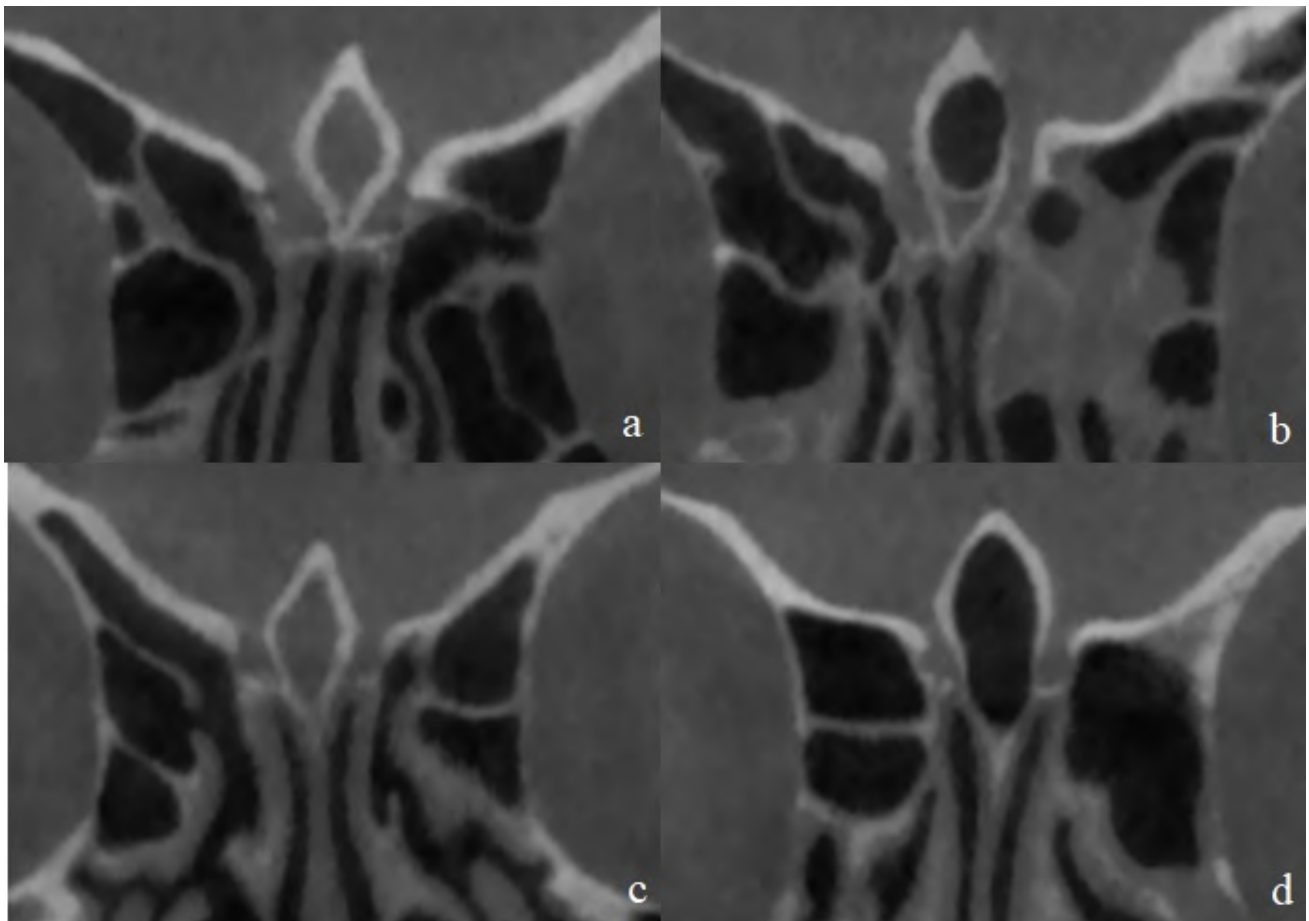
Fig. 2.- Sample images of the classification of crista galli. (a) Type I, (b) Type IP, (c) Type II, (d) Type IIP.

Table 1. Pneumatization and classification of crista galli

	Type I N (%)	Type II N (%)	Type III N (%)	Total N (%)
Pneumatization	1 (0.4)	4 (1.6)	0 (0)	5 (2.04)
Non-Pneumatization	161 (65.7)	79 (32.2)	0 (0)	240 (97.96)
Total	162 (66.1)	83 (33.8)	0 (0)	245 (100)
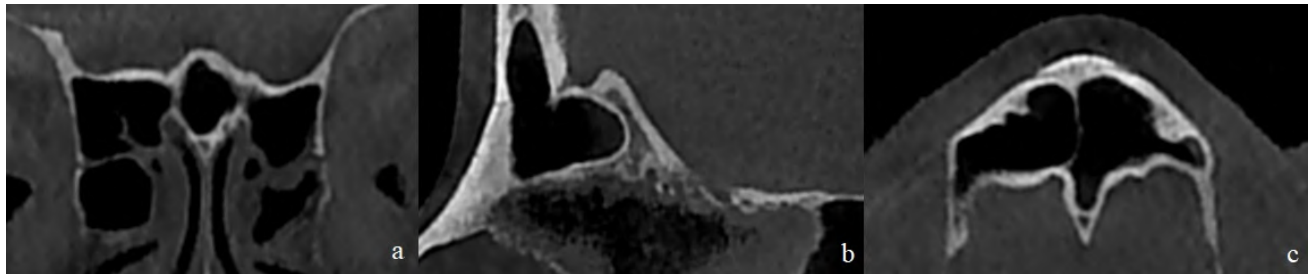
Fig. 3.- Pneumatized crista galli originating from the frontal sinus. (a) Coronal view, (b) Sagittal view, (c) Axial view.
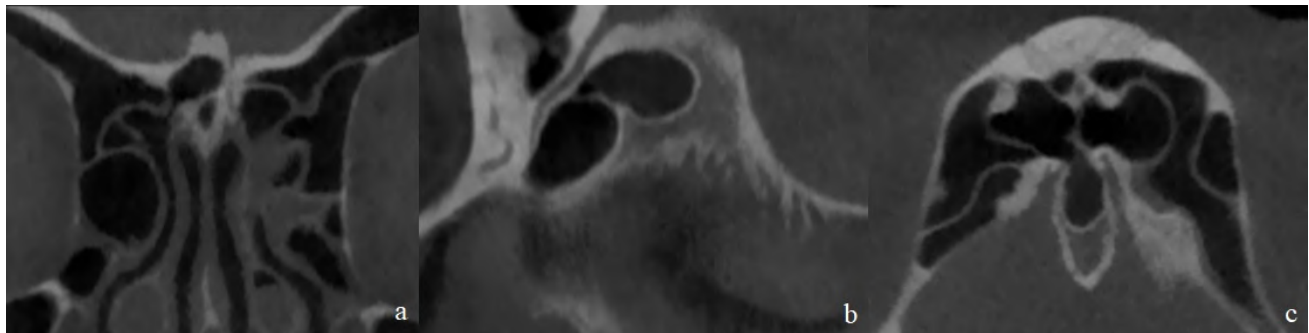
Fig. 4.- Pneumatized crista galli originating from the ethmoid sinus. (a) Coronal view, (b) Sagittal view, (c) Axial view.

Table 2 presents the height, length and width measurements of the CG. There was no significant difference in these values according to gender (p>0.05). In CGs without pneumatization, the heights in type I (N=161) and type II (N=79) were 12.6±2.2 and 14.3±2.5 mm, the widths were 4.1±1.2 and 4.5±1.1 mm, the lengths were 12.2±1.7 and 13.0±1.6 mm, respectively. There was a statistically significant difference between height, width, length values and the types of CG (Type I and Type II) (p=0.000, p=0.008, p=0.002). Type II CGs were larger than type I CGs.

Besides, it was investigated whether there is a correlation between the dimensions of CG and age. No statistically significant correlation was

Table 2. Measurement values of males, females and total

	Female (N:178)				Male (N:62)				Total (N:240)				
	Mean	SD	Min.	Max.	Mean	SD	Min.	Max.	Mean	SD	Min.	Max.	p-value
CG Height	13.2	2.4	6.2	19.8	13.1	2.5	8.0	20.0	13.2	2.4	6.2	20.0	0.647
CG Width	4.3	1.2	1.3	7.5	4.1	1.2	1.8	6.6	4.3	1.2	1.3	7.5	0.179
CG Length	12.4	1.7	7.8	16.1	12.7	1.6	9.8	17.6	12.5	1.7	7.8	17.6	0.289

CG: Crista galli, N: Number of patients, SD: Standard deviation, Min.: Minimum value, Max.: Maximum value.

found between the height, width and length of the CG and the age (r=0.093, p=0.148; r=-0.038, p=0.555; r=0.035; p=0.583).

DISCUSSION

CG is an important anatomical structure in endoscopic sinus and skull-base surgery (Metin-Tellioglu and Polat, 2019). This is due to its location, shape and dimensions. It projects superiorly into the intracranial space and is in contact with vital anatomical structures. The falx cerebri separating the right and left cerebral hemispheres connects to the CG. Besides, the CG is closely adjacent to the superior sagittal sinus. The superior sagittal sinus can start just in front of the CG. In the treatment of anterior skull base tumors, crista galli may need to be removed during endoscopic transcribriform surgery (Lee et al., 2011). Due to its location, there is a risk of injury to important vascular structures and leakage of cerebrospinal fluid (CSF) during surgery (Acar et al., 2020). It has been suggested that when pneumatization is present in the CG, it is more difficult to minimize CSF leak, and the surgeon should pay particular attention to the degree of pneumatization to prevent leakage. The location, dimensions and variations of CG should be well understood before surgery to avoid complications (Akiyama and Kondo, 2020).

PCG can include chronic sinusitis (Manea and Mladina, 2016), mucocele (Cervantes and Lal, 2014; Shidanshid et al., 2015), or dermoid cyst (Hajiioannou et al., 2010). In a histopathological study, PCG was detected in 5 out of 109 specimens. Chronic inflammation has been reported in all PCGs (Marjanovic Kavanagh et al., 2020). Recently, Takaki et al. (2021) reported that they detected erosion in CG with a dural arteriovenous fistula in a 38-year-old female patient. They suggested that external erosion of CG could be a sign of an aggressive dural arteriovenous fistula and should be carefully investigated. For this reason, CG should be examined, and the presence of PCG should be determined if present.

PCG was examined by various methods such as histopathological (Marjanovic Kavanagh et al., 2020), computed tomography (CT) (Som et al., 2009; Kim et al., 2012; Poje et al., 2014;

Kamala et al., 2016; Metin-Tellioglu and Polat, 2019; Acar et al., 2020; Akiyama and Kondo, 2020) and CBCT (Mladina et al., 2017; Uçar et al., 2021). CBCT provides reliable and accurate measurements of bone structures in three axes. CBCT has advantages such as less radiation dose, shorter scanning time and low cost compared to CT (Scarfe et al., 2006; Ludlow and Ivanovic, 2008). For this reason, we preferred to use images obtained with CBCT in our study.

The prevalence of PCG reported in the literature ranges from 2.4% to 43% (Bašić et al., 1999; Som et al., 2009; Hajiioannou et al., 2010; Kaygusuz et al., 2014; Poje et al., 2014; Rereddy et al., 2014; Turna et al., 2014; Shpilberg et al., 2015; Dasar and Gokce, 2016; Manea and Mladina, 2016; Çalışkan et al., 2017; Devaraja et al., 2019; Metin-Tellioglu and Polat, 2019; Sommer et al., 2019; Acar et al., 2020; Akiyama and Kondo, 2020; Marjanovic Kavanagh et al., 2020; Uçar et al., 2021). In studies conducted in the Turkish population, the prevalence of PCG varies between 3.3 and 29.8% (Kaygusuz et al., 2014; Dasar and Gokce, 2016; Çalışkan et al., 2017; Sommer et al., 2019; Acar et al., 2020; Uçar et al., 2021). In our study, PCG was observed in only 5 patients (2.04%). It was a very low percentage, both according to studies in the same population and studies worldwide. A wide range of different PCG rates in the literature may have resulted from differences in racial, method and sample sizes.

Embryologically, since CG develops from the ethmoid bone, it makes sense for pneumatization to occur in the ethmoid complex. The pneumatization was thought to be caused by the ethmoid cells displaced to the frontal recess area (Som et al., 2009). However, it has been suggested that pneumatization may also originate from the frontal sinus immediately adjacent to the CG (Kim et al., 2012). Som et al. (2009) reported in their study that pneumatization in CG originated from the frontal sinus. Kim et al. (2012) reported that each pneumatization was associated with the frontal sinus, and that only one patient with bilateral undeveloped frontal sinuses had PCG connected to the ethmoid sinus. Kamala et al. (2016) found that 80% of PCGs originated from the frontal sinus and 20% from the ethmoid sinus. Akiyama et

Table 3. The distribution of crista galli's classification in previous studies

	Imagine Technique	Number of Patients	Type I (%)	Type II (%)	Type III (%)
Hajiioannou et al., 2010	CT	99	28.3	63.6	8.1
Kim et al., 2012	CT	818	13.9	84.2	1.8
Poje et al., 2014	CT	527	22.6	56.4	20.9
Kamala et al., 2016	CT	114	12.5	82.5	5
Acar et al., 2020	CT	402	18.3	64.9	16.8
Present Study	CBCT	245	66.2	33.8	0

al. (2020) detected 28 PCG (9.3%) in 300 patients, and reported that 17 of them originated from the frontal sinus and 11 from the ethmoid sinus. In our study, 4 of 5 PCGs detected were associated with the frontal sinus (80%), and 1 with the ethmoid sinus (20%). It is important to know whether the PCG originates from the frontal or ethmoid sinus in the selection of the surgical procedure to be applied. It has been reported that more care should be taken to prevent CSF leak and infection in PCGs associated with the ethmoid sinus (Akiyama and Kondo, 2020).

CG removal may be required during endoscopic anterior skull-base surgery, depending on the extent of the pathology. Given that the anterior ethmoid skull base is only a few millimeters thick, it is important to know the dimensions of the CG during this procedure (Lee et al., 2011). Mladina et al. (2017) reported the mean height, width and length of CG as 10.1 ± 3.1 mm, 3.0 ± 1.2 mm and 7.1 ± 2.5 mm, respectively. Akiyama et al.(2020) reported the mean height, width and length as 15.9 ± 3.2 mm, 4.9 ± 1.3 mm and 13.5 ± 2.8 mm, respectively. In our study, the mean height, width and length were 13.2 ± 2.4 mm, 4.3 ± 1.2 mm and 12.5 ± 1.7 mm, and these values did not differ significantly by gender. This study presented values in the middle of two previous studies that performed morphometric measurements of CG. We think that more studies with larger sample sizes are needed in order to define standard sizes and ethnic differences.

Hajiioannou et al. (2010) classified the position of CG in coronal and axial CT sections according to CP in their study. When examining the position of CG relative to CP, evaluating only in axial and coronal sections is insufficient, because CP is an inclined structure. Examinations performed together with the sagittal section will provide more accurate results. In addition, sagittal examinations are recommended to be performed in the median plane (Poje et al., 2014). Classification of the position of CG relative to CP was compared with previous studies, together with the imaging technique and the number of patients, in Table 3. The ratio of all CGs with or without pneumatization in the studies is given. A very different result was obtained compared to previous studies (Hajiioannou et al., 2010; Kim et al., 2012; Poje et al., 2014; Kamala et al., 2016; Acar et al., 2020). Type II was the most common in all of the studies. In our study, when all CGs were evaluated, surprisingly, type I (66.2%) was observed most frequently and type III was not observed. This difference may be due to the detection of CG types in coronal sections in our study and then confirmation in sagittal sections.

CONCLUSION

In conclusion, our study provided information about the morphology of CG, and found that PCG was observed at a low rate (2.04%) compared to previous studies. It was observed that the PCG originated mainly from the frontal sinus (80%). With a CBCT scan, the position of CG relative to CP and the relationship of CG with paranasal sinuses and other important anatomical structures can be determined, and this may be effective in providing safer surgical operations and preventing surgical complications. We think that further research with the large sample groups is necessary to determine the morphometry of CG and to compare the prevalence of PCG effectively.

REFERENCES

ACAR G, CICEKCIBASI AE, KOPLAY M, KELESOGLU KS (2020) The relationship between the pneumatization patterns of the frontal sinus, crista galli and nasal septum: a tomography study. *Turk Neurosurg,* 30(4): 532-541.

AKIYAMA O, KONDO A (2020) Classification of crista galli pneumatization and clinical considerations for anterior skull base surgery. *J Clin Neurosci,* 82(Pt B): 225-230.

BAŠIĆ N, BAŠIĆ V, JUKIĆ T, BAŠIĆ M, JELIĆ M, HAT J (1999) Computed tomographic imaging to determine the frequency of anatomical variations in pneumatization of the ethmoid bone. *Eur Arch Otorhinolaryngol,* 256(2): 69-71.

CERVANTES SS, LAL D (2014) Crista galli mucocele: endoscopic marsupialization via frontoethmoid approach. *Int Forum Allergy Rhinol,* 4(7): 598-602.

ÇALıŞKAN A, SUMER AP, BULUT E (2017) Evaluation of anatomical variations of the nasal cavity and ethmoidal complex on cone-beam computed tomography. *Oral Radiol,* 33(1): 51-59.

DASAR U, GOKCE E (2016) Evaluation of variations in sinonasal region with computed tomography. *World J Radiol,* 8(1): 98-108.

DEVARAJA K, DORESWAMY SM, PUJARY K, RAMASWAMY B, PILLAI S (2019) Anatomical variations of the nose and paranasal sinuses: a computed tomographic study. *Indian J Otolaryngol Head Neck Surg,* 71(Suppl 3): 2231-2240.

HAJIIOANNOU J, OWENS D, WHITTET HB (2010) Evaluation of anatomical variation of the crista galli using computed tomography. *Clin Anat,* 23(4): 370-373.

KAMALA E, SHANMUGAM U, VAITHEES G, KUMAR N (2016) A computerized tomographic study of morphology and pneumatization of crista Galli. *Int J Anat Res,* 4: 2429-2433.

KAYGUSUZ A, HAKSEVER M, AKDUMAN D, ASLAN S, SAYAR Z (2014) Sinonasal anatomical variations: their relationship with chronic rhinosinusitis and effect on the severity of disease-a computerized tomography assisted anatomical and clinical study. *Indian J Otolaryngol Head Neck Surg,* 66(3): 260-266.

KIM JJ, CHO JH, CHOI JW, LIM HW, SONG YJ, CHOI SJ, YEO NK (2012) Morphologic analysis of crista galli using computed tomography. *J Rhinol,* 19(2): 91-95.

LEE JM, RANSOM E, LEE JYK, PALMER JN, CHIU AG (2011) Endoscopic anterior skull base surgery: intraoperative considerations of the crista galli. *Skull base,* 21(2): 83-86.

LUDLOW JB, IVANOVIC M (2008) Comparative dosimetry of dental CBCT devices and 64-slice CT for oral and maxillofacial radiology. *Oral Surg Oral Med Oral Pathol Oral Radiol Endod,* 106(1): 106-114.

MANEA C, MLADINA R (2016) Crista galli sinusitis – a radiological impression or a real clinical entity. *Rom J Rhinol,* 6(23): 167-171.

MARJANOVIC KAVANAGH M, TOKIC T, JAKOVCEVIC A, SMILJANIC R, BUMBER B, PRSTACIC R (2020) Pneumatized crista galli: a histopathologic study. *Otolaryngol Head Neck Surg,* 163(3): 517-521.

METIN-TELLIOGLU A, POLAT Y (2019) The incidence of sinus crista galli in children and adults. A computerized tomography study. *Int J Morphol,* 37: 735-738.

MIN HJ, KIM KS (2016) Frontal headache caused by infection of pneumatized crista galli. *J Craniofac Surg,* 27(4): e352-354.

MLADINA R, ANTUNOVIĆ R, CINGI C, MULUK NB, SKITARELIĆ N, MALIĆ M (2017) An anatomical study of pneumatized crista galli. *Neurosurg Rev,* 40(4): 671-678.

PAPADOPOULOU AM, CHRYSIKOS D, SAMOLIS A, TSAKOTOS G, TROUPIS T (2021) Anatomical variations of the nasal cavities and paranasal sinuses: A systematic review. *Cureus,* 13(1): e12727.

POJE G, MLADINA R, SKITARELIĆ N, MARJANOVIĆ KAVANAGH M (2014) Some radiological and clinical aspects of the sinus crista galli. *Rom J Rhinol,* 4(13): 31-36.

REREDDY SK, JOHNSON DM, WISE SK (2014) Markers of increased aeration in the paranasal sinuses and along the skull base: association between anatomic variants. *Am J Rhinol Allergy,* 28(6): 477-482.

SCARFE WC, FARMAN AG, SUKOVIC P (2006) Clinical applications of cone-beam computed tomography in dental practice. *J Can Dent Assoc,* 72(1): 75-80.

SHIDANSHID M, TAGHI AS, KUCHAI R, SALEH HA (2015) Endoscopic resection of a mucocele of the crista galli. *Ear Nose Throat J,* 94(9): E23-25.

SHPILBERG KA, DANIEL SC, DOSHI AH, LAWSON W, SOM PM (2015) CT of anatomic variants of the paranasal sinuses and nasal cavity: poor correlation with radiologically significant rhinosinusitis but importance in surgical planning. *AJR Am J Roentgenol,* 204(6): 1255-1260.

SOCHER JA, SANTOS PG, CORREA VC, SILVA LC (2013) Endoscopic surgery in the treatment of crista galli pneumatization evolving with localized frontal headaches. *Int Arch Otorhinolaryngol,* 17(3): 246-250.

SOM PM, PARK EE, NAIDICH TP, LAWSON W (2009) Crista galli pneumatization is an extension of the adjacent frontal sinuses. *AJNR Am J Neuroradiol,* 30(1): 31-33.

SOMMER F, HOFFMANN TK, HARTER L, DÖSCHER J, KLEINER S, LINDEMANN J, LEUNIG A (2019) Incidence of anatomical variations according to the International Frontal Sinus Anatomy Classification (IFAC) and their coincidence with radiological sings of opacification. *Eur Arch Otorhinolaryngol,* 276(11): 3139-3146.

TAKAKI Y, TSUTSUMI S, TERAMOTO S, NONAKA S, OKURA H, SUZUKI T, ISHII H (2021) Dural arteriovenous fistula with crista galli erosion in a patient with suspected sinusitis. *Radiol Case Rep,* 16(5): 1028-1031.

TURNA O, AYBAR M, KARAGOZ Y, TUZCU G (2014) Anatomic variations of the paranasal sinus region: evaluation with multidetector CT. *Istanbul Medical J,* 15: 104-109.

UÇAR H, BAHŞI I, ORHAN M, YALÇIN ED (2021) The radiological evaluation of the crista galli and its clinical implications for anterior skull base surgery. *J Craniofac Surg,* 32(5): 1928-1930.

Kaempferol protects the tongue in experimentally induced diabetic rats: a histological and immunohistochemical study

Nermeen M. Faheem[1, 2], Amgad G. Elsaid[1, 2]

[1]Department of Physiotherapy, College of Applied Medical Sciences, Taif University, P.O.Box 11099, Taif 21944, Saudi Arabia.
[2]Department of Anatomy and Embryology, Faculty of Medicine, Ain Shams University, postal code 11566,Cairo, Egypt.

SUMMARY

Uncontrolled diabetes impairs the taste response. Kaempferol is known to possess antioxidant and anti-inflammatory activity and to protect various tissues against diabetes. Here, the potential protective role of kaempferol was investigated against the tongue complications induced by diabetes. Four experimental groups were established (n = 10 each), including control group; kaempferol group, rats received kaempferol orally at dose of 100 mg/kg /day; diabetic group, rats received intraperitoneal STZ (60 mg/kg, single dose) and diabetic with kaempferol group. After eight weeks, all animals were sacrificed, The tongues were dissected and processed for light microscopic examination using haematoxylin and eosin stain, Verhoeff-Van Giesson's stain and immunohistochemical staining for Bcl-2 and PCNA and for SEM examination. Serum blood glucose, TNF-α and IL-6 were measured. Morphometric and statistical analyses were performed. The diabetic with kaempferol group showed preserved histological and morphological structure of filiform and fungiform papillae. Area percentage of collagen fibers was significantly reduced. Immunohistochemical findings revealed significantly increased Bcl-2 surface area and increased PCNA immunopositive cells as compared with the diabetic group. Also, this group revealed significant improvement of the serum levels of blood glucose, TNF-α and IL-6. These findings suggest that kaempferol attenuates histological diabetic-induced changes through its anti-inflammatory and anti-apoptotic effects, and modulates PCNA expression. Therefore, kaempferol can be used as adjuvant therapy in diabetic tongue.

Key words: Diabetes – Kaempferol – Tongue – Bcl-2 – PCNA

INTRODUCTION

The tongue is composed of several tissues, including epithelial, neural, and connective tissues, and also contains taste buds, which are located in the lingual papillae. The function of the taste buds is to detect sweet, bitter, and other chemical stimuli (Mistretta and Kumari, 2017).

It is known that patients with uncontrolled diabetes suffer from taste alterations. This abnormality in the taste sensation of these patients affects their choice of nutrients, leading to more consumption of sweet-tasting foods that aggravate hyperglycemia (De Carli et al., 2018)

Corresponding author:
Nermeen Faheem.
dr.nermeenmf21@yahoo.com

Diabetes mellitus is an irreversible condition. It is a slowly developing but progressive state, and its progression takes several years (Lindstrom et al., 2018). Therefore, the ultimate aim of health care is to try to prevent diabetes or at least delay its development, which is much better than treating the disease after it occurs (Gothai et al., 2016).

Recently, there has been increased interest in the use of medications from natural sources in the management of medical conditions such as diabetes (Gothai et al., 2016). Over the past decade, oxidative stress has been claimed as a leading cause in the development of diabetic complications (Ali and Agha, 2009). Natural antioxidant products have gained much attention for use as medicines and food supplements. Antioxidant compounds have shown high effectiveness due to several pharmacological properties (Taghvaei and Jafari, 2015). Potent antioxidant properties can be obtained from flavonoids, which can suppress the inflammatory cytokines and increase the cell sensitivity to insulin (Rendeiro et al., 2012).

Kaempferol, a naturally occurring flavonoid, is found in tea, tomato, broccoli, grapefruit, nuts and other plant sources (Yoshida et al., 2008). The pharmacological properties of kaempferol include antioxidant, anti-inflammatory, and anticancer activities (Park et al., 2009). Several studies have proven that intake of kaempferol protects various tissues against diabetes such as kidney (Sharma et al., 2019), heart (Chen et al., 2018) and pancreas (Zhang and Liu, 2011). The purpose of this study is to demonstrate the protective role of kaempferol against the tongue complications induced by diabetes.

MATERIAL AND METHODS

Experimental animals

Forty male albino rats (12 weeks old, weighing between 150 and 250 g) were used. The rats were locally bred at the animal house of the Research Center and Bilharzial Research Unit, Faculty of Medicine, Ain Shams University. The rats were treated in accordance with relevant guidelines and regulations approved by the animal Committee of Ain Shams University.

The rats were left two weeks for acclimatization, and all efforts were made to minimize animal suffering. The rats were housed in stainless-steel cages, five rats per cage. The animals were fed on standard laboratory chow and allowed free access to water in an air-conditioned room with a 12-hour-light/12-hour-dark cycle and at a temperature of 25 °C.

Induction of diabetes

After 12 hours of fasting, the animals of model groups received a single 60 mg/kg intraperitoneal injection of Streptozotocin (STZ) dissolved in 0.1mol/L sodium citrate buffer, PH 4.5. The animals were allowed to drink 5% glucose solution to overcome STZ-induced hypoglycemia. After 72 hours, animals with blood glucose levels greater than 200 mg/dL were considered diabetic (Faheem and Askary 2017).

Drug and chemicals: STZ and kaempferol were purchased from Sigma–Aldrich (St. Louis, MO, USA).

Experimental design

The rats were divided into four groups (n=10):

- Control group (given citrate buffer once by intraperitoneal injection).

- Kaempferol group**:** rats received kaempferol dissolved in 5% dimethylsulfoxide orally at a dose of 100 mg/kg body weight/day for eight weeks (Al-Numair et al., 2015).

- Diabetic group: included STZ diabetic rats.

- Diabetic with kaempferol group: it included STZ diabetic rats that received kaempferol immediately after being diagnosed as diabetic at the same dose, route of administration and duration as the kaempferol group.

Sampling Blood

Samples were obtained from the veins of animals' tails under gentle ether anesthesia every two weeks, and then centrifuged for 15 minutes. The separated serum was used for the detection of serum glucose. At the end of the experiment, blood samples were collected and serum tumor necrosis factor (TNF-α)

and IL-6 were measured by ELISA kits (RayBiotech, Inc., GA, USA), according to the manufacturer's instructions. The animals were sacrificed by high dose of ether anesthesia. From each animal, the tongue was removed, and the anterior two-thirds of the tongue were dissected. Then, each specimen was cut longitudinally into two halves. Half of them were fixed in 10% formaldehyde and processed for the preparation of paraffin sections (5-µm). The sections were stained by H&E stain and Verhoeff-Van Giesson's stain (Bancroft and Layton 2013). The other halves of the specimens were washed by phosphate-buffered saline (PBS), and fixed in glutaraldehyde solution. The specimens were processed for examination using a Philips Scanning Electron Microscope (XL30; Philips, Amsterdam, the Netherlands) at the Scanning EM Unit of the Anatomy Department, Faculty of Medicine, Ain Shams University (Duro et al., 2012).

Immunohistochemical study for Bcl-2 and PCNA

Using poly-L-lysine-coated slides, tongue sections were prepared and heated in an oven for twenty five minutes at 60ºC. After heating, sections were deparaffinized in xylene and rehydrated in graded alcohol. Sodium citrate buffer of concentration 10 mM was heated till boiling in a microwave for antigen retrieval. Succinctly, 0.03% hydrogen peroxide sodium azide was used to block the endogenous peroxidase for five minutes followed by washing the tissue sections carefully using wash buffer, and then half of the specimens were incubated with antiapoptotic protein Bcl-2 biotinylated primary antibodies, and the other halves were incubated with anti- PCNA primary antibody for fifteen minutes. Diaminobenzidine substrate chromagen was applied to the sections and incubated for eight minutes, followed by careful wash and hematoxylin counterstaining were applied. Positive cells expressing PCNA were identified by brown nuclei, while Bcl-2 was demonstrated brown cytoplasmic staining (Buchwalow and Bocker, 2010).

Quantitative morphometric study

Five sections were randomly chosen from each group. Ten fields per section were taken from high-power images (400x), and the Image J software program was used to detect:

1. Area percentage occupied by Bcl-2 immunopositive cells.

2. Percentage of PCNA immunopositive cells.

3. Area percentage occupied by collagen fibers using Verhoeff-Van Giesson's stain.

Statistical analysis

The results were represented as mean ± Standard Deviation (±SD). All statistical comparisons between the four studied groups were analyzed via the one-way ANOVA, followed by post hoc test for multiple comparisons. All statistical analyses were performed using SPSS software (SPSS Inc., Chicago, Illinois, USA).

RESULTS

Serum blood glucose, TNF-α and IL-6 levels

The diabetic rats had significantly ($P < 0.05$) elevated serum blood glucose levels as compared with control rats. Meanwhile, the diabetic with kaempferol group had significantly ($P < 0.05$) reduced the glucose levels when compared with the diabetic group (Fig. 1A). Treatment of the diabetic rats with kaempferol significantly decreased ($P < 0.05$) serum TNF-α and IL-6 levels as compared with the diabetic group. However, diabetic rats treated with kaempferol showed significantly higher levels ($P < 0.05$) when compared with control and kaempferol groups (Fig. 1B).

Light microscopic results

Histological examination of tongues of the control group showed the usual tongue architecture. The dorsal surface of the tongue was covered with keratinized stratified squamous epithelium with normal lingual papillae and regularly arranged skeletal muscle fibers (Fig. 2A). No observable differences between the control and kaempferol groups were detected (Fig. 2B). However, the diabetic group showed variable histological changes. The dorsal surface showed thickened keratin layer, attenuated lingual papillae and irregularly arranged muscles with

congested blood vessels in-between (Fig. 2C). On the other hand, the dorsal surface of the diabetic with kaempferol group showed improvement with regular arrangement of the covering epithelium and a thinner keratin layer than the diabetic group. Indeed, the skeletal muscle fibers were regularly arranged (Fig. 2D).

In the control group, filiform papillae were elongated, conical in shape, and had a definitive connective tissue core. Fungiform papillae were localized between filiform ones, showing a broad flat surface, a solitary well defined intraepithelial

taste bud, relatively thinner keratin layer and richly vascular stroma (Fig. 3A). Kaempferol group showed no observable difference from findings presented in the control group (Fig. 3B). However, the diabetic group showed variable histological changes. The dorsal surface showed hyperkeratosis, attenuated papilla with inflammatory cells infiltration and congested blood vessels in the lamina propria**.** Most filiform papillae showed flattening of their tips with reduced connective tissue core. Moreover, fungiform papillae were apparently shorter with a thicker keratin layer than the control group. Furthermore,
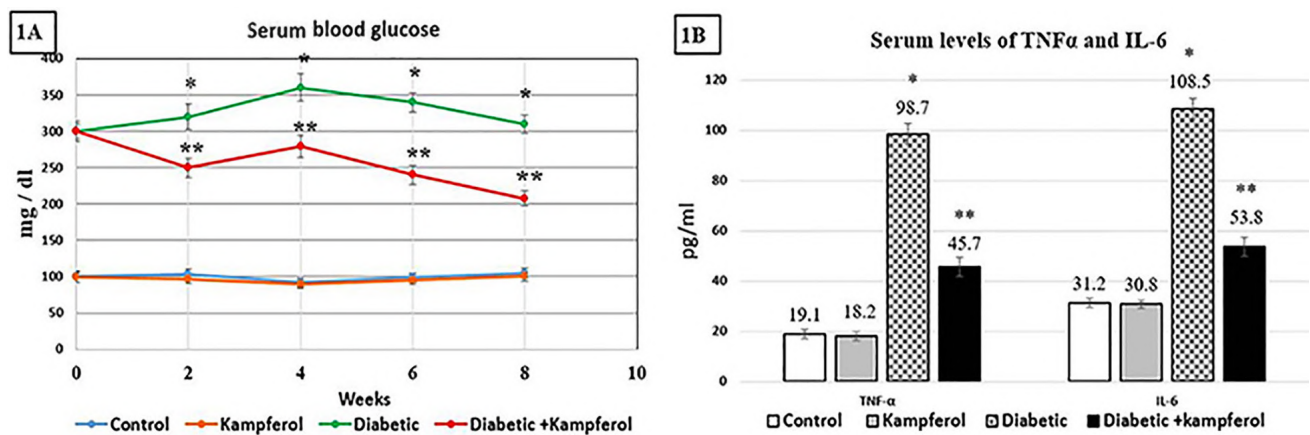
Fig. 1.- A. Means±SD of serum blood glucose levels (mg/dl) at 2nd, 4th, 6th and 8th week. B. Means ± standard deviations of serum TNF-α and serum IL -6 (pg/ml) in the studied groups. P < 0.05 (*) vs other groups, (**) vs control and kaempferol groups.
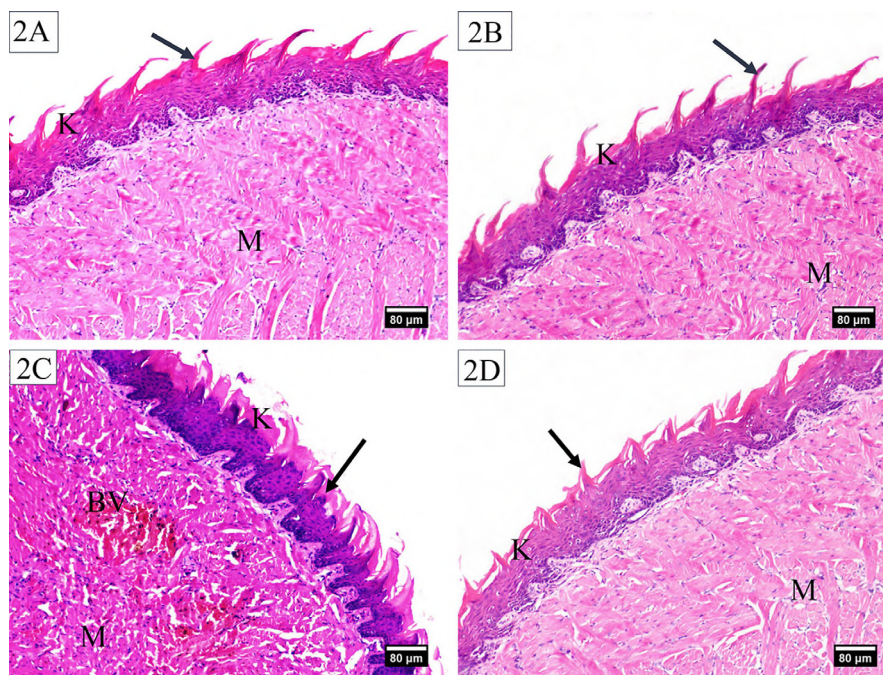

Fig. 2.- Photomicrographs of the dorsal surface of the tongue stained by H&E. A and B. Control and kaempferol groups showing keratinized epithelium (K), lingual papillae (arrow) and regularly arranged skeletal muscle fibers (M). C. Diabetic group showing thickened keratin layer (K), attenuated papillae (arrow), irregularly arranged muscle fibers (M) and congested blood vessels inbetween the muscles (BV). D. Diabetic with kaempferol group showing keratinized epithelium (K), conserved lingual papillae (arrow) and regular arrangement of skeletal muscle fibers (M).

the taste buds of the diabetic group showed variable alterations in the form of a marginal arrangement of the cells with a halo centre (Fig. 3C). In addition, other histological alterations were detected in this group, such as separation of the covering keratin, reduced connective tissue core, shallow epithelial ridges, and variable signs of vacuolar degeneration, pyknotic nuclei, hyperchromatic nuclei and crescent like nuclei in keratinocytes (Fig. 3D). On the other hand, the dorsal surface of the anterior two-thirds of the tongue of the diabetic with kaempferol group, showed prominent lingual papillae with conserved underlying connective tissue. Most filiform papillae of this group showed a preserved thread like shape with pointed ends and thin smooth keratin (Fig. 3E). The fungiform papilla of this group closely resembled those of the control group. Their taste buds appeared barrel-shaped with apparently normal cells (Fig. 3F).

In both control and kaempferol groups, the trench of the circumvallate papillae was generally covered with non-keratinized stratified squamous epithelium with normal taste buds (Fig. 4A, B). However, the trench of the diabetic group was diminished with disrupted epithelial covering.

Many taste buds were vacuolated. Areas of diffuse leucocytic infiltration were detected in the lamina propria (Fig. 4C). Meanwhile, the trench of the circumvallate papillae of the diabetic with kaempferol group were apparently normal and covered with non-keratinized stratified squamous epithelium. Numerous pale, regularly arranged taste buds were observed in its lateral walls. Each taste bud is formed of cluster of pale-staining cells which opens into the surface by means of a taste pore (Fig. 4D).

Van Giesson-stained sections of both control and kaempferol groups showed dense, positively stained collagen fibers in the lamina propria of the ventral surface (Fig. 5A, B), while the ventral surface of the diabetic group showed faint, dispersed collagen fibers in the lamina propria (Fig. 5C). Meanwhile, the diabetic with kaempferol group showed regularly arranged, positively stained collagen fibers (Fig. 4D). Statistical comparison of the collagen fibers area percentage in Van Giesson stained sections revealed that the collagen area percentage of the diabetic with kaempferol group was significantly ($P < 0.05$) increased as compared with the diabetic group (Table 1).
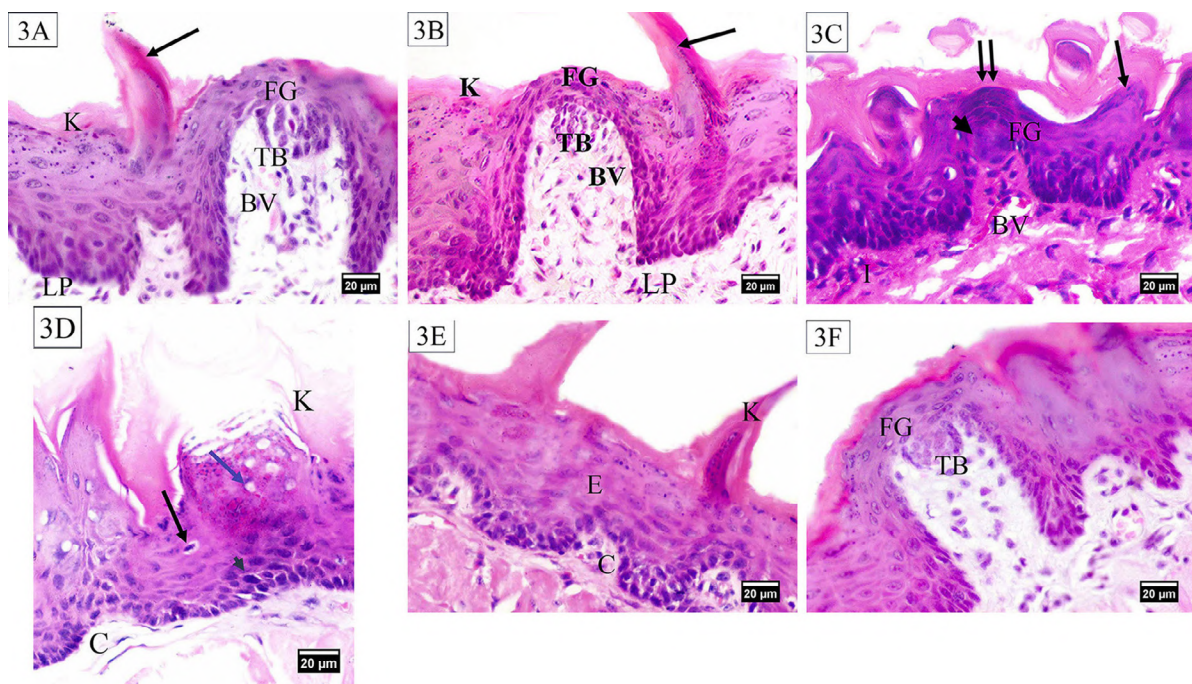
Fig. 3.- Photomicrographs of the dorsal surface of the tongue stained by H&E. A and B. Control and kaempferol groups showing keratinized epithelium (K), conical filiform papilla (arrow), fungiform papilla (FG) with taste bud (TB), lamina propria (LP) and blood vessels (BV). C, D. Diabetic group showing C. Filiform papilla with flattened tips (arrow), fungiform papillae (FG) with thickened keratin layer (double arrows), taste bud with peripheral margination of the cells and empty centre (arrow head), congested blood vessels (BV) and inflammatory cells infiltration (I). D. Vacuolated cytoplasm and pyknotic nuclei (black arrow), crescent-like nuclei (blue arrow), hyperchromatic nuclei (arrow head), separated keratin (K) and reduced connective tissue core (C). E, F. Diabetic with kaempferol group showing: E. Surface epithelium (E), filiform papilla with thin keratin layer (K) and conserved connective tissue papilla (C). F. Fungiform papilla (FG) and its taste bud (TB).

Bcl-2 and PCNA immunostaining results

Immunohistochemical staining for the antiapoptotic marker Bcl-2 showed moderately positive cytoplasmic reaction in the basal and suprabasal layers of the tongue epithelium of the control group (Fig. 6A). Similarly, the kaempferol group disclosed similar results (Fig. 6B). On the other hand, the diabetic group revealed negative to mild cytoplasmic reaction in the tongue epithelium (Fig. 6C). Meanwhile, the diabetic with kaempferol group showed a moderate positive cytoplasmic reaction in the tongue epithelium (Fig. 6D). Statistical analysis revealed significantly increased area percentage of Bcl2 positive cells *(P*
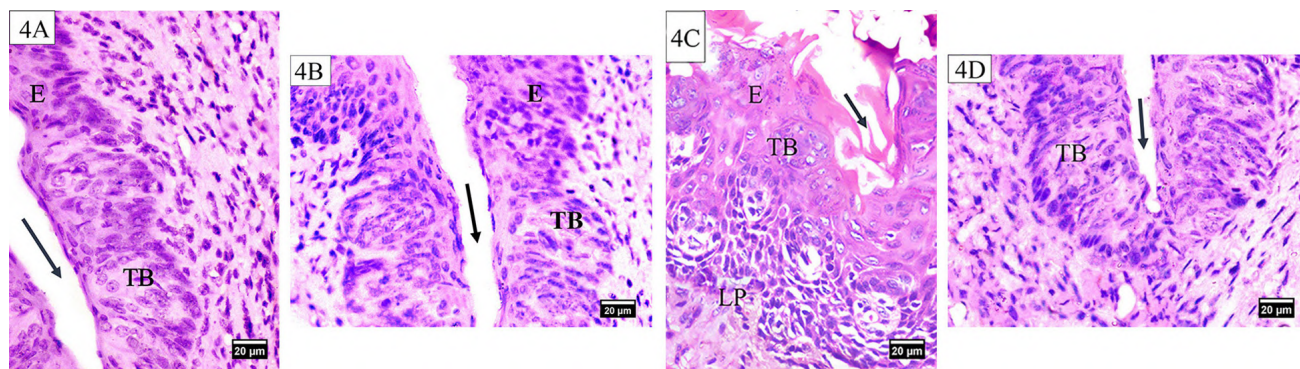
Fig. 4.- Photomicrographs of the dorsal surface of the tongue stained by H&E. A and B. Control and kaempferol groups showing a trench of a circumvallate papillae (arrow) covered with non-keratinized stratified squamous epithelium (E). Note the taste buds (TB) on the trench. C. Diabetic group showing disrupted epithelial covering of circumvallate papilla (E), vacuolated taste bud (TB) and diminished trench of the circumvallate papillae (arrow). Notice diffuse leucocytic infiltration in the lamina propria (LP). D. Diabetic with kaempferol group showing a trench of the circumvallate papillae (arrow) with regularly arranged taste buds (TB).
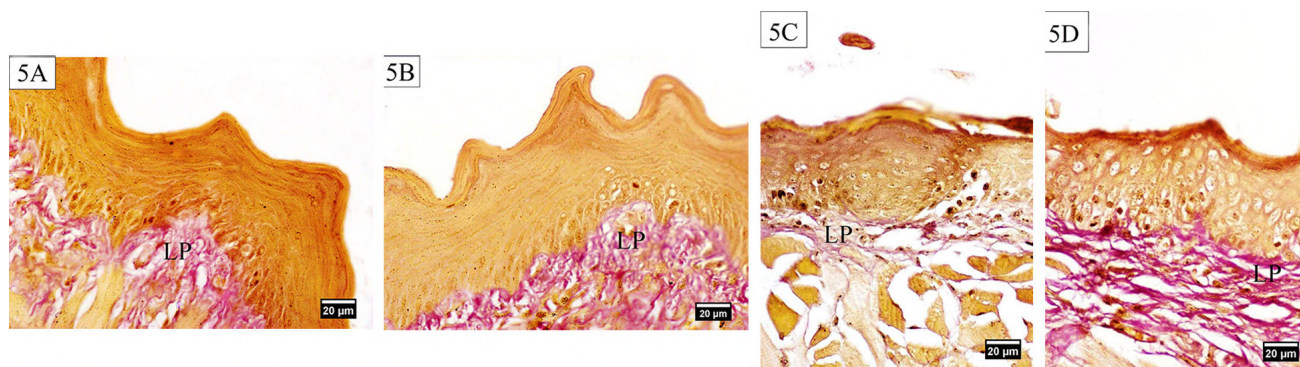
Fig. 5.- Photomicrographs of the ventral surface of the tongue stained by Van Gieson Stain. A and B. Control and kaempferol groups showing dense positively stained collagen fibers into the lamina propria (LP). C. Diabetic group showing faint dispersed collagen fibers into the lamina propria (LP). D. Diabetic with kaempferol group showing dense positively stained collagen fibers into the lamina propria (LP).

Table 1. Comparison between the studied groups regarding the morphometric data

Parameter	Control group	Kaempferol group	Diabetic group	Diabetic with kaempferol group
Mean area percent of collagen fibers	16.04 ± 0.95	15.85 ± 0.89	8.4 [a,b] ± 2	13.1 [a,b,c] ± 1.03
Mean area percent of Bcl2 immunopositive cells	38.6 ± 3.3	38.9 ± 2.6	9.3 [a,b] ± 2.8	28.3 [a,b,c] ± 3.2
percent of PCNA immunopositive cells	85 ± 3.7	83 [a] ± 3.8	32 [a,b] ± 4.5	68 [a,b,c] ± 4.1

Data are expressed as mean ± SD. p > 0.05: no significant difference, p < 0.05: significant difference.
a Significantly different from the control group
b Significantly different from the kaempferol group
c Significant different from the diabetic group

< 0.05) in the diabetic with kaempferol group as compared with the diabetic group (Table 1).

PCNA immunohistochemical staining showed PCNA positive cells in the basal and para-basal cells of the tongue epithelium (Fig. 7A). Indeed, kaempferol group revealed identical findings (Fig. 7B). However, the diabetic group showed few PCNA positive nuclei (Fig. 7C). Furthermore, the diabetic with kaempferol group showed PCNA positive nuclei mainly in the basal cell layer of the tongue epithelium (Fig. 7D). Statistical analysis revealed significantly increased PCNA positive cell percentage *(P < 0.05)* in the diabetic with kaempferol group as compared with diabetic group (Table 1).

Scanning electron microscopic results

The dorsal surface of the tongue of the control group was covered by many filiform papillae. They were elongated, conical and lightly curved papillae with intact pointed tips. Fungiform papillae were seen intermittently between the filiform ones. They were broad and had a

flattened, smooth nearly rounded upper portion with an apparent central taste pore. Scanty rough keratinized cells were seen on fungiform and at the basal part of the surrounding filiform papillae (Fig. 8A). Examination of tongue sections of the kaempferol group showed no observable difference from the results of the control group (Fig. 8B). On the other hand, the tongue papillae of the diabetic group showed a noticeable atrophy. Filiform papillae were short, discrete and disarranged in various directions. The apical parts of some papillae were bifurcated. Meanwhile, other papillae showed detached upper portions. Furthermore, some filiform papillae showed an irregular heavily keratinized base (Fig. 8C). Some fungiform papillae were shorter than the control and had a rough nearly rounded upper portion, with a wrinkled, keratinized epithelial covering. Upper portions with an indistinct taste pore were observed (Fig. 8D). In the diabetic with kaempferol group, the tongue papillae appeared orderly arranged. Filiform papillae revealed a regular distribution and inclination. Most of their
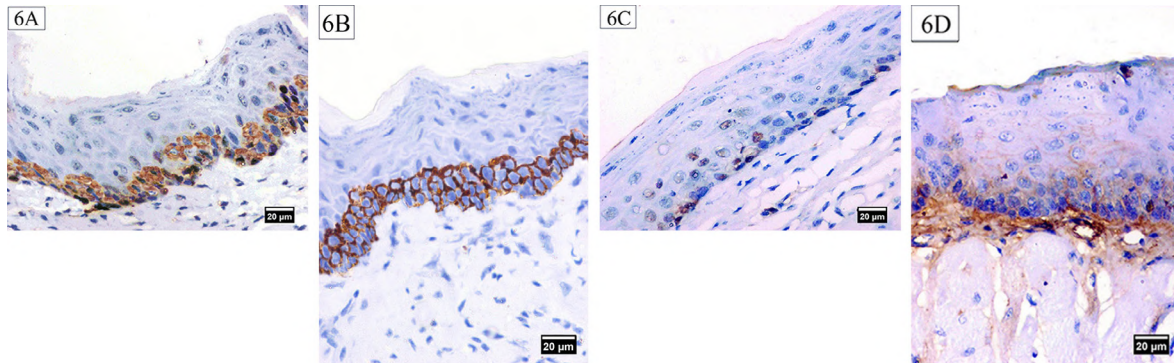
Fig. 6.- Immunohistochemical staining for the Bcl-2 of the ventral surface of the tongue. A and B. Control and kaempferol groups showing moderate positive cytoplasmic reaction in tongue epithelium. C. Diabetic group showing mild cytoplasmic reaction in tongue epithelium. D. Diabetic with kaempferol group showing moderate positive cytoplasmic reaction in tongue epithelium.
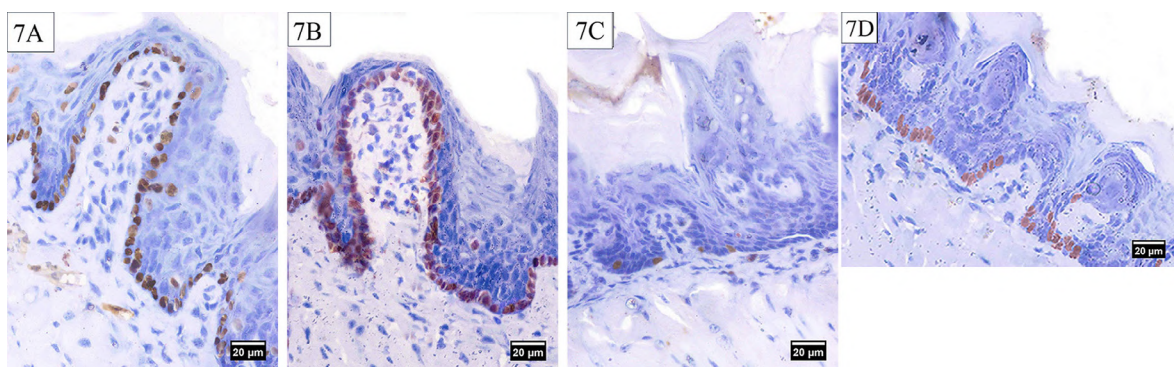
Fig. 7.- Immunohistochemical staining for the PCNA of the dorsal surface of the tongue. A and B. Control and kaempferol groups showing PCNA positive nuclei in the basal cell and para-basal cells of the tongue epithelium. C. Diabetic group showing few PCNA positive nuclei. D. Diabetic with kaempferol group showing PCNA positive nuclei mainly in the basal cell layer of the tongue epithelium.

tips were tapering and directed to one side (Fig. 8E). Fungiform papillae were located in between them with an orderly arranged epithelial covering and a clear organized gustatory pore (Fig. 8F).

DISCUSSION

Flavonoids are antioxidants that are found abundantly in nature in a variety of plants. Among these natural flavonoids, kaempferol is a member of the flavonol subclass widely distributed in many edible plants. Kaempferol has a potent superoxide scavenger activity, antioxidant and anti-inflammatory effects in vitro and in vivo (Du et al., 2018).

In the present study, treatment of the diabetic rats with kaempferol significantly improved the alteration of glucose levels. Al-Numair et al. (2015) concluded that administration of kaempferol to the diabetic rats adjusted plasma glucose and insulin near to normal levels. Consistently, another study showed that oral administration of kaempferol improved glucose homeostasis through reducing hepatic gluconeogenesis and decreasing glycogenolysis in streptozotocin-induced diabetic mice (Alkhalidy et al., 2018).

In the diabetic group of the present study, SEM examination revealed that filiform papillae appeared short, discrete and disarranged in various directions, while fungiform papillae were atrophied with indistinct taste pores. That atrophy of the tongue could be attributed to chronic inflammation which leads to alterations in microvasculature and innervation due to DM. Moreover, the atrophic changes might be related to the decreased cell proliferation (Mohsen et al., 2019), and to the increased apoptosis (Soleymaninejad et al., 2017; Hamza et al., 2018).

In addition, the circumvallate papilla of the diabetic group showed disrupted epithelial covering with diminished trench and many vacuolated taste buds. Pai et al. (2007) contributed the decreased taste buds per circumvallate papilla in the diabetic rats to the significantly reduced taste cells innervation. Taste impairment in diabetes could include a defect of the taste receptors, peripheral neuropathy and microangiopathy (Perros et al., 1996). Kishore et al. (2018) indicated that kaempferol can be considered as a natural antidiabetic agent and can be used as an adjuvant therapy to diabetic neuropathic pain.

Our results showed that treatment of diabetic rats with kaempferol significantly reduced serum proinflammatory cytokines TNFα and IL6 levels as compared with the diabetic group. Hyperglycemia induces the expression
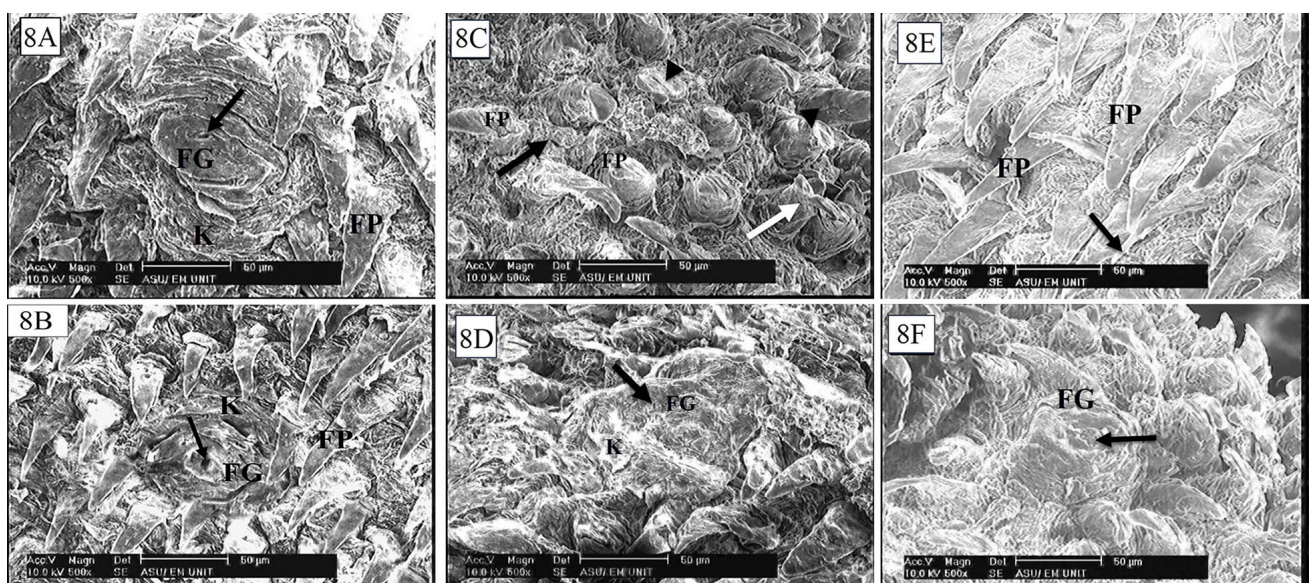
Fig. 8.- Scanning electron micrographs of the the dorsal surface of the tongue. A and B. Control and kaempferol groups showing filiform papillae (FP) and fungiform papilla (FG) with an apparent taste pore (arrow). Notice few rough keratinized cells seen on fungiform (K). C, D. Diabetic group showing C. Irregularly arranged filiform papillae (FP), bifurcated papilla (white arrow) and highly keratinized interpapillary ridges (black arrow). Notice complete loss of the upper portions of some papilla (arrow head). D. Atrophied fungiform papilla (FG) with wrinkled keratin (K) and indistinct taste pore (arrow). (E, F) Diabetic with kaempferol group showing E. Filiform papillae with regular distribution and inclination (FP). Notice the tapering ends of most of papillae (arrow). F. Fungiform papilla (FG) with a well-defined regular gustatory pore (arrow).

of pro-inflammatory cytokines including TNFα and IL-6 which in turn exacerbates oxidative stress (Fuentes-Antrás et al., 2014). Kaempferol reduced hyperglycemia-induced TNF-α and IL-6 expression in heart tissues of STZ-induced diabetic mice. Moreover, kaempferol prevented macrophage infiltration (Chen et al., 2018). Kaempferol significantly preserved oxidant-antioxidant status, attenuating inflammation and apoptosis by inhibiting the mitogen-activated protein kinase (MAPK) pathways, which are responsible for several inflammatory mediators' synthesis such as TNFα and IL-6 and oxidative damage in diabetic rats (Suchal et al., 2017).

In addition, the observed atrophic changes in lingual papillae in our SEM results could be attributed to the observed vacuolar degeneration and nuclear apoptosis. Treatment of diabetic rats with kaempferol ameliorated the vacuolation and nuclear apoptosis in lingual papillae, and this was confirmed by increased Bcl-2 immunopositive cells. These vacuolations were observed in previous studies of diabetes effect on several tissues (Zickri et al., 2012; Faheem and Askary 2017). Sivitz and Yorek (2010) explained these vacuolations on the basis of glucose-induced mitochondrial dysfunction, accumulated reactive oxygen species and oxidative stress. Wu et al. (2020) reported the ability of kaempferol to translocate Bcl-2 to the mitochondria and improve mitochondrial functions as oxidative phosphorylation, ATP production and increasing mitochondrial respiration. Kaempferol treatment improved cell survival, repressed cellular death and improved Bcl-2 expression in pancreatic β-cells with chronic hyperglycemia (Zhang and Liu, 2011).

Suchal et al. (2017), stated that kaempferol inhibited apoptosis by reducing Bax expression and caspase3, decreasing the pro-apoptotic proteins and augmenting the expression of Bcl2. Kaempferol also ameliorated the apoptotic changes of osteoblastic cells as proven by the increased Bcl-2 expression (Adhikary et al., 2018). In contrast, another study suggested that kaempferol induced apoptosis by increasing the Bax/Bcl 2 ratio; this cytotoxic action was more evident in leukemia cells than in normal leukocytes (Moradzadeh et al., 2018).

In the present study, the diabetic rats treated with kaempferol revealed significant improvement of collagen surface area in Van Giesson-stained sections as compared with the diabetic group. Diabetes impedes the integrity of dermal collagen (Argyropoulos et al., 2016). Desta et al. (2010), reported that the number of apoptotic fibroblasts and neutrophils increased while the number of normal fibroblasts and the connective tissue volume decreased in diabetic gingival connective tissue. Dag et al. (2014) explained collagen changes on the basis of hyperglycemia which reduced fibroblast proliferation and altered collagen. Ozay et al. (2019) concluded that kaempferol regulated collagen formation and collagen fibrils by elevating the hydroxyproline levels.

In the current study, the statistical results of the diabetic group revealed significant reduction in the mean number of PCNA positive cells indicating reduced epithelial cell proliferation. Similar findings were observed by Mohsen et al. (2019). Kaempferol treatment significantly enhanced the cell viability, elevated the protein levels of PCNA and Cyclin D1, which are the key cell proliferation marker molecules (Nagy et al., 2019).

CONCLUSION

The results of the current work suggest that kaempferol prevented the histological and morphological diabetic induced tongue alterations. Moreover, kaempferol modulates inflammatory promarkers TNF-α, IL-6 and positively affects the antiapoptotic marker (Bcl-2) and the cell proliferation PCNA marker. Thus, our results showed that kaempferol can be used as an adjuvant natural therapy for tongue complications induced by diabetes.

REFERENCES

ADHIKARY S, CHOUDHARY D, AHMAD N, KARVANDE A, KUMAR A, BANALA VT, MISHRA PR, TRIVEDI R (2018) Dietary flavonoid kaempferol inhibits glucocorticoid-induced bone loss by promoting osteoblast survival. *Nutrition*, 53: 64-76.

ALI MM, AGHA FG (2009) Amelioration of streptozotocin-induced diabetes mellitus, oxidative stress and dyslipidemia in rats by tomato extract lycopene. *Scand J Clin Lab Invest*, 69(3): 371-379.

ALKHALIDY H, MOORE W, WANG Y, LUO J, MCMILLAN RP, ZHEN W, ZHOU K, LIU D (2018) The flavonoid kaempferol ameliorates streptozotocin-induced diabetes by suppressing hepatic glucose production. *Molecules*, 23(9): 2338.

AL-NUMAIR KS, CHANDRAMOHAN G, VEERAMANI C, ALSAIF MA (2015) Ameliorative effect of kaempferol, a flavonoid, on oxidative stress in streptozotocin-induced diabetic rats. *Redox Rep,* 20(5): 198-209.

ARGYROPOULOS AJ, ROBICHAUD P, BALIMUNKWE RM, FISHER GJ, HAMMERBERG C, YAN Y, QUAN T (2016) Alterations of dermal connective tissue collagen in diabetes: molecular basis of aged-appearing skin. *PLoS One,* 11(4): e0153806.

BANCROFT JD, LAYTON C (2013) The hematoxylin and eosin, connective mesenchymal tissues with their stains. In: Suvarna SK, Layton C, Bancroft JD (editors). *Bancroft's Theory and practice of histological techniques.* 7th edition. Churchill Livingstone: Philadelphia, pp 173-212.

BUCHWALOW IB, BÖCKER W (2010) Immunohistochemistry: basics and methods. Heidelberg: Springer, pp 31-39.

CHEN X, QIAN J, WANG L, LI J, ZHAO Y, HAN J, KHAN Z, CHEN X, WANG J, LIANG G (2018) Kaempferol attenuates hyperglycemia-induced cardiac injuries by inhibiting inflammatory responses and oxidative stress. *Endocrine,* 60(1): 83-94.

DAG A, TULES FIRAT E, UYSAL E, KETANI S, AYDIN KETANI M (2014) Histological investigation of the impact of streptozotocin-induced experimental diabetes on the healthy gingivae of rats. *Biotechnol Biotechnol Equip,* 28(4): 710-715.

DE CARLI L, GAMBINO R, LUBRANO C, ROSATO R, BONGIOVANNI D, LANFRANCO F, BROGLIO F, GHIGO E, BO S (2018) Impaired taste sensation in type 2 diabetic patients without chronic complications: a case-control study. *J Endocrinol Invest,* 41(7): 765-772.

DESTA T, LI J, CHINO T, GRAVES DT (2010) Altered fibroblast proliferation and apoptosis in diabetic gingival wounds. *J Dent Res,* 89(6): 609-614.

DU W, AN Y, HE X, ZHANG D, HE W (2018) Protection of kaempferol on oxidative stress-induced retinal pigment epithelial cell damage. *Oxid Med Cell Longev,* 2018: 1610751.

DURO CC, CIENA AP, DE ALMEIDA SR, RIGHETTI MM, GRISOLIA DDE F, ISSA JP, DA SILVA MC, WATANABE IS (2012) Qualitative study of young, adult, and aged Wistar rats temporomandibular synovial membrane employing light, scanning, and transmission electron microscopy. *Microsc Res Tech,* 75(11): 1522-1527.

FAHEEM NM, EL ASKARY A (2017) Neuroprotective role of curcumin on the hippocampus against the structural and serological alterations of streptozotocin-induced diabetes in Sprague-Dawely rats. *Iran J Basic Med Sci,* 20(6): 690-699.

FUENTES-ANTRÁS J, IOAN AM, TUÑÓN J, EGIDO J, LORENZO O (2014) Activation of toll-like receptors and inflammasome complexes in the diabetic cardiomyopathy-associated inflammation. *Int J Endocrinol,* 2014: 847827.

GOTHAI S, GANESAN P, PARK SY, FAKURAZI S, CHOI DK, ARULSELVAN P (2016) Natural phyto-bioactive compounds for the treatment of type 2 diabetes: inflammation as a target. *Nutrients,* 8(8): 461.

HAMZA AA, FIKRY EM, ABDALLAH W, AMIN A (2018) Mechanistic insights into the augmented effect of bone marrow mesenchymal stem cells and thiazolidinediones in streptozotocin-nicotinamide induced diabetic rats. *Sci Rep,* 8(1): 9827.

KISHORE L, KAUR N, SINGH R (2018) Effect of kaempferol isolated from seeds of Eruca sativa on changes of pain sensitivity in streptozotocin-induced diabetic neuropathy. *Inflammopharmacology,* 26(4): 993-1003.

LINDSTROM J, PELTONEN M, ERIKSSON JG, ILANNE-PARIKKA P, AUNOLA S, KEINANEN-KIUKAANNIEMI S, UUSITUPA M, TUOMILEHTO J (2013) Improved lifestyle and decreased diabetes risk over 13 years: long-term follow-up of the randomised Finnish Diabetes Prevention Study (DPS). *Diabetologia,* 56(2): 284-293.

MISTRETTA CM, KUMARI A (2017) Tongue and taste organ biology and function: homeostasis maintained by hedgehog signaling. *Annu Rev Physiol,* 79: 335-356.

MOHSEN ROM, HALAWA AM, HASSAN R (2019) Role of bone marrow-derived stem cells versus insulin on filiform and fungiform papillae of diabetic albino rats (light, fluorescent and scanning electron microscopic study). *Acta Histochem,* 121(7): 812-822.

MORADZADEH M, TABARRAEI A, SADEGHNIA HR, GHORBANI A, MOHAMADKHANI A, ERFANIAN S, SAHEBKAR A (2018) Kaempferol increases apoptosis in human acute promyelocytic leukemia cells and inhibits multidrug resistance genes. *J Cell Biochem,* 119(2): 2288-2297.

NAGY T, FISI V, FRANK D, KÁTAI E, NAGY Z, MISETA A (2019) Hyperglycemia-induced aberrant cell proliferation; a metabolic challenge mediated by protein O-GlcNAc modification. *Cells,* 8(9): 999.

OZAY Y, GUZEL S, YUMRUTAŞ O, PEHLIVANOĞLU B, ERDOGDU İH, YILDIRIM Z, TURK BA, DARCAN S (2019) Wound healing effect of kaempferol in diabetic and nondiabetic rats. *J Surg Res,* 233: 284-296.

PAI MH, KO TL, CHOU HC (2007) Effects of streptozotocin-induced diabetes on taste buds in rat vallate papillae. *Acta Histochem,* 109: 200-207.

PARK MJ, LEE EK, HEO HS, KIM MS, SUNG B, KIM MK, LEE J, KIM ND, ANTON S, CHOI JS, YU BP, CHUNG HY (2009) The anti-inflammatory effect of kaempferol in aged kidney tissues: the involvement of nuclear factor-kappaB via nuclear factor-inducing kinase/IkappaB kinase and mitogen-activated protein kinase pathways. *J Med Food,* 12(2): 351-358.

PERROS P, MACFARLANE TW, COUNSELL C, FRIER BM (1996) Altered taste sensation in newly-diagnosed NIDDM. *Diabetes Care,* 19(7): 768-770.

RENDEIRO C, GUERREIRO JD, WILLIAMS CM, SPENCER JP (2012) Flavonoids as modulators of memory and learning: molecular interactions resulting in behavioural effects. *Proc Nutr Soc,* 71(2): 246-262.

SHARMA D, GONDALIYA P, TIWARI V, KALIA K (2019) Kaempferol attenuates diabetic nephropathy by inhibiting RhoA/Rho-kinase mediated inflammatory signalling. *Biomed Pharmacother,* 109: 1610-1619.

SIVITZ WI, YOREK MA (2010) Mitochondrial dysfunction in diabetes: from molecular mechanisms to functional significance and therapeutic opportunities. *Antioxid Redox Signal,* 12(4): 537-577.

SOLEYMANINEJAD M, JOURSARAEI SG, FEIZI F, ANARKOOLI IJ (2017) The effects of lycopene and insulin on histological changes and the expression level of Bcl-2 family genes in the hippocampus of streptozotocin-induced diabetic rats. *J Diabetes Res,* 2017: 4650939.

SUCHAL K, MALIK S, KHAN SI, MALHOTRA RK, GOYAL SN, BHATIA J, OJHA S, ARYA DS (2017) Molecular pathways involved in the amelioration of myocardial injury in diabetic rats by kaempferol. *Int J Mol Sci,* 18(5): 1001.

TAGHVAEI M, JAFARI SM (2015) Application and stability of natural antioxidants in edible oils in order to substitute synthetic additives. *J Food Sci Technol,* 52(3): 1272-1282.

WU W, YANG B, QIAO Y, ZHOU Q, HE H, HE M (2020) Kaempferol protects mitochondria and alleviates damages against endotheliotoxicity induced by doxorubicin. *Biomed Pharmacother,* 126: 110040.

YOSHIDA T, KONISHI M, HORINAKA M, ASUDA T, GODA AE, TANIGUCHI H, YANO K, WAKADA M, SAKAI T (2008) Kaempferol sensitizes colon cancer cells to TRAIL-induced apoptosis. *Biochem Biophys Res Commun,* 375(1): 129-133.

ZHANG Y, LIU D (2011) Flavonol kaempferol improves chronic hyperglycemia-impaired pancreatic beta-cell viability and insulin secretory function. *Eur J Pharmacol,* 670(1): 325-332.

ZICKRI MB, AHMAD NA, MAADAWI ZM, MOHAMADY YK, METWALLY HG (2012) Effect of stem cell therapy on induced diabetic keratopathy in albino rat. *Int J Stem Cells,* 5(1): 57-64.

Anatomical study of the anterolateral perforators of the thigh and its clinical applications

Habiba A.T.M. El-Shennawy¹, Elsayed S. Atta-Allah², Ehab M. Elzawawy³, Sally M.M.H. Omar⁴

¹*Assistant lecturer, Department of Anatomy and Embryology, Faculty of Medicine, Alexandria University, Alexandria, Egypt*

² *Professor, Department of Anatomy and Embryology, Faculty of Medicine, Alexandria University, Alexandria, Egypt*

³ *Professor, Department of Anatomy and Embryology, Faculty of Medicine, University of Alexandria and National University of Science and Technology,Oman. Alexandria, Egypt*

⁴ *Lecturer, Department of Anatomy and Embryology, Faculty of Medicine, Alexandria University, Alexandria, Egypt*

SUMMARY

Anterior thigh skin continued over the years to provide advantageous donor sites for reconstructing defects all over the body. Reconstructive surgery has undergone unceasing alterations and modifications with the sole purpose of securing the best aesthetic and functional outputs. Of these alterations, a landmark shift was brought about by the concept of axiality, which stated that flaps should be categorized according to their vasculature. From there on, more attention was directed to understanding the precise arterial supply of the skin. This article aims to study the cutaneous perforators of the anterolateral thigh and explains their significance in flap design.

The material of the present study included thirty fresh cadaveric lower limbs. The external iliac artery (EIA) was injected with colored latex. Superficial, then deep, dissections were undertaken under a magnifying lens to locate the perforators and identify their type according to Cormack's and Lamberty's tripartite system: direct, fasciocutaneous and musculocutaneous perforators.

The length and diameter of the perforators were measured.

Anterolateral thigh skin was divided into 3 squares. Square 1 is the upper square and comprises the skin over tensor fascia lata (TFL). It is primarily based on the lateral circumflex femoral artery (LCFA), mainly its transverse branch (TB). It divided into three muscular arteries to TFL upon entry of the muscle; upper, middle and lower, and they provided a musculocutaneous perforator in 100%, 60% and 40%, respectively. Squares 2 (middle) and square 3 (lower) are those infamously called the anterolateral thigh flap (ALTF). They are the rest of the anterolateral thigh skin below the TFL and down to the knee. They are mainly based on the descending branch (DB) of the LCFA. It gave two fasciocutaneous perforators at its beginning and termination in all cases; the highest one was for square 2 and the lowest for square 3. The anterolateral thigh skin is richly supplied by a mixture of the three types of perforators. The segmental nature of the perforators arising from the (DB) of the LCFA, together with the superbly long

Corresponding author:
Dr. Sally Mahmoud Mohamed Hussein Omar, Department of Anatomy and Embryology, Faculty of Medicine, Alexandria University, Alexandria, Egypt, E Mail: omarsasa@ymail.com

course of the artery itself, grants the famous ALTF its versatility.

Key words: Anterolateral thigh – Perforators – Flap

INTRODUCTION

Throughout the years, the lower limb in general and the thigh specifically remained the largest and preferred donor site in the human body for flap harvest (Landuyt, 2006). This is due to the rich vascularity, ease of access, ability to obtain large surface areas for tissue coverage, versatility in the flap design and the hidden postoperative donor site scar (Chan et al., 2014; Morris and Taylor, 2013; Geddes et al., 2013).

The development of regional and free flaps has been, and continues to be, the most exciting and essential of the advances in plastic surgery. The ability to guarantee survival of the transferred tissue continued to pose a challenge, and it is not until the early nineteenth century that another milestone was reached when researchers came to understand that the anticipated survival of a flap depended primarily on its vascularization (Morris et al., 2010; Cormack and Lamberty, 1994).

However, the dilemma of good flap survival with minimal thickness persisted to provoke anatomists and surgeons to search for methods to secure the vitality of thin flaps. This was made possible with the emergence of perforator flaps between the 1980s and 1990s (Park et al., 2018).

It is for these reasons that sound knowledge of the vascular anatomy of the human skin provides the framework for successful flap elevation. Therefore, it is essential for the reconstructive surgeon to have a proper understanding of the vascular anatomy of the integument.

In perforator-based flaps, the impetus of vascular knowledge has shifted from the source artery to the perforator itself. By definition, a perforator is any vessel that pierces the upper layer of the deep fascia to supply the overlying subcutaneous tissue and the skin (Chan et al., 2014; Cormack and Lamberty, 1994; Mathes and Nahai, 1997).

Cormack and Lamberty's tripartite system proved to be the simplest yet most practical for classification of perforators (Timmons, 1985).

They categorized them according to the path taken from the parent vessels into three main types: direct cutaneous perforators, fasciocutaneous perforators and musculocutaneous perforators. In essence, a single perforator can be a mixture of two types (Cormack and Lamberty, 1994).

MATERIAL AND METHODS

The study was conducted on 30 fresh cadaveric lower limbs obtained from the department of Human Anatomy and Embryology, Alexandria Faculty of Medicine. Injection material comprised ammonium solution 25% concentration, tap water, liquid rubber as a solidifying matter and a red liquid dye. The material was intravascularly injected through catheters of different sizes. For magnification: an overhead times three magnifier was used with a built-in LED light source. Measuring instruments included a digital Vernier Caliper and a flexible measuring tape.

A high inguinal incision was made above and parallel to the intermediate third of the line extending from the anterior superior iliac spine (ASIS) to the pubic tubercle (PT). Careful dissection was then undertaken through the layers of the abdominal wall until visualization of the EIA.

Once identified, catheterization of the artery was done followed by flushing with ammonium solution to dissolve any possible thrombi. Afterwards, a mixture of Latex, water and a red dye was injected with an average of 30-50 ml of the mixture and the cadaver was allowed to cool down to 4°C for one week to solidify the latex before dissection. The previously cut inguinal incision was then extended medially and then downwards from the PT along the whole length of the medial thigh till the medial tibial condyle (MTC). The direction of skin elevation was from medial to lateral till the posterior (lateral) edge of the Vastus Lateralis (VL).

The anterolateral thigh territory was divided into three squares according to four cardinal lines. The first line extending between ASIS to the lateral patellar margin, and the second line corresponds to the lateral margin of the thigh which is presented by a line tangential to the greater trochanter extending to the lateral tibial condyle (LTC). This column was subdivided to three regions; upper

(square 1), middle (square 2) and lower (square 3), according to two horizontal planes. One at the level of apex of the femoral triangle and the other midway between the first horizontal line and the knee joint line. This produced a total of three squares, and each will be regarded as a separate entity with its own perforators. The type and origin were then determined, and the following measures were taken using the digital caliper and flexible tape: diameter, length, underrunning distance and site. The three fundamental types were: Type 1, Direct cutaneous; Type 2, Fasciocutaneous, and Type 3, Musculotcutaneous. This also warrants that there may be a combined type.

RESULTS

Square 1:

This area comprised the skin over TFL. It is relatively rich in vascularity, and was mainly supplied by the superficial circumflex iliac perforator. A total of 7 perforators were observed as follows:

- The superficial circumflex iliac perforator in 30 limbs (100%).
- One lateral fasciocutaneous perforator from the ascending branch (AB) of LCFA in 6 limbs (20%).
- Three musculocutaneous perforators from the TB of LCFA: the first in 30 limbs (100%), the second in 20 limbs (66.6%), and the last in 12 limbs (40%).
- Two fasciocutaneous perforators from the DB of the LCFA: one from the oblique branch (OB) in 8 limbs (26.6%) and another from the main stem of DB in all limbs.

The AB of the LCFA arose at an average distance of 12.25±0.7 cm inferomedial to the ASIS. It came off undercover of Sartorius (S) then ascended upwards towards the ASIS superficial to the iliopsoas (IP) and upper part of rectus femoris (RF). It finally appeared after passing between S and TFL at a mean distance of 4.2±0.5 cm below the ASIS. Its mean caliber was 2±0.1 mm and total running distance was 11±0.8 cm (Fig. 1).
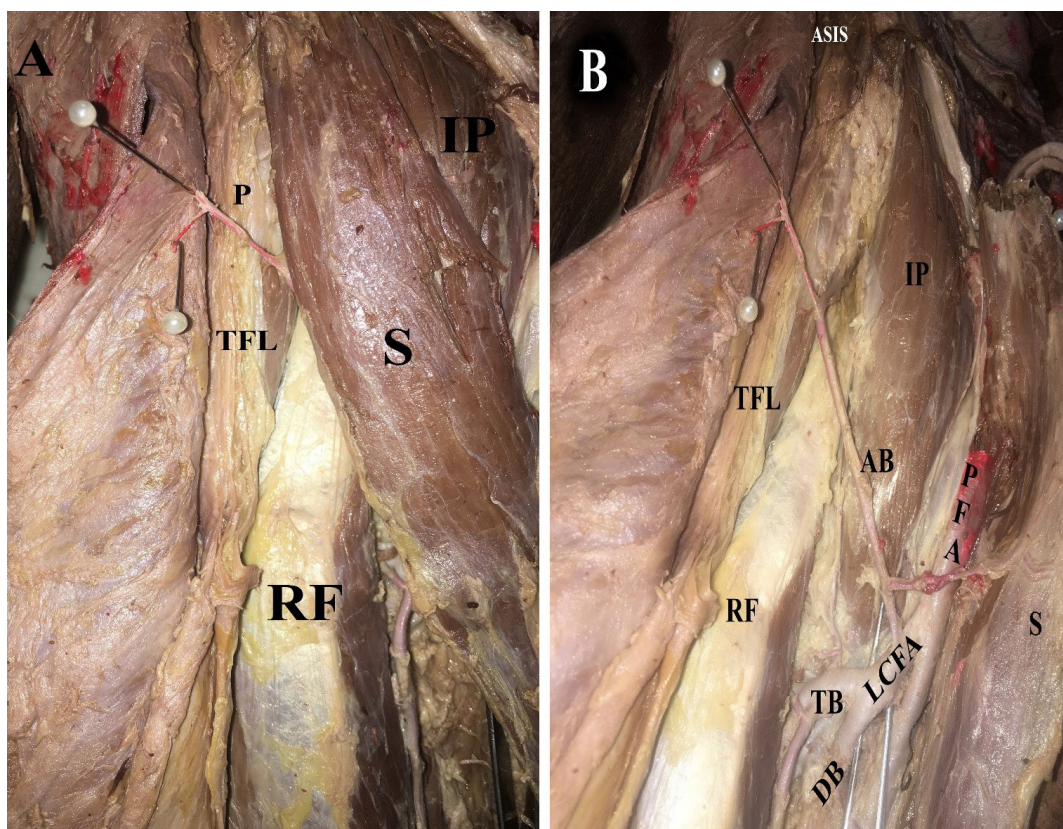
Fig. 1.- A: a photograph of the uppermost lateral skin of right thigh showing a fasciocutaneous perforator (P) emerging between sartorius (S) and tensor fasciae latae (TFL)., **B:** after medial reflection of S, this perforator is the termination of the ascending branch (AB) of the lateral circumflex femoral artery (LCFA). It is noticed that the AB came off the profunda femoris artery (PFA) under S and continued to run over the iliopsoas (IP) and upper rectus femoris (RF) to finally emerge between S and TFL supplying an area of skin (Sk) just below the anterior superior iliac spine (ASIS). TB: transverse branch, DB: Descending branch.

The TB of LCFA arose deep to the S and the RF to enter the substance of TFL. Upon its entrance, it divided into three branches: upper, middle and lower. The three branches gave corresponding musculocutaneous perforators, yet with different percentages (Fig. 2). The musculotcutaneous perforator of the upper division was constant in all limbs, the second branch gave its perforator in 20 limbs (66.6 %), and lastly the third was the least (40%). The site of the three musculocutaneous perforators were 8.8±0.2 cm, 10.16±0.2 cm, and 11±0.5 cm below the ASIS respectively. The largest and the longest was the first with a mean caliber of 0.7±0.2 mm and length of 3.5±0.7 cm, followed by the second, whose diameter was 0.47±0.09 mm and length was 0.48±0.1 cm and lastly the third with a caliber of 0.46±0.1 mm and length of 0.39±0.1 cm.

The DB of LCFA in this square gave two fasciocutaneous perforators one from the main stem and another from its OB. The DB of LCFA took origin from the LCFA deep to the S and RF, then continued inferolaterally to reach the anterior border of the VL, where it gave in all limbs a fasciocutaneous perforator, which emerged between the RF and VL at a mean distance of 18.1±1 cm inferomedial to the ASIS. This perforator also continued downwards for a mean distance of 3±1 cm to supply square 2. Its mean diameter was 1.2±0.1 mm, and mean total length was 8.5±0.2 cm. Additionally, in 8 limbs (26.6 %), the DB of LCFA gave OB before it reached the anterior border of VL, in which case this OB also gave a fasciocutaneous perforator that emerged between RF and VL. It appeared at a mean distance of 15±0.5 cm below and medial to the ASIS. Its mean diameter was 1.2±0.2 mm, and its length was 4.8±0.4 cm. The DB of LCFA then continued downwards sandwiched between VL and vastus intermedius (VI). The two perforators are shown in Fig. 3.
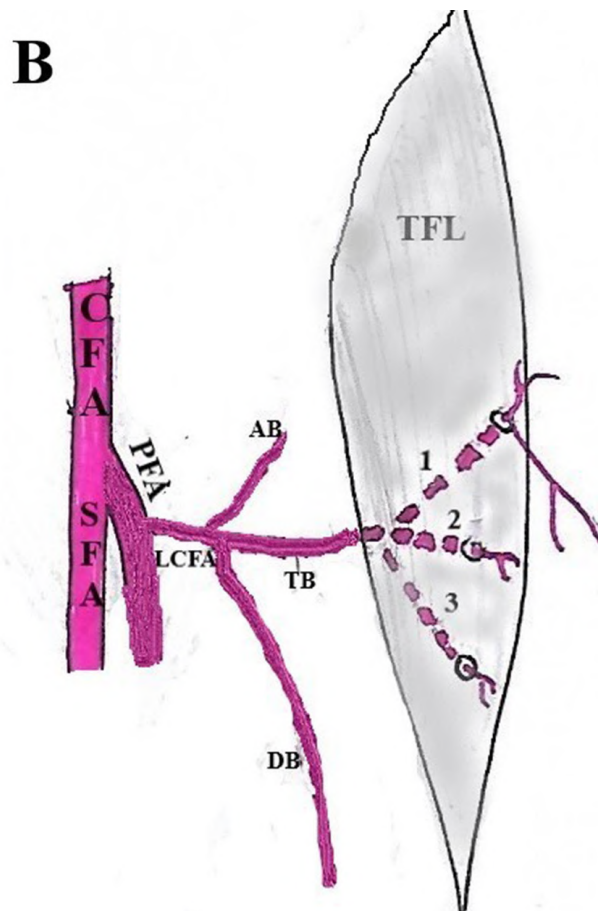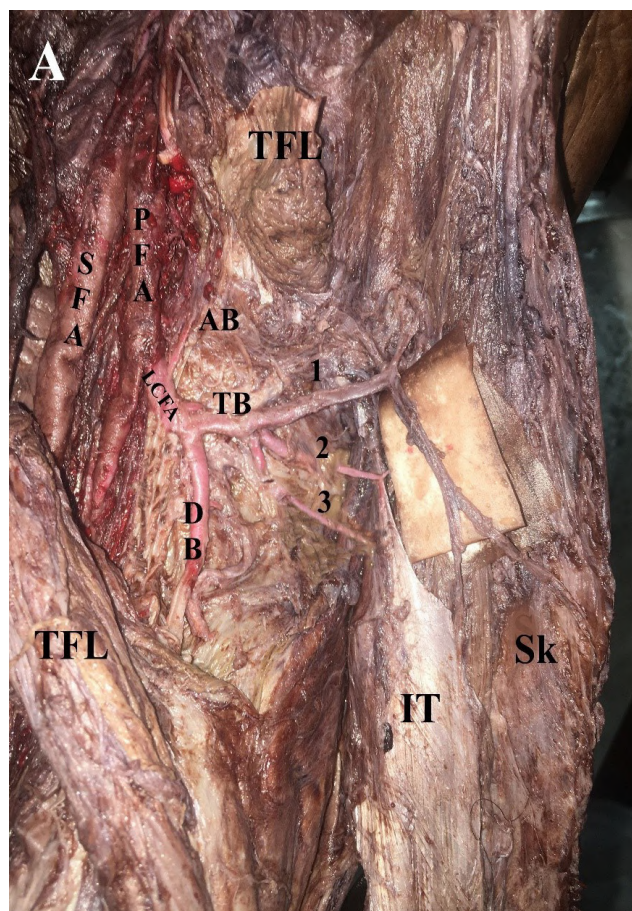
Fig. 2.- A: a photograph of the upper lateral area of left thigh showing the tensor fasciae latae (TFL) divided to reveal inside it the pattern of division of the transverse branch (TB) of the lateral circumflex femoral artery (LCFA). The TB ramified to three branches; upper 1, middle 2, and lower 3, each giving respective musculocutaneous perforators. It is noticed that the sizes of the perforators decreased from the first to the third branch., **B:** is a diagrammatic illustration. CFA: Common femoral artery, SFA: superficial femoral artery, PFA: profunda femoris artery, IT: iliotibial tract, Sk: Skin, AB: ascending branch, DB: descending branch.

The mean length (cm), mean diameter (mm) and distance from ASIS (cm) of all identified perforators in square 1 are shown in Table 1.

Square 2:

This is the area over the middle bulkiest portion of the VL. This area displayed the highest percentage of type 2 and 3 perforators. All perforators came from the DB of LCFA, except one fasciocutaneous perforator from the profunda femoris artery (PFA) as follows:

• One fasciocutaneous perforator from the DB of LCFA, which was shared with the above square in 30 limbs (100%).

• Four musculocutaneous VL perforators from the DB of LCFA, three of which were present in all limbs 100% and one in 25 limbs (83.3 %).

The DB of LCFA took origin 13.3±0.4 cm inferomedial to the ASIS. It ran for about 1-2 cm, then gave an OB during its course towards the VL in 8 limbs. Upon its arrival at the anterior border of VL, it constantly provided a fasciocutaneous perforator (Fig. 3). Afterwards, it continued downwards between the VL and VI, where it gave off four musculocutaneous perforators. Three of these were present in all limbs and one was found in 25 limbs. From above downwards, they were located at distances 22.15±0.4, 25.3±0.7,
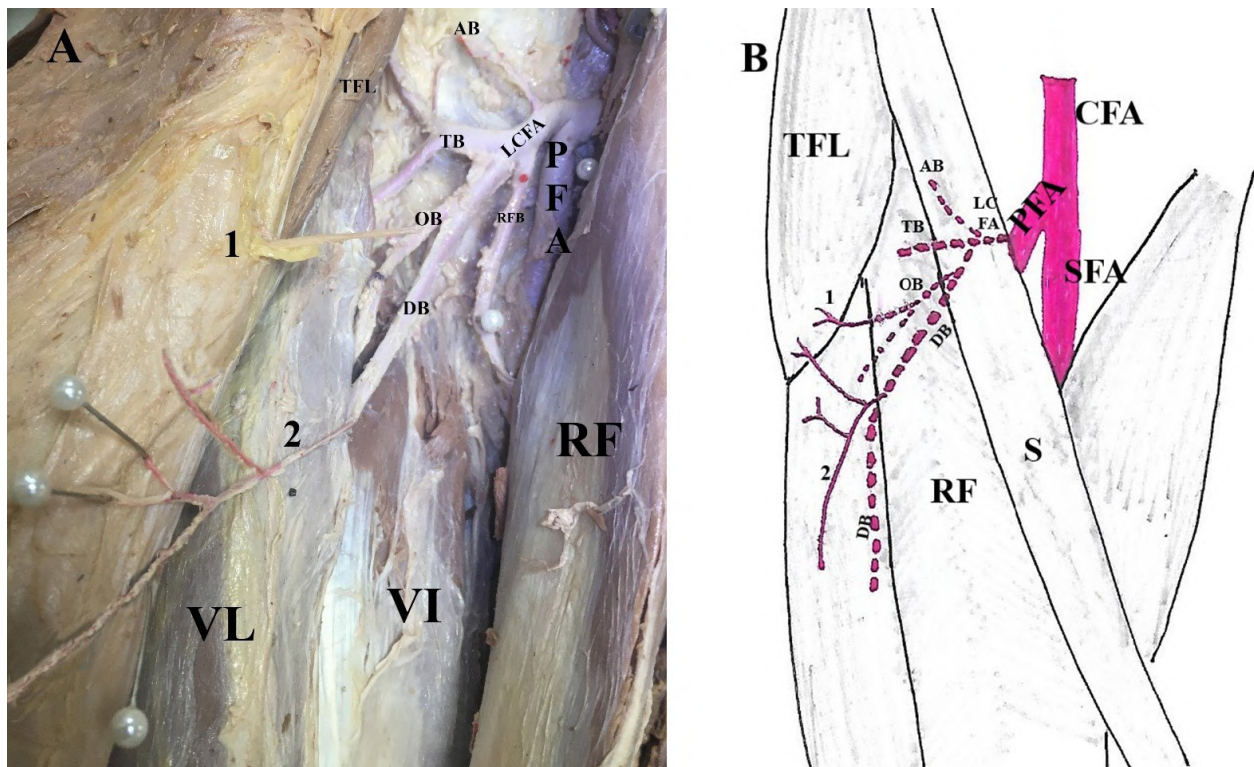
Fig. 3.- A: a photograph of the upper lateral part of right thigh showing two fasciocutaneous perforators (1 and 2) emerging between the rectus femoris (RF) which is reflected medially and vastus lateralis (VL). The first originated from the oblique branch (OB) of lateral circumflex femoral artery (LCFA) and the second from the descending branch (DB) at the anterior border of VL. The DB then disappeared between VL and vastus intermedius (VI). These two perforators supply the lower part of the skin (Sk) over the tensor fasciae latae (TFL) and the second continued to some distance downwards to reach the square below, **B:** is a diagrammatic illustration with the RF in place. CFA: common femoral artery, SFA: superficial femoral artery, PFA: profunda femoris artery, AB: Ascending branch, TB: Transverse branch, RFB: Rectus femoris branch.

Table 1. The mean length (cm), mean diameter (mm) and distance from ASIS (cm) of all identified perforators in square 1

Origin of perforator	AB of the LCFA	TB of LCFA			DB of LCFA	
		First	second	third	From main stem	From OB
Mean length (cm)	11±0.8	3.5±0.7	0.48±0.1	0.39±0.1	8.5±0.2	4.8±0.4
Mean diameter (mm)	2±0.1	0.7±0.2	0.47±0.09	0.46±0.1	1.2±0.1	1.2±0.2
Distance from ASIS	4.2±0.5	8.8±0.2	10.16±0.2	11±0.5	18.1±1	15±0.5

26.9±2.3, and 27.5±0.6 cm distal to the ASIS. The size of these perforators gradually decreased as we go downwards; their mean calibers were 0.69±0.2, 0.54±0.1, 0.54±0.06, 0.5±0.1 mm and mean lengths were 2.4±0.2, 1.69±0.1, 1.38±0.2, 0.6±0.1 cm respectively (Fig. 4). The mean length (cm), mean diameter (mm) and distance from ASIS (cm) of all identified perforators in square 2 are shown in Table 2.

Square 3:

This is the area over the lowest part of the VL. It received the termination of the DB of LCFA in addition to superolateral genicular artery (SLGA) from the popliteal artery (PA). A total of 4 perforators were found as follows:

- Two musculocutaneous from the DB of LCFA; one in 30 limbs (100%) and the other in 20 limbs (66.6%).
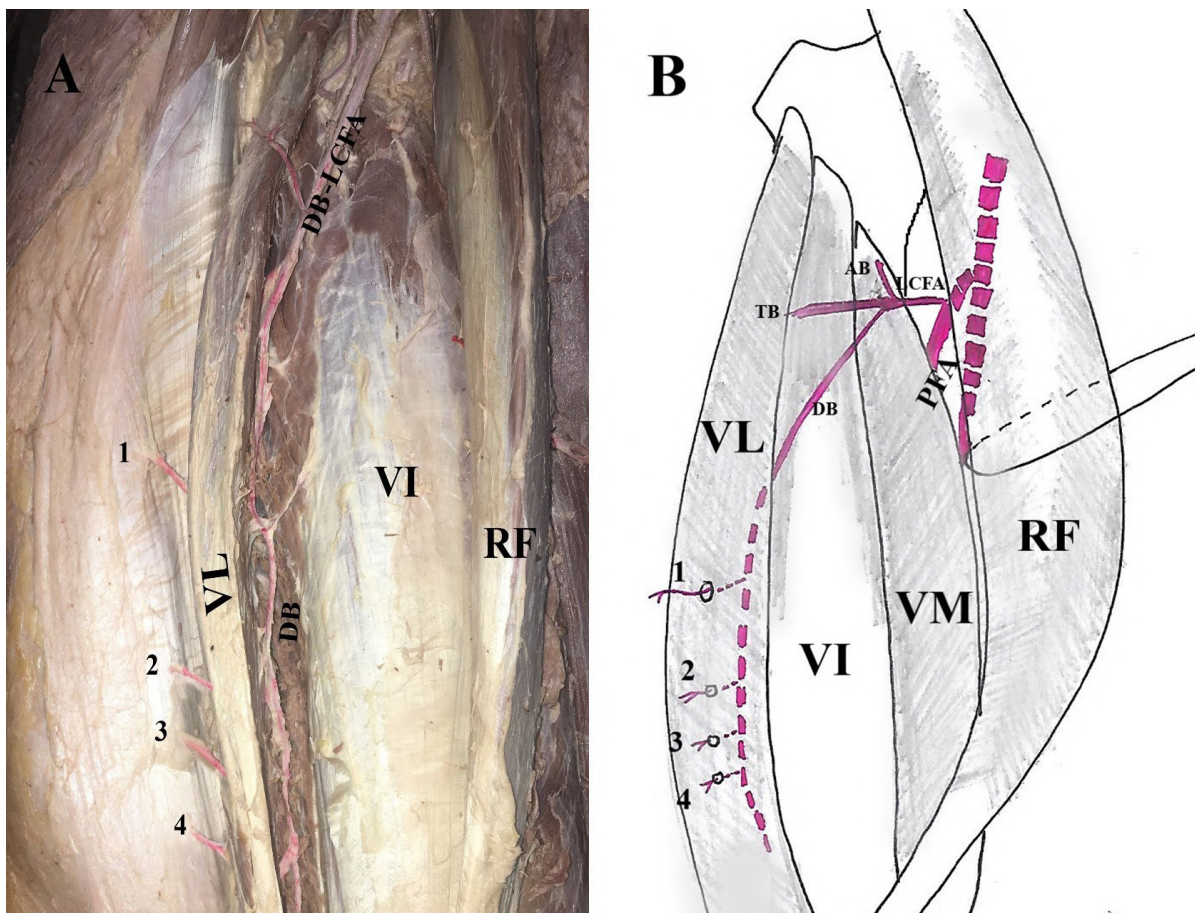
Fig. 4.- A: a photograph of the front of right thigh showing the Descending branch (DB) of lateral circumflex femoral artery (LCFA) passing between the vastus lateralis (VL) and Vastus intermedius (VI) giving off several musculocutaneous perforators (1, 2, 3, and 4) through the vastus lateralis. The rectus femoris (RF) is reflected medially., **B:** is a diagrammatic illustration. PFA: profunda femoris artery, AB: ascending branch, TB: transverse branch, VM: Vastus medialis. Sk: Skin.

Table 2. The mean length (cm), mean diameter (mm) and distance from ASIS (cm) of all identified perforators in square 2

Origin of perforator	Four musculocutaneous perforators from the DB of LCFA			
	First	**Second**	**Third**	**Fourth**
Mean length (cm)	2.4±0.2	1.69±0.1	1.38±0.2	0.6±0.1
Mean diameter (mm)	0.69±0.2	0.54±0.1	0.54±0.06	0.5±0.1
Distance from ASIS	22.15±0.4	25.3±0.7	26.9±2.3	27.5±0.6

- The lowest fasciocutaneous perforator of the DB of LCFA in all limbs.

- SLGA from the PA in all limbs.

The terminal part of the DB of LCFA in this region gives off two musculocutaneous perforators. They were located at a mean distance of 11.5±2.7 and 11±0.8 cm proximal to LTC. Their mean diameters were 0.4±0.09 and 0.5±0.5 mm and their lengths were 1.13±0.1 and 1.12±0.09 cm. The DB of LCFA gave a fasciocutaneous perforator that emerged between the tendinous part of RF and VL at a point 8.7±0.6 cm above LTC. It measured 0.5±0.1 mm in diameter and 1.4±0.1 cm in length (Fig. 5). All perforators that came from the DB of the LCFA to the anterolateral thigh skin were shown in figure 6. The perforators were 2-4 cm apart.

In all cases, the SLGA arose from the PA at a mean distance of 7.7±0.5 cm above LTC, then ran laterally in the lateral intercompartmental septum to emerge between the short head of biceps posteriorly and the VL anteriorly. It then curved anteriorly dividing into two branches to supply an area of skin overlying the VL and even continued to some distance medially over the tendinous RF. Its mean diameter was 2.1±0.06 mm and total length was 9.3±0.54 cm. (Fig. 7).

The mean length (cm), mean diameter (mm) and distance from LTC (cm) of all identified perforators in square 3 are shown in Table 3.

DISCUSSION

Many factors co-exist to define the reliability of a potential flap, such as its color, hairiness, elasticity, thickness and cutaneous sensitivity (Cormack and Lamberty, 1994). However, this study stresses the importance of sound knowledge of vascular anatomy as a cornerstone to carry out a successful tissue transfer. Anatomical studies help explore well-vascularized skin areas and prove them suitable choices as potential flaps.

Flaps have evolved from muscle-based flaps to specific perforator-based flaps. This preserves the underlying muscle, reduces donor site morbidity, and adds greater versatility to the design of a flap. Better understanding of the vascular anatomy of the skin can greatly advance and improve flap design (Mohan and Saint-Cyr, 2015).

The anterolateral thigh flap based on the DB of LCFA was first reported as a new free flap by Song et al. (1984). It was developed for widespread clinical applications by Koshima et al. (1993) and Kimata et al. (1998). It continued over the years
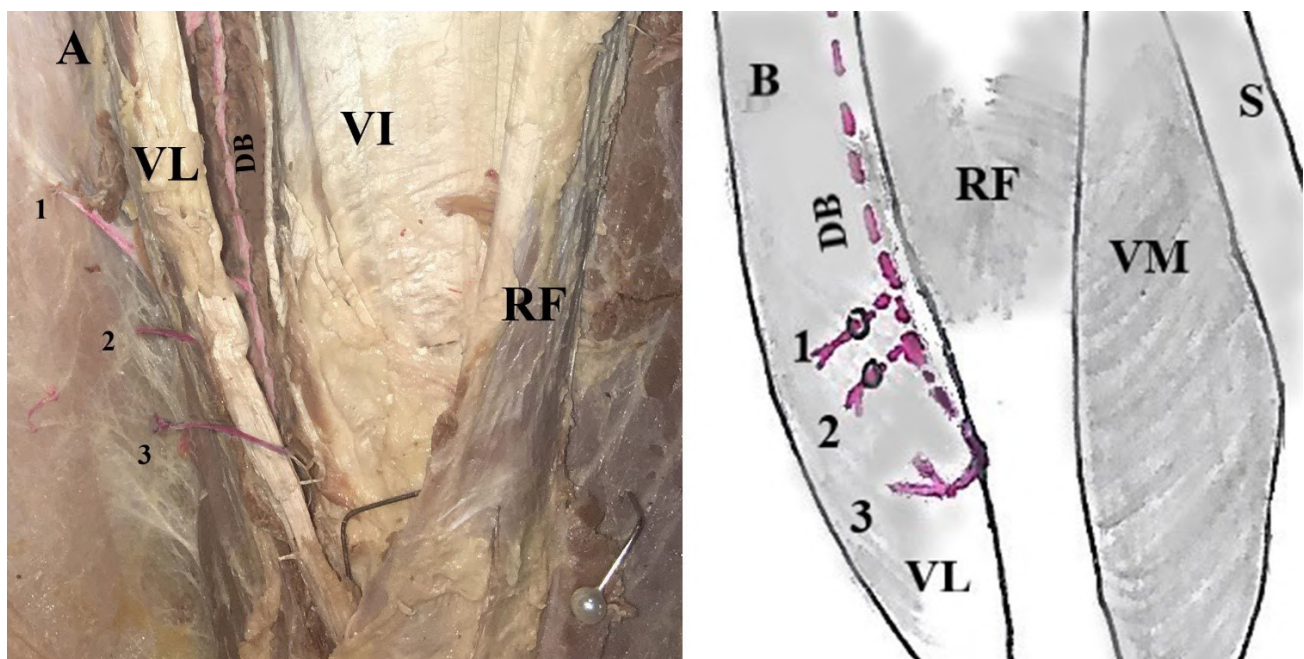
Fig. 5. A: a photograph of right thigh showing the right terminal part of the descending branch (DB) of the lateral circumflex femoral artery of LCFA giving three perforators laterally (1, 2 and 3). Perforators 1 and 2 are musculocutaneous and 3 is a fasciocutaneous perforator that passed between the lowest part of rectus femoris (RF) and vastus lateralis (VL)., **B:** is a diagrammatic illustration. VI: vastus intermedius, VM: vastus medialis, S: sartorius. Sk: Skin.

to present many advantages like its moderate thickness, and large area with availability of different tissues, which allow for aesthetic and functional refinement. It can be as thin as the radial forearm flap and hence, much preferred as a donor site since the forearm flap leaves a visible scar (Terrell et al., 2018; Succio, 2014). Yet, in many times it showed difficult dissection as the perforating arteries of the DB of the LCFA that exhibited widely different anatomic variations especially the distally-based flap (Terrell et al., 2018).

The LCFA was reported in literature to have variable origin. Cormack and Lamberty (1994) stated that 75% arose from the PFA, while the remainder arose directly from the femoral artery. They also stated that the DB may arise directly from the PFA. Maricivech et al. (2017) reported that the LCFA originated from the PFA (83%),

the common femoral artery (13.5%), and the superficial femoral artery (3.5%).

The results of the present study showed that the main LCFA arose from the PFA in all cases. It divided into its three classical branches; AB, TB and DB. The DB of the LCFA is classically described to originate deep to S and RF, then descended downwards on the medial border of the VL and intervened between it and RF, then between the VL and VI as it continued downwards to terminate inside the VL near the knee (Landuyt, 2006; Kimata et al. 1998; Yamada et al., 2014; Standring, 2008).

This study showed that the DB of the LCFA originated deep to the S and RF, then continued infero-laterally to reach the anterior border of the VL. At this point it provided OB in 26.6% of cases. It then continued downwards, sandwiched between
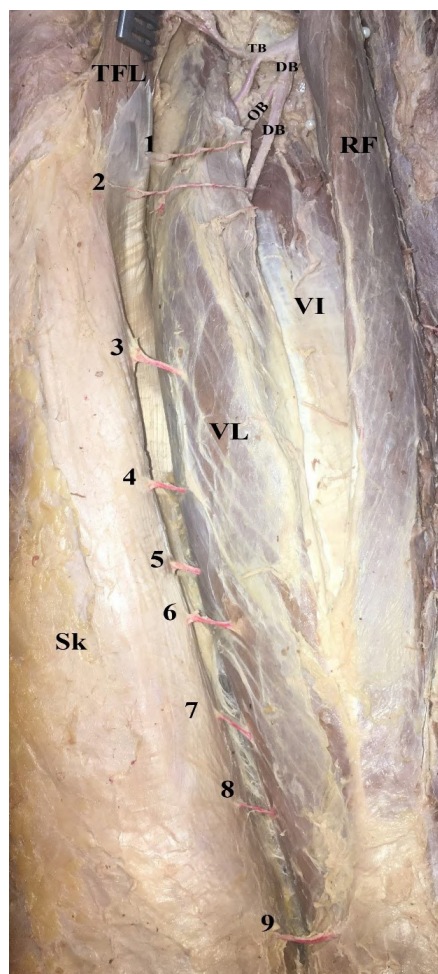
Fig. 6.- A photograph of the anterolateral aspect of right thigh showing the fasciocutaneous and musculocutaneous perforators collectively that originated from the descending branch DB of the lateral circumflex femoral artery. There are nine perforators (1 to 9). Perforators 1, 2, and 9 are fasciocutaneous. Perforator 1 originated from the oblique branch (OB) followed by perforator 2 from the main stem of the DB and perforator 9 is the lowest fasciocutaneous perforator emerging between the lowest tendinous parts of rectus femoris (RF) and vastus lateralis (VL). Perforators 3, 4, 5, 6, 7, and 8 are musculocutaneous perforators through VL. TB: Transverse branch, TFL: Tensor fasciae latae, VI: Vastus intermedius, Sk: Skin.
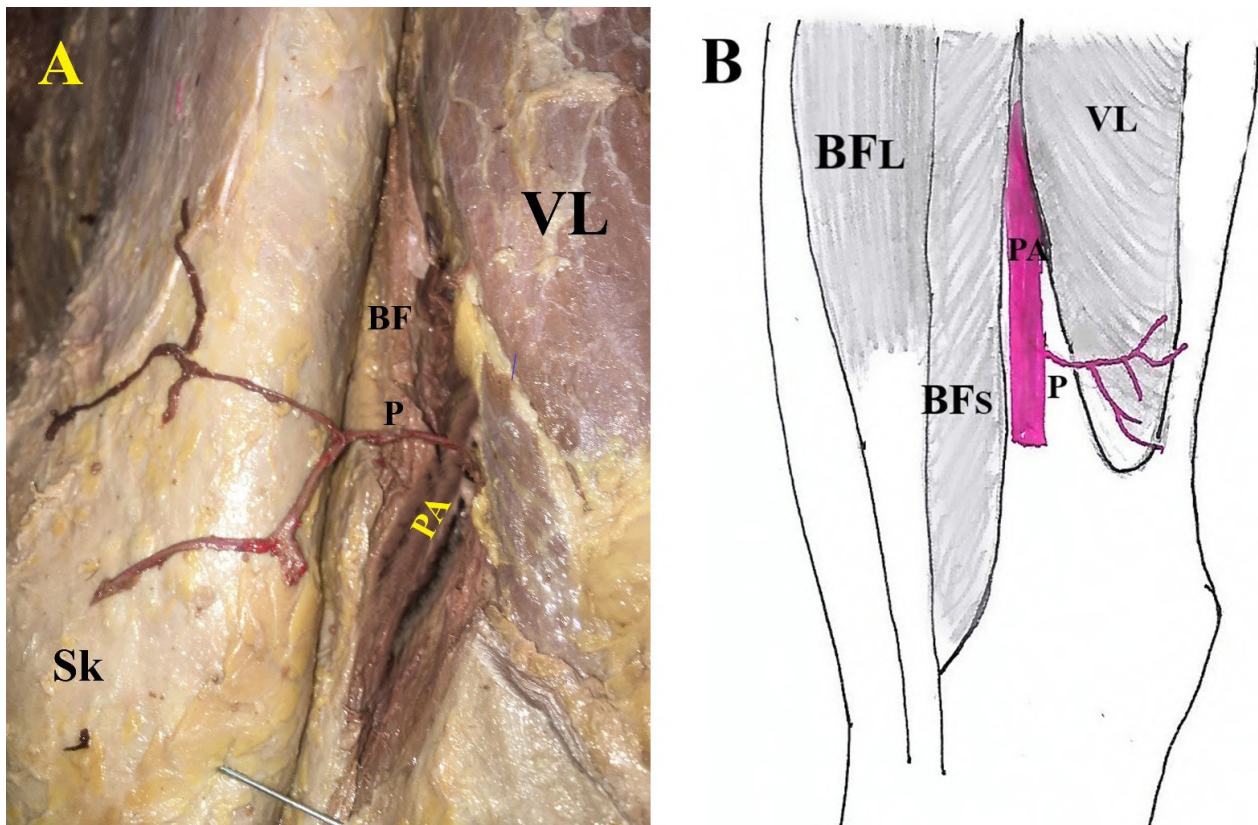
Fig. 7.- **A:** a photograph of the lower lateral area of right thigh showing the popliteal artery (PA) giving off a lateral fasciocutaneous perforator (P) between the biceps femoris (BF) and the vastus Lateralis (VL). It curved around the lower lateral border of VL dividing into two branches to supply the overlying skin (Sk)., **B:** is a diagrammatic illustration, BFL: long head of Biceps femoris, BFs: short head, IT: Iliotibial tract.

Table 3. The mean length (cm), mean diameter (mm) and distance from LTC (cm) of all identified perforators in square 3

Origin of perforator	Musculocutaneous from DB of LCFA		Lowest fasciocutaneous perforator of the DB of LCFA	SLGA from the PA
	First	Second		
Mean length (cm)	1.13±0.1	1.12±0.09	1.4±0.1	9.3±0.54
Mean diameter (mm)	0.4±0.09	0.5±0.5	0.5±0.1	2.1±0.06
Distance from LTC	11.5±2.7	11±0.8	8.7±0.6	7.7±0.5

VL and VI giving off several fasciocutaneous and musculocutaneous perforators; it finally terminated by giving its lowest fasciocutaneous perforator between the distal tendinous part of VL and RF.

Yamada et al. (2014) conducted a study on 38 cadaveric lower limbs and found that the anterolateral thigh flap received 1-7 perforators from the DB of the LCFA; 17.9% of which were fasciocutaneous and 82.1% were musculocutaneous through VL. Yu et al. (2004) developed a system to classify them according to their remoteness from the ASIS into A, most proximal; B, middle, and C, most distal.

In the present study, the squares equivalent to the classical ALTF are 2 and 3 along with the lowest part of square 1 at the distal end of the

TFL muscle. In these squares, the DB of the LCFA provided 2-10 perforators (7.76 ± 1.61), 29.1% of which were fasciocutaneous and 70.8% were musculocutaneous. The fasciocutaneous ones arose from the upper and lower ends of DB of the LCFA, while the musculocutaneous were present in the middle along most of the course of the artery. The most proximal fasciocutaneous perforators arose from the OB of DB of the LCFA in 26.6% of cases, and from the start of the DB of the LCFA in 100 % of limbs. Using Yu et al classification, all the perforators in this region could be divided into A: most proximal with a mean distance of 16.5 ± 0.5 cm, B: middle with a mean distance of 25.47±1 cm, and C: most distal with a mean distance of 29.26 ± 1.6 cm away from the ASIS.

There was considerable variation in the number of perforators identified in the ALT free flap. Two cadaver studies reported eight perforators in the explored thighs (Choi et al. 2007; Malhotra et al, 2008). Hsieh et al. (2021) conducted a study on thirty-seven patients undergoing subfacial anterolateral thigh flap, and reported an average of 3.1 perforators found on each thigh. With other clinical studies, the incidence of no perforator being found ranges from 0.89 to 5.4 percent (Lakhiani et al., 2012). In a systematic review by Lakhiani et al. (2012), where they ran an aggregate analysis of 2895 cases from all the published clinical, cadaveric, and angiographic studies, the overall incidence of perforator absence was found to be 1.8 percent. Furthermore, in another systematic review published by Smith et al. (2017) the mean number of perforators was found to be 2.1 in clinical studies and 2.7 in cadaveric studies.

Zachara et al. (2013) divided the perforators in the ALTF according to their mean external diameter into thin (less than 0.5 mm), medium (0.5-1 mm) and thick (more than 1 mm). They found in their study that 35% of the perforators were thin, 35% were medium and 29.2% were thick.

In this study, it was found that most of the perforators of the DB of the LCFA were medium-sized with a percentage of 62.2%, while 21.25 % were thin and lastly 16.3% were thick. Abdel Hamid (1994) and Cormack and Lamberty (1985) agreed that the higher perforators are thicker, and the caliber decreases from above downwards. This study conforms to this finding.

This study found that the DB of the LCFA exhibits a segmental pattern of branching, giving off its perforators at more or less fixed distances tuntil its termination. This segmentation was exploited in reconstructive surgery by Hallock (2009), who first introduced the concept of chimeric flaps. He defined this flap as that which consists of multiple independent flaps, each having an independent vascular supply, with all pedicles linked to a common source parent vessel. He stated that the ALTF is the prototype of this flap, as it can be split into smaller segments that have independent vascular supply, yet attached to one source artery; the DB of the LCFA. Chou et al.(2006) reported that two fasciocutaneous flaps associated with independent skin vessels could be reliably harvested from the same descending branch of the LCFA for the simultaneous reconstruction of two separate defects.

In addition to the DB of the LCFA, Yamada et al. (2014) stated that the anterolateral thigh is also supplied distally by a fasciocutaneous branch of the SLGA. Its branches reached as high as the midthigh point (Yamada et al., 2014). Gstoettner et al. (2019) stated that its furthest branch entered the skin at 8.8 cm above the knee joint line.

The present study found that the SLGA provided a fasciocutaneous perforator in all cases. It pierced the deep fascia at a mean distance of 7.7±0.5 cm above the LTC to continue forwards and medially. This artery provided excellent parameters in terms of length and caliber. Its mean length was 9.3±0.54 cm and its mean diameter was 2.1±0.06 mm. This long pedicle provides considerable length to the equivalent flap, which can be further extended distally to cover the upper leg defects. This flap is downward extended ALTF (DEALTF).

From the previous description of the perforators of the DB of the LCFA and the SLGA, the design of the chimeric ALTF could be illustrated (Fig. 8).

Of the very first who illustrated the definitive anatomy and clinical use of the TFL flap were Hill et al. (1978), who described it in their study as a pedicled rotation flap based on the TB of the LCFA. Little and Lyons (1983), on the other hand, stated that the main pedicle to the TFL muscle is the AB. Zufferey et al. (1988) added that the distal part of the muscle is supplied by musculocutaneous perforators that come off directly from the PFA. That is why authors like Kalandar and Morris (2019) reported that there is some confusion regarding its arterial supply, and found in their study that the muscle is mostly dependent on the AB of LCFA, and there was only one case where it presented dual blood supply from the AB and TB of LCFA. They all agreed that the skin over the TFL is supplied by musculocutaneous perforators from the underlying muscular artery. Zufferey et al. (1988) added that the skin also receives fasciocutaneous perforators from the DB.
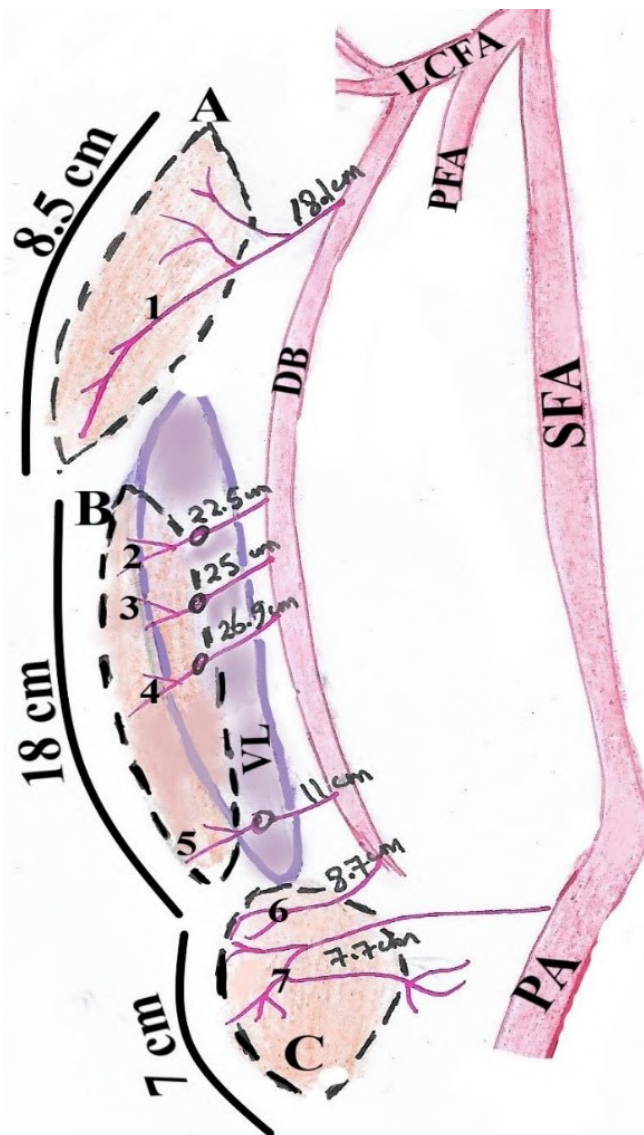
Fig. 8.- A diagrammatic picture of the possible design of the chimeric anterolateral thigh flap (ALTF) of the right thigh. Three possible ALTFs (A, B and C) can be raised. Flap A can be raised on the first fasciocutaneous perforator (1) of the descending branch (DB) of lateral circumflex femoral artery (LCFA). It took origin at a mean distance of 18.1 cm distal to the ASIS. The flap is up to 8.5 cm in length. Flap B can be raised on the musculocutaneous perforators (2, 3, 4, and 5) of the DB which took origin from it at mean distances of 22.5, 25, 26.9 cm from the ASIS and the lowest at a mean distance of 11 cm from the lateral tibial condyle (LTC). This flap can reach up to 18 cm in length. Flap C can be raised on the last fasciocutaneous perforator (6) of the DB which took origin at mean distance of 8.7 cm above the LTC, and on the lateral fasciocutaneous perforator (7) of the popliteal artery (PA) which took origin at a mean distance of 7.7 cm above the LTC. This flap can reach up to 7 cm in length. PFA: Profunda femoris artery, SFA: Superficial femoral artery.

CONCLUSION

After the accomplishment of the present work, one can conclude that: The anterolateral thigh skin is richly supplied by a mixture of the three types of perforators. The segmental nature of the perforators arising from the DB of the LCFA together with the superbly long course of the artery itself grants the famous ALTF its versatility as a chimeric flap. The highest fasciocutaneous perforator of the DB of the LCFA, which spanned squares 1 and 2, makes it a good choice for either local or free flaps. Its long pedicles warrant better mobility if used as island flap.

REFERENCES

ABDEL HAMID FAM (1994) Detailed anatomical study of musculo-fascio-cutaneous blood supply of the thigh. In: El Kalaa FA, Osman MZ, El Tahan AK (editors). Alexandria: Alex-Uni F.O. *Medicine*. Fathia Ahmed Mohamed Abdel Hamid.

CHAN JC, WARD J, QUONDAMATTEO F, DOCKERY P, KELLY JL (2014) Skin thickness of the anterior, anteromedial, and anterolateral thigh: a cadaveric study for split-skin graft donor sites. *Arch Plast Surg*, 41(6): 673-678.

CHOI SW, PARK JY, HUR MS et al (2007) An anatomic assessment on perforators of the lateral circumflex femoral artery for anterolateral thigh flap. *J Craniofac Surg*, 18(4): 866-871.

CHOU EK, ULUSAL B, ULUSAL A, WEI FC, LIN CH, TSAO CK (2006) Using the descending branch of the lateral femoral circumflex vessel as a source of two independent flaps. *Plastic Reconstr Surg*, 117: 2059-2063.

CORMACK GC, LAMBERTY BGH (1985) The blood supply of thigh skin. *Plast Reconstr Surg*, 75(3): 342-354.

CORMACK GC, LAMBERTY BGH (1994) The arterial anatomy of skin flaps. Edinburgh: Churchill Livingstone.

GEDDES CR, TANG M, YANG D, MORRIS SF (2013) Lower extremity: anatomy of the integument of the lower extremity. Perforator Flaps: Anatomy, Technique & Clinical applications. 2nd ed. Missouri: Quality Medical Publishing, p 667.

GSTOETTNER C, MAYER JA, AMAN M, SALMINGER S, BÜRGER H, HIRTLER L, WENINGER W, ASZMANN OC (2019) Cutaneous angiosome of the chimeric SLGA perforator flap: Anatomical study and clinical considerations. *J Plast Reconstr Aesthet Surg*, 72(7): 1142-1149.

HALLOCK GG (2009) Classification of flaps. In: Wei F-C, Mardini S (editors). *Flaps and Reconstructive Surgery*. Edinburgh: W.B. Saunders, pp 7-15.

HILL H, NAHAI F, VASCONEZ L (1978) The tensor fascia lata myocutaneous free flap. *Plast Reconstr Surg*, 61: 517-522.

HSIEH F, LEOW OQY, CHEONG CF, HUNG SY, TSAO CK (2021) Musculoseptocutaneous perforator of anterolateral thigh flap: a clinical study. *Plastic Reconstr Surg*, 147(1): 103e-110e.

KALANDAR A, MORRIS SF (2019) Three-dimensional vascular anatomical study of the tensor fasciae latae muscle and perforators. J Reconstr Microsurg, 35(6): 389-394.

KIMATA Y, UCHIYAMA K, EBIHARA S, NAKATSUKA T, HARII K (1998) Anatomic variations and technical problems of the anterolateral thigh flap: a report of 74 cases. Plast Reconstr Surg, 102: 1517-1523.

KOSHIMA I, FUKUDA H, YAMAMOTO H, MORIGUCHI T, SOEDA S, OHTA S (1993) Free anterolateral thigh flaps for reconstruction of head and neck defects. *Plast Reconstr Surg*, 92: 421-428.

KOSHIMA I, YAMAMOTO H, HOSODA M, MORIGUCHI T, ORITA Y, NAGAYAMA H (1993) Free combined composite flaps using the lateral circumflex femoral system for repair of massive defects of the head and neck regions. *Plast Reconstr Surg*, 92: 411-420.

LAKHIANI C, LEE MR, SAINT-CYR M (2012) Vascular anatomy of the anterolateral thigh flap: A systematic review. *Plast Reconstr Surg*, 130: 1254-1268.

LANDUYT KV (2006) The anterolateral thigh flap for lower extremity reconstruction. *Semin Plast Surg*, 20(2): 127-132.

LITTLE J, LYONS J (1983) The gluteus medius–tensor fasciae latae flap. *Plast Reconstr Surg*, 71: 366-371.

MALHOTRA K, LIAN TS, CHAKRADEO V (2008) Vascular anatomy of anterolateral thigh flap. *Laryngoscope*, 118(4): 589-592.

MARICEVICH M, BYKOWSKI M, SCHUSTERMAN M, KATZEL E, GIMBEL M (2017) Lateral thigh perforator flap for breast reconstruction: computed tomographic angiography analysis and clinical series. *J Plast Reconstr Aesthet Surg*, 70(5): 577-584.

MATHES SJ, NAHAI F (1997) The evolution of reconstructive surgery. *Semin Plast Surg*, 10: 81-88.

MOHAN A, SAINT-CYR M (2015) Anatomic and physiological fundamentals for autologous breast reconstruction. *Gland Surg*, 4: 116-133.

MORRIS SF, TAYLOR GI (2013) Fundamentals: History of perforator flap surgery. *Perforator Flaps: Anatomy, Technique & Clinical applications*. 2nd ed. Missouri: Quality Medical Publishing: 36.

MORRIS SF, TANG M, ALMUTARI K, GEDDES C, YANG D (2010) The anatomic basis of perforator flaps. *Clin Plastic Surg*, 37(4): 553-570.

PARK SO, CHANG H, IMANISHI N (2018) Anatomic basis for flap thinning. *Arch Plast Surg*, 45(4): 298-303.

SMITH RK, WYKES J, MARTIN DT, NILES N (2017) Perforator variability in the anterolateral thigh free flap: A systematic review. *Surg Radiol Anat*, 39: 779-789.

SONG YG, CHEN GZ, SONG YL (1984) The free thigh flap: a new free flap concept based on the septocutaneous artery. **Br J Plast Surg**, 37(2): 149-159.

STANDRING S (2008) Gray's Anatomy: The Anatomical Basis of Clinical Practice. 40th ed. Spain: Churchill Livingstone Elsevier, pp 1331-1334.

SUCCIO G (2014) Anatomy of lateral femoral circumflex artery perforators in planning of anterolateral thigh flap: utility of CT. Pilot study. *Anat Physiol*, 04.

TERRELL M, ROBERTS W, PRICE CW, SLATER M, LOUKAS M, SCHOBER J (2018) Anatomy of the pedicled anterolateral thigh flap for phalloplasty in transitioning-males. *Clin Anat*, 31(2): 160-168.

TIMMONS M (1985) Landmarks in the anatomical study of the blood supply of the skin. *Br J Plast Surg*, 38: 197-207.

YAMADA S, OKAMOTO H, SEKIYA I, WADA I, KOBAYASHI M, GOTO H, et al (2014) Anatomical basis of distally based anterolateral thigh flap. *J Plast Surg Hand Surg*, 48(3): 197-200.

YU P (2004) Characteristics of the anterolateral thigh flap in a Western population. *Head Neck*, 26: 759-769.

ZACHARA M, DROZDOWSKI P, WYSOCKI M, SIEWIERA I, WOJCICKI P (2013) Anatomical variability of the anterolateral thigh flap perforators between sexes: a cadaveric study. *Eur J Plast Surg*, 36(3): 179-184.

ZUFFEREY J, DOERFL J, KRUPP S (1988) The anatomical basis for delaying the musculocutaneous tensor fascia lata flap with a distal extension. *Eur J Plast Surg*, 11: 109-116.

A rare case of os paratrapezium

María Jesús Rivera Vegas[1], Francisco J. Valderrama-Canales[2]

[1] *Plastic and reconstructive Department. Hospital Universitario de Burgos. Avda. Islas Baleares, 3. 09006 Burgos. Spain*

[2] *Anatomy Department. Faculty of Medicine. Complutense University of Madrid. Plaza de Ramón y Cajal. 28040 Madrid. Spain*

SUMMARY

A rare case of an anatomical variant of the carpal bones, an os paratrapezium, is reported. Since Vesalius described the first wrist supernumerary bone in the sixteenth century, around 20 different accessory carpal bones have been identified; global references to them can be found in the literature, but previous references to the os paratrapezium are extremely scarce.

The case reported here is an incidental radiological finding, in a 69-year-old woman. After some clinical sessions and an intensive study of the available literature, any clinical, pathological, or other anatomical conditions were discarded, and the structure was identified as a paratrapezium, an accessory carpal ossicle.

A few more than twenty accessory carpal bones have been described in the literature, and its development and presence have been associated to a non-fused primary ossification centre. Occurrence of a paratrapezium within the accessory carpal bones has been reported as exceptional; however, as happens with all the carpal supernumerary ossicles, it is relevant to be aware of its existence, and to get an accurate analysis of wrist radiologic image findings to avoid both anatomical and clinical misdiagnosis.

Key words: Anatomical variants – Os paratrapezium – Carpal bones – Supernumerary carpal bones – Carpal ossicles

INTRODUCTION

Vesalius (1543) describes the first supernumerary carpal bone, later noted by Gruber (1870), and, since that, about 20 accessory bones have been described within the carpus, especially during the late nineteenth and early twentieth centuries; the opus by Bergman and colleagues (1996) review the extensive work by W. Gruber and W. Pfitzner.

Publications on carpal bone variability are above all about carpal bone coalitions (Gottschalk et al., 2016), but there are few papers about supernumerary bones. Among those scarce reports, most of the outstanding publications on supernumerary carpal bones are reviews with general descriptions and historical approaches to those pioneer nineteenth and twentieth centuries works (Bergman et al., 1996; Freyschmidt et al., 2003; Keats TE, Anderson 2013; Hayat and Loukas, 2016). Those studies reporting specific supernumerary bones mainly refer to the os centrale carpi, os styloideum, ossa epitriquetrum and hipotriquetrum, os triangularis, os hamuli propium, os radiale externum, and ossa epilunatum and hipolunatum (Bergman et al., 1996; Timins, 1999; Freyschmidt et al., 2003; Keats TE, Anderson 2013; Hayat and Loukas, 2016).

The remaining of the known accessory bones have exceptional literature reports, as is the case of the paratrapezium, that, to our knowledge,

Corresponding author:
Francisco J. Valderrama-Canales. Anatomy Department. Faculty of Medicine. Complutense University of Madrid. Plaza de Ramón y Cajal. 28040 Madrid. Spain. E-mail: fvalde@med.ucm.es

was firstly described by de Cuveland (1957), and lately referenced in a publication on the topic "carpal bones variations" (Freyschmidt et al., 2003). However, other relevant documents do not mention it (Timins, 1999; Hayat and Loukas, 2016), thus reinforcing the interest of this case report on this carpal os variant.

CASE REPORT

A 69 year-old woman admitted in the emergency department, University Hospital of Burgos (Spain), referred an accidental fall on the right hand; the physical exploration of her right forearm, wrist and hand evidenced pain and discreet functional impotence. During the follow-up, at the department of plastic and reconstructive surgery, the thenar eminence of her right hand looked elevated, but no acute inflammatory signs or redness were seen (Fig. 1A). The patient still showed discrete residual pain to the deep touch, but no alterations of the

sensitivity, vascularization, or motility in the thumb axis were found. Within simple radiology exploration, a bone-like structure was identified in the volar side, beside, but independent of, both trapezius and first metacarpal base (Fig. 1B, C). To complete the study, a multi-slice helical CT was performed, and the image evidenced an oval shaped bone-like structure (axis measures 12x16x18 mm), with clearly definable cortical and trabecular bone, close to the palmar aspect of the trapezius and the base of the first metacarpal (Fig. 1D). To confirm the diagnosis, a biopsy of the structure was performed under local anaesthesia, and the anatomical pathology results yield an histologically well-defined bone with adjacent fibrous connective tissues, with no histological signs of malignancy; hence, differential diagnoses such as osteochondroma, accompanying ossicles from reactive rhizarthrosis, or fibrous periostitis were ruled out.
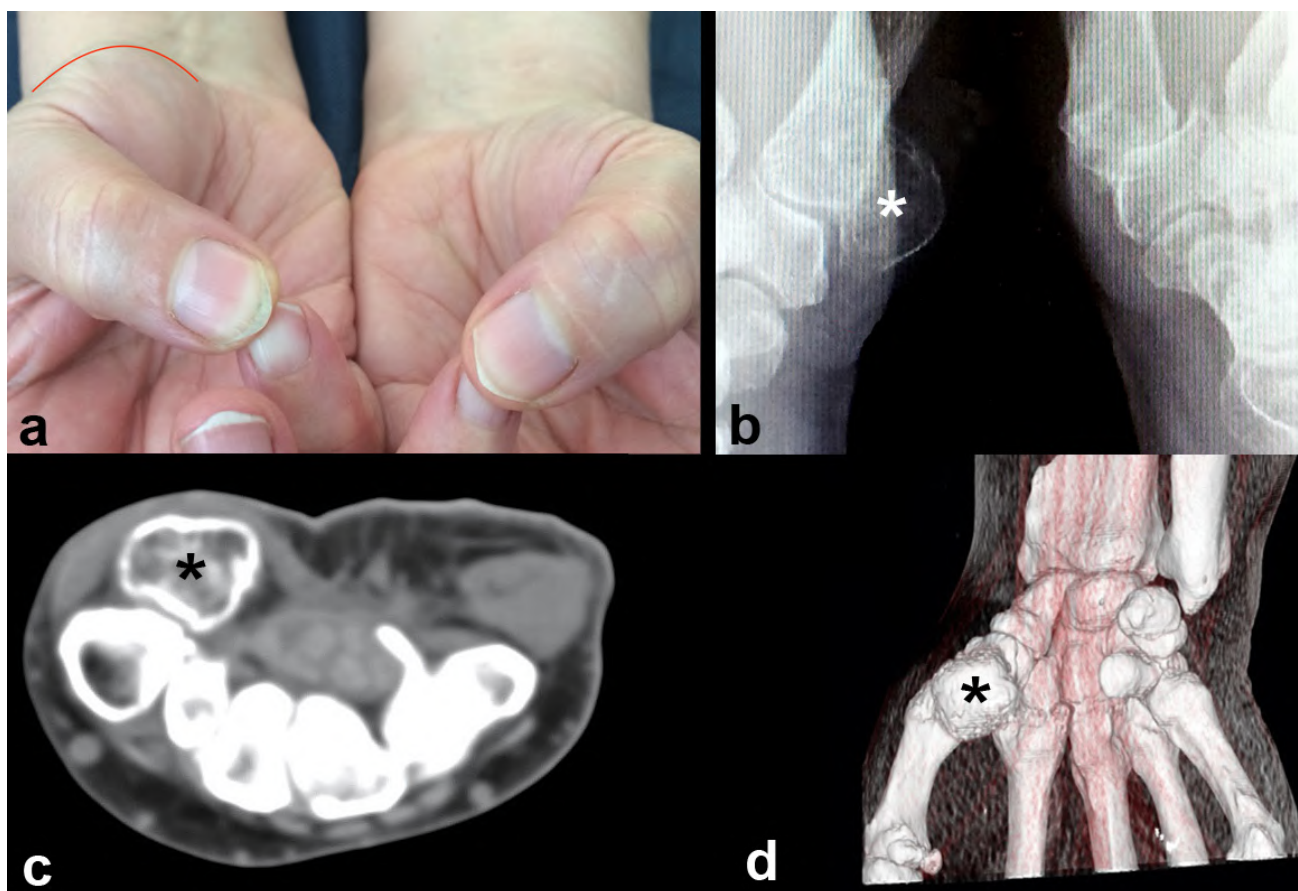
Fig. 1.- **1A.** Image of both hands of the patient. On the right thenar eminence an elevation can be observed, the red line outlining it, corresponding to the subjacent bone-like structure presence. **1B.** Radiological image of the patient's right hand in oblique projection. The bone-like structure can be observed (white asterisk) anterior both to trapezium bone and the base of the first metacarpal. **1C.** Axial CT-scan section image. The bone-like structure is an isolated supernumerary formation (black asterisk) fully independent of the surrounding adjacent bones. **1D.** Three-dimensional CT-scan reconstruction showing the anterior surface of the supernumerary bone-like structure (black asterisk).

After discussing the radiological and histological results with the patient, it was decided to adopt a conservative treatment.

DISCUSSION

The case report describes the incidental finding of a supernumerary carpal bone.

Taking into account the bone position and relationships, together with the exhaustive review of the literature on the topic, the most feasible identification of the structure is a paratrapezium bone, a rare anatomical variation (de Cuveland, 1957; Freyschmidt et al., 2003). Supernumerary bone diagnosis usually follows incidental after traumatic antecedents leading to radiologic exploration (Timins, 1999; Freyschmidt et al., 2003; Hayat and Loukas, 2016), as is the case of this report.

Including the paratrapezium, to our knowledge firstly described by de Cuveland (1957), Freyschmidt and colleagues (2003) recognize five supernumerary ossa associated to the trapezium: lateral radial, epitrapezium, secondary trapezium, secondary trapezoideum, and paratrapezium.

During discussions on the case, the clinical history, as well as the evidence from image and histopathologic studies, lead to discarded pathological structures or conditions moving to identify the bone-like formation as a supernumerary carpal bone.

The patient's medical history related a left nephrectomy –in the early nineties- due to a pyelonephritis that was under control by the urology service until 2013, with normal clinical and analytical outcomes of the remaining kidney. Biochemical parameters, reviewed between 2011 and 2019, were normal, with the exception of an insignificant elevation in the levels of uric acid that did not need any medical treatment. Within the anamnesis, the patient denied having previously had gouty tophi, in any location, or having suffered previous trauma or pain at the right wrist.

Differential diagnoses ruled out by the anatomopathological results were calcification of soft tissue, bone or soft tissue tumour, such as osteochondroma, periosteal chondroma, reactive fibrous periostitis, or Nora's disease and accompanying ossicles of reactive rhizarthrosis. Osteochondroma in the carpus are rare, with twenty-one cases reported in the literature, and just two in the trapezium (Freyschmidt et al., 2003). Other very uncommon possibilities, in the context of genetic diseases affecting the bones of the hand, as Holt-Oram syndrome, Larsen syndrome, otopalatodigital syndrome, and hand-foot-uterus syndrome (Freyschmidt et al., 2003) can be rejected as, beyond the demonstrated normal bone histology, the anatomical variation presented herein is isolated, unilateral, and not associated to any other skeletal pathological condition of the patient.

The number of carpal bones can increase or decrease by processes related to ossification centres, thus resulting in anatomical variations (Bergman et al., 1996; Timmins, 1999; Freyschmidt et al., 2003; Gottschalk et al., 2016; Hayat and Loukas, 2016). Supernumerary bones can occur due to a lack of fusion of ossification centres (bipartite bones), whereas absence of carpal bones may be due to agenesis or hypoplasia, or fusion of ossification centres belonging to different adjacent bones (Timmins, 1999; Freyschmidt et al., 2003; Senecail et al., 2007; Gottschalk et al., 2016; Hayat and Loukas, 2016). Congenital origin of the supernumerary bones is a discussed matter (Freyschmidt et al., 2003; Senecail et al., 2007) and, in fact, only in central and triangular bones the congenital origin has been confirmed (Senecail et al., 2007).

Carpal supernumerary bones are known but rare. The *os vesalianum carpi*, a small bone at the lateral aspect of the carpus adjacent to the fifth metacarpal and hamate, first described by Vesalius (1543), was not reported again, more than three centuries later, until the pioneer work by Gruber (1870); its frequency has been reported of about 0.1% (Bergman et al., 1996). According to the *os vesalianum carpi* anecdote, radiologic series indicate general incidence of carpal supernumerary bones between 0.3% (Bogart, 1932) and 1.6% (O'Rahilly, 1953).

CONCLUSION

In conclusion, within radiologists, clinicians, and anatomists, it is relevant to be aware on supernumerary carpal bones, since they can have impact in differential diagnoses among various pathologies of the wrist.

Author contributions

MJRV: identification and follow up of the case, clinical data collection, and manuscript review. FJVC: anatomical data collection, manuscript writing, and final decision on the manuscript.

REFERENCES

BERGMAN RA, AFIFI AK, MIYAUCHI RM (1996) Illustrated Encyclopedia of Human Anatomic Variations: opus V: Skeletal System. URL: https://www.anatomyatlases.org/AnatomicVariants/SkeletalSystem/Regions/UpperLimb.shtml [accessed December 2020]

BOGART FB (1932) Variations of the bones of the writs. *Am J Roentgenol*, 32: 638-646.

DE CUVELAND E (1957) Über das Paratrapezium. *Arch Orthop Unfall-Chir*, 48(6): 722-724.

FREYSCHMIDT J, BROSSMANN J, WIENS J, STERNBERG A (2003) Upper extremity. The hand. Carpus (wrist). In: Freyschmidt J, Brossmann J, Wiens J, Sternberg A (editors). *Borderlands of the normal and early pathologic in skeletal radiography*. 5th ed. New York: Thieme, pp 132-137.

GOTTSCHALK MB, DANILEVICH M, GOTTSCHALK HP (2016) Carpal coalitions and metacarpal synostoses: A Review. *Hand (NY)*, 11(3): 271-277. doi: 10.1177/1558944715614860

GRUBER W (1870) Beiträge zu den secundären Handwurzelknöchen des Menschen. *Arch Anat Physiol Wissen Med*, 490-498.

HAYAT M, LOUKAS M (2016) Radius, ulna, carpals, metacarpals, and phalanges. In: Tubbs RS, Shoja MM, Loukas M (eds). *Bergman's Comprehensive Encyclopedia of Human Anatomic Variation*. New York: Wiley Blackwell, pp 68-75.

KEATS TE, ANDERSON MW (2013) The upper extremity. The carpals. In: Keats TE, Anderson MW (eds). Atlas of Normal Roentgen Variants That May Simulate Disease. Philadelphia: Elsevier Saunders, pp 414-453.

O'RAHILLY R (1953) A survey of carpal and tarsal anomalies. *J Bone Joint Surg Am*, 35: 626-642.

SENECAIL B, PERRUEZ H, COLIN D (2007) Variations numériques et synostoses congénitales des os du carpe. *Morphologie*, 91: 2-13.

TIMINS ME (1999) Osseous anatomic variants of the wrist: findings on MR imaging. *Am J Roentgenol*, 173(2): 339-344.

VESALIUS A (1543) De humanis corporis fabrica libri septem. Basilea: Ex officina Joannis Oporini, pp 115-119.

'Y' shaped gallbladder associated with accessory cystic and hepatic arteries

Mangala M. Pai[1], Hemalatha Bangera[2], Amit Massand[3], B.V. Murlimanju[4], Latha V. Prabhu[5], Y. Lakshmisha Rao[6]

[1]Professor and Head, Department of Anatomy, Kasturba Medical College, Mangalore, Manipal Academy of Higher Education, Manipal, India.

[2]Assistant Professor, Department of Anatomy, Father Muller's Medical College, Kankanady, Mangalore, India.

[3]Tutor, Department of Anatomy, Kasturba Medical College, Mangalore, Manipal Academy of Higher Education, Manipal, India.

[4]Associate Professor, Department of Anatomy, Kasturba Medical College, Mangalore, Manipal Academy of Higher Education, Manipal, India.

[5]Professor, Department of Anatomy, Kasturba Medical College, Mangalore, Manipal Academy of Higher Education, Manipal, India.

[6]Tutor, Department of Anatomy, Kasturba Medical College, Mangalore, Manipal Academy of Higher Education, Manipal, India.

SUMMARY

We found variations in the gallbladder, hepatic artery, and cystic artery in an embalmed male cadaver in which all were noted double. Both the gallbladders had separate fundus, neck, and body, but their ducts were short and fused to form a single cystic duct. According to the literature, this pattern falls under 'Y-shaped' gall bladder. After opening the gallbladders, there were no gallstones found. It was noted that the accessory hepatic artery was also a content of the Calot's triangle. This accessory hepatic artery was branching from the coeliac artery. The accessory cystic artery was branching from the accessory right hepatic artery. The anatomical details of the hepatic artery variations are significant because, during upper abdominal surgeries, it is important to preserve the hepatic arterial supply. In laparoscopic surgeries, the knowledge of variations of the gallbladder and cystic artery is essential to prevent their iatrogenic complications, such as arterial damage and biliary tract injury. The radiologists also need to have knowledge about duplication of the gall bladder, cystic and hepatic arteries to avoid misinterpretation.

Key words: Cholecystitis – Cystic Duct – Gallbladder – Hepatic Artery

INTRODUCTION

Knowledge of variations of the gallbladder (GB) and its arterial supply is essential to laparoscopic surgeons. Double GB is an infrequent inborn anomaly, seen in 1 among 4000 live births (Boyden, 1926). If the double GB is not diagnosed beforesurgery, it could be hard for the operating surgeon to find out the exact position of the second GB (Puneet et al., 2006). Congenital malformation of the GB and its topographical variations have a greater risk of intraoperative complications, like injury to the biliary ducts during laparoscopy (Badagabettu et al., 2016). In biliary laparoscopic surgery, knowledge of the variation of cystic artery and GB are very important. It was reported

Corresponding author:
B.V. Murlimanju
flutemist@gmail.com

that the anatomical variations of GB could hinder the biliary outflow, which leads to biliary stasis. The anatomical variants of GB cause inflammation of the gall bladder, which is known as cholecystitis, and also the formation of gall stones, cholelithiasis. Failure to detect an accessory GB will affect the prognosis of a case of cholecystitis. This may result in repeated attacks of symptoms of cholecystitis (Nayak et al., 2014). Preoperative diagnosis of double GB can be done by using ultrasound abdomen, computed tomogram scan, oral cholecystogram, endoscopic retrograde cholangio pancraetogram, magnetic resonance imaging scan, and scintigraphy (Puneet et al., 2006). However, the morphological variants of GB can cause diagnostic dilemmas to the radiologist and laparoscopic surgeons (Nayak et al., 2018). Gorecki et al. (1998) had an experience of a double GB, which was identified only during a laparoscopy. In this case, they shifted from laparoscopic surgery to laparotomy to avoid complications.

The hepatic artery should not be injured in case of abdominal surgeries to avoid hepatic ischemic complications. To achieve this, the knowledge of the variant origin and branching of the hepatic artery is important. The origin of the cystic artery is often variable, and information about accessory cystic artery and variant origin of it is important in laparoscopic surgery. In this case, we report duplication of the GB, which was associated with accessory hepatic and cystic arteries, which were observed in an anatomical specimen.

CASE REPORT

In a routine dissection performed to teach medical students, it was found that the variations were obvious in the extrahepatic biliary apparatus. This was in a 60-year-old well-built and nourished male cadaver in whom the GB, hepatic artery, and cystic artery were noted double (Fig. 1). The 'Y-shaped' gallbladder associated with accessory cystic and hepatic arteries in this study is schematically represented in Fig. 2. Both the GBs were having separate fundus, neck, and body (Fig. 1), but their ducts were short and fused to form a single cystic duct (Fig. 3). The GB's were located in the single GB fossa. After opening both the GBs,
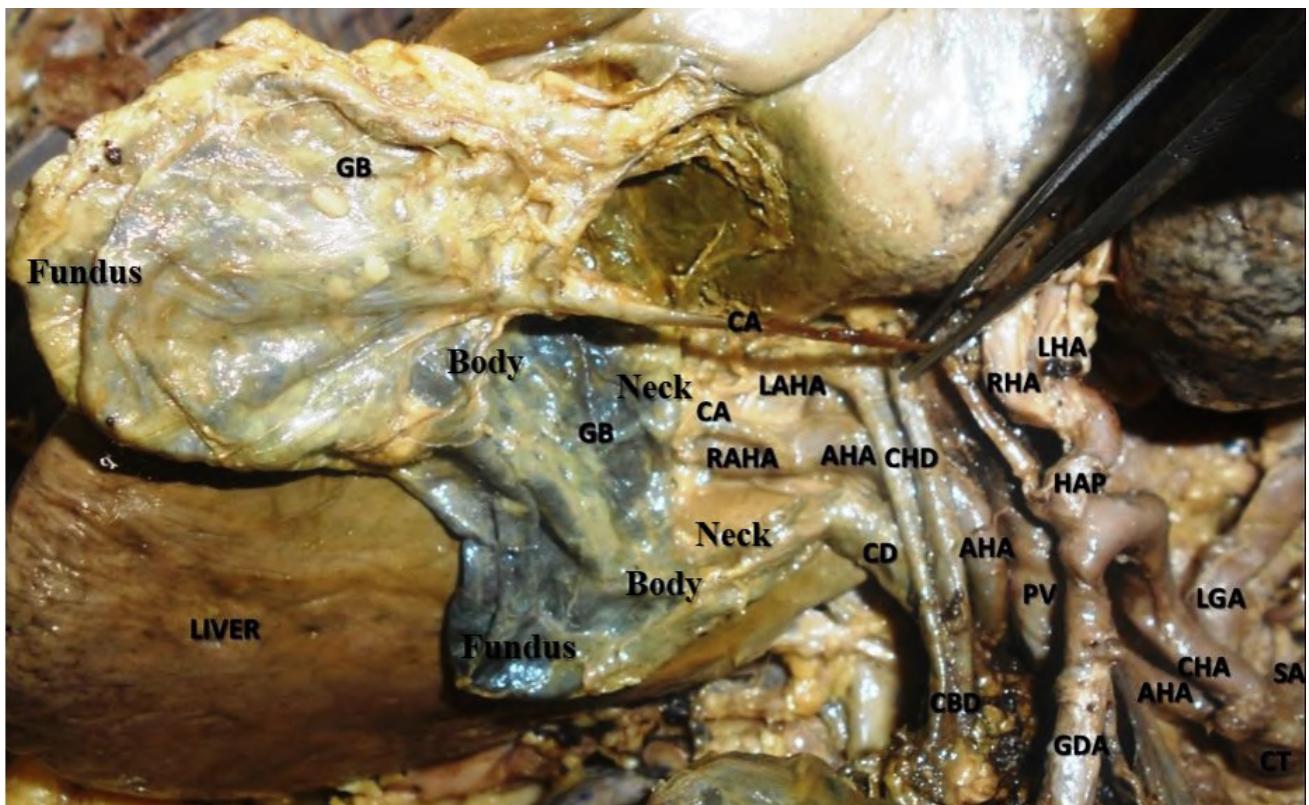
Fig. 1.- Cadaver showing double gallbladder (Y-shaped), double cystic artery and double hepatic artery. The fundus, body and neck of both the gall bladders are also visible (AHA-accessory hepatic artery, CA-cystic artery, CD-cystic duct, CBD-common bile duct, CHA-common hepatic artery, CHD-common hepatic duct, CT-coeliac trunk, GB- gall bladder, GDA-gastroduodenal artery, HAP-hepatic artery proper, LHA-left hepatic artery, LAHA-left accessory hepatic artery, LGA-left gastric artery, PV-portal vein, RHA-right hepatic artery, RAHA-right accessory hepatic artery, SA-splenic artery).

there were no gallstones found (Fig. 4) in the interior of both the gall bladders.

It was noted that the accessory hepatic artery (AHA) was an additional content of the triangle of Calot (Fig. 3). This AHA arose as an extra branch from the coeliac trunk. AHA was observed on the right side of the portal vein and left to the common bile duct (Fig. 1). AHA gave two branches as right accessory hepatic artery (RAHA) and left accessory hepatic artery (LAHA). The common hepatic artery was found normal in its origin and course. Then, it divided into the hepatic artery proper and gastroduodenal artery. Later, the hepatic artery proper gave left and right hepatic arteries near the porta hepatis (Fig. 1). There were two cystic arteries: one was too long and the other was short (Fig. 3). One of the cystic arteries branched from the hepatic artery proper and the other arose from the right accessory hepatic artery (RAHA). These two cystic arteries supplied one GB each (Fig. 3).

DISCUSSION

During the 3rd week of intrauterine life, the cells from the hepatic bud proliferate towards the septum transversum and lead to the formation of the bile duct. This small ventral outgrowth, which forms the bile duct, also contributes to the formation of the GB along with the cystic duct (Sadler, 2017). The GB developing from the caudal end of the hepatic diverticulum happens in the 4th week of development (Gotohda et al., 2000). The embryological basis of the duplication of the GB is due to unusual branching of the developing biliary tree during the division of the caudal end of the hepatic diverticulum (Kothari et al., 2005). Boyden (1926) classified the double GB morphologically into bilobed GB and true duplication. True duplication, which was noted by him, was divided into Y and H-shaped GBs. In H-shaped double GB, two cystic ducts coming from two different GB enter the common bile duct. Whereas in 'Y-shaped' GB, two cystic ducts
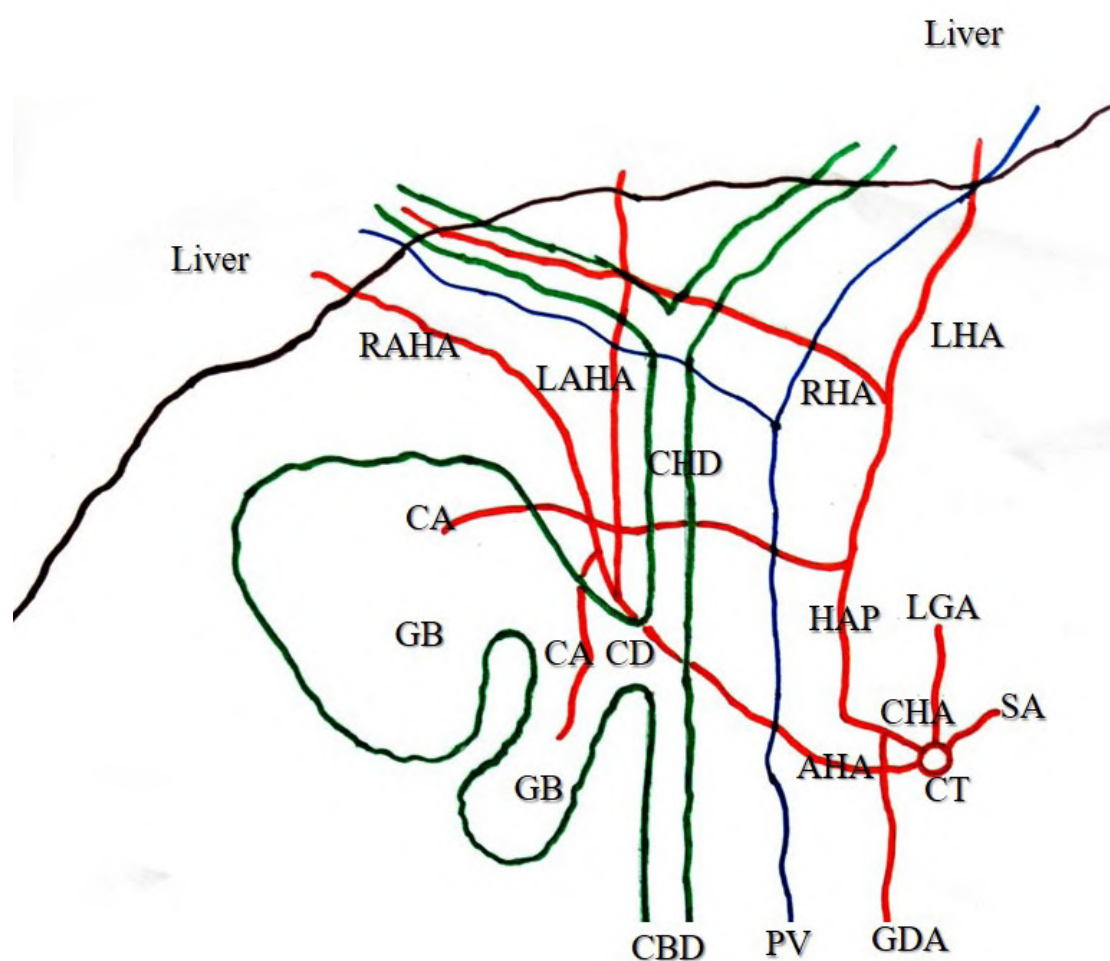
Fig. 2.- Schematic representation of the 'Y' shaped gallbladder associated with accessory cystic and hepatic arteries in this study.
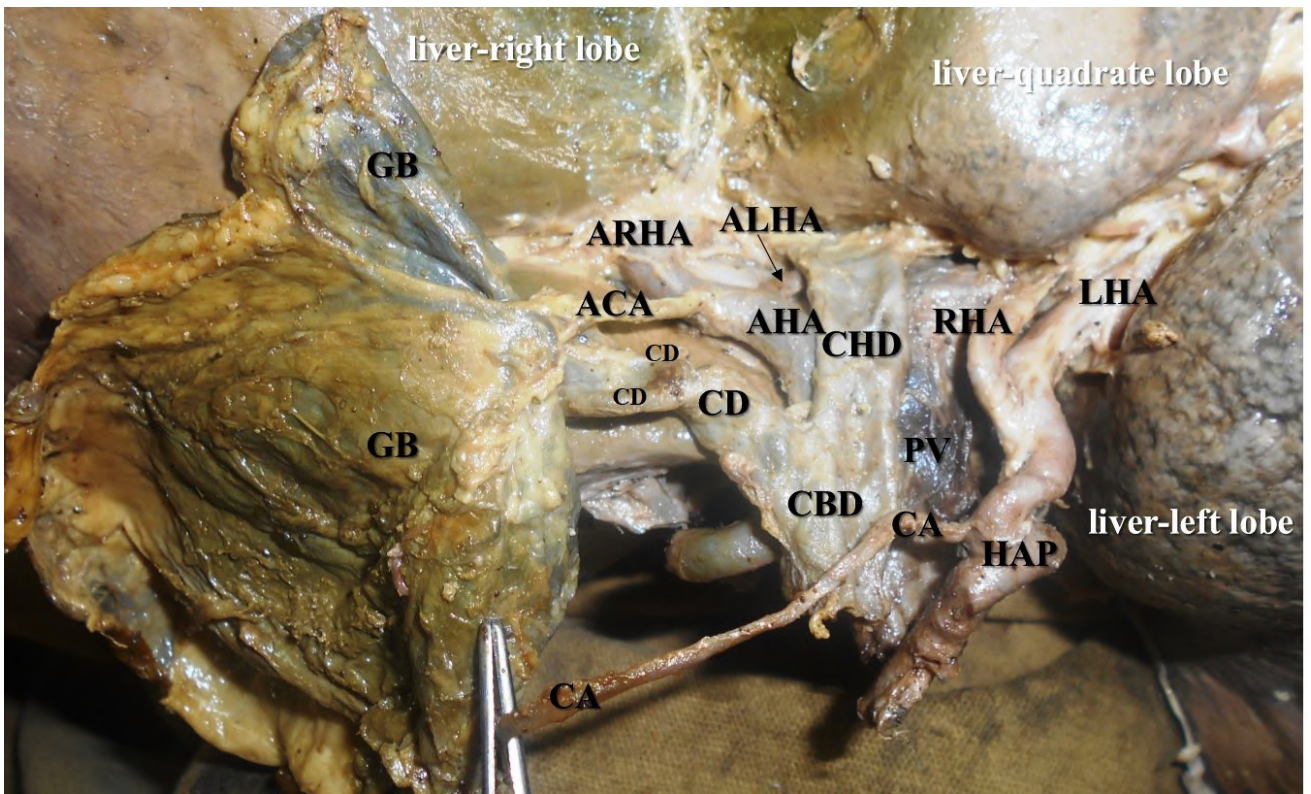
Fig. 3.- Picture of the same anatomical variation of the 'Y' shaped gall bladder, which is showing the ACA. It is clearly seen that their ducts were short and fused to form a single cystic duct (ACA-accessory cystic artery, ARHA-accessory right hepatic artery, ALHA-accessory left hepatic artery.

Fig. 4.- Showing the interior of both the gall bladders (↓) and there were no gall stones.

join together and enter into the CBD. In 'Y-shaped' GB, both the GBs occupy the single GB fossa. In the present case, it was observed that the GBs had a single cystic duct, and this morphological variant falls into 'Y-shaped' GB as per Boyden's (1926) classification. The 'Y' GB occurs when two separate GBs, each with its own cystic duct, form a common cystic duct before entering the common bile duct (Apolo Romero et al., 2018). Due to the bifurcation of primordial GB, the case of true duplication is seen in the 5th and 6th weeks of intrauterine life (Mazziotti et al., 2001).

The ultrasound evaluation of GB is routinely done for the right hypochondriac pain. This is highly sensitive in assessing the gallstones, cholecystitis and detecting anatomical variations of the GB. However, in the setting of patients with double GB, ultrasonography scanning might not rule it out from other conditions, like choledochal cyst (Apolo Romero et al., 2018). Double GB is usually asymptomatic and the chance of getting the disease in it is equal to the normal GB (Goiney et al., 1985). Gigot et al. (1997) opined that the commonest complication of double GB is cholelithiasis, which can occur either in one lobe or both lobes. The surgical removal of GB is not advised in these patients of double GB, who did not show any symptoms. However, cholecystectomy is recommended in symptomatic patients. Both the GBs should be removed at a time, even if the disease is seen only in one of the lobes.

Morphological knowledge about variations of the hepatic arterial tree-like AHA is important. During upper abdominal surgeries, it is essential to preserve the hepatic arterial supply to prevent complications like hepatic ischemia. Failure of identification of AHA can lead to iatrogenic injury to this vessel, which can lead to catastrophic bleeding. The origin of the cystic arteries is often variable. It is described as a branch of the right hepatic artery, but may also originate from the hepatic artery proper. In the present case, there were two cystic arteries, one of them branching from the RAHA, and the other from the hepatic artery proper. Rupture of cystic arteries can cause bleeding in the operation site and may obscure the laparoscopic view.

The most commonly performed laparoscopic procedure today is cholecystectomy (Rajapandian et al., 2017). The morphological knowledge about the double GB, accessory cystic and hepatic arteries may help laparoscopic surgeons if these are not diagnosed preoperatively. This has potential implications intraoperatively and postoperatively. It is suggested to perform an intraoperative cholangiogram during the cholecystectomy procedure for the better delineation of biliary tree anatomy. This can prevent catastrophic vasculo-biliary complications (Rajapandian et al., 2017).

The morphological information on twofold GB, accessory hepatic, and cystic arteries can diminish the dangers of inconveniences because of biliary and blood vessel damage. The iatrogenic injury to the common bile duct or other important nearby structures can be prevented (Apolo Romero et al., 2018). Knowledge about the variations of the hepatobiliary region is enlightening to the advanced surgical techniques and modern technology. This will reduce the risk encountered during the surgical procedures in this region.

CONCLUSION

We believe that the present report is enlightening to the laparoscopic surgeons and radiologists to prevent misinterpretations and subsequent complications.

REFERENCES

APOLO ROMERO EX, GÁLVEZ SALAZAR PF, ESTRADA CHANDI JA, GONZÁLEZ ANDRADE F, MOLINA PROAÑO GA, MESÍAS ANDRADE FC, CADENA BAQUERO JC (2018) Gallbladder duplication and cholecystitis. *J Surg Case Rep*, 7: 1-3.

BADAGABETTU SN, PADUR AA, KUMAR N, REGHUNATHAN D (2016) Absence of the celiac trunk and trifurcation of the common hepatic artery: a case report. *J Vasc Bras*, 15: 259-262.

BOYDEN EA (1926) The accessory gallbladder. An embryological and comparative study of aberrant biliary vesicles occurring in man and in domestic mammals. *Am J Anat*, 38: 177.

GIGOT J, VAN BEERS B, GONCETTE L, ETIENNE J, COLLARD A, JADOUL P, THERASSE A, OTTE JB, KESTENS P (1997) Laparoscopic treatment of gallbladder duplication. A plea for removal of both gallbladders. *Surg Endosc*, 11: 479-482.

GOINEY RC, SCHOENECKER SA, CYR DR, SHUMAN WP, PETERS MJ, COOPERBERG PL (1985) Sonography of gallbladder duplication and differential considerations. *AJR Am J Roentgenol*, 145: 241-243.

GORECKI PJ, ANDREI VE, MUSACCHIO T, SCHEIN M (1998) Double gallbladder originating from left hepatic duct: a case report and review of literature. *JSLS*, 2: 337-339.

GOTOHDA N, ITANO S, HORIKI S, ENDO A, NAKAO A, TERADA N, TANAKA N (2000) Gallbladder agenesis with no other biliary tract abnormality: report of a case and review of the literature. *J Hepatobiliary Pancreat Surg*, 7: 327-330.

KOTHARI PR, KUMAR T, JIWANE A, PAUL S, KUTUMBALE R, KULKARNI B (2005) Unusual features of gall bladder duplication cyst with review of the literature. *Pediatr Surg Int*, 21: 552-554.

MAZZIOTTI S, MINUTOLI F, BLANDINO A, VINCI S, SALAMONE I, GAETA M (2001) Gallbladder duplication: MR cholangiography demonstration. *Abdom Imaging*, 26: 287-289.

NAYAK SB, SHETTY SD, SURENDRAN S, JETTI R, KUMAR N, SIRASANAGANDLA SR (2014) Double gallbladder completely enclosed in a cystogastric fold of peritoneum. *Anat Cell Biol*, 47: 132-134.

NAYAK SB, AITHAL AP, PADAVINANGADI A, PRABHU G (2018) Double pouched, sigmoid gallbladder that can cause a diagnostic dilemma to radiologists: a case report. *Anat Cell Biol*, 51: 209-211.

PUNEET, TIWARY SK, AGARWAL S, SINGH S, KHANNA A (2006) *Double gallbladder*. *Internet J Gastroenterol*, 4: 2.

RAJAPANDIAN S, JANKAR SV, NAYAK DS, CHITTAWADGI B, SABNIS SC, SATHYAMOORTHY R, PARTHASARATHI R, SENTHILNATHAN P, RAJ PP, PALANIVELU C (2017) Laparoscopic management of 'Y-shaped' gallbladder duplication with review of literature. *J Minim Access Surg*, 13: 231-233.

SADLER TW (2017) Langman's Medical Embryology. 13th ed. New Delhi: Wolters Kluwer, p 236.

Coverage of anatomical discoveries in the Dutch-speaking popular press

Jelle Stans

Affiliated researcher, Institute for Globally Distributed Open Research and Education, Beringen, Belgium

INTRODUCTION

Anatomical discoveries often draw interest not only from the scientific community but also from the general public. The lay audience usually does not obtain information about these developments through the academic literature, but through the popular press. Therefore, there is an important role for popular science journalism to correctly inform the public about new advances in the field of anatomy and its subdisciplines. This means that, on one side, technical language can be transformed into information that everybody can digest, opening up research to the general public. On the other hand, there is also the risk of misrepresenting the research findings and, therefore, misinformation about the discoveries that were made.

As a small case study, the Dutch-speaking literature from Belgium (Flanders) and the Netherlands was searched regarding three different recent anatomical studies: (1) the description of the anterolateral ligament of the knee (Claes et al., 2013), (2) the description of the re-classification of the mesentery as an organ (Coffey and O'Leary, 2016); (3) the description of the interstitium (Benias et al., 2018). For each of these cases, a brief comparison was made between the original publication and relevant popular reports of the findings. Where relevant, academic replies by other authors are discussed.

ANTEROLATERAL LIGAMENT

In 2013, Claes and colleagues published on the anatomical aspects of the anterolateral ligament situated at the knee after a cadaveric study (Claes et al., 2013). Little Dutch-language press coverage in the same year was identified. However, in 2018 the local network *TV Limburg* reported on a new type of operation on the anterior cruciate ligament that also involved the anterolateral ligament (Rondags, 2018). Here, it was mentioned that the team of Dr Bellemans discovered the ligament five years earlier. He also elaborated briefly on this discovery in an interview with *Het Laatste Nieuws* (Heylen, 2019). Perhaps due to the nature of the popular coverage of the findings, no link was made to the original publication. However, the conclusion of the findings and their clinical implications were discussed thoroughly. Less attention was given to the nature of the study itself. All reports of the finding spoke about the discovery of a new ligament, while the publication itself is more nuanced and talks about the first detailed anatomical description (Claes et al., 2013).

Corresponding author:
Jelle Stans
jelle.stans@hotmail.be

MESENTERY

In 2016, Coffey and O'Leary stated that insights into anatomical and functional characteristics warranted the classification of the mesentery as an organ. This idea was further developed in 2020 (Coffey et al., 2020). This statement has been controversial and has been challenged by authors such as Neumann (2018). An article by *Gazet van Antwerpen* (MTM, 2017) reported on this publication as the discovery of a new organ of the digestive tract. Additionally, the article states that the mesentery was discovered by Da Vinci and afterwards ignored until recent times. The Flemish public broadcaster *VRT* also published an article about the publication (De Roy, 2017). This article reports about the classification of the mesentery as a new organ. An article in the *De Morgen* and *De Volkskrant* provided a critical view on the statement that a new organ was discovered and went more in depth into the specific positions (Veldhuizen, 2017a, b). The statement that the mesentery was ignored since Da Vinci is very strong and should perhaps be nuanced. Obviously, the mesentery has been the subject of research over the years (Soffers et al., 2015; Li et al., 2016). The fact that this publication convincingly showed that the mesentery should be regarded as an organ has been challenged by several authors (Neumann, 2018; Spasov et al., 2019). This information was often omitted from the popular coverage.

INTERSTITIUM

In 2018, Benias and colleagues described the macroscopic and microscopic anatomical characteristics of the interstitium. An article in *Het Nieuwsblad* explained the findings and provided insights into its applications in cancer research (ADB, 2018). The article correctly states that there was still disagreement within the scientific community whether or not the interstitium concerns an organ in its own right. A similar remark was made by *Algemeen Dagblad* (Naber, 2018). Several academic authors questioned the re-classification of the interstitium as an organ (Neumann, 2018; Mubarak, 2018). *Het Laatste Nieuws* stated that no new organ was discovered, but that its structure was elucidated (LB, 2018).

The article stated that the scientists claimed that a new organ was discovered. Interestingly, however, there is no proposal for re-classification of the interstitium as an organ in the original publication.

CONCLUSION

A few conclusions can be drawn from these observations. First of all, several of the popular press articles described the discussed findings as the discovery of new organs or the re-classification as organs of existing structures. These statements are controversial by themselves. Neumann, for example, stated that new organ discoveries in gross anatomy are unlikely (MTM, 2017). This was, however, often clarified in the articles. A second observation is that, in this case study, the popular science articles often did not refer to the original publication. Therefore, it may not be easy for readers to verify the claims made. However, lay people may not have access to the original articles, due to the need for journal subscriptions, even if they did manage to find the originals. Lastly, and perhaps most importantly, it is clear that a lot of the popular press coverage relating the anatomical findings explained them in lay language, and discussed potential scientific and clinical implications. Further research could be conducted to assess whether the same conclusions can be drawn from popular coverage in other languages.

REFERENCES

ADB. (2018, 28 March). Ontdekking van nieuw "orgaan" kan helpen in de strijd tegen kanker. *Het Nieuwsblad*. https://www.nieuwsblad.be/cnt/dmf20180328_03434287

BENIAS PC, WELLS RG, SACKEY-ABOAGYE B, KLAVAN H, REIDY J, BUONOCORE D, MIRANDA M, KORNACKI S, WAYNE M, CARR-LOCKE DL, THEISE ND (2018) Structure and distribution of an unrecognized interstitium in human tissues. *Sci Rep*, 8(1): 4947. https://doi.org/10.1038/s41598-018-23062-6.

CLAES S, VEREECKE E, MAES M, VICTOR J, VERDONK P, BELLEMANS J (2013) Anatomy of the anterolateral ligament of the knee. *J Anat*, 223(4): 321-328. https://doi.org/10.1111/joa.12087

COFFEY JC, O'LEARY DP (2016) The mesentery: structure, function, and role in disease. *Lancet Gastroenterol Hepatol*, 1(3): 238-247. https://doi.org/10.1016/S2468-1253(16)30026-7

COFFEY JC, WALSH D, BYRNES KG, HOHENBERGER W, HEALD RJ (2020) Mesentery – a 'New' organ. *Emerg Top Life Sci*, 4(2): 191-206. https://doi.org/10.1042/ETLS20200006

DE ROY L (2017, 03 January) Het menselijk lichaam heeft er officieel een orgaan bij. VRT. https://www.vrt.be/vrtnws/nl/2017/01/03/het_menselijk_lichaamheefterofficieeleenorgaanbij-1-2858953/

HEYLEN S (2019, 27 January) Kniechirurg Johan Bellemans neemt in 'Topdokters' geen blad voor de mond: "Mijn ontslag bij Gasthuisberg, dat was de inquisitie zelve". *Het Laatste Nieuws*. https://www.hln.be/tv/kniechirurg-johan-bellemans-neemt-in-topdokters-geen-blad-voor-de-mond-mijn-ontslag-bij-gasthuisberg-dat-was-de-inquisitie-zelve-br-br~a78bd3f8f/

LB. (2018, 28 March) Interstitium: geen "nieuw orgaan", maar nieuwe inzichten openen wel perspectieven. *Het Laatste Nieuws*. https://www.hln.be/medisch/interstitium-geen-nieuw-orgaan-maar-nieuwe-inzichten-openen-wel-perspectieven~a9cbf599/

LI Y, ZHU W, ZUO L, SHEN B (2016) The role of the mesentery in Crohn's disease: the contributions of nerves, vessels, lymphatics, and fat to the pathogenesis and disease course. *Inflamm Bowel Dis*, 22(6): 1483-1495. https://doi.org/10.1097/MIB.0000000000000791

MTM. (2017, 04 January). Nieuw orgaan in het menselijk lichaam ontdekt. *Gazet van Antwerpen*. https://www.gva.be/cnt/dmf20170104_02657169

MUBARAK H (2018) The interstitium (the pre-lymphatic region), is it a newfound 'Organ'. *Iraqi JMS*, 16(3): 230-231.

NABER C (2018, 28 March) Wetenschappers ontdekken 'nieuw orgaan' in menselijk lichaam. *Algemeen Dagblad*. https://www.ad.nl/buitenland/wetenschappers-ontdekken-nieuw-orgaan-in-menselijk-lichaam~a8ca2330/

NEUMANN PE (2018) Another new organ! is this a golden age of discovery in anatomy? *Clin Anat*, 31(5): 648-649. https://doi.org/10.1002/ca.23184

RONDAGS L (2018, 10 September) Nieuwe techniek voor knie-operatie van ZOL minimaliseert risico op complicaties. *TV Limburg*. https://www.tvl.be/nieuws/nieuwe-techniek-voor-knie-operatie-van-zol-minimaliseert-risico-op-complicaties-65121

SOFFERS JH, Hikspoors JP, Mekonen HK, Koehler SE, Lamers WH (2015) The growth pattern of the human intestine and its mesentery. *BMC Dev Biol*, 15: 31. https://doi.org/10.1186/s12861-015-0081-x

SPASOV T, POP-TRAYKOVA L, ISOSKI D, IVANOVA I, DIMITROV N (2019) Mesentery – A new or already known human organ. *Trakia J Sci*, 17(Suppl 2): 100-102.

VELDHUIZEN R (2017a, 16 January) Artsen ontdekken nieuw orgaan: klopt dit wel?. *De Morgen*. https://www.demorgen.be/nieuws/artsen-ontdekken-nieuw-orgaan-klopt-dit-wel~b7031335/

VELDHUIZEN R (2017b, 16 January) Artsen ontdekken nieuw orgaan: klopt dit wel?. *De Volkskrant*. https://www.volkskrant.nl/nieuws-achtergrond/artsen-ontdekken-nieuw-orgaan-klopt-dit-wel~b1a00596/#:~:text=Vandaag%3A%20artsen%20hebben%20een%20nieuw%20orgaan%20ontdekt.&text=Komen%20ze%20nu-%20mee.,te%20hebben%20ontdekt%3A%20het%20mesenterium.

The Relevance of Terminologia Anatomica and the Federative International Programme of Anatomical Terminology (FIPAT)

R. Shane Tubbs

Professor of Neurosurgery, Neurology, Surgery, Otolaryngology, and Structural and Cellular Biology. Tulane University School of Medicine, New Orleans, Louisiana, USA

Dear Editor,

The Federative International Programme of Anatomical Terminology (FIPAT) is one of many committees/programs of the International Federation of Associations of Anatomists (IFAA), which was founded in 1903. Other committees include those related to education, scientific publications, anatomical research, equality and diversity, and ethics and medical humanities. These various groups are overseen by the IFAA Executive Committee composed of a president, past president, secretaries, treasurer, and the chairs of the other committees and Programs.

FIPAT is composed of a chair, secretary, working groups and their leaders. The working groups are made up of approximately 50 members from anatomists from around the world. Drafts of the Terminologies arise in the specific working groups and are reviewed by the group, leaders of the other FIPAT committees, the IFAA Executive, and finally, approved by Member Societies with final approval given by the General Assembly of the IFAA. The Terminologies serve as the internationally agreed upon official anatomical nomenclature.

As all anatomists will undoubtedly agree, it is very important to have a standardized reference for terminology in the anatomical sciences. As anatomical terms can vary from country to country, a dedicated go-to source for official terminology is important when communicating with a global audience e.g., peer review publications. Additionally, often, the anatomical terminology used by clinicians can vary and often uses non-standard terminology e.g., eponyms. Therefore, without a standardization of anatomy terms, the potential for a tower of Babel might occur. As unequivocal communication is so essential in the descriptive nature of the anatomical sciences, standardization is of paramount importance.

For the IFAA terminologies, Latin is the official language. There are many reasons for this, and in some countries Latin terms are used for teaching and communication in the anatomical sciences e.g., textbooks. For the Terminologies, which are readily found online (https://fipat.library.dal.ca/TA2/), one can find a seven-column system (Fig. 1). The first column is used to provide a unique identification number to the anatomical term. The second column lists the official Latin term for the anatomical structure. Following this, in a third

column, when a Latin synonym exists, it is listed. Columns four and five list the British and US English spellings of the term, respectively. Finally, in the seventh column, an English synonym, when appropriate, is listed and includes any common eponyms.

An initial move forward in regard to standardization of anatomical terminology came by way of the Basel *Nomina Anatomica*, which was approved in 1895 by the Congress of the Anatomische Gesellschaft. This would be followed by revisions in 1933 and 1935 in Birmingham and Jena, respectively. Later, in 1950, the International Anatomical Nomenclature Committee (IANC) was established by the IFAA. Then, in 1955, *Nomina Anatomica* was approved in Paris at the sixth Congress meeting. *Nomina Anatomica* would go through several editions in the 1960s, 1970s, and 1980s, with the latter including Nomina Histologica and *Nomina Embryologica*. In the late 1980s, a dispute between the IFAA and IANC resulted in a sixth edition of *Nomina Anatomica* being published, but without IFAA approval. Derived from this dispute, in 1998, *Terminologia Anatomica* was produced by the Federative Committee on Anatomical Terminology (FCAT), a committee of the IFAA. In 1999, FCAT was changed to Federative International Committee on Anatomical Terminology (FICAT),

which is now, since 2009, known as FIPAT. FIPAT has produced *Terminologia Embryologica*, first and second editions, *Terminologia Neuroanatomica*, and in 2019, TA2. TNA, TE2 and TA2 are all available online. Currently, a second edition of *Terminologia Histologica* is underway in addition to several newer terminologies including *Termionologia Oroanatomica and Terminologia Anatomica Anthropologica*.

Unlike in the past, where a print copy of the book was necessary and the required index searching, which was inconvenient, the online archive for the Terminologies allows them to be 'living documents', includes errata sections, and includes a TA2 Viewer. To increase the use and ease of accessing TA, the TA2 Viewer is now available (https://ta2viewer.openanatomy.org). This is a searchable, dynamic web application of TA2, and is a collaboration between the IFAA and the Open Anatomy Project at the Brigham and Women's Hospital (Boston, USA). The Viewer is a powerful tool not only for searching TA2; it also includes links to the use of the term on various search engines e.g., Google. Additionally, links to Medical Subject Headings (MeSH) terms, important online resources such as *Gray's Anatomy* (20thedition) published in Philadelphia in 1918, and informatics sites such as the Foundational Model of Anatomy (FMA) from the Structural Informatics Group

		Latin term	Latin synonym	UK English	US English	English synonym	Other
351		Systemata musculoskeletalia		Musculoskeletal systems	Musculoskeletal systems		
352		Systema skeletale	Skeleton	Skeletal system	Skeletal system	Skeleton	Sceletum *Endnote 56*
353		**SKELETON AXIALE**		**AXIAL SKELETON**	**AXIAL SKELETON**		Sceletum axiale
354		Neurocranium		Neurocranium	Neurocranium		Brain box; Cranium cerebrale
355		Viscerocranium		Viscerocranium	Viscerocranium		Cranium viscerale
356		Ossa faciei		Facial bones	Facial bones		Cranium faciale; Skeleton faciei; Skeleton faciale; Facial skeleton
357		Chondrocranium		Chondrocranium	Chondrocranium		
358		Desmocranium		Desmocranium	Desmocranium		
359		**SKELETON APPENDICULARE**		**APPENDICULAR SKELETON**	**APPENDICULAR SKELETON**		Sceletum appendiculare
360		Skeleton membrorum superiorum		Skeleton of upper limbs	Skeleton of upper limbs		
361		Cingulum pectorale	Cingulum membrorum superiorum	Pectoral girdle	Pectoral girdle	Upper limb girdle; Shoulder girdle	Cingulum membri superioris; Cingulum extremitatum superiorum; Cingulum extremitatum thoracicarum
362		Skeleton partis liberae membri superioris	Skeleton membri superioris liberi	Skeleton of free upper limb	Skeleton of free upper limb		Skeleton extremitatis superioris liberae; Skeleton extremitatis thoracicae liberae
363		Skeleton membrorum inferiorum		Skeleton of lower limbs	Skeleton of lower limbs		
364		Cingulum pelvicum	Cingulum membrorum inferiorum	Pelvic girdle	Pelvic girdle	Lower limb girdle	Cingulum membri inferioris; Cingulum extremitatum inferiororum; Cingulum extremitatum pelvinarum
365		Skeleton partis liberae membri inferioris	Skeleton membri inferioris liberi	Skeleton of free lower limb	Skeleton of free lower limb		Skeleton extremitatis inferioris liberae; Skeleton extremitatis pelvinae liberae
366		**OSSA**		**BONES**	**BONES**		Osteologia
367		Os membranaceum		Membranous bone	Membranous bone	Membrane bone	
368		Os endochondrale		Endochondral bone	Endochondral bone	Cartilaginous bone	
369		Os longum		Long bone	Long bone		
370		Os breve		Short bone	Short bone		
371		Os planum		Flat bone	Flat bone		
372		Os irregulare		Irregular bone	Irregular bone		
373		Os pneumaticum		Pneumatised bone	Pneumatized bone		
374		Os sesamoideum		Sesamoid bone	Sesamoid bone		

Fig. 1.- Example of the seven-column system found in TA2. Note that this same system is used throughout the IFAA Terminologies.

are included. The reader is encouraged to take advantage of this resource.

Anatomical terminology must avoid ambiguity. To this end, the standardized and internationally agreed upon nomenclature provided by the IFAA's Terminologies is important not only to the anatomist but also practitioners of medicine and the lay public. Although a single collection of tens of thousands of terms will never be perfect (Chmielewski and Domagała, 2020), constantly revising and reevaluating the IFAA's Terminologies will help to keep these terms relevant now and into the future (Neumann et al., 2017a; Neumann et al., 2017b; Neumann et al., 2020).

 Sincerely,

Shane Tubbs

Chair, FIPAT

REFERENCES

CHMIELEWSKI PP, DOMAGAŁA ZA (2020) Terminologia Anatomica and its practical usage: pitfalls and how to avoid them. Folia Morphol (Warsz), 79(2): 198-204.

NEUMANN PE, BAUD R, SPRUMONT P (2017a) Ordering by the numbers in anatomy and by letters Too. Clin Anat, 30(6): 700-702.

NEUMANN PE, BAUD R, SPRUMONT P (2017b) Human anatomy nomenclature rules for the computer age. Clin Anat, 30(3): 300-302.

NEUMANN PE, GEST TR, TUBBS RS (2020) The principles of anatomical nomenclature revision: They're more like guidelines anyway. Clin Anat, 33(3):327-331.

Author Index to Volume 25, 2021